

Nanoparticles Mimicking Viral Infections: Novel Approaches for Targeted Drug Delivery

Dissertation to obtain the Degree of Doctor of Natural Sciences

(Dr. rer. nat)

From the Faculty of Chemistry and Pharmacy

University of Regensburg



Presented by

Melanie Bresinsky

From Kulmbach

2024

Melanie Bresinsky

Nanoparticles Mimicking Viral Infections: Novel Approaches for Targeted Drug Delivery

This work was carried out from February 2021 to October 2024 at the Department of Pharmaceutical Technology of the University of Regensburg.

The thesis was prepared under the supervision of Prof. Dr. Achim Göpferich.

Doctoral application submitted on: 30th October 2024

To my family.

“Imagination is more important than knowledge.”

Albert Einstein

Table of contents

| | | |
|------------------|--|-----|
| Chapter 1 | Introduction - Control of Biomedical Nanoparticle Distribution and Drug Release <i>In Vivo</i> by Complex Particle Design Strategies | 13 |
| Chapter 2 | Goals of the Thesis | 87 |
| Chapter 3 | Long-term Residence and Efficacy of Adenovirus-mimetic Nanoparticles in Renal Target Tissue..... | 99 |
| Chapter 4 | Ectoenzymes as Promising Cell Identification Structures for the High Avidity Targeting of Polymeric Nanoparticles | 153 |
| Chapter 5 | Conditional Cell-Penetrating Peptide Exposure as Selective Nanoparticle Uptake Signal | 205 |
| Chapter 6 | Nanoparticles Mimicking the Viral Infection Pathway for Targeting SARS-CoV-2 Host Cells..... | 267 |
| Chapter 7 | Summary and Conclusion..... | 307 |
| Appendix | | 315 |

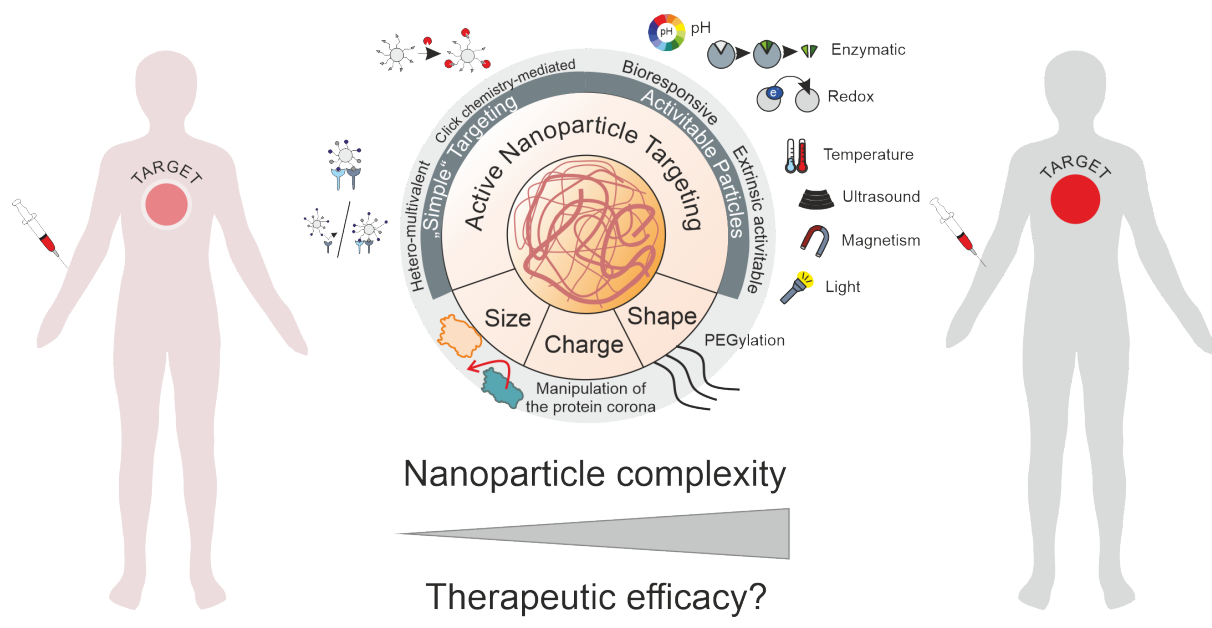
Chapter 1

Introduction - Control of Biomedical Nanoparticle
Distribution and Drug Release *In Vivo* by Complex
Particle Design Strategies

Chapter 1

Abstract

The utilization of targeted nanoparticles as a selective drug delivery system is a powerful tool to increase the amount of active substance reaching the target site. This can increase therapeutic efficacy while reducing adverse drug effects. However, nanoparticles face several challenges: upon injection, the immediate adhesion of plasma proteins may mask targeting ligands, thereby diminishing the target cell selectivity. In addition, opsonization can lead to premature clearance and the widespread presence of receptors or enzymes limits the accuracy of target cell recognition. Nanoparticles may also suffer from endosomal entrapment, and controlled drug release can be hindered by premature burst release or insufficient particle retention at the target site. Various strategies have been developed to address these adverse events, such as the implementation of switchable particle properties, regulating the composition of the formed protein corona, or using click-chemistry based targeting approaches. This has resulted in increasingly complex particle designs, raising the question of whether this development actually improves the therapeutic efficacy *in vivo*. This review provides an overview of the challenges in targeted drug delivery and explores potential solutions described in the literature. Subsequently, appropriate strategies for the development of nanoparticulate drug delivery concepts are discussed.



Critical aspects of active targeted drug delivery

Nanoparticle design strategies

Opportunities and limitations of “control by design”

Chapter 1

1 Introduction

The use of nanoparticles as drug delivery systems is a promising approach to enhance the efficacy of drugs while limiting adverse drug effects. To precisely control the distribution *in vivo*, the particles are designed to accumulate in the target tissue or specific target cells through interactions between targeting ligands and cell surface structures [1,2]. However, upon administration, biomedical nanoparticles for therapeutic or diagnostic applications face a variety of obstacles [3]. Depending on the route of administration, such as intramuscular (i.m.) [4], subcutaneous (s.c.) [5], intravenous (i.v.) [6], oral, [7] intravitreal [8], pulmonary [9], or nasal [10] complex biological barriers must be overcome [11]. Oral drug delivery with nanoparticles is hampered by the acidic gastric environment and the secretion of mucus that protects the GI tract can efficiently trap and remove administered particles [12]. Nanoparticle administration via inhalation is challenging due to biological barriers in the respiratory system, such as mucus, ciliated cells, or clearance by resident macrophages [13]. Another prominent example is the excessive clearance by the mononuclear phagocyte system (MPS), which is of general concern, but plays a major role in distinct administration routes like subcutaneous (s.c.) injection [5].

In addition, once nanoparticles enter biological media, the adsorption of proteins on their surface alters the pre-formed particle properties. As a result, not only particle distribution [14], but also toxicity [15], stability [16], clearance [17], and cargo leaching [16] can be affected, which may be a major bottleneck for therapeutic efficacy. Moreover, many target structures are located intracellularly. Since the cell membrane represents a natural barrier, preventing direct entry into the cytoplasm, particle internalization is often essential [18,19]. One challenge at this point is that the majority of nanoparticles are taken up via endocytic uptake pathways. Thus, they may suffer from endosomal entrapment and degradation by acidification and lysosomal enzyme activity [20,21]. In addition, drug release must occur between entry into the cytosol and exocytosis from the target cell. Therefore, premature drug release [22,23], as well as insufficient intracellular particle residence time might be a handicap to therapeutic efficacy [24].

Due to this multitude of requirements to be fulfilled simultaneously, there has been a paradigm shift in the development of biomedical nanoparticles. While early approaches focused on tailoring physicochemical properties, so-called passive targeting [25–27], or modifying the particle surface with a single targeting ligand to identify target cells in a key-lock principle [28,29], the objective has changed to precisely control the nanoparticles' fate. Thus, multiple

Chapter 1

factors such as protein attachment, biodistribution, nanoparticle internalization, drug release, or exocytosis are coordinated, which frequently results in highly complex particle designs [30,31].

We outline different strategies to overcome respective hurdles, such as adapting the particle size, charge, or surface, and the implementation of switchable particle characteristics, which are activated by signals such as changes in pH value, redox potential, enzymatic cleavage, ultrasonic, light, temperature, or magnetism. Moreover, we illustrate further innovative strategies, such as optimizing particle distribution and uptake by subsequent ligand attachment in biological media by click chemistry [32,33] or targeting via the specific manipulation of the formed protein corona [34]. Finally, we critically examine the possibilities and limitations of influencing the particles' fate by synthetical nanoparticle design. Since i.v. particle injection is the most common route of application for the development of nanoparticles, which additionally offers the advantage that the entire amount of administered substance reaches the systemic circulation and is not consumed by administration-route specific barriers [35], the review is focused on this route of application.

2 Critical Aspects for Targeted Drug Delivery

2.1 Protein Corona Assembly

Immediately upon the first contact with blood, plasma proteins adsorb to the nanoparticle surface and create altered particle properties, which change their pharmacological profile (Fig. 1a) [36–38]. The composition of the formed protein corona and thus the particles' "biological identity" strongly depends on the particle size, charge [39] and surface chemistry [40], and has a high impact on the NP fate *in vivo*. The protein adsorption, which affects positively charged particles to a particularly high degree [41], is associated with several challenges: the corona interferes with ligands tethered to the nanoparticle surface, hampering interactions with targeting motifs [42,43]. Furthermore, the adsorption of so-called opsonins promotes an immune response [44–46] and frequently leads to premature clearance by the MPS [46,47]. Since an adequate nanoparticle circulation time is essential to reach the target tissue [48], the prevention of fast MPS-mediated clearance is of major significance. Moreover, the protein corona changes the drug release profile of nanocarriers [49], diminishing the controllability of NP-based drug therapy.

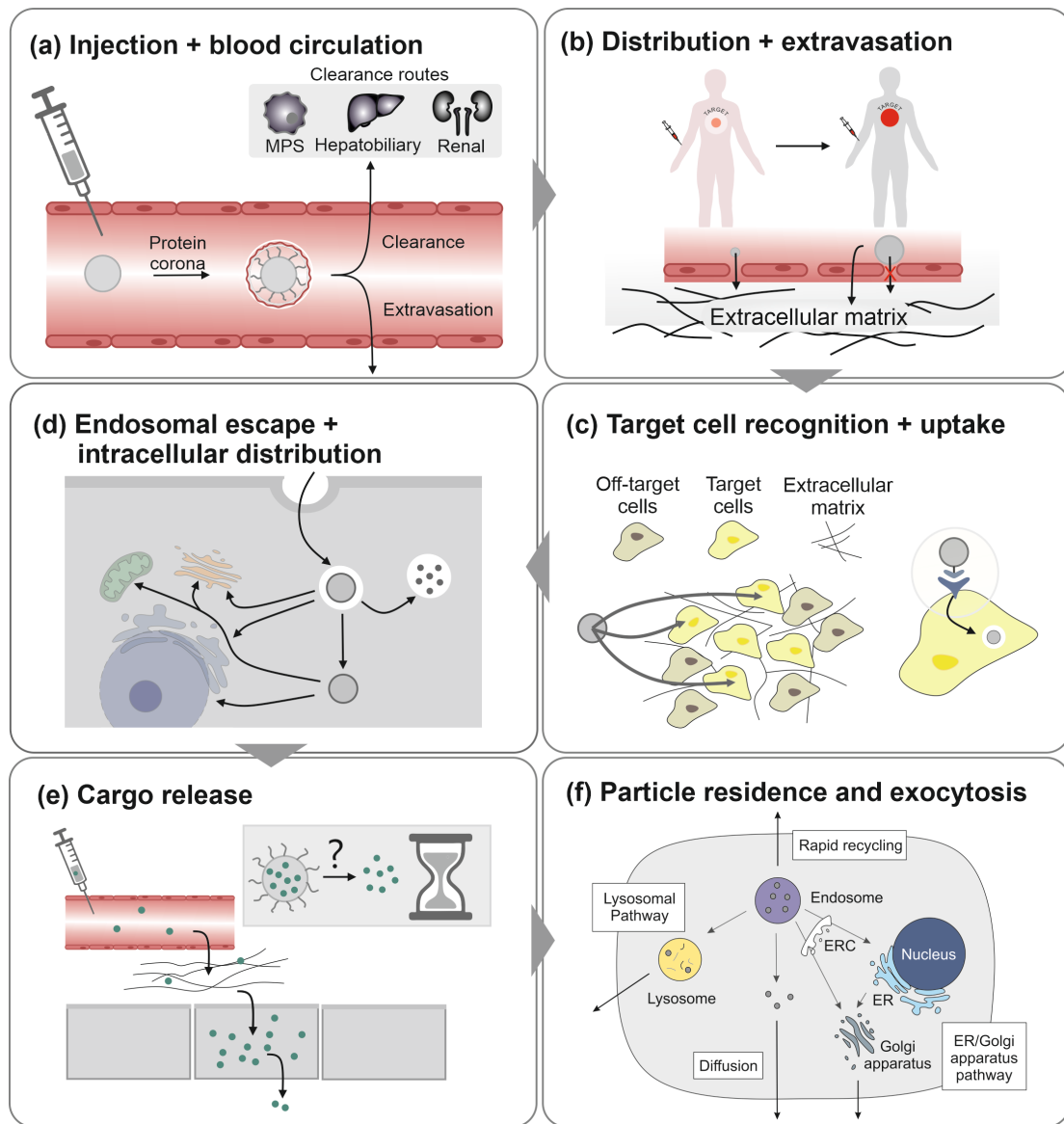


Figure 1. Critical aspects of nanoparticle distribution and drug release from injection to elimination. (a) Immediately after i.v. injection, the particles are localized in the systemic circulation and various proteins bind to the particle surface. This results in an altered particle structure, which can strongly differ from the original design. (b) The NPs are distributed throughout the body with the objective of extravasating from blood vessels at their target tissue. (c) Due to specific nanoparticle surface modifications, the drug carrier is supposed to identify its target cells and be taken up without premature clearance or accumulation in off-target tissues. (d) As NPs are mainly internalized via endocytic uptake processes, most particles are initially localized inside endosomes, from which they must escape to avoid lysosomal degradation and reach the cytoplasm or specific organelles. (e) For nanoparticles as drug delivery systems, both temporal and spatial control of the drug release are essential for therapeutic efficacy and to minimize adverse drug effects. (f) One decisive factor in this case is the particle residence time, to achieve a suitable time frame for drug release before NP exocytosis and elimination.

2.2 Extravasation and Target Cell Identification

The NPs must pass the vascular endothelial barrier to reach their target tissue (Fig. 1b) [50]. Extravasation is mainly performed in two different ways: via fenestrations between endothelial cells or transcellularly. Additionally, there are special pathways, such as extravasation via transcytoscopic holes in glomerular endothelial cells [51]. The endothelial fenestrations are mainly below 10 nm and thus only permeable for very small particles. Larger particles need to pass the vascular endothelial barrier transcellularly through endocytotic pathways such as micropinocytosis, phagocytosis, clathrin-mediated endocytosis, and the caveolae-mediated pathway and thus partially receptor-dependent [35]. While very small particles with a size below 6 nm are rapidly excreted by renal clearance mechanism, larger particles tend to remain in circulation longer and subsequently undergo hepatobiliary elimination [35,52]. Upon extravasation, the particles are localized in the extracellular matrix (ECM), which may nonspecifically interact with particle surfaces and thus hamper target cell internalization. In particular positively charged NPs are affected due to interactions with the negatively charged ECM [53].

For preferential accumulation in target cells, the particles must discriminate between target and off-target tissue by precise biomolecular recognition strategies (Fig. 1c) [54–57]. Therefore, ligands which interact with certain cell surface structures, such as receptors or ectoenzymes in a key lock principle, are tethered to the nanoparticle surface [56,58,59]. Ligand types that are implemented in the nanoparticle design are peptides [60], small molecules [61], aptamers [62], polysaccharides [63], or proteins [64], which can also be categorized in agonists [59], antagonists [65], substrates [66], inhibitors [58], or antibodies [67,68] for the corresponding target structures. In the simplest case, one type of ligand interacts with one target structure, which is especially promising for highly specific targeting motifs or structures that are strongly overexpressed in certain tissues. This plays a particularly important role in cancer therapy, e.g. nanoparticles functionalized with cancer-targeting antibodies, such as anti-CD133 [69], anti-HER2 [70], or anti-CD44 antibodies [71], as cancer tissue differs considerably from healthy tissues regarding morphology, cell metabolism, or the expression of cell surface markers [72]. However, since many receptors or enzymes are expressed not exclusively in one cell type, but ubiquitously in the organism, using only one ligand for target cell identification may cause reduced selectivity.

Chapter 1

2.3 Nanoparticle Uptake and Endosomal Entrapment

Many target structures are localized intracellularly. Therefore, efficient nanoparticle uptake is often required. Nanoparticle internalization can be divided in endocytic (Fig. 2a-e) and direct (Fig. 2f) uptake, whereas endocytic uptake pathways play the major role for nanoparticles [46].

Upon endocytosis, particle binding is followed by their engulfment with subsequent budding of endocytic vesicles to the cell interior [46]. Thus, the internalized particles do not have direct access to the cytoplasm or cellular organelles [54]. Depending on the uptake mechanism, the vesicles are sorted, fused, dissociated, or matured to lysosomes and can either be exocytosed, recycled, or trafficked to different organelles, involving motor proteins, such as kinesin, dynein, and myosin, that shuttle vesicular cargos along microtubules or via actin filaments (Fig. 1d) [19,54]. For many applications, the entrapment inside endocytic vesicles is undesirable since target structures are localized inside the cytosol or at specific subcellular organelles. Additionally, the maturation of early endosomes to lysosomes leads to acidification of the vesicles and a combination of lysosomal enzyme activity, and acidic pH values promote cargo degradation, which may be beneficial in some cases [73], but often reduces the therapeutic efficacy [74].

Direct translocation, on the other hand, promotes direct access to the cytoplasm and organelles, faster delivery kinetics, and minimal lysosomal degradation [54,75,76], but is rarely reported and the permeation mechanisms are poorly described [75]. It is known that direct uptake pathways are particularly important for very small particles since nanoparticles require a critical minimum size of around 5-10 nm to be taken up endocytically [77].

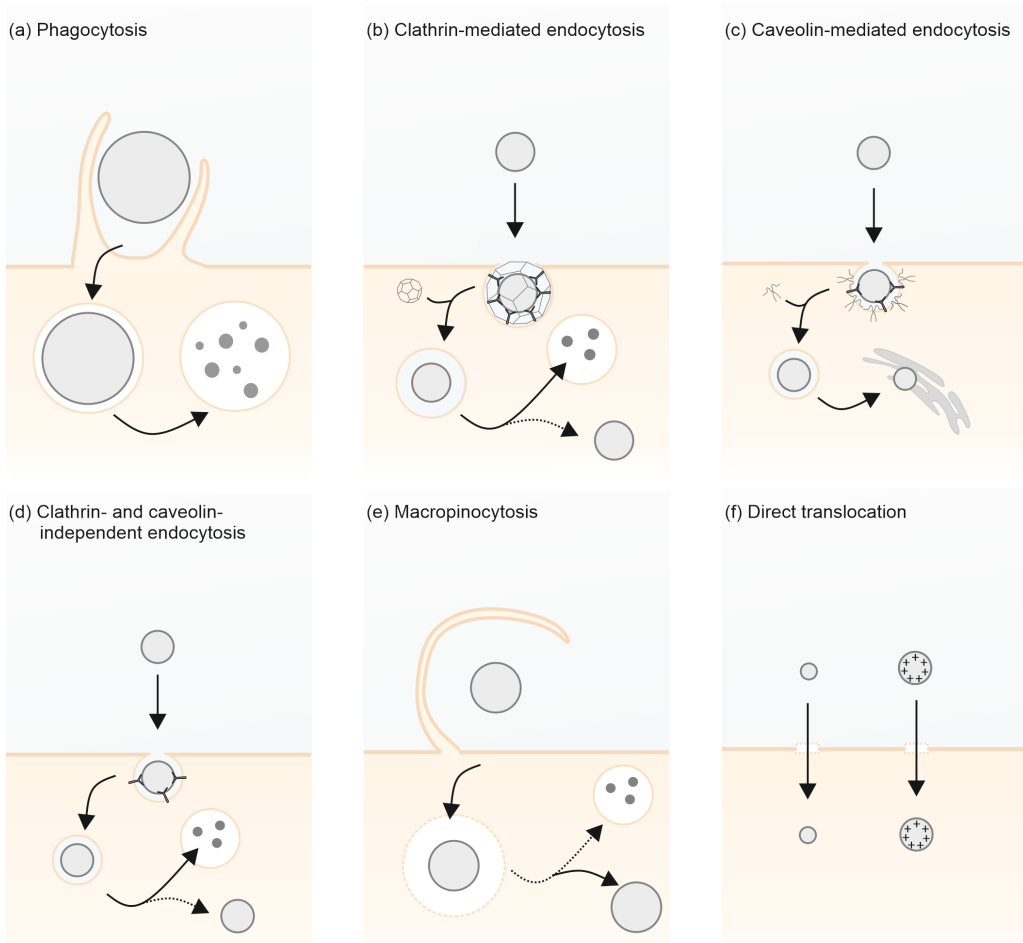


Figure 2. Schematic overview of nanoparticle internalization pathways. (a) Phagocytosis, the ingestion of large particles through protrusions of the plasma membrane, is mainly important for immune cells such as macrophages, monocytes, neutrophils, or dendritic cells [78,79]. All non-phagocytotic but endocytotic uptake processes are summarized as pinocytosis, which is the engulfment of smaller particles [80]. (b) Clathrin-mediated endocytosis (CME) generally depends on the formation of ligand-receptor complexes [80] and is thus highly important for the internalization of actively targeted nanoparticles [18]. Among other proteins, clathrin generates and stabilizes membrane curvatures, so-called clathrin-coated pits (CCPs). These pits are then pinched off the membrane with the help of a GTPase enzyme called dynamin [81], leading to the budding of vesicles with a size from 100-500 nm into the cytosol [54]. The resulting vesicles ultimately lose their clathrin coat and fuse to early endosomes [82,83], which frequently leads to lysosomal degradation due to endosomal entrapment [80]. The occurrence of clathrin-coated pits has been demonstrated to influence nanoparticle avidity and therefore also distribution in target and off-target cells in cell culture experiments [84,85]. (c) Caveolae-mediated endocytosis is a related process, in which the protein caveolin is the decisive factor for structural stabilization and membrane budding. The flask-shaped plasma membrane invaginations are 50-80 nm in size and therefore enable the uptake of smaller particles than CCPs [86,87], which are reported with sizes of up to 200 nm [88]. Since caveolae-mediated endocytosis results in the formation

Chapter 1

of caveosomes, which possess a neutral pH and may bypass lysosomes and thus digestive environments, this uptake way is beneficial regarding cargo stability [80,89,90]. However, caveolae-mediated uptake is very slow with half times higher than 20 min [91]. **(d)** Clathrin/caveolae-independent endocytosis (CCIE) involves vesicle formation supported by actin and actin-associated proteins [92] or lipid rafts. These are cholesterol and sphingolipid-rich domains within the plasma membrane, which are free-diffusing and may be internalized following the binding of ligands to receptors or glycolipids that are localized within the raft [54,80,91]. Lipid raft-mediated uptake is discussed for the internalization of nanoparticles modified with particular cell-penetrating peptides (CPPs) and nucleic acids [54,93]. Furthermore, CCIE is especially interesting for nanoparticles modified with folic acid, which is frequently used for tumor-specific targeting concepts, since the folate receptor internalizes by this route [94]. **(e)** Macropinocytosis is characterized by the formation of large membrane extensions, which are formed by rearrangement of the cytoskeleton. During re-fusion with the plasma membrane, vesicles between 0.5 and 10 μM in size filled with extracellular fluid are formed and transported into the cell interior [18,46]. These vesicles, called macropinosomes, undergo acidification and fusion similar to endosomes [18]. In macropinocytotic uptake, all particles that are dissolved in the internalized extracellular fluid are taken up, which is why this uptake way is not directly regulated by the activation of a receptor [46]. Furthermore, macropinocytosis is a possible uptake way of particles whose size exceeds that of CCPs or caveolae. **(f)** Direct translocation is mainly limited to highly positively charged or very small particles. This uptake pathway enables immediate and fast entry into the cytosol.

2.4 Drug Release

There are two conflicting objectives in controlling drug release: to prevent premature release into the bloodstream and to ensure rapid release once the particles have reached their target site (Fig. 1e). Besides the NP type, the exact composition, structure, and physical and chemical interactions of the individual components are important for the drug release characteristics. In this context, the nanoparticle manufacturing method is also an important factor [95]. Drug release can be categorized into diffusion, solvent-controlled, chemical, and stimulated release [95,96]. Diffusion-controlled release, which is forced by a concentration gradient, is important for almost all kinds of drug release from a dosage form, especially for capsule-like systems, where the drug is dispersed or dissolved inside a core [95,97,98]. Due to the concentration dependence, diffusion-controlled release often shows a high initial release that decreases over time [95]. Solvent-controlled release, which means osmotic- or swelling-controlled release, is primarily relevant for carriers with semi-permeable membranes or three-dimensional crosslinked materials like hydrogels [99], whereas drug release via chemical

interactions is mainly associated with the degradation of the carrier matrix. The degradability and time are highly material-dependent [100,101]. Since non-biodegradable particles such as metal colloids or ceramics might accumulate and cause cytotoxicity, the usage of biodegradable materials is mostly preferred [100,101]. Frequently utilized materials in this context are biodegradable polymers such as poly(ϵ -caprolactone) (PCL), polylactide (PLA), and poly(lactide-co-glycolide) (PLGA), mesoporous silica nanoparticles, or lipid nanoparticles. Stimulated drug release, triggered for example by a pH shift in the environment or changes in the redox potential, enables temporal and spatial control of the drug release and thus might be advantageous [102].

2.5 Exocytosis and Intracellular Particle Residence Time

The intracellular particle residence time is a critical factor for the efficacy of a nanotherapeutic system. It is determined by two factors: nanoparticle exocytosis and degradation [103]. The main exocytosis pathways are diffusion, rapid recycling, and the lysosomal or the ER/Golgi apparatus pathway (Fig. 1f) [103]. The formation, fusion, transport, and excretion of nanoparticle-loaded vesicles in this context are controlled by the endocytic recycling compartment (ERC), which is a microtubular organelle that is distributed in the cytoplasm [104,105]. As described in chapter 2.4, the majority of internalized particles end up in early endosomes, which have the function of controlling the reutilization or degradation of membrane components [106]. Therefore, some of the internalized particles return directly to the plasma membrane and are ejected [104,105]. This exocytosis mechanism, known as rapid recycling [103], possesses half-life times of two minutes or less [105], hardly offering time for intracellular drug release. The most important exocytosis mechanism is the lysosomal pathway. In this case, the early endosomes undergo a maturation process from early to late endosomes and ultimately to lysosomes [106]. Nanoparticles suffering from endosomal entrapment [107] are digested by lysosomal enzymes and acidic pH values and the vesicle content is expelled. Therefore, the endosomal escape capability is a critical factor for particle residence time [108]. Moreover, optional via the endoplasmic reticulum [109], nanoparticles may be transported to the Golgi apparatus and transported to the cell surface for excretion via secretory vesicles [103].

3 Nanoparticle Design Strategies

3.1 Manipulation of the Protein Corona

Various strategies have been developed to avoid or control the formation of the protein corona, thus preventing premature clearance, and obtaining the synthesized nanoparticle characteristics [34,110,111]. The topic is of utmost significance and has been reviewed in detail [112]. The most commonly used method to hinder protein adsorption is the stealth coating of nanoparticles with polyethylene glycol (PEG) [113–115], but also other hydrophilic polymers can be utilized according to this method [116]. The PEG chains provide a hydrated layer on the particle surface, reducing protein adsorption [48], frequently referred to as “stealth effect” [47]. The repulsive effect depends on the polymer’s molecular weight, conformation, and surface density [46], and can prolong the half-life time of blood circulation from a few minutes to several hours [40,46]. A further strategy was presented by Müller et al. (2017) [111]. The research group coated nanoparticles with tunable surfactants to control the unspecific protein adsorption and aggregation of particles by a non-covalent approach that could be applied to any particle type without high synthetic effort. However, the formation of a protein corona does not only have negative effects: the adsorption of so-called dysopsonins actively prevents phagocytosis by immune cells, which prolongs blood circulation (Fig. 3). Furthermore, dysopsonins can contribute to reduced toxicity and colloidal stability of NPs [117]. Typical dysopsonins are for example albumin, clusterin, also called apolipoprotein J, and transferrin, which is why studies were performed that deal with the intentional coating of NP surfaces with these proteins to exploit the protein corona for improved drug delivery [117–120]. Additionally, the protein corona can be utilized for specific nanoparticle targeting [121]. One example is the protein corona manipulation via polysorbate precoating, which facilitates the adsorption of apolipoprotein to the nanoparticle surface and thus enables brain targeting [122,123]. Furthermore, Zhang et al. (2015) [124] developed a retinol-conjugated polyetherimine nanoparticle system that selectively attaches the retinol-binding protein 4 (RBP4), which targets hepatic stellate cells and thus could be used for the treatment of hepatic fibrosis. Therefore, the aim is not necessarily to completely prevent protein attachment, but to ensure that the corona is formed by desired proteins that enable immune escape or that are targeted to distinct cells. The amount, type, and affinity of adsorbed proteins can be altered by changes in the nanoparticle surface chemistry, size, shape, and precoating, which was summarized in recently published reviews by Zhao et al. (2024) [34] or Kim et al. (2023) [48].

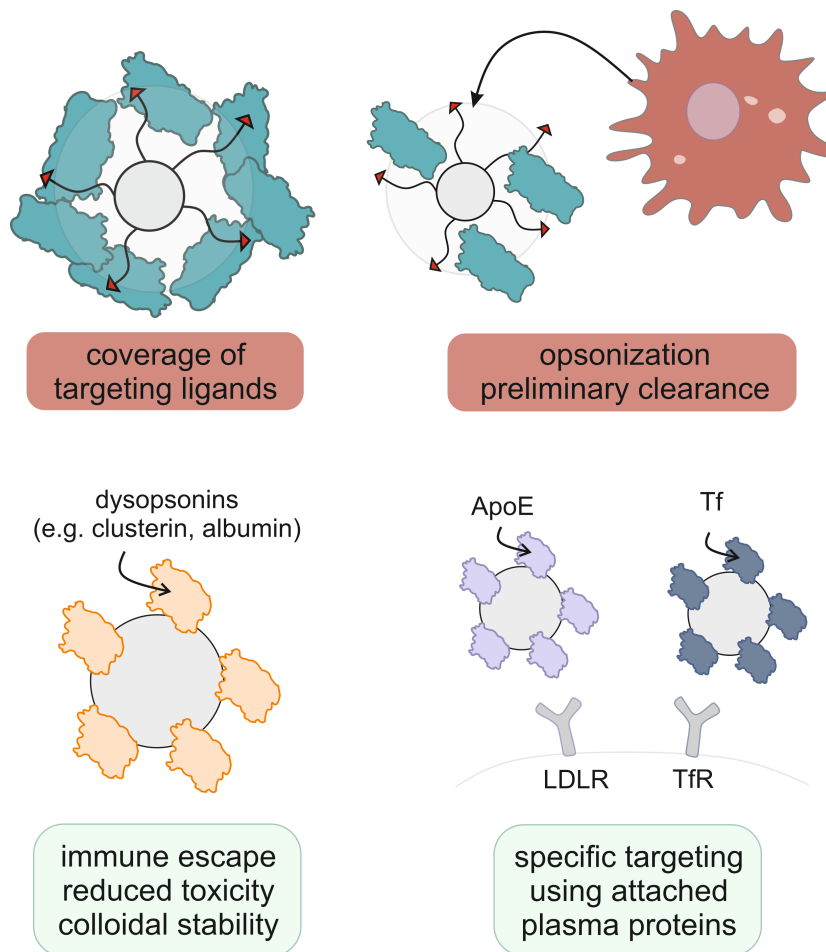


Figure 3. Consequences of protein corona formation. Protein attachment is frequently correlated with a negative impact due to the coverage of targeting ligands, resulting in suppressed target cell selectivity, or premature MPS clearance due to opsonization. Nevertheless, the protein corona may also have positive effects due to the attachment of dysopsonins or proteins such as transferrin (Tf) or apolipoprotein E (ApoE), which can be utilized for specific nanoparticle targeting [121].

3.2 Control of Nanoparticle Extravasation and Target Cell Recognition

To reach their target cells, nanoparticles must pass the endothelial barrier of blood vessels. While larger particles have more interactions with the cell membrane and smaller particles require less energy to form vesicles upon particle uptake, there is an optimal size range for endothelial internalization and thus transcellular extravasation of about 50-70 nm [35]. In certain tissues, such as tumors, glomeruli, or hepatic sinusoids, larger fenestrations facilitate the paracellular extravasation of larger NPs [51,125,126]. Accordingly, it may be advantageous to adjust the particle diameter to the size of the extended fenestrations or to choose a size range that allows transcellular passage through the endothelial barrier.

Chapter 1

To identify target cells, targeting ligands are attached to the nanoparticle surface. Depending on the type of ligand, different effects can be observed: antagonistic ligands or enzyme inhibitors mediate binding to the cell membrane without direct uptake [58,127]. In contrast, the interaction of receptor agonists as ligands usually induces receptor-mediated nanoparticle internalization [128,129]. Antibodies used as targeting ligands can also induce cellular uptake [130,131]. Substrates of ectoenzymes attached to the nanoparticle surface are cleaved and subsequently released, so no direct particle uptake is expected. However, enzymatic processing can unveil structures on the nanoparticle surface that subsequently promote cell internalization (Fig. 4) [66]. Consequently, besides the target structure, the pharmacological characteristics of the targeting ligands have a major influence on the efficacy of the drug delivery system and must be taken into account in the nanoparticle design [18,132].

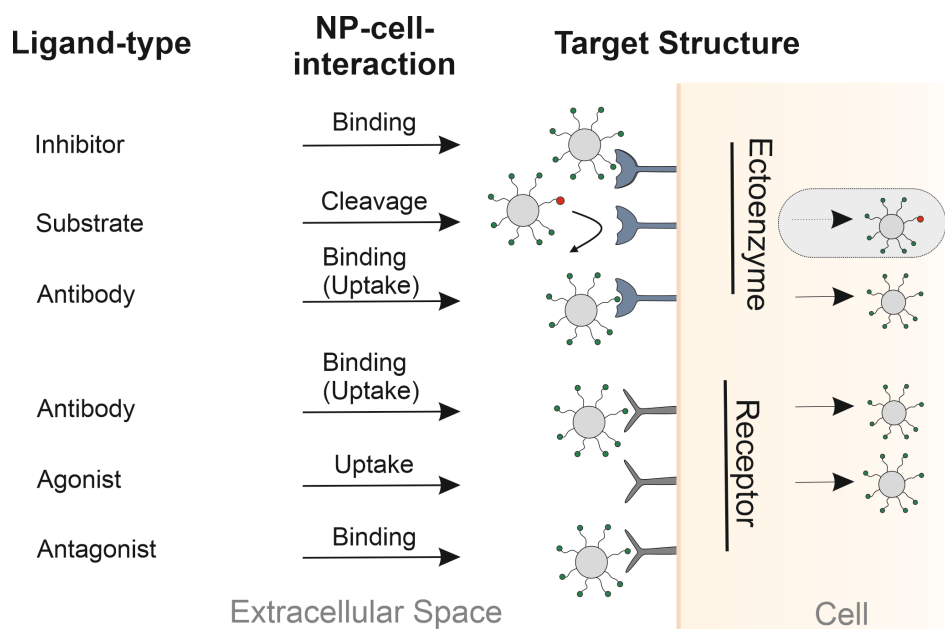


Figure 4. Nanoparticle-cell interactions based on the ligand type and the target structure. Enzyme inhibitors or antagonistic receptor ligands mainly bind to the target structures expressed on the cell surface, thus anchoring the particle to the target cell surface. For antibodies, both cell surface binding and uptake have been described. Receptor agonists often promote receptor-mediated uptake into the target cells. Enzyme substrates attached to the nanoparticle surface are cleaved, which does not result in immediate uptake. However, the associated release of receptor agonists or other uptake signals may secondarily trigger nanoparticle uptake.

Since most targeting motifs are expressed in a variety of cells throughout the body and are rarely exclusively expressed or at least significantly overexpressed in a single cell type, the combination of different ligands, which is also known as hetero-multivalent targeting, has

significant advantages over the use of a single ligand type [59,133–135]. By simultaneous binding of several ligands to different target structures, both targeting efficiency and specificity can be increased [136]. The corresponding theoretical and thermodynamic background was described in an excellent review by Woythe et al. (2021) [137]. However, for multi-target interactions, several attributes should be taken into account: the addressed targeting structures should not have downregulating effects via intracellular receptor consumption pathways, the ligand density should be optimized to the expression density in the target tissue, and the bioconjugation strategy has to be adjusted to facilitate the interaction between ligand and target structure, for example by the setting of spacer length and linker chemistries [134]. A possibility to further increase the target cell selectivity of hetero-multivalent targeting approaches, by steric shielding of one ligand type, was published by Fleischmann et al. (2020) [59]. Only after the binding of a primary ligand to a receptor expressed on the target cell surface, the newly achieved spatial proximity reveals a previously hidden second ligand, which ultimately leads to nanoparticle internalization.

3.3 Promotion of Endosomal Escape and Direct Penetration

Since reaching the cytosol is essential for the efficacy of many nanotherapeutics, numerous strategies have been developed to promote endosomal escape or direct penetration of the cell membrane. The most common endosomal escape strategies can be categorized in the so-called “proton sponge effect” or osmotic rupture, the swelling effect, the destabilization of the membrane by pore formation or disruption, and membrane fusion. All aim to destabilize the endocytic vesicles and thus allow nanoparticle trafficking to the cytosol (Fig. 5) [138,139]. Besides, new approaches are being developed that should diminish endosomal entrapment, such as the thiol-disulfide exchange strategy: Kanjilal et al. (2022) [140] demonstrated that disulfide bonds as NP functionality may enhance cellular uptake and endosomal escape. The underlying mechanisms are still not clear, but the research group proposed that the covalent contact between the membrane thiols and the nanogel strained the packing of the endosomal membranes and thus promoted cargo leakage. Stahl et al. (2022) [73] used endosomal enzyme activity to promote endosomal escape: a substrate of the protease cathepsin S (CatS), which is found in early endosomes of dendritic cells, was used as a linker between a model antigen and polymeric nanoparticles as carrier. Enzymatic processing of the nanoparticle surface enabled selective release of the antigen, allowing its endosomal escape.

Chapter 1

Another strategy to prevent endosomal entrapment is to adjust the particle design to achieve prioritization for specific uptake pathways. Particularly high nanoparticle surface charges and cell-penetrating peptide modifications promote non-endocytic uptake [76,141,142], using transient holes that are generated in the bilayer membrane in response to strong local potential differences, which are resealed after particle uptake [143,144]. In addition to the particle charge, also the shape has an impact on the translocation behavior and can result in varying cell entry mechanisms [143]. This has been shown for dendrimers as an example. A spheroidal shape was more efficient in permeabilizing the plasma membrane than linear poly-l-lysine polymers [145].

Besides direct internalization, modifications promoting macropinocytosis or caveolae-mediated endocytosis could be favorable regarding subcellular targeting, since macropinosomes possess relatively leaky vesicular structures that facilitate escape into the cytosol [146]. The caveolar pathway to enter cells provides a nonacidic and less digestive route for cellular uptake [89]. The cargo internalized by caveolin-mediated endocytosis may be directly transported to processing organelles such as the Golgi apparatus (GA) or the endoplasmic reticulum (ER), avoiding lysosomal degradation [80,89]. However, while the attachment of cell-penetrating peptides to the particle surface supports direct NP internalization and also particle uptake via macropinocytosis [147,148], the regulation of particle uptake via caveolae-mediated endocytosis and the resulting particle fate is still unclear and controversially discussed. One approach to direct the NP uptake towards caveolae-related endocytosis to circumvent lysosomal degradation was established by Chen et al. (2022) [149]. The research group developed a biomimetic system using NP cancer cell membrane camouflage. However, the factor which likely influenced the rate and route of endocytosis to the greatest extent is the formed protein corona [150]. Additionally, the cell type has an impact [151–153]. At this point, there is a lack of more detailed studies dealing with the control of NP uptake via specific pathways and clarifying the subsequent distribution processes.

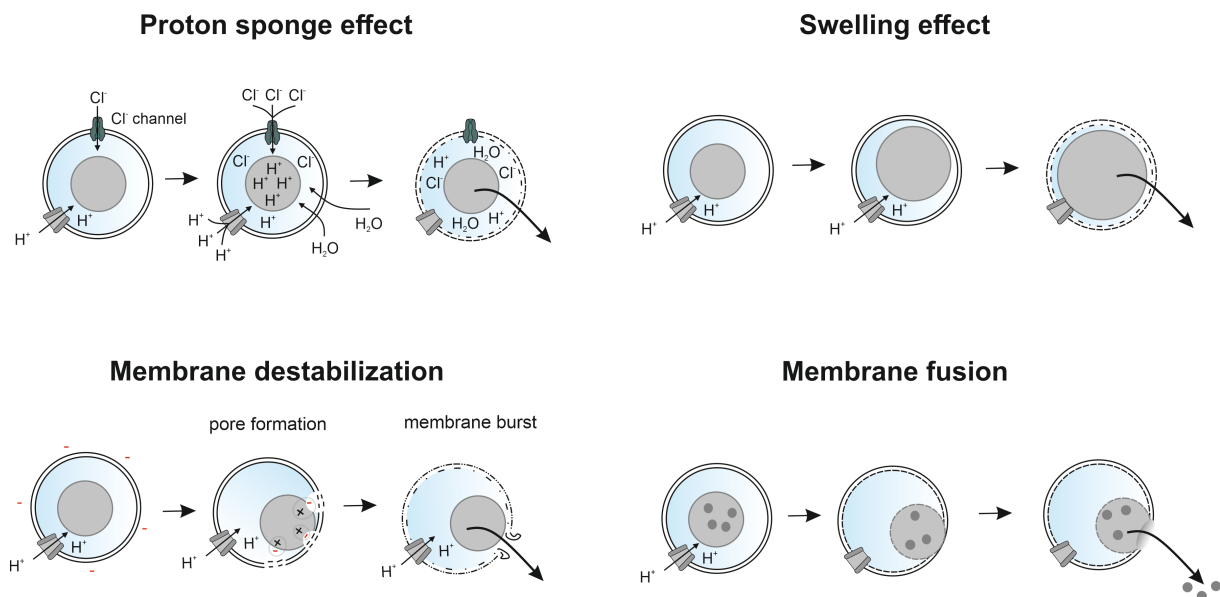


Figure 5. Mechanisms of endosomal escape. The proton sponge effect is caused by endocytosed compounds that are protonated upon H^+ -ion influx during the acidification of endosomes in the maturation to late endosomes or lysosomes [98]. Consequently, those substances possess a buffering capacity that counteracts the acidification of the endosomal compartment [99]. This promotes further ATP-driven influx of protons, accompanied by chloride ions and water molecules. The resulting osmotic pressure ultimately leads to membrane rupture and thus to the release of the entrapped components [97]. The swelling effect describes drug release caused by the swelling of certain structural compounds, mainly polymers, caused by pH shifts or changes in ionic concentrations [99]. The most important mechanism for persistent membrane destabilization, causing pore formation or also membrane rupture, is the membrane “flip-flop” caused by cationic charges [154]. Since the outer layers of endosomes are mainly composed of negatively charged phospholipids, positively charged cargos induce a flip of the outer layers to the intraluminal side of the endosome. The resulting formation of charge-neutral pairs results in membrane reorganization and non-lamellar phase changes, which ultimately cause membrane destabilization [155,156]. Membrane fusion is a process that is inspired by viruses such as the influenza virus, utilizing the hemagglutinin (HA)-2 subunit as a fusogenic agent [154]. HA-2 is converted from a hydrophilic, anionic coil at neutral pH to a hydrophobic helical conformation in an acidic environment, enabling the fusion of the viral membrane with the cellular membrane [139]. This mechanism can be adapted for the endosomal escape of nanoparticles by the attachment of fusogenic peptides to the NP surface, which leads to fusion with the lipid bilayer and release from endosomal entrapment. Many reviews are focusing on these mechanisms to which we would like to refer for more detailed information [138,139,157,158].

Chapter 1

3.4 Delay of Particle Exocytosis

Although low intracellular particle residence time is a limiting factor for therapy efficacy, only a few studies deal with the analysis of nanoparticle exocytosis or the prolongation of particle retention in the target tissue [54]. The nanoparticle size has a high impact in this case [159]. Most studies agree that smaller particle sizes promote faster elimination from the cells [108,160–162]. One reason frequently postulated is that smaller NPs have fewer receptor-ligand interactions, which lead to a lower overall intracellular binding and therefore facilitate the release of the particles [108,160,163]. Thus, increasing the particle size could be useful to prolong intracellular retention. Furthermore, there is a low number of studies developing strategies to decrease NP exocytosis rates. Chen et al. (2022) [149] discussed that a rapid exocytosis of nanoparticles causes unsatisfactory results of ER-targeting approaches. Therefore, they investigated a strategy to enhance NP-mediated immunotherapy by exocytosis blockade with brefeldin A (BFA) by coat protein type I (COPI) vesicle transport inhibition. Thus, they achieved an 11-fold increase in intracellular retention of the NPs at 24 h. Yanes et al. (2013) [164] decreased the exocytosis rates of mesoporous silica nanoparticles to prolong the retention in cancer cells and thus enhance drug delivery. The combination of camptothecin-loaded particles with baflomycin A1 or U18666A led to an increase in cell-killing efficacy. Kim et al. (2015) [162] established a strategy to regulate the exocytosis rate of gold nanoparticles via host-guest chemistry. By complexation of the NPs inside cells using cucurbit[7]uril (CB[7]), larger particles were assembled that inhibited exocytosis. While the intracellular amount of gold NPs without CB[7] treatment decreased to 34 % after 24 h, no significant change was observed for cells treated with CB[7] containing media.

3.5 Switchable Nanoparticle Characteristics

One strategy that is currently widely applied is the development of switchable particle properties. In this case, either intrinsic or extrinsic stimuli are utilized to adapt the properties of nanoparticles to the current requirements in a temporally and spatially coordinated manner. An exemplary application for switchable nanoparticle designs is triggering a charge conversion of the nanoparticle surface (Fig. 6). Higher amounts of positive charges enhance cellular uptake, which was shown in various studies [165,166]. Since cationic particle charges also play a major role regarding endosomal escape mechanisms, the implementation of cationic compounds in NP targeting strategies might be highly advantageous. However, it is critical to take into

consideration that positive charges promote increased protein adsorption and thus tend to premature clearance [167], show a higher tendency to interact with the ECM [168], and are known to possess cytotoxic effects [169]. In contrast, particles with a negative surface charge tend to interact less with the ECM and are less susceptible to opsinization but show lower internalization rates. Triggered charge reversal can be used to obtain the benefits of both surface charges.

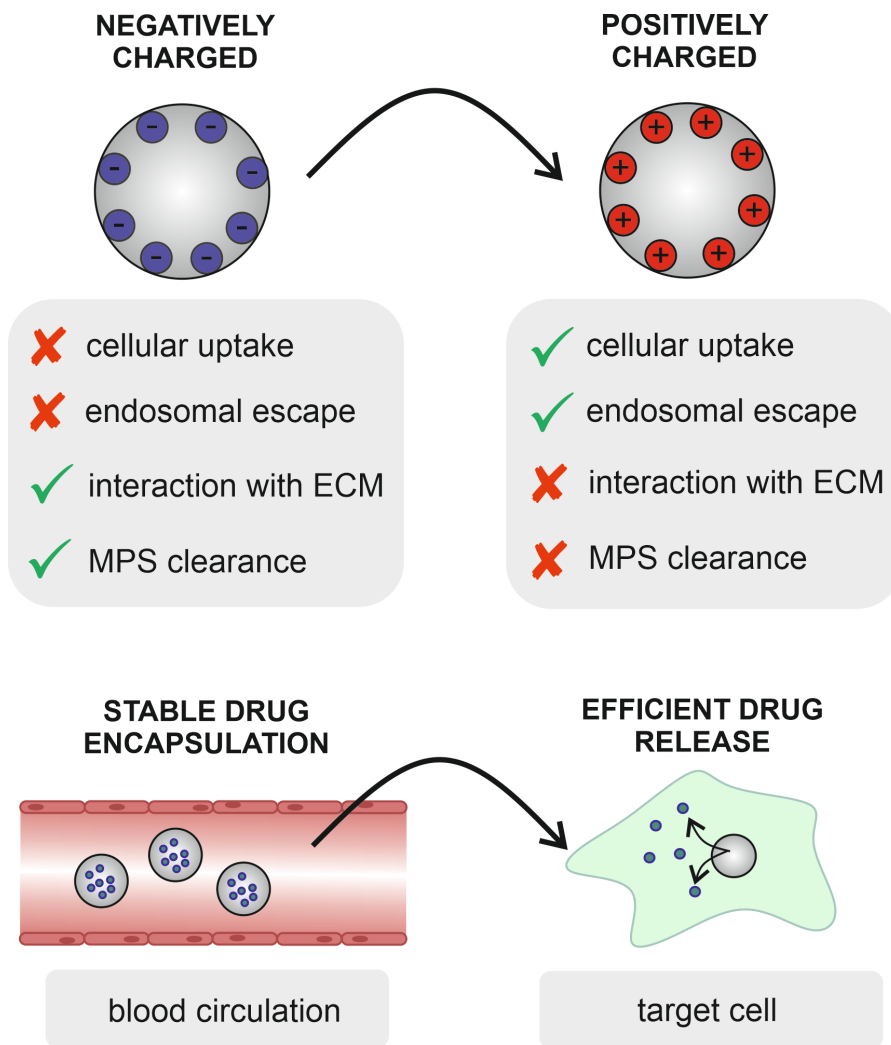


Figure 6. Applications of switchable nanoparticle designs. Stimuli-controlled charge conversion can switch the initially favorable negative surface with reduced MPS clearance and interaction with the ECM to a positive surface charge with improved NP uptake and endosomal escape. Furthermore, stimuli-responsive compounds can induce sterically and temporally controlled drug release in the target tissue.

Another common application for switchable particle designs is controlled drug release. While stable encapsulation is necessary during blood circulation to prevent adverse drug effects due to premature release, an efficient drug release is required in the target tissue. Thus, releasing

Chapter 1

the drug due to an intrinsic or extrinsic signal can improve therapy efficacy [170]. Activation of nanoparticles can be achieved by a variety of different mechanisms, as shown in figure 7. An overview of different switchable nanoparticle design concepts is shown in table 1.

Nanoparticle activation mechanisms

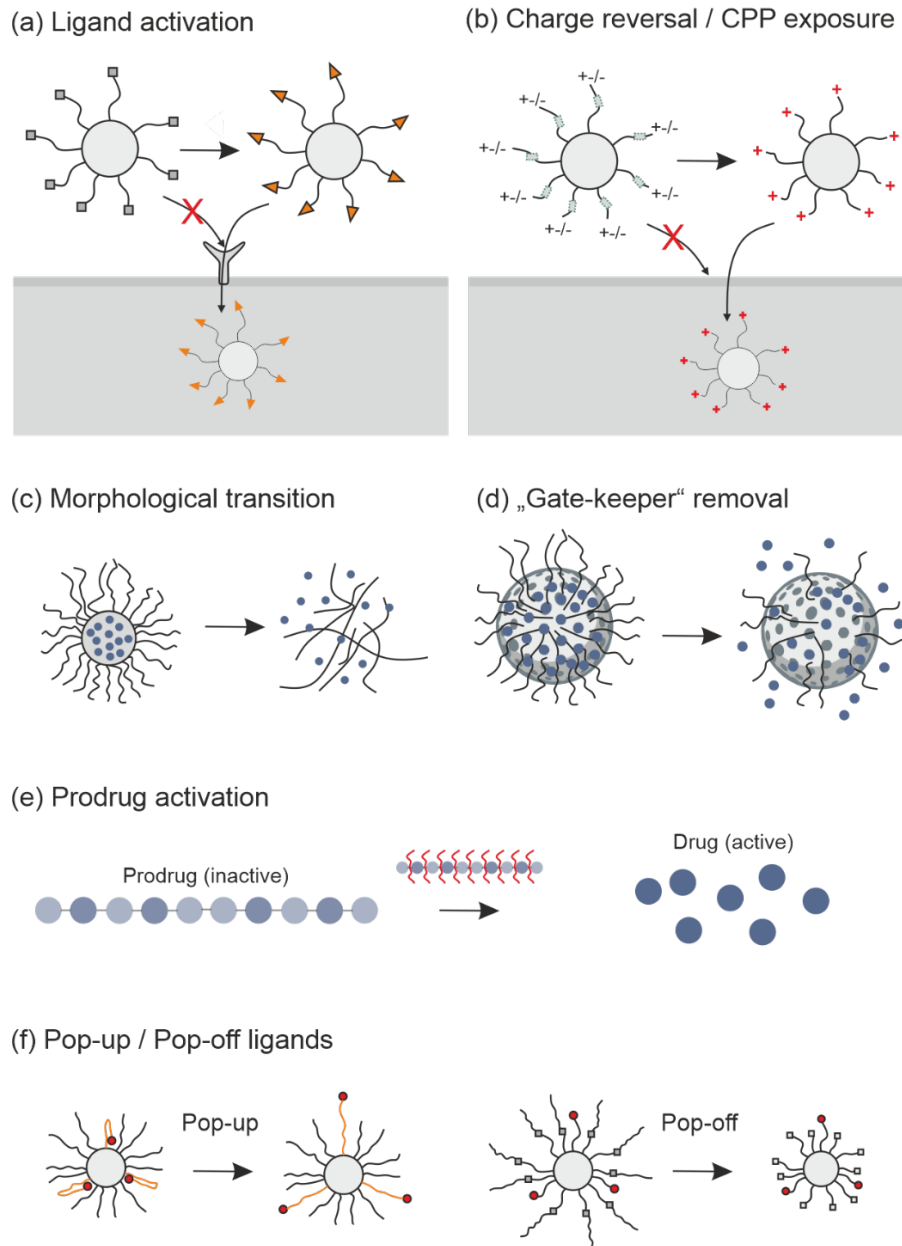


Figure 7. Nanoparticle activation mechanisms in switchable particle designs. (a) Activation of initially inactive targeting ligands by enzymatic cleavage (e.g. Ang I \rightarrow Ang II \rightarrow binding to AT1R). (b) Charge reversal from negative/neutral to positive enables reduced clearance and interaction with the ECM combined with preferential uptake and endosomal escape. (c) Morphological transition such as decomposition in an acidic environment allows spatially and temporally controlled drug release.

Introduction

(d) Gatekeeper removal from mesoporous silica nanoparticles leads to controlled drug release from the nanoparticle pores. **(e)** Activation of an inactivated poly prodrug by releasing individual drug molecules, e.g. by enzymatic cleavage. **(f)** Utilization of pop-up ligands that unfold in response to a distinct signal and become visible on the particle surface or pop-off ligands that are cleaved and thus expose sterically shielded compounds of the nanoparticle structure.

Chapter 1

| Stimulus | NP-system | Responsive Moiety | Target/Activator | Concept | Objective | Associated Disease | Ref. |
|------------|---|--|---|---|---|---|-------|
| pH | PEG- <i>b</i> -P(TMBPEC-co-AC) polymer | Acetal | Endo-/lysosomal compartments | Hydrolytic degradation (morphological transition) | Drug release (paclitaxel, PTX) | Tumor, not further specified | [171] |
| | Liposomes modified with pH-sensitive polymer (PEG-PLL-DMA) | Cleavable amide linkage formed between PEG-PLL and DMA | pH 6.5 in tumor microenvironment, pH 5.0 in endo- and lysosomes | Charge reversal and NO generation | Endosomal escape and controlled drug release (PTX), overcoming multidrug resistance | Cancer, not further specified | [172] |
| | Poly(β -amino esters) (PAE) as core and PEG-biotin on the particle surface, decorated with anti-ICAM1 antibody via biotin-avidin interaction | PAE ester | Lower pH values in inflammatory tissues | Nanoparticle targeting via anti-ICAM1 antibody + nanoparticle disassembly (morphological transition) \rightarrow drug release in inflammatory tissue | Drug (TPCA-1) release from the nanoparticle core | Acute lung inflammation/injury | [173] |
| GSH | Poly-HCPT as inner core, lipid-PEG as outer shell, LA as surface layer | Disulfide bond in the poly- HCPT structure | GSH in tumor tissue | Targeting via LA, GSH in cytoplasm, morphological transition , drug (siBcl-2) and HCPT release | Fast release of intact HCPT molecules and encapsulated siBcl-2 | Liver cancer | [174] |
| | PEGylated mesoporous silica core-shell NPs | Disulfide linkers for PEG attachment | GSH in tumor tissue | Shell cleavage (morphological transition) following drug release | PTX release | Breast cancer | [102] |
| | Polymeric nanoparticles (Cys- 8E Cys-PDSA) | Disulfide bond in PDSA polymer | Increased GSH levels in cardiac fibroblasts after myocardial infarction | S-S bond cleavage and thus NP degradation (morphological transition) | Drug release of encapsulated PF543 (sphingosine kinase 1 inhibitor) | Cardiac fibrosis induced by myocardial infarction | [175] |

Introduction

| | | | | | | | |
|---------------|--|---|--|--|---|--|-------|
| ROS | DSPE-PEG polymer-NPs | Thioketal-bond in polyMTO | Intra-cellular ROS increased in tumor tissue | Chain-breakage caused release of mitoxantrone (MTO) | Tumor targeting, deep tumor-penetration, on-site drug activation by prodrug cleavage | Cancer therapy, not further specified | [176] |
| | Polymer-cinnamaldehyde (CA) conjugate NPs | Thioacetal linker of polymer chain and CA | ROS levels increased in inflamed tissues | The functional aldehyde group of CA was protected via chemical conjugation to the polymer via a ROS-responsive thioacetal linker | CA release upon oxidative stress in inflammatory tissue with ROS-scavenging activity | Broad range of inflammatory diseases e.g. rheumatoid arthritis or ulcerative colitis | [170] |
| Enzyme | PLGA/PLA-PEG polymer NPs | Angiotensin I | Angiotensin-converting enzyme (ACE) | Ligand Cleavage (Ang I → Ang II) | NP Uptake | Diabetic nephropathy | [66] |
| | Quantum dots (QD) | α-Aminobutyric acid | γ-glutamyl transpeptidase (GGT) | Charge Reversal | NP uptake / deep penetration | Tumor, not further specified | [167] |
| | PLG-g-LPEG/TAC | MMP9 cleavable peptide sequence (Gly-Pro-Leu-Gly-Leu) | Matrix metallo-proteinase 9 (MMP9) | Morphological transition from spherical NPs to microscale aggregate-like scaffolds | Cargo (tacrolimus) release | Rejection after liver transplantation | [177] |
| | MSN-HSA-PBA-DOX | MMP2 substrate (functional peptide R8-PVGLIG) | Matrix metallo-proteinase 2 (MMP2) | Breakdown intracellular linker | Enhanced endocytosis (targeting ligand PBA, exposed CPP) drug release (DOX) | Tumor, not further specified | [178] |
| Light | Self-assembled block copolymer nanoparticles | Ruthenium complex-based photocage | Near-infrared (NIR) light | Release of Ru complexes (prodrug activation, cleavage photocage) | Combined chemotherapy via drug (tetrahydrocannabinol, THC) release and photodynamic therapy | Tumor, not further specified | [179] |

Chapter 1

| | | | | | | | |
|--------------------------|--|--|--|---|--|---|-------|
| Temper- ature | Polysarcosine (PSAR)- <i>b</i> -(<i>N</i> -(2- hydroxypropyl)- methacrylamide) (PHPMA) NPs | Polysarcosine with 3.5 % of PHPMA | Moderate increase in solution temperature | Changes in particle morphology and shrinkage upon temperature increase | Doxorubicin release in response to subtile thermal stimulation (increase in environmental temperature to 41 °C). | Breast cancer | [180] |
| Ultrasound | Polymer-grafted mesoporous silica nanoparticles | Copolymer p(MeO ₂ MA)- co-THPMA with LCST below 37 °C; upon US irradiation the hydrophobic tetrahydropro- pyranyl groups in the polymer backbone were cleaved leading to hydrophilic methacrylate and increasing the LCST over 37 °C | US | Drug loading at 4 °C (open conformation), polymer collapses at 37 °C (closed conformation) upon US irradiation in cancer → pore opening (gate- keeper removal) and drug release | Controlled drug release in the tumor tissue upon US irradiation; fluorescein was used as model cargo | Cancer, not specified | [181] |
| Magnetism | Poly-paclitaxel/ cyclodextrin- superparamag- netic iron oxide nanoparticle (SPION) | Iron oxide core | Altering magnetic field (AMF) | Host-guest interaction between β- cyclodextrin- SPION and poly paclitaxel (pPTX) to form nano-assembly with cluster structures of SPIONs | Enhanced magnetic guidance for targeted nanotherapy | Anticancer therapy, not specified | [182] |
| | Fe ₃ O ₄ -NPs coated with a silica-PEG shell and loaded with doxorubicin (Dox) | Iron oxide core | AMF | Local heating of the particle core which accelerated Dox release | Controlled drug release in tumor tissue | Anticancer therapy, not specified | [183] |
| | Hybrid nanogels composing of thermo-responsive polymers and SPIONS | Iron oxide core | AMF | Local heating which accelerated Dox release | Controlled drug release in tumor tissue | Cancer, not specified | [184] |

Introduction

| | | | | | | | |
|--|--|---|---|---|---|--------------------------|-------|
| Multiple responsive | AUS-PM(PCL-SS-PCL-MPC deblock copolymer) TMT-DOX | TMT (receptor-mediated endocytosis), disulfide (GSH-sensitive), PCL (pH sensitive) gold (sound-sensitive) | TMT receptor, GSH, pH in tumor tissue, gold (ultra-sound responsive) | PCL core breakdown under pH 5.5, disulfide linkage → | DOX release, ROS generation, cytotoxicity in cancer cells increased ROS production when exposed to ultrasound stimulation | Metastatic breast cancer | [185] |
| Enzyme/pH dual-responsive NPs based on human heavy-chain ferritin (HFn), modified with Anti-PD-L1 peptide CLP002 and MMP-2/9 substrate peptide | MMP-2/9 substrate peptide, pH-mediated recombinant ferritin (CMFn) | Matrix metallo-proteinase-2/9 (MMP-2/9) over-expressed within the tumor microenvironment, acidic pH | MMP-2/9 cleaves linkage of CLP002 → blockade of PD-1 receptor, release of oxaliplatin in lysosomes after endosomal uptake → synergistic values within lysosomes | Tumor-targeted delivery and controlled release of the CLP002 and the lysosomes after endosomal uptake → synergistic values within lysosomes | Cancer therapy, not further specified | [186] | |
| pH-responsive polymer, photocatalyst eosin Y, ROS-sensitive prodrug protection group | PAEMA, eosin Y, (460 nm) | Acidic pH value in tumor tissue, light irradiation (460 nm) | Protonation PAEMA → morphological transition, exposure of the photocatalyst eosin Y, light irradiation → prodrug activation | Targeted prodrug activation within the acidic tumor environment in combination with photo-dynamic generation of ROS for remediation of cancerous tissue | Cancer therapy, not further specified | [187] | |

Table 1. Overview of activatable, smart nanoparticle systems. Abbreviations: ACE, angiotensin-converting enzyme; AMF, altering magnetic fields; CA, cinnamaldehyde; Cys, Cysteine; DMA, dimethylmaleic anhydride; DOX, doxorubicin; GGT, γ -glutamyl transpeptidase; GSH, glutathione; HFn, heavy chain ferritin; HAS, human serum albumin; HCPT, 10-hydroxycamptothecin; ICAM1, intracellular adhesion molecule 1; LCST, lower critical solution temperature; MMP, matrix-metalloproteinase; MSN, mesoporous silica nanoparticles; MTO, mitoxantrone; NIR, near infrared; PEG-*b*-P(TMBPEC-*co*-AC), poly(ethylene glycol)-*b*-poly(mono-2,3,6-trimethoxy benzylidene-pentaerythritol carbonate-*co*-acryloyl carbonate); PAE, poly(β -amino esters); PAEMA, poly(2-azepane ethylmethacrylate); PBA, phenylboronic acid; PDSA, poly (disulfide amide); PEG, polyethylene

Chapter 1

glycole; PHPMA, *N*-(2-hydroxypropyl)methacrylamide; PLA, poly lactide acid; PLG, poly (L-glutamic acid); PLGA, poly(lactic-co-glycolic) acid; pLL, poly-L-lysine; p(MEO₂MA), poly(2-(2-methoxyethoxy)ethyl methacrylate); PSAR, polysarcosine; PTX, paclitaxel; QDs, Quantum dots; ROS, reactive oxygen species; Ru, Ruthenium; SPION, superparamagnetic iron oxide; TAC, tacrolimus; THPMA, 2-tetrahydropyranyl methacrylate; TMT, ten-tumor metastasis targeting peptide; US, ultrasound.

3.5.1 Bioresponsive Nanoparticles

For intrinsically activatable or bioresponsive nanoparticles, physiologically or pathologically occurring conditions in certain tissues or at the subcellular level are used to trigger a specific effect, for example, the activation of a targeting ligand or a prodrug, a morphological transition, or the removal of a gatekeeper, which has prevented drug release (Fig. 7). This is enabled by the incorporation of switching capabilities in the particle structure, which react to changes in the pH value or redox gradients, or can be cleaved by certain enzymes [188].

As already pointed out, nanoparticles are mainly internalized via endocytic pathways and thus primarily localized inside endosomes [189]. Endosomes possess a pH value of about 5.5-6.3 [190] and are consequently more acidic than other organelles [191] or the cytoplasm, which has a pH value of 7.0 to 7.4 [192]. Furthermore, early endosomes undergo a maturation process to late endosomes and ultimately lysosomes, which are even more acidic with pH values between 4.5 and 5 [190]. Since the extracellular pH value, under physiological conditions, is in the neutral to slightly alkaline range (pH 7.3-7.4) [191], the entry of nanoparticles into an acidic environment by particle uptake can be used as a trigger for nanoparticle activation. Additionally, there are differences in extracellular pH values, which can be utilized for nanoparticle targeting. The most popular example is the slightly acidic extracellular environment around hypoxic tumor tissue. Here the pH value can drop to 6.4 to 6.8 since cancer cells are metabolizing glucose via lactate-producing pathways [193]. For the development of pH-dependent particles, different strategies have been implemented, e.g. the equipment with acid labile linkers (Tab. 2), charge-shifting polymers, or particle crosslinking. These features should lead to changes in size, shape, surface chemistry, particle disassembly, and cargo release, respectively [194]. One example is the concept of Zhang et al. (2019) [173]. The work group investigated pH-responsive nanoparticles targeting the lungs for the therapy of acute lung inflammation. They implemented pH-responsive polymers in their particle design for a site-specific drug release in the target tissue. After targeting the ICAM-1 receptor via ICAM-1 antibodies tethered to the nanoparticle surface, the previously stable particle core,

Introduction

consisting of poly(β -amino esters) (PAE), was degraded due to the lower pH values of inflammatory tissues, resulting in the release of the anti-inflammatory model agent TPCA-1 (Fig. 7c). Lee et al. (2008) [195] utilized super pH-sensitive polymers for the design of nanoparticles with a ligand pop-up activation (Fig. 7f). In an acidic environment, the protonation of the previously folded poly(L-lactic acid)-*b*-poly(ethylene glycol)-*b*-poly(L-histidine)-TAT block copolymer causes polymer extension and the CPP TAT is revealed on the particle surface, which leads to particle uptake.

| pH-labile linker | Reaction mechanism | Ref. |
|------------------|--------------------|-----------|
| Acetal/Ketal | | [196,197] |
| Hydrazone | | [198,199] |
| Imine | | [200] |
| Oxime | | [201] |
| Ortho ester | | [202] |
| Borate ester | | [203,204] |
| Vinyl ether | | [205,206] |
| Amide | | [207] |

Table 2. pH-labile linkers as pH-activatable NP structures with corresponding activation mechanisms.

Analogous to particle activation via naturally occurring pH gradients, also redox gradients can be utilized for nanoparticle activation. In this case, instead of acid-cleavable linkers, redox-cleavable linkers are implemented in the particle design. An overview of such oxidizable and reducible linkers is shown in table 3. Glutathione (GSH), which is a tripeptide cell protective

Chapter 1

antioxidant [208], is mainly responsible for the activation of reductive-responsive nanoparticles by interacting with for example disulfide bonds (S-S) or diselenide bonds (Se-Se). GSH exists ubiquitously in the human body and participates in various biological functions like gene expression, cell proliferation, or apoptosis [209]. The highest intracellular GSH concentration is found in the cytosol with physiological average values of 2-10 mM. Since the extracellular concentration of GSH is around 100- to 1000-fold lower (2-20 μ M), the particles are stable during blood circulation and cleavage of the linkers occurs after particle uptake. Therefore, GSH-responsiveness is an ideal stimulus to accomplish efficient intracellular, while avoiding unspecific extracellular, drug release [210]. The oxidative cleavage of linkers is usually caused by reactive oxygen species (ROS), like hydrogen peroxide (H_2O_2), hydroxyl radicals ($OH\cdot$), or singlet oxygen (1O_2). These highly reactive molecules are primarily generated in mitochondria and contribute to human immunity [211]. Prominent examples of oxidative responsive linkers are sulfur- or selenium-containing, or arylboronic ester linkages [211]. Since ROS as well as GSH levels are significantly increased in the tumor microenvironment, redox-responsive on-site activation of nanoparticles is promising in the context of cancer therapy [174]. One example is the investigation of ROS-responsive poly-prodrug nanoparticles with triggered drug release for cancer therapy by Xu et al. (2017) [176], which combined target cell recognition and uptake with on-site prodrug activation. The established NP platform was composed of three components: the poly-prodrug, forming the inner core, which was supposed to respond to increased ROS concentration with a release of the activated drug molecules (Fig. 7e), the outer shell, consisting of polyethylene glycol, and the targeting ligand, internalizing RGD (iRGD), which was supposed to enhance selectivity and tissue penetration. Another application field of ROS-responsive nanoparticles is the treatment of chronically inflammatory diseases such as rheumatoid arthritis or ulcerative colitis [170]. Zhang et al. (2023) [170] established polymeric prodrug nanoparticles, in which the drug, cinnamaldehyde (CA), was protected by an oxidative-cleavable conjugation to a PEG polymer, causing the self-assembly of polymer-drug-conjugate nanoparticles. The functional aldehyde group is only released by ROS activity in inflammatory tissues, where CA acts anti-inflammatory due to its ROS-scavenging activity (Fig. 7c). Furthermore, Ji et al. (2023) [175] established GSH-responsive polymeric nanoparticles, consisting of poly(disulfide amide) (PDSA) polymers [212], which are disassembled due to the reductive conditions after myocardial infarction by cleavage of the disulfide bonds (Fig. 7c). In this way, the release of the encapsulated drug, the sphingosine kinase 1 inhibitor PF543, was triggered inside the cardiac fibroblast target cells. The research group has thus provided an efficient strategy for the pharmacological intervention of cardiac fibrosis.

| Redox response | Redox-responsive linker | Reaction mechanism | Ref. |
|-----------------------------------|-------------------------------|--------------------|-----------|
| Reductive cleavage | Disulfide bond | | [213,214] |
| Reductive cleavage | Diselenide bond | | [215,216] |
| Oxidative cleavage | Diselenide bond | | [217] |
| Oxidative cleavage | Thioketal-based linker | | [218] |
| Oxidative cleavage | Thiocarbam at-based linker | | [219] |
| Oxidative structural dissociation | Selenium containing polymers | | [220] |
| Oxidative structural dissociation | Tellurium containing polymers | | [221,222] |
| Oxidative cleavage | Arylboronic ester | | [223-225] |

Table 3. Redox-activatable NP structures and activation mechanisms.

Enzymes can also be used for the bioresponsive activation of nanoparticles. Therefore, substrates of the corresponding enzymes are integrated into the particle design. Compared to pH- or redox-responsive structures, enzyme-responsiveness has the advantage that the application is not limited to certain tissues, such as tumor tissue or inflamed areas, but can be adapted to almost all cell types. Various strategies have been developed, which enable either particle uptake or controlled drug release: Maslanka et al. (2019) [66] designed polymeric core-shell nanoparticles, with the ligand angiotensin I (Ang I) tethered to the surface. Due to the enzymatic cleavage of the ligand by the angiotensin-converting enzyme (ACE), Ang I was converted to angiotensin II. Thus, the nanoparticle presented a receptor agonist for the AT1 receptor (AT1R), which led to particle binding and uptake (Fig. 7a). The enzymatic ligand activation increased the target cell selectivity and enabled preferential uptake in mesangial cells that express both ACE and the AT1R. Li et al. (2014) [226] developed nanoparticles, which

Chapter 1

were activated by cleavage of a PEG-shielding unit by the matrix metalloproteinase 7 (MMP-7). The pop-up activation strategy (Fig. 7f) revealed the targeting ligand folic acid (FA) and thus enabled selective uptake in FA-overexpressing breast cancer cells. Another approach to improve nanoparticle uptake after enzymatic activation is the charge reversal strategy, performed by Dai et al. (2024) (Fig. 7b) [167]. The research group implemented a γ -glutamyl-transpeptidase (GGT)-activatable motif into the modular peptide, which was used as a ligand for quantum dots. The initially terminal amino acid, which caused a zwitterionic charge on the QD surface, was removed by cleavage of the peptide bond, releasing a positively charged primary amine on the particle surface. Due to the charge reversal, the QDs showed enhanced cellular uptake and deep tumor penetration. According to this principle, also cell-penetrating peptides may be released. They are not exclusively, but to a large extent, polycationic, and therefore also cause charge reversal [227]. However, enzymatic activation cannot only improve uptake, but also achieve a temporally and spatially stringently coordinated cargo release. One example of this is the work of Luo et al. (2024) [177], which enabled a specific cargo release of tacrolimus in the liver allograft to overcome an acute rejection. The nanoparticles were composed of tacrolimus, which was covalently conjugated to matrix metalloproteinase 9 (MMP9)-cleavable peptide-containing polymers. Since MMP is overexpressed in rejected liver allografts, enzymatic cleavage of the particles in the target tissue caused a morphological transition from spherical micellar nanoparticles to microscale aggregate-like scaffolds and thus a site-specific drug release (Fig. 7c). A further approach to control drug release by enzymatic responsibility was the cleavage of an end-capping and thus sealing agent for the mesopores of mesoporous silica nanoparticles (MSN), which was attached to the particle surface via a MMP-2 cleavable peptidic substrate (Fig. 7d) [178].

3.5.2 *Extrinsically-Activatable Nanoparticle Characteristics*

Besides intrinsic signals, also extrinsic stimuli can be utilized for nanoparticle activation. In this case, light of different wavelengths, magnetism, ultrasound, or temperature changes can be applied, depending on the nanoparticle type and its structural features.

Three main groups of photo-activatable compounds are used for the regulation of the distribution, uptake, or cargo release of light-responsive nanoparticles. “Phototriggers” are photolabile protection groups (PPGs) that undergo irreversible photolysis reactions [228], “photosensitizers” are used for the controllable generation of ROS, e.g. singlet oxygen (${}^1\text{O}_2$), hydroxyl radicals or superoxides, also heat, and nitric oxide (NO), that trigger a photo response,

Introduction

while “photoswitches” perform reversible regulation by photoisomerization [179,229,230]. Since light can be regulated very precisely in area, time, and dosage, light-responsive targeting strategies have been widely applied [229,230]. Especially PPGs are frequently used for targeting systems, which allow the controlled release of a variety of caged compounds, such as functional groups, drugs, enzymes, neurotransmitters, or fluorophores [231]. The phototrigger should meet several prerequisites: a highly controllable and predictable photolysis mechanism, low cytotoxicity and a high quantum yield, good solubility, and stability in physiological media [229]. Furthermore, PPGs should provide sufficient absorption of at least 300 nm or higher and the photolysis products themselves should not absorb in this range, as this would result in a competitive behavior between PPGs and lysis products [229,232]. For the majority of light-responsive moieties an excitation in the UV range is required. This has two fundamental disadvantages: UV light has a higher potential for cell damage and low tissue penetration (< 1 cm) through light scattering and absorption of intrinsic biological chromophores, including hemoglobin, oxyhemoglobin, and melanin [229,233]. Therefore, an increasing number of near-infrared (NIR)-responsive approaches that are activated by light at wavelengths from 700 to 950 nm [179] have been developed in recent years. NIR light is not only safer, but can also penetrate deeper into biological tissue [179,217,233]. A light-responsive approach developed by He et al. (2023) [179] coordinated a ruthenium-based photocage to the anticancer drug tetrahydrocurcumin (THC), which served as a ligand of self-assembled nanoparticles of amphiphilic block copolymers. The photocage primarily inhibited the anticancer properties of THC. Only after cleavage of the photocage by NIR light at 760 nm, the drug was released, resulting in inhibited tumor proliferation. Examples of further commonly used PPGs are shown in figure 8.

Chapter 1

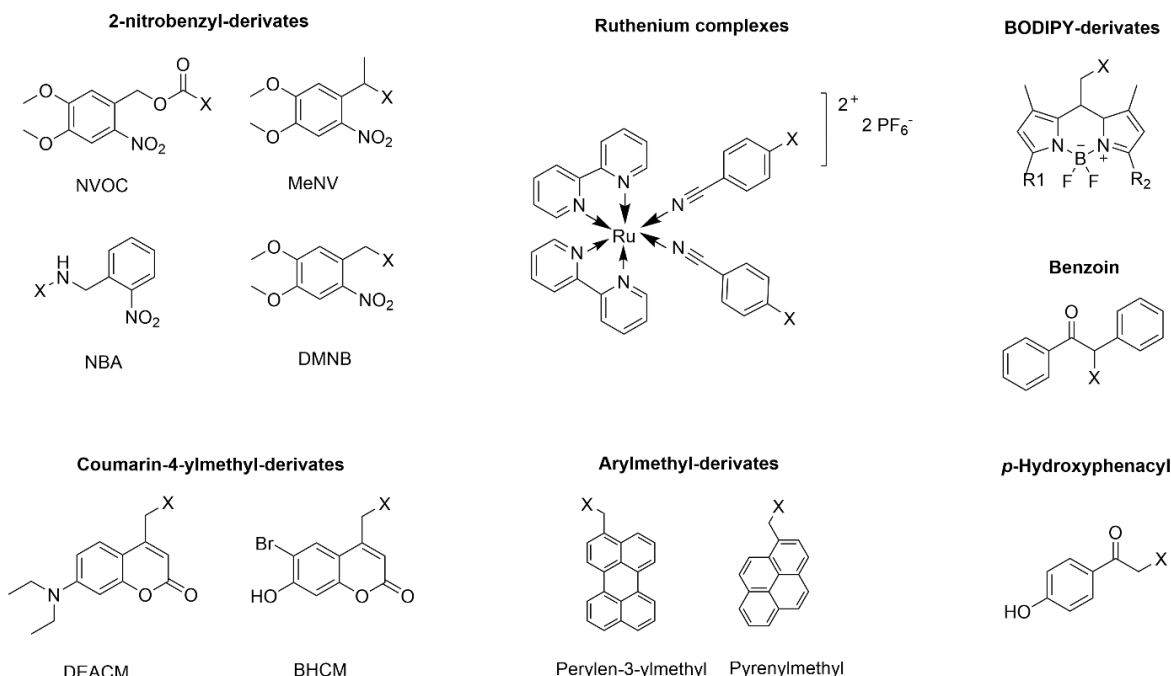


Figure 8. Structures of representative PPGs.

Thermo-responsiveness describes the ability to respond to changes in temperature with alterations in size, shape, solubility, or the release of an encapsulated drug [234]. Temperature-responsive polymers play an important role in this context [235]. The general idea of thermo-responsive polymers is that by changing the temperature, an encapsulated drug is released due to conformational changes of the polymer structure. They possess either a lower critical solution temperature (LCST) or an upper critical solution temperature (UCST) in aqueous medium [235,236]. For polymers with a LCST, heating leads to polymer shrinkage, and the cargo is ejected from its nanocarrier. The NP size either decreases in terms of colloidally stable particles or increases due to particle aggregation [234,235]. UCST polymers are soluble above a certain temperature. Therefore, after a temperature increase above this value, the encapsulated drug is released by particle disassembly [237]. Consequently, the application of moderate hyperthermia up to 43 °C, obtained by e.g. microwaves [238], radiofrequency [239], NIR [240], ultrasound [241], or magnetic fluid hyperthermia [242], for a prolonged period, enables particle activation [235]. By this principle, Yu et al. (2019) [180] investigated thermo-responsive particles based on polysarcosine-polymers, grafted with 3.5 % of (*N*-(2-hydroxypropyl)methacrylamide) for the treatment of different kinds of breast cancer. Doxorubicin (Dox) release was strictly controlled by an increase of the environmental temperature to 41 °C. For more detailed information we refer to reviews that give an overview of suitable thermo-responsive polymers and particle structures [235,243,244].

Introduction

Ultrasonic responsiveness is also mainly concerned with the controlled release of encapsulated compounds from nanoparticles. Ultrasound exposure causes physical disruption, structural changes, or chemical reactions of the drug carrier as a result of thermal or mechanical effects triggered by cavitation or radiation forces [245]. This method can be applied to many different types of nanoparticles, such as polymer NPs, liposomes, gold particles, or carbon nanotubes [245]. An advantage compared to particle stimulation using external light is that low-frequency ultrasound can penetrate deep into soft tissues [246]. Additionally, ultrasonic stimulation can induce a transient increase of blood vessel permeability, which promotes extravasation of the nanoparticles and thus increases cellular uptake in the target tissue [247]. Ultrasound-responsive nanocarriers are being investigated mainly in the context of cancer treatment [245]. An example of an ultrasound-responsive nanoparticle design was presented by Paris et al. (2015) [181]. The research group investigated polymer-grafted mesoporous silica nanoparticles with copolymers as pore gatekeepers. The nanoparticles were loaded at 4 °C, where the polymer showed an open conformation. At 37 °C, the copolymer collapsed, resulting in closed pores that could be injected without premature drug release. Only after ultrasound irradiation, the polymer structure changed towards a helical conformation, causing the opening of the mesoporous network and thus drug release. Furthermore, sonopermeation is an explored strategy to promote drug delivery across the blood-brain-barrier (BBB). Hark et al. (2024) [248] used the combination of ultrasound and RGD-coated polymeric microbubbles to induce temporally and spatially controlled opening of the BBB and thus mediate drug delivery by a polymeric drug carrier in an inflamed endothelium-pericyte co-culture model.

Altering magnetic fields (AMF) can be utilized to spatially and temporally control the distribution of NPs to target sites or to promote a magnetothermal drug release by hyperthermic bond-breaking or thermally induced permeability changes [245,249]. One example is the work of Jeon et al. (2016) [182]. The work group investigated poly-paclitaxel/cyclodextrin-superparamagnetic iron oxide nanoparticle (SPION) nano-assemblies that were actively guided to the tumor via an externally applied magnetic field. They established a method of NP clustering that additionally provides the possibility of magnetically induced targeting even to cancers deep in the body. Demin et al. (2022) [183] established magnetism-responsive particles with a Fe_3O_4 core and a silica-polyethyleneglycol (SiO₂/PEG) shell, which were loaded with a high level of doxorubicin (Dox) to target different cancer cell lines. The application of an alternating magnetic field led to local heating of the particle core, which accelerated Dox release. A similar drug release mechanism triggered by magnetic hyperthermia was performed

Chapter 1

in the study of Cazares-Cortes et al. (2017) [184], with hybrid nanogels composed of thermoresponsive polymers and SPIONS.

3.6 Dual- and Multi-responsive Particles

Recently, increasingly complex concepts for targeted drug delivery have been developed. They combine at least two or even more orchestrated steps to enable stringent control of nanoparticle distribution and drug release.

Liu et al. (2024) [186] demonstrated an enzyme/pH dual-responsive particle system for improved tumor immune chemotherapy. The immune checkpoint inhibitor CLP002 was tethered to the surface of ferritin-based particles via a peptidic linkage motif containing the substrate of the matrix metalloproteinase-2/9 (MMP-2/9). Cleavage of the substrate led to the release of the free drug, resulting in the inhibition of its receptor, the PD-L1 receptor. A second drug, oxaliplatin (OXA), was encapsulated into the nanoparticle core. OXA was released due to acidic NP disassembly in lysosomes upon endosomal uptake, which led to a combined immuno-chemotherapy (Fig. 9A).

Another multi-responsive approach was established by Maghsoudian et al. (2024) [185], who combined pH-, redox-, and ultrasonic-responsiveness (Fig. 9B). The objective of the study was to develop a biocompatible and stable bioactive zwitterionic micelle for the treatment of metastatic breast cancer. The prepared nanomicelles, which served as drug carrier for doxorubicin, were composed of a zwitterionic polymer of methyl methacryloyl phosphoryl cholin, and poly caprolactone (PCL) with a gold core. The integration of gold into the micelle core led to enhanced stability during circulation in the blood stream and served as sound-sensitive agent. The ten-tumor metastasis targeting (TMT) peptide was tethered to the micellar surface and enabled specific target cell recognition and receptor-mediated endocytosis. Additionally, the copolymers were modified to incorporate a disulfide structure. When exposed to ultrasound stimulation, these disulfide linkages led to an increased ROS production and similarly a reduction of the GSH level, which had cell-toxic effects. Furthermore, under a pH of 5.5, which is related to conditions in tumor tissue, the breakdown of PCL increased the release of the encapsulated drug in the target tissue. The findings of this study suggested that the established micellar nanocarriers can induce apoptosis in cancer cells and thus hold great potential for the treatment of metastatic breast cancer.

Introduction

Li et al. (2024) [187] combined targeted prodrug activation within the acidic tumor microenvironment with the photodynamic generation of ROS. Therefore, a pH-responsive photocatalytic system has been developed that selectively generates ROS and further activates prodrugs in a cascade reaction. At a pH of 7.4, the synthesized switchable poly(ethylene glycol)-*b*-poly(2-azepane ethylmethacrylate)-*b*-2-(methacryloyloxy)ethyl 2-(2,4,5,7-tetrabromo-3,6-dihydroxy-9*H*-xanthen-9-yl)benzoate(PEG₁₁₃-*b*-PAEMA₅₀-EYHEMA₁) polymer chains self-assembled to form polymeric nanoparticles. Due to the protonation of the PAEMA block, the particles disassembled and exposed the photocatalyst eosin Y. Upon light irradiation, the active eosin Y generated ROS, which led to ROS-induced cleavage of protection groups and thus activation of prodrugs with anticancerous activity (Fig. 9C).

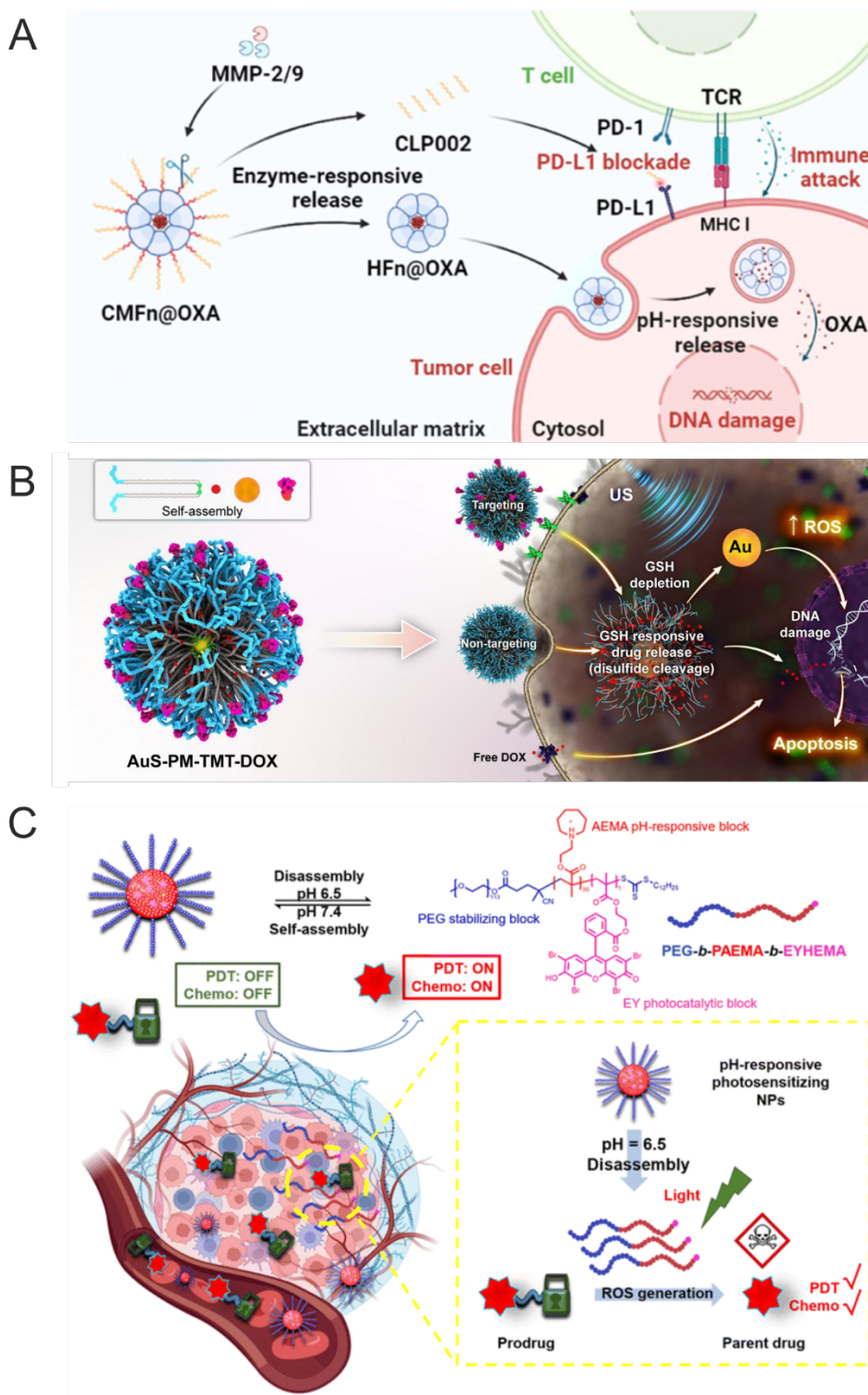


Figure 9. Concepts of multi-responsive targeting systems. (A) Reprinted with permission from Ref. [225] Copyright (2024) American Chemical Society. Due to the enzymatic cleavage of MMP-2/9 the first active ingredient, CLP002 is released, which inhibits the PD-L1 receptor on the cell surface. Disassembly in the acidic environment of the endo-lysosomal compartment leads to the release of the second drug OXA. (B) Reprinted with permission from Ref. [185] Copyright (2024) American Chemical Society. Target cell recognition and endocytosis are mediated by the ten-tumor metastasis targeting (TMT) peptide. Ultrasonic stimulation of disulfide linkages increased the ROS production and

simultaneously led to a decrease in the GSH level. The disassembly of polycaprolactone (PCL) under acidic conditions in the tumor microenvironment ultimately triggered the release of the encapsulated drug DOX. **(C)** Reproduction of material from Polymer Chemistry with permission from the Royal Society of Chemistry [187]. The nanoparticle disassembly in an acidic environment reveals the photocatalyst eosin Y. Upon light irradiation eosin Y then produces ROS, activating prodrugs for cancer therapy.

3.7 Subsequent Particle Modification via Bioorthogonal Click Chemistry

Another innovative strategy to control NP biodistribution is the subsequent particle modification via bioorthogonal reactions taking place *in vivo*. Bioorthogonal chemistry, which is a further development of copper-based click chemistry, meets requirements such as outstanding selectivity, feasibility in mild aqueous conditions, and high yields with a rapid reaction rate [250,251]. Since the functional groups of the reactant and the product do not interact with functional biomolecules and, as in contrast to the original click-chemistry, no toxic catalysts are necessary, bioorthogonal reactions can take place on cell surfaces or in the cytosol of living cells [251,252]. To influence particle biodistribution, pre-targeting (PT) concepts have been investigated that rely on highly specific covalent interactions between two bioorthogonal entities, of which the nanoparticle carries the first reactive group, while the other one is tagged for example to an antibody, a fluorophore, or a drug [252,253]. Either, the tagged ligand is initially injected, forming a targeting moiety for the subsequently administered nanoparticles, or targeted nanoparticles are injected first and a subsequently injected drug or label reacts with the NP localized at the site of action (Fig. 10) [252]. The most studied reaction types in this context are the inverse electron-demand Diels-Alder cycloaddition (IEDDA) reaction [253,254] and the strain-promoted alkyne azide cycloaddition (SPAAC) [255,256]. So far, PT has mostly been applied in the context of tumor targeting [33,257,258] and in particular in the positron emission tomography (PET) imaging of tumors [253,259,260]. Nevertheless, this strategy could also be utilized for controlled biodistribution and drug delivery to other tissues by adapting the targeting moieties accordingly. One advantage of bioorthogonal chemistry-based targeting is that it allows a simple, flexible, and universally applicable NP modification. By tethering one click entity to the NP surface, the NP can easily be modified with a multitude of click partners and is thus suitable for various applications. Many counteracting molecules functionalized with bioorthogonal entities are commercially available and can thus serve as targeting ligands. Furthermore, the attachment of quite small click-entities prevents NP aggregation and crosslinking, which might be problematic for macromolecular ligands such as monoclonal

Chapter 1

antibodies (mAbs) or avidin. As a result, NP modification and purification are facilitated [252]. Additionally, PT may increase targeting effects by the amplification of available binding sites. One monoclonal antibody (mAb) can be tagged with up to 30 trans-cyclooctene (TCO) molecules, allowing the binding of several NPs [32], which simplifies detection in tumor imaging, but may also increase therapy efficacy for targeted drug delivery [32,252]. The research group of Yoo et al. (2019) [32] established a pretargeting strategy using TCO-modified trastuzumab as targeting moiety and tetrazine-modified, drug-loaded nanoparticles that should be delivered to the site of action. The click-chemistry mediated binding allowed enhanced tumor targeting and thus showed that pretargeting is a promising strategy to maximize the amount of drug reaching the target site. For a more precise description of the reactions and possible biomedical applications of nanoparticles using bioorthogonal chemistry, we would like to refer to reviews focused on this topic [252,261].

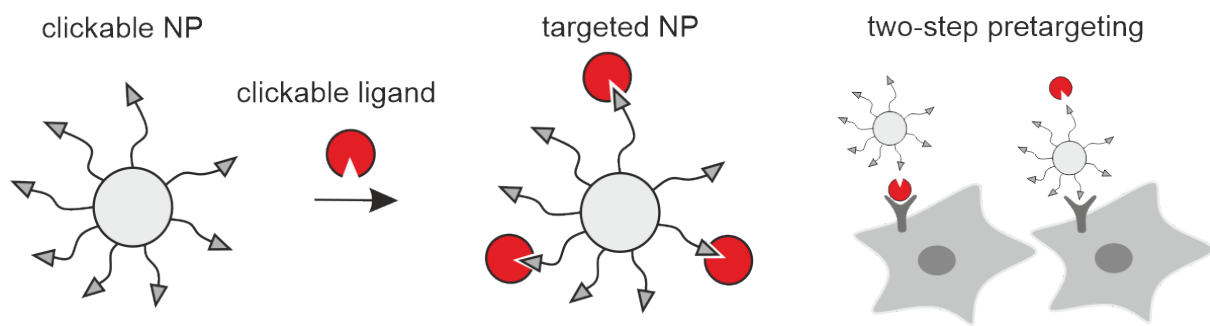


Figure 10. Nanoparticle targeting using bioorthogonal chemistry. The target cell selectivity of nanoparticles can be increased by pretargeting concepts with a click-reaction between the nanoparticle and a clickable ligand at the site of action. Either a targeting ligand, e.g. an antibody, is administered first, which then serves as an anchor point for the drug-loaded nanoparticle (two-step pretargeting, left), or the nanoparticle itself binds to target cells via targeting ligands, which are attached to the NP surface. In a second step, a drug modified with a click entity can react with the nanoparticle and thus be addressed to the target tissue (two-step pretargeting, right).

4 Opportunities and Limitations of Complex Nanoparticle Design Strategies

Due to conflicting requirements and changing demands during the targeting and drug delivery process, the design of targeted nanoparticles is highly challenging [172]. Therefore, a systematic approach that considers the most important aspects of the specific application could improve therapeutic outcomes. However, this inevitably leads to more complex particle designs, complicating nanoparticle preparation, and hampering the reproducibility of results. Additionally, the attachment of a protein corona in biological media can alter the particles' identity, making it difficult to predict if *in vitro* processes will translate to living organisms [48,150]. Despite these challenges, several research groups have demonstrated that complex nanoparticle design can achieve very promising targeting results *in vivo*.

Maslanka et al (2020) [262] showed successful targeting of enzyme-responsive, hetero-multivalent particles to renal target tissue. Therefore, in the first step, the nanoparticles bound to the angiotensin II receptor type I (AT1R) of mesangial cells via the AT1R inhibitor EXP3174. Subsequently, the previously inactive second ligand angiotensin I was cleaved by the angiotensin-converting enzyme (ACE), which was expressed on the cell surface. The resulting active ligand, angiotensin II, attached to the AT1R on the cell surface, promoting receptor-mediated uptake into the target cells. The amount of the dual-modified, enzyme-responsive nanoparticles reaching the target tissue *in vivo* was considerably higher than the amount of unmodified particles or particles with single-ligand modification. This demonstrated the superiority of the complex, 3-step targeting concept compared to simple nanoparticle targeting (Fig. 11A).

Li et al. (2024) [263] developed a switchable crosslinked paclitaxel(PTX)-nanoformulation (BPM-PD@PTX) for the precise drug delivery to non-small cell lung cancer (NSCLC) brain metastases (Fig. 11B). The formulation incorporated an ultra-pH-sensitive boronate ester linkage and a lipid-like amphiphilic molecule, forming small-sized micelles and nanocomplexes by rapid crosslinking with PTX being loaded. This resulted in excellent biocompatibility and prolongation of the blood circulation time. The ultra-pH-sensitive boronate esters sealed the nanoformulation and effectively prevented premature drug release. Additionally, the external maltobionic acid (MA) groups of BPM-PD@PTX induced glucose transporter 1 (GLUT1)-mediated transcytosis in the blood-brain barrier and blood-tumor barrier. The lower pH value in the extratumoral microenvironment (pH 6.8-6.5) resulted in

Chapter 1

transformational changes, forming smaller non-crosslinked micelles with enhanced penetrability. As a result, 5-borono-2-pyridinecarboxylic acid formed new boronate ester bonds with the sialic acid, which is overexpressed in NSCLC cells, enabling precise PTX delivery. Thus, the research group could achieve highly effective PTX delivery for NSCLC brain metastases with reduced adverse reactions and improved therapeutic efficacy and thus surpass the clinical PTX-nanoformulation (nab-PTX).

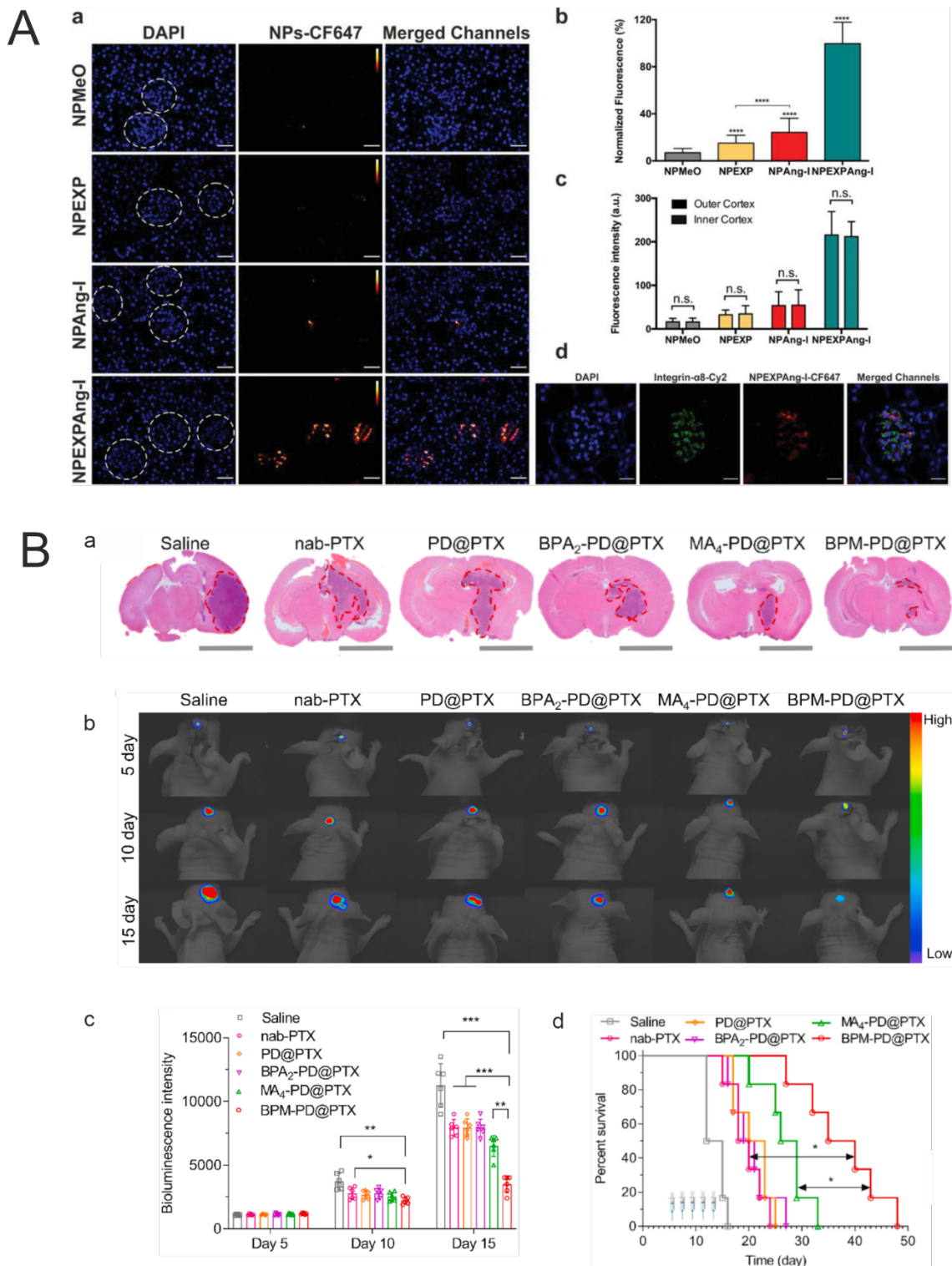


Figure 11. *In vivo* investigations of nanoparticle targeting concepts. (A) Reprinted with permission from Ref. [262]. Investigation of the NP-associated fluorescence in kidney glomeruli analyzed via fluorescence microscopy. a) Kidney glomeruli (highlighted with white, dotted circles) treated with different particle formulations (without ligand, single ligand modification, hetero-multivalent particle design with enzyme-responsibility). Scale bar: 40 μ m. b) Quantitative analysis of glomerular NP-associated fluorescence. c) Comparison of the NP fluorescence of the inner and outer cortex.

Chapter 1

d) Localization of NP-EXP-Ang-I via CLSM combined with integrin- α 8-staining of mesangial cells. Scale bar: 20 μ m **(B)** Reprinted with permission from Ref. [263]. Comparison of nanoparticle albumin-bound PTX (nab-PTX) with nanoformulation where PTX is loaded between two types of dendrimer-modified amphiphilic molecules (BPA₂-PD and MA₄-PD) and sealed using ultra-pH-sensitive boronate ester linkages (BPM-PD@PTX), preventing premature drug release. Furthermore, the effect was compared to PTX combined with the individual components (PD@PTX, BPA₂-PD@PTX, MA₄-PD@PTX). a) Hematoxylin-eosin (HE) staining of the brain at day 15 after tumor inoculation. Scale bar: 300 μ m. b) Tumor growth evaluation by bioluminescence imaging. c) Quantitative analysis of bioluminescence staining (n = 6). d) Kaplan-Meier survival curve during treatment (n = 6).

5 Conclusion

The previous illustrations emphasize the complexity of nanoparticle targeting and targeted drug delivery. On the one hand, numerous factors must be balanced to develop a particle design that meets all requirements. On the other hand, extremely complex particle structures impede the reproducible particle manufacturing. Furthermore, the synthesized particle identity may differ significantly from the biological identity *in vivo*. Nevertheless, there is growing evidence that a moderately complex, multi-step particle activation *in situ* holds great potential to address current challenges in targeted nanotherapy. In conclusion, the development of nanoparticle-based drug delivery systems with a controlled time-variant structure, that changes during an application depending on the task the nanoparticle has to master, seems rather advantageous. Therefore, key factors relevant to each specific application need to be identified and implemented into nanoparticle design. Finally, the efficacy of the developed concepts needs to be verified in case-by-case studies *in vivo* to obtain reliable results.

References

- [1] M. Walter, H. Weißbach, F. Gembardt, S. Halder, K. Schorr, D. Fleischmann, V. Todorov, C. Hugo, A. Goepferich, Long-term residence and efficacy of adenovirus-mimetic nanoparticles in renal target tissue, *Journal of Drug Targeting* (2024) 1–13. <https://doi.org/10.1080/1061186X.2024.2390628>.
- [2] J. Yoo, C. Park, G. Yi, D. Lee, H. Koo, Active Targeting Strategies Using Biological Ligands for Nanoparticle Drug Delivery Systems, *Cancers* 11 (2019) 640. <https://doi.org/10.3390/cancers11050640>.
- [3] S. Maslanka Figueroa, D. Fleischmann, A. Goepferich, Biomedical nanoparticle design: What we can learn from viruses, *J. Control. Release* 329 (2021) 552–569. <https://doi.org/10.1016/j.jconrel.2020.09.045>.
- [4] K. Elbrink, S. van Hees, R. Chamanza, D. Roelant, T. Loomans, R. Holm, F. Kiekens, Application of solid lipid nanoparticles as a long-term drug delivery platform for intramuscular and subcutaneous administration: In vitro and in vivo evaluation, *Eur. J. Pharm. Biopharm.* 163 (2021) 158–170. <https://doi.org/10.1016/j.ejpb.2021.04.004>.
- [5] T. Stack, Y. Liu, M. Frey, S. Bobbala, M. Vincent, E. Scott, Enhancing subcutaneous injection and target tissue accumulation of nanoparticles via co-administration with macropinocytosis inhibitory nanoparticles (MiNP), *Nanoscale Horiz.* 6 (2021) 393–400. <https://doi.org/10.1039/D0NH00679C>.
- [6] B. Rama, A.J. Ribeiro, Role of nanotechnology in the prolonged release of drugs by the subcutaneous route, *Expert Opin. Drug Deliv.* 20 (2023) 559–577. <https://doi.org/10.1080/17425247.2023.2214362>.
- [7] G.M. Demirbolat, L. Altintas, S. Yilmaz, I.T. Degim, Development of Orally Applicable, Combinatorial Drug-Loaded Nanoparticles for the Treatment of Fibrosarcoma, *Journal of pharmaceutical sciences* 107 (2018) 1398–1407. <https://doi.org/10.1016/j.xphs.2018.01.006>.
- [8] X. Huang, Y. Chau, Intravitreal nanoparticles for retinal delivery, *Drug Discovery Today* 24 (2019) 1510–1523. <https://doi.org/10.1016/j.drudis.2019.05.005>.
- [9] W. Yang, J.I. Peters, R.O. Williams, Inhaled nanoparticles--a current review, *International Journal of Pharmaceutics* 356 (2008) 239–247. <https://doi.org/10.1016/j.ijpharm.2008.02.011>.
- [10] M.Q. Le, R. Carpentier, I. Lantier, C. Ducournau, I. Dimier-Poisson, D. Betbeder, Residence time and uptake of porous and cationic maltodextrin-based nanoparticles in the

Introduction

nasal mucosa: Comparison with anionic and cationic nanoparticles, *International Journal of Pharmaceutics* 550 (2018) 316–324. <https://doi.org/10.1016/j.ijpharm.2018.08.054>.

[11] H. Meng, W. Leong, K.W. Leong, C. Chen, Y. Zhao, Walking the line: The fate of nanomaterials at biological barriers, *Biomaterials* 174 (2018) 41–53. <https://doi.org/10.1016/j.biomaterials.2018.04.056>.

[12] L.M. Ensign, R. Cone, J. Hanes, Oral drug delivery with polymeric nanoparticles: the gastrointestinal mucus barriers, *Adv. Drug Deliv. Rev.* 64 (2012) 557–570. <https://doi.org/10.1016/j.addr.2011.12.009>.

[13] W.-H. Lee, C.-Y. Loo, D. Traini, P.M. Young, Inhalation of nanoparticle-based drug for lung cancer treatment: Advantages and challenges, *Asian Journal of Pharmaceutical Sciences* 10 (2015) 481–489. <https://doi.org/10.1016/j.ajps.2015.08.009>.

[14] V. Mirshafiee, M. Mahmoudi, K. Lou, J. Cheng, M.L. Kraft, Protein corona significantly reduces active targeting yield, *Chem. Commun.* 49 (2013) 2557–2559. <https://doi.org/10.1039/C3CC37307J>.

[15] Y.K. Lee, E.-J. Choi, T.J. Webster, S.-H. Kim, D. Khang, Effect of the protein corona on nanoparticles for modulating cytotoxicity and immunotoxicity, *Int. J. Nanomedicine* 10 (2015) 97–113. <https://doi.org/10.2147/IJN.S72998>.

[16] K. Abstiens, S. Maslanka Figueroa, M. Gregoritza, A.M. Goepferich, Interaction of functionalized nanoparticles with serum proteins and its impact on colloidal stability and cargo leaching, *Soft Matter* 15 (2019) 709–720. <https://doi.org/10.1039/C8SM02189A>.

[17] P.P. Karmali, D. Simberg, Interactions of nanoparticles with plasma proteins: implication on clearance and toxicity of drug delivery systems, *Expert Opin. Drug Deliv.* 8 (2011) 343–357. <https://doi.org/10.1517/17425247.2011.554818>.

[18] B. Yameen, W.I. Choi, C. Vilos, A. Swami, J. Shi, O.C. Farokhzad, Insight into nanoparticle cellular uptake and intracellular targeting, *J. Control. Release* 190 (2014) 485–499. <https://doi.org/10.1016/j.jconrel.2014.06.038>.

[19] L.Y.T. Chou, K. Ming, W.C.W. Chan, Strategies for the intracellular delivery of nanoparticles, *Chemical Society Reviews* 40 (2011) 233–245. <https://doi.org/10.1039/c0cs00003e>.

[20] F. Nadal-Bufi, S.T. Henriques, 2020. How to overcome endosomal entrapment of cell-penetrating peptides to release the therapeutic potential of peptides? *Peptide Science* 112, e24168. <https://doi.org/10.1002/pep2.24168>.

[21] D. Pei, M. Buyanova, Overcoming Endosomal Entrapment in Drug Delivery, *Bioconjug. Chem.* 30 (2019) 273–283. <https://doi.org/10.1021/acs.bioconjchem.8b00778>.

Chapter 1

[22] J. Li, L. Sun, Y. Liu, H. Yao, S. Jiang, YunzhuPu, Y. Li, Y. Zhang, To reduce premature drug release while ensuring burst intracellular drug release of solid lipid nanoparticle-based drug delivery system with clathrin modification, *Nanomedicine* 15 (2019) 108–118. <https://doi.org/10.1016/j.nano.2018.05.014>.

[23] T. Miller, S. Breyer, G. van Colen, W. Mier, U. Haberkorn, S. Geissler, S. Voss, M. Weigandt, A. Goepferich, Premature drug release of polymeric micelles and its effects on tumor targeting, *International Journal of Pharmaceutics* 445 (2013) 117–124. <https://doi.org/10.1016/j.ijpharm.2013.01.059>.

[24] L. Chen, C. Liu, Y. Xiang, J. Lyu, Z. Zhou, T. Gong, H. Gao, L. Li, Y. Huang, Exocytosis blockade of endoplasmic reticulum-targeted nanoparticle enhances immunotherapy, *Nano Today* 42 (2022) 101356. <https://doi.org/10.1016/j.nantod.2021.101356>.

[25] J.W. Hickey, J.L. Santos, J.-M. Williford, H.-Q. Mao, Control of polymeric nanoparticle size to improve therapeutic delivery, *J. Control. Release* 219 (2015) 536–547. <https://doi.org/10.1016/j.jconrel.2015.10.006>.

[26] X. Duan, Y. Li, Physicochemical characteristics of nanoparticles affect circulation, biodistribution, cellular internalization, and trafficking, *Small* 9 (2013) 1521–1532. <https://doi.org/10.1002/smll.201201390>.

[27] T.D. Clemons, R. Singh, A. Sorolla, N. Chaudhari, A. Hubbard, K.S. Iyer, Distinction Between Active and Passive Targeting of Nanoparticles Dictate Their Overall Therapeutic Efficacy, *Langmuir* 34 (2018) 15343–15349. <https://doi.org/10.1021/acs.langmuir.8b02946>.

[28] K.F. Pirollo, E.H. Chang, Does a targeting ligand influence nanoparticle tumor localization or uptake?, *Trends in Biotechnology* 26 (2008) 552–558. <https://doi.org/10.1016/j.tibtech.2008.06.007>.

[29] P. Kocbek, N. Obermajer, M. Cegnar, J. Kos, J. Kristl, Targeting cancer cells using PLGA nanoparticles surface modified with monoclonal antibody, *J. Control. Release* 120 (2007) 18–26. <https://doi.org/10.1016/j.jconrel.2007.03.012>.

[30] B.K. Lee, Y.H. Yun, K. Park, Smart Nanoparticles for Drug Delivery: Boundaries and Opportunities, *Chem. Eng. Sci.* 125 (2015) 158–164. <https://doi.org/10.1016/j.ces.2014.06.042>.

[31] S.-Y. Qin, A.-Q. Zhang, X.-Z. Zhang, Recent Advances in Targeted Tumor Chemotherapy Based on Smart Nanomedicines, *Small* 14 (2018) e1802417. <https://doi.org/10.1002/smll.201802417>.

Introduction

[32] J. Yoo, S. Choi, J. Son, G. Yi, E. Kim, H. Koo, Click chemistry-mediated tumor-targeting of SN38-loaded nanoparticles using trastuzumab, *Biochemical and Biophysical Research Communications* 515 (2019) 207–213. <https://doi.org/10.1016/j.bbrc.2019.05.128>.

[33] G. von Maltzahn, Y. Ren, J.-H. Park, D.-H. Min, V.R. Kotamraju, J. Jayakumar, V. Fogal, M.J. Sailor, E. Ruoslahti, S.N. Bhatia, In vivo tumor cell targeting with "click" nanoparticles, *Bioconjug. Chem.* 19 (2008) 1570–1578. <https://doi.org/10.1021/bc800077y>.

[34] T. Zhao, M. Ren, J. Shi, H. Wang, J. Bai, W. Du, B. Xiang, Engineering the protein corona: Strategies, effects, and future directions in nanoparticle therapeutics, *Biomed. Pharmacother.* 175 (2024) 116627. <https://doi.org/10.1016/j.biopha.2024.116627>.

[35] M. Xu, Y. Qi, G. Liu, Y. Song, X. Jiang, B. Du, Size-Dependent In Vivo Transport of Nanoparticles: Implications for Delivery, Targeting, and Clearance, *ACS Nano* 17 (2023) 20825–20849. <https://doi.org/10.1021/acsnano.3c05853>.

[36] S.A. Dilliard, D.J. Siegwart, Passive, active and endogenous organ-targeted lipid and polymer nanoparticles for delivery of genetic drugs, *Nat Rev Mater* 8 (2023) 282–300. <https://doi.org/10.1038/s41578-022-00529-7>.

[37] M. Lck, B.-R. Paulke, W. Schrder, T. Blunk, R.H. Mller, Analysis of plasma protein adsorption on polymeric nanoparticles with different surface characteristics, *J. Biomed. Mater. Res.* 39 (1998) 478–485. [https://doi.org/10.1002/\(SICI\)1097-4636\(19980305\)39:3<478:AID-JBM19>3.0.CO;2-6](https://doi.org/10.1002/(SICI)1097-4636(19980305)39:3<478:AID-JBM19>3.0.CO;2-6).

[38] S. Tenzer, D. Docter, J. Kuharev, A. Musyanovych, V. Fetz, R. Hecht, F. Schlenk, D. Fischer, K. Kiouptsi, C. Reinhardt, K. Landfester, H. Schild, M. Maskos, S.K. Knauer, R.H. Stauber, Rapid formation of plasma protein corona critically affects nanoparticle pathophysiology, *Nat. Nanotechnol.* 8 (2013) 772–781. <https://doi.org/10.1038/nnano.2013.181>.

[39] M. Lundqvist, J. Stigler, G. Elia, I. Lynch, T. Cedervall, K.A. Dawson, Nanoparticle size and surface properties determine the protein corona with possible implications for biological impacts, *Proc. Natl. Acad. Sci. U. S. A.* 105 (2008) 14265–14270. <https://doi.org/10.1073/pnas.0805135105>.

[40] L.E. González-García, M.N. MacGregor, R.M. Visalakshan, A. Lazarian, A.A. Cavallaro, S. Morsbach, A. Mierczynska-Vasilev, V. Mailänder, K. Landfester, K. Vasilev, Nanoparticles Surface Chemistry Influence on Protein Corona Composition and Inflammatory Responses, *Nanomaterials* 12 (2022) 682. <https://doi.org/10.3390/nano12040682>.

Chapter 1

[41] C. Marques, M.J. Hajipour, C. Marets, A. Oudot, R. Safavi-sohi, M. Guillemin, G. Borchard, O. Jordan, L. Saviot, L. Maurizi, Identification of the Proteins Determining the Blood Circulation Time of Nanoparticles, *ACS Nano* 17 (2023) 12458–12470. <https://doi.org/10.1021/acsnano.3c02041>.

[42] W. Xiao, Y. Wang, H. Zhang, Y. Liu, R. Xie, X. He, Y. Zhou, L. Liang, H. Gao, The protein corona hampers the transcytosis of transferrin-modified nanoparticles through blood-brain barrier and attenuates their targeting ability to brain tumor, *Biomaterials* 274 (2021) 120888. <https://doi.org/10.1016/j.biomaterials.2021.120888>.

[43] A. Salvati, A.S. Pitek, M.P. Monopoli, K. Prapainop, F.B. Bombelli, D.R. Hristov, P.M. Kelly, C. Åberg, E. Mahon, K.A. Dawson, Transferrin-functionalized nanoparticles lose their targeting capabilities when a biomolecule corona adsorbs on the surface, *Nat. Nanotechnol.* 8 (2013) 137–143. <https://doi.org/10.1038/nnano.2012.237>.

[44] S. Stolnik, L. Illum, S.S. Davis, Long circulating microparticulate drug carriers, *Adv. Drug Deliv. Rev.* 16 (1995) 195–214. [https://doi.org/10.1016/0169-409X\(95\)00025-3](https://doi.org/10.1016/0169-409X(95)00025-3).

[45] K. Ogawara, K. Furumoto, Y. Takakura, M. Hashida, K. Higaki, T. Kimura, Surface hydrophobicity of particles is not necessarily the most important determinant in their in vivo disposition after intravenous administration in rats, *Journal of Controlled Release* 77 (2001) 191–198. [https://doi.org/10.1016/s0168-3659\(01\)00468-0](https://doi.org/10.1016/s0168-3659(01)00468-0).

[46] S. Behzadi, V. Serpooshan, W. Tao, M.A. Hamaly, M.Y. Alkawareek, E.C. Dreaden, D. Brown, A.M. Alkilany, O.C. Farokhzad, M. Mahmoudi, Cellular uptake of nanoparticles: journey inside the cell, *Chemical Society Reviews* 46 (2017) 4218–4244. <https://doi.org/10.1039/C6CS00636A>.

[47] Z. Hussain, S. Khan, M. Imran, M. Sohail, S.W.A. Shah, M. de Matas, PEGylation: a promising strategy to overcome challenges to cancer-targeted nanomedicines: a review of challenges to clinical transition and promising resolution, *Drug Deliv. and Transl. Res.* 9 (2019) 721–734. <https://doi.org/10.1007/s13346-019-00631-4>.

[48] W. Kim, N.K. Ly, Y. He, Y. Li, Z. Yuan, Y. Yeo, Protein corona: Friend or foe? Co-opting serum proteins for nanoparticle delivery, *Adv. Drug Deliv. Rev.* 192 (2023) 114635. <https://doi.org/10.1016/j.addr.2022.114635>.

[49] S. Behzadi, V. Serpooshan, R. Sakhtianchi, B. Müller, K. Landfester, D. Crespy, M. Mahmoudi, Protein corona change the drug release profile of nanocarriers: the "overlooked" factor at the nanobio interface, *Colloids Surf. B Biointerfaces* 123 (2014) 143–149. <https://doi.org/10.1016/j.colsurfb.2014.09.009>.

Introduction

[50] A. Chrastina, K.A. Massey, J.E. Schnitzer, Overcoming in vivo barriers to targeted nanodelivery, *Wiley Interdisciplinary Reviews: Nanomedicine and Nanobiotechnology* 3 (2011) 421–437. <https://doi.org/10.1002/wnan.143>.

[51] S.C. Satchell, F. Braet, Glomerular endothelial cell fenestrations: an integral component of the glomerular filtration barrier, *Am. J. Physiol. Renal Physiol.* 296 (2009) F947-56. <https://doi.org/10.1152/ajprenal.90601.2008>.

[52] H.S. Choi, W. Liu, P. Misra, E. Tanaka, J.P. Zimmer, B. Itty Ipe, M.G. Bawendi, J.V. Frangioni, Renal clearance of quantum dots, *Nat Biotechnol* 25 (2007) 1165–1170. <https://doi.org/10.1038/nbt1340>.

[53] A.B. Engin, D. Nikitovic, M. Neagu, P. Henrich-Noack, A.O. Docea, M.I. Shtilman, K. Golokhvast, A.M. Tsatsakis, Mechanistic understanding of nanoparticles' interactions with extracellular matrix: the cell and immune system, *Part Fibre Toxicol* 14 (2017) 22. <https://doi.org/10.1186/s12989-017-0199-z>.

[54] N.D. Donahue, H. Acar, S. Wilhelm, Concepts of nanoparticle cellular uptake, intracellular trafficking, and kinetics in nanomedicine, *Adv. Drug Deliv. Rev.* 143 (2019) 68–96. <https://doi.org/10.1016/j.addr.2019.04.008>.

[55] V.P. Chauhan, R.K. Jain, Strategies for advancing cancer nanomedicine, *Nature Mater* 12 (2013) 958–962. <https://doi.org/10.1038/nmat3792>.

[56] O. Zimmer, A. Goepferich, On the uncertainty of the correlation between nanoparticle avidity and biodistribution, *Eur. J. Pharm. Biopharm.* 198 (2024) 114240. <https://doi.org/10.1016/j.ejpb.2024.114240>.

[57] J. Yoo, C. Park, G. Yi, D. Lee, H. Koo, Active Targeting Strategies Using Biological Ligands for Nanoparticle Drug Delivery Systems, *Cancers* 11 (2019) 640. <https://doi.org/10.3390/cancers11050640>.

[58] M. Walter, F. Baumann, K. Schorr, A. Goepferich, Ectoenzymes as Promising Cell Identification Structures for the High Avidity Targeting of Polymeric Nanoparticles, *International Journal of Pharmaceutics* (2023) 123453. <https://doi.org/10.1016/j.ijpharm.2023.123453>.

[59] D. Fleischmann, S. Maslanka Figueroa, S. Beck, K. Abstiens, R. Witzgall, F. Schweda, P. Tauber, A. Goepferich, Adenovirus-Mimetic Nanoparticles: Sequential Ligand-Receptor Interplay as a Universal Tool for Enhanced In Vitro/In Vivo Cell Identification, *ACS Appl. Mater. Interfaces* 12 (2020) 34689–34702. <https://doi.org/10.1021/acsami.0c10057>.

[60] B. Mao, C. Liu, W. Zheng, X. Li, R. Ge, H. Shen, X. Guo, Q. Lian, X. Shen, C. Li, Cyclic cRGDfk peptide and Chlorin e6 functionalized silk fibroin nanoparticles for targeted drug

Chapter 1

delivery and photodynamic therapy, *Biomaterials* 161 (2018) 306–320. <https://doi.org/10.1016/j.biomaterials.2018.01.045>.

[61] S. Deshayes, H. Cabral, T. Ishii, Y. Miura, S. Kobayashi, T. Yamashita, A. Matsumoto, Y. Miyahara, N. Nishiyama, K. Kataoka, Phenylboronic acid-installed polymeric micelles for targeting sialylated epitopes in solid tumors, *J. Am. Chem. Soc.* 135 (2013) 15501–15507. <https://doi.org/10.1021/ja406406h>.

[62] H. Jo, C. Ban, Aptamer-nanoparticle complexes as powerful diagnostic and therapeutic tools, *Exp Mol Med* 48 (2016) e230. <https://doi.org/10.1038/emm.2016.44>.

[63] K.Y. Choi, H.Y. Yoon, J.-H. Kim, S.M. Bae, R.-W. Park, Y.M. Kang, I.-S. Kim, I.C. Kwon, K. Choi, S.Y. Jeong, K. Kim, J.H. Park, Smart nanocarrier based on PEGylated hyaluronic acid for cancer therapy, *ACS Nano* 5 (2011) 8591–8599. <https://doi.org/10.1021/nn202070n>.

[64] A.C. Marques, P.J. Costa, S. Velho, M.H. Amaral, Functionalizing nanoparticles with cancer-targeting antibodies: A comparison of strategies, *J. Control. Release* 320 (2020) 180–200. <https://doi.org/10.1016/j.jconrel.2020.01.035>.

[65] R. Hennig, A. Ohlmann, J. Staffel, K. Pollinger, A. Haunberger, M. Breunig, F. Schweda, E.R. Tamm, A. Goepferich, Multivalent nanoparticles bind the retinal and choroidal vasculature, *J. Control. Release* 220 (2015) 265–274. <https://doi.org/10.1016/j.jconrel.2015.10.033>.

[66] S. Maslanka Figueroa, A. Veser, K. Abstiens, D. Fleischmann, S. Beck, A. Goepferich, Influenza A virus mimetic nanoparticles trigger selective cell uptake, *Proc. Natl. Acad. Sci. U. S. A.* 116 (2019) 9831–9836. <https://doi.org/10.1073/pnas.1902563116>.

[67] S. Goodall, M.L. Jones, S. Mahler, Monoclonal antibody-targeted polymeric nanoparticles for cancer therapy – future prospects, *J of Chemical Tech & Biotech* 90 (2015) 1169–1176. <https://doi.org/10.1002/jctb.4555>.

[68] A. Alibakhshi, F. Abarghooi Kahaki, S. Ahangarzadeh, H. Yaghoobi, F. Yarian, R. Arezumand, J. Ranjbari, A. Mokhtarzadeh, M. de La Guardia, Targeted cancer therapy through antibody fragments-decorated nanomedicines, *J. Control. Release* 268 (2017) 323–334. <https://doi.org/10.1016/j.jconrel.2017.10.036>.

[69] S.-T. Ning, S.-Y. Lee, M.-F. Wei, C.-L. Peng, S.Y.-F. Lin, M.-H. Tsai, P.-C. Lee, Y.-H. Shih, C.-Y. Lin, T.-Y. Luo, M.-J. Shieh, Targeting Colorectal Cancer Stem-Like Cells with Anti-CD133 Antibody-Conjugated SN-38 Nanoparticles, *ACS Appl. Mater. Interfaces* 8 (2016) 17793–17804. <https://doi.org/10.1021/acsami.6b04403>.

Introduction

[70] E.B. Souto, S. Doktorovova, J.R. Campos, P. Martins-Lopes, A.M. Silva, Surface-tailored anti-HER2/neu-solid lipid nanoparticles for site-specific targeting MCF-7 and BT-474 breast cancer cells, *Eur. J. Pharm. Sci.* 128 (2019) 27–35. <https://doi.org/10.1016/j.ejps.2018.11.022>.

[71] J. Wei, J. Sun, Y. Liu, Enhanced targeting of prostate cancer-initiating cells by salinomycin-encapsulated lipid-PLGA nanoparticles linked with CD44 antibodies, *Oncol. Lett.* 17 (2019) 4024–4033. <https://doi.org/10.3892/ol.2019.10050>.

[72] D. Fleischmann, A. Goepferich, General sites of nanoparticle biodistribution as a novel opportunity for nanomedicine, *Eur. J. Pharm. Biopharm.* 166 (2021) 44–60. <https://doi.org/10.1016/j.ejpb.2021.05.027>.

[73] M. Stahl, J. Holzinger, S. Bülow, A.M. Goepferich, Enzyme-triggered antigen release enhances cross-presentation by dendritic cells, *Nanomedicine* 42 (2022) 102545. <https://doi.org/10.1016/j.nano.2022.102545>.

[74] R.A. Petros, J.M. Desimone, Strategies in the design of nanoparticles for therapeutic applications, *Nat Rev Drug Discov* 9 (2010) 615–627. <https://doi.org/10.1038/nrd2591>.

[75] P. Panja, N.R. Jana, Arginine-Terminated Nanoparticles of <10 nm Size for Direct Membrane Penetration and Protein Delivery for Straight Access to Cytosol and Nucleus, *The Journal of Physical Chemistry Letters* 11 (2020) 2363–2368. <https://doi.org/10.1021/acs.jpclett.0c00176>.

[76] S. Ghosh, P. Panja, C. Dalal, N.R. Jana, Arginine-Terminated, Chemically Designed Nanoparticle for Direct Cell Translocation, *ACS Applied Bio Materials* 2 (2019) 339–348. <https://doi.org/10.1021/acsabm.8b00617>.

[77] S. Zhang, H. Gao, G. Bao, Physical Principles of Nanoparticle Cellular Endocytosis, *ACS Nano* 9 (2015) 8655–8671. <https://doi.org/10.1021/acsnano.5b03184>.

[78] H.H. Gustafson, D. Holt-Casper, D.W. Grainger, H. Ghandehari, Nanoparticle Uptake: The Phagocyte Problem, *Nano Today* 10 (2015) 487–510. <https://doi.org/10.1016/j.nantod.2015.06.006>.

[79] J.A. Swanson, Shaping cups into phagosomes and macropinosomes, *Nat Rev Mol Cell Biol* 9 (2008) 639–649. <https://doi.org/10.1038/nrm2447>.

[80] J.G. Huang, T. Leshuk, F.X. Gu, Emerging nanomaterials for targeting subcellular organelles, *Nano Today* 6 (2011) 478–492. <https://doi.org/10.1016/j.nantod.2011.08.002>.

[81] J.-P. Mattila, A.V. Shnyrova, A.C. Sundborger, E.R. Hortelano, M. Fuhrmans, S. Neumann, M. Müller, J.E. Hinshaw, S.L. Schmid, V.A. Frolov, A hemi-fission

Chapter 1

intermediate links two mechanistically distinct stages of membrane fission, *Nature* 524 (2015) 109–113. <https://doi.org/10.1038/nature14509>.

[82] C.M. Da Luz, M.S.P. Boyles, P. Falagan-Lotsch, M.R. Pereira, H.R. Tutumi, E. de Oliveira Santos, N.B. Martins, M. Himly, A. Sommer, I. Foissner, A. Duschl, J.M. Granjeiro, P.E.C. Leite, Poly-lactic acid nanoparticles (PLA-NP) promote physiological modifications in lung epithelial cells and are internalized by clathrin-coated pits and lipid rafts, *J Nanobiotechnol* 15 (2017) 11. <https://doi.org/10.1186/s12951-016-0238-1>.

[83] A. El-Sayed, H. Harashima, Endocytosis of gene delivery vectors: from clathrin-dependent to lipid raft-mediated endocytosis, *Molecular Therapy* 21 (2013) 1118–1130. <https://doi.org/10.1038/mt.2013.54>.

[84] O. Zimmer, A. Goepferich, How clathrin-coated pits control nanoparticle avidity for cells, *Nanoscale Horiz.* 8 (2023) 256–269. <https://doi.org/10.1039/d2nh00543c>.

[85] O. Zimmer, M. Walter, M. Remmert, O. Maier, R. Witzgall, A. Goepferich, Impact of interferon- γ on the target cell tropism of nanoparticles, *J. Control. Release* 362 (2023) 325–341. <https://doi.org/10.1016/j.jconrel.2023.08.034>.

[86] L. Pelkmans, A. Helenius, Endocytosis via caveolae, *Traffic* 3 (2002) 311–320. <https://doi.org/10.1034/j.1600-0854.2002.30501.x>.

[87] K.G. Rothberg, J.E. Heuser, W.C. Donzell, Y.S. Ying, J.R. Glenney, R.G. Anderson, Caveolin, a protein component of caveolae membrane coats, *Cell* 68 (1992) 673–682. [https://doi.org/10.1016/0092-8674\(92\)90143-Z](https://doi.org/10.1016/0092-8674(92)90143-Z).

[88] M. Sousa de Almeida, E. Susnik, B. Drasler, P. Taladriz-Blanco, A. Petri-Fink, B. Rothen-Rutishauser, Understanding nanoparticle endocytosis to improve targeting strategies in nanomedicine, *Chemical Society Reviews* 50 (2021) 5397–5434. <https://doi.org/10.1039/D0CS01127D>.

[89] A. Ferrari, V. Pellegrini, C. Arcangeli, A. Fittipaldi, M. Giacca, F. Beltram, Caveolae-mediated internalization of extracellular HIV-1 tat fusion proteins visualized in real time, *Mol. Ther.* 8 (2003) 284–294. [https://doi.org/10.1016/S1525-0016\(03\)00122-9](https://doi.org/10.1016/S1525-0016(03)00122-9).

[90] E. Blanco, H. Shen, M. Ferrari, Principles of nanoparticle design for overcoming biological barriers to drug delivery, *Nat Biotechnol* 33 (2015) 941–951. <https://doi.org/10.1038/nbt.3330>.

[91] S.D. Conner, S.L. Schmid, Regulated portals of entry into the cell, *Nature* 422 (2003) 37–44. <https://doi.org/10.1038/nature01451>.

[92] A.S. Robertson, E. Smythe, K.R. Ayscough, Functions of actin in endocytosis, *Cell. Mol. Life Sci.* 66 (2009) 2049–2065. <https://doi.org/10.1007/s00018-009-0001-y>.

Introduction

[93] X. Chen, S. Shank, P.B. Davis, A.G. Ziady, Nucleolin-Mediated Cellular Trafficking of DNA Nanoparticle Is Lipid Raft and Microtubule Dependent and Can Be Modulated by Glucocorticoid, *Mol. Ther.* 19 (2011) 93–102. <https://doi.org/10.1038/mt.2010.214>.

[94] Y. Lu, P.S. Low, Folate-mediated delivery of macromolecular anticancer therapeutic agents, *Adv. Drug Deliv. Rev.* 64 (2012) 342–352. <https://doi.org/10.1016/j.addr.2012.09.020>.

[95] G.-H. Son, B.-J. Lee, C.-W. Cho, Mechanisms of drug release from advanced drug formulations such as polymeric-based drug-delivery systems and lipid nanoparticles, *Journal of Pharmaceutical Investigation* 47 (2017) 287–296. <https://doi.org/10.1007/s40005-017-0320-1>.

[96] R. Langer, N. Peppas, Chemical and Physical Structure of Polymers as Carriers for Controlled Release of Bioactive Agents: A Review, *Journal of Macromolecular Science, Part C* 23 (1983) 61–126. <https://doi.org/10.1080/07366578308079439>.

[97] E. Cauchetier, M. Deniau, H. Fessi, A. Astier, M. Paul, Atovaquone-loaded nanocapsules: influence of the nature of the polymer on their in vitro characteristics, *International Journal of Pharmaceutics* 250 (2003) 273–281. [https://doi.org/10.1016/S0378-5173\(02\)00556-2](https://doi.org/10.1016/S0378-5173(02)00556-2).

[98] J. Siepmann, F. Siepmann, Modeling of diffusion controlled drug delivery, *J. Control. Release* 161 (2012) 351–362. <https://doi.org/10.1016/j.jconrel.2011.10.006>.

[99] C.-C. Lin, A.T. Metters, Hydrogels in controlled release formulations: network design and mathematical modeling, *Adv. Drug Deliv. Rev.* 58 (2006) 1379–1408. <https://doi.org/10.1016/j.addr.2006.09.004>.

[100] S. Naahidi, M. Jafari, F. Edalat, K. Raymond, A. Khademhosseini, P. Chen, Biocompatibility of engineered nanoparticles for drug delivery, *J. Control. Release* 166 (2013) 182–194. <https://doi.org/10.1016/j.jconrel.2012.12.013>.

[101] D.E. Owens, N.A. Peppas, Opsonization, biodistribution, and pharmacokinetics of polymeric nanoparticles, *International Journal of Pharmaceutics* 307 (2006) 93–102. <https://doi.org/10.1016/j.ijpharm.2005.10.010>.

[102] S. Shahbaz, M. Esmaeili, M. Hosein Fathian Nasab, Z. Imani, R. Bafkary, M. Amini, F. Atyabi, R. Dinarvand, PEGylated mesoporous silica core-shell redox-responsive nanoparticles for delivering paclitaxel to breast cancer cells, *International Journal of Pharmaceutics* (2024) 124024. <https://doi.org/10.1016/j.ijpharm.2024.124024>.

[103] J. Liu, Y.-Y. Liu, C.-S. Li, A. Cao, H. Wang, Exocytosis of Nanoparticles: A Comprehensive Review, *Nanomaterials* 13 (2023) 2215. <https://doi.org/10.3390/nano13152215>.

Chapter 1

[104]S. Malik, W.M. Saltzman, R. Bahal, Extracellular vesicles mediated exocytosis of antisense peptide nucleic acids, *Mol. Ther. Nucleic Acids* 25 (2021) 302–315. <https://doi.org/10.1016/j.omtn.2021.07.018>.

[105]F.R. Maxfield, T.E. McGraw, Endocytic recycling, *Nat. Rev. Mol. Cell Biol.* 5 (2004) 121–132. <https://doi.org/10.1038/nrm1315>.

[106]C.C. Scott, F. Vacca, J. Gruenberg, Endosome maturation, transport and functions, *Seminars in Cell & Developmental Biology* 31 (2014) 2–10. <https://doi.org/10.1016/j.semcdb.2014.03.034>.

[107]Z. Chu, Y. Huang, Q. Tao, Q. Li, Cellular uptake, evolution, and excretion of silica nanoparticles in human cells, *Nanoscale* 3 (2011) 3291–3299. <https://doi.org/10.1039/C1NR10499C>.

[108]L. Peng, M. He, B. Chen, Q. Wu, Z. Zhang, D. Pang, Y. Zhu, B. Hu, Cellular uptake, elimination and toxicity of CdSe/ZnS quantum dots in HepG2 cells, *Biomaterials* 34 (2013) 9545–9558. <https://doi.org/10.1016/j.biomaterials.2013.08.038>.

[109]A. Sipos, K.-J. Kim, R.H. Chow, P. Flodby, Z. Borok, E.D. Crandall, Alveolar epithelial cell processing of nanoparticles activates autophagy and lysosomal exocytosis, *Am. J. Physiol. Lung Cell. Mol. Physiol.* 315 (2018) L286-L300. <https://doi.org/10.1152/ajplung.00108.2018>.

[110]I. Alberg, S. Kramer, M. Schinnerer, Q. Hu, C. Seidl, C. Leps, N. Drude, D. Möckel, C. Rijcken, T. Lammers, M. Diken, M. Maskos, S. Morsbach, K. Landfester, S. Tenzer, M. Barz, R. Zentel, Polymeric Nanoparticles with Neglectable Protein Corona, *Small* 16 (2020) e1907574. <https://doi.org/10.1002/smll.201907574>.

[111]J. Müller, K.N. Bauer, D. Prozeller, J. Simon, V. Mailänder, F.R. Wurm, S. Winzen, K. Landfester, Coating nanoparticles with tunable surfactants facilitates control over the protein corona, *Biomaterials* 115 (2017) 1–8. <https://doi.org/10.1016/j.biomaterials.2016.11.015>.

[112]M. Barz, W.J. Parak, R. Zentel, Concepts and Approaches to Reduce or Avoid Protein Corona Formation on Nanoparticles: Challenges and Opportunities, *Advanced Science* 11 (2024) e2402935. <https://doi.org/10.1002/advs.202402935>.

[113]Z. Amoozgar, Y. Yeo, Recent advances in stealth coating of nanoparticle drug delivery systems, *Wiley Interdisciplinary Reviews: Nanomedicine and Nanobiotechnology* 4 (2012) 219–233. <https://doi.org/10.1002/wnan.1157>.

Introduction

[114]S. Essa, J.M. Rabanel, P. Hildgen, Characterization of rhodamine loaded PEG-g-PLA nanoparticles (NPs): effect of poly(ethylene glycol) grafting density, *International Journal of Pharmaceutics* 411 (2011) 178–187. <https://doi.org/10.1016/j.ijpharm.2011.02.039>.

[115]X. Shan, C. Liu, Y. Yuan, F. Xu, X. Tao, Y. Sheng, H. Zhou, In vitro macrophage uptake and in vivo biodistribution of long-circulation nanoparticles with poly(ethylene-glycol)-modified PLA (BAB type) triblock copolymer, *Colloids Surf. B Biointerfaces* 72 (2009) 303–311. <https://doi.org/10.1016/j.colsurfb.2009.04.017>.

[116]T.U. Wani, S.N. Raza, N.A. Khan, Nanoparticle opsonization: forces involved and protection by long chain polymers, *Polym. Bull.* 77 (2020) 3865–3889. <https://doi.org/10.1007/s00289-019-02924-7>.

[117]H. Li, Y. Wang, Q. Tang, D. Yin, C. Tang, E. He, L. Zou, Q. Peng, The protein corona and its effects on nanoparticle-based drug delivery systems, *Acta Biomaterialia* 129 (2021) 57–72. <https://doi.org/10.1016/j.actbio.2021.05.019>.

[118]Z. Li, D. Li, Q. Li, C. Luo, J. Li, L. Kou, D. Zhang, H. Zhang, S. Zhao, Q. Kan, J. Liu, P. Zhang, X. Liu, Y. Sun, Y. Wang, Z. He, J. Sun, In situ low-immunogenic albumin-conjugating-corona guiding nanoparticles for tumor-targeting chemotherapy, *Biomater. Sci.* 6 (2018) 2681–2693. <https://doi.org/10.1039/C8BM00692J>.

[119]Z. Zhang, J. Guan, Z. Jiang, Y. Yang, J. Liu, W. Hua, Y. Mao, C. Li, W. Lu, J. Qian, C. Zhan, Brain-targeted drug delivery by manipulating protein corona functions, *Nat Commun* 10 (2019) 3561. <https://doi.org/10.1038/s41467-019-11593-z>.

[120]W. Ren, J. Chang, C. Yan, X. Qian, L. Long, B. He, X. Yuan, C. Kang, D. Betbeder, J. Sheng, P. Pu, Development of transferrin functionalized poly(ethylene glycol)/poly(lactic acid) amphiphilic block copolymeric micelles as a potential delivery system targeting brain glioma, *J Mater Sci: Mater Med* 21 (2010) 2673–2681. <https://doi.org/10.1007/s10856-010-4106-5>.

[121]D. Chen, S. Ganesh, W. Wang, M. Amiji, Protein Corona-Enabled Systemic Delivery and Targeting of Nanoparticles, *AAPS J* 22 (2020) 83. <https://doi.org/10.1208/s12248-020-00464-x>.

[122]R. Dal Magro, B. Albertini, S. Beretta, R. Rigolio, E. Donzelli, A. Chiorazzi, M. Ricci, P. Blasi, G. Sancini, Artificial apolipoprotein corona enables nanoparticle brain targeting, *Nanomedicine* 14 (2018) 429–438. <https://doi.org/10.1016/j.nano.2017.11.008>.

[123]T.M. Göppert, R.H. Müller, Polysorbate-stabilized solid lipid nanoparticles as colloidal carriers for intravenous targeting of drugs to the brain: comparison of plasma protein

Chapter 1

adsorption patterns, *Journal of Drug Targeting* 13 (2005) 179–187. <https://doi.org/10.1080/10611860500071292>.

[124] Z. Zhang, C. Wang, Y. Zha, W. Hu, Z. Gao, Y. Zang, J. Chen, J. Zhang, L. Dong, Corona-directed nucleic acid delivery into hepatic stellate cells for liver fibrosis therapy, *ACS Nano* 9 (2015) 2405–2419. <https://doi.org/10.1021/nn505166x>.

[125] W.G. Roberts, G.E. Palade, Neovasculature Induced by Vascular Endothelial Growth Factor Is Fenestrated, *Cancer Res* 57 (1997) 765–772.

[126] A. Warren, V.C. Cogger, I.M. Arias, R.S. McCuskey, D.G. Le Couteur, Liver sinusoidal endothelial fenestrations in caveolin-1 knockout mice, *Microcirculation* (New York, N.Y. 1994) 17 (2010) 32–38. <https://doi.org/10.1111/j.1549-8719.2009.00004.x>.

[127] W. Hild, K. Pollinger, A. Caporale, C. Cabrele, M. Keller, N. Pluym, A. Buschauer, R. Rachel, J. Tessmar, M. Breunig, A. Goepferich, G protein-coupled receptors function as logic gates for nanoparticle binding and cell uptake, *Proc. Natl. Acad. Sci. U. S. A.* 107 (2010) 10667–10672. <https://doi.org/10.1073/pnas.0912782107>.

[128] W. Lu, C. Xiong, R. Zhang, L. Shi, M. Huang, G. Zhang, S. Song, Q. Huang, G. Liu, C. Li, Receptor-mediated transcytosis: a mechanism for active extravascular transport of nanoparticles in solid tumors, *J. Control. Release* 161 (2012) 959–966. <https://doi.org/10.1016/j.jconrel.2012.05.014>.

[129] Y. Liu, C.K.K. Choi, H. Hong, Y. Xiao, M.L. Kwok, H. Liu, X.Y. Tian, C.H.J. Choi, Dopamine Receptor-Mediated Binding and Cellular Uptake of Polydopamine-Coated Nanoparticles, *ACS Nano* 15 (2021) 13871–13890. <https://doi.org/10.1021/acsnano.1c06081>.

[130] S. Han, T. Zal, K.V. Sokolov, Fate of Antibody-Targeted Ultrasmall Gold Nanoparticles in Cancer Cells after Receptor-Mediated Uptake, *ACS Nano* 15 (2021) 9495–9508. <https://doi.org/10.1021/acsnano.0c08128>.

[131] H. Wartlick, K. Michaelis, S. Balthasar, K. Strebhardt, J. Kreuter, K. Langer, Highly specific HER2-mediated cellular uptake of antibody-modified nanoparticles in tumour cells, *Journal of Drug Targeting* 12 (2004) 461–471. <https://doi.org/10.1080/10611860400010697>.

[132] L. Rajendran, H.-J. Knölker, K. Simons, Subcellular targeting strategies for drug design and delivery, *Nat Rev Drug Discov* 9 (2010) 29–42. <https://doi.org/10.1038/nrd2897>.

[133] R.M. Levine, E. Kokkoli, Dual-ligand $\alpha 5\beta 1$ and $\alpha 6\beta 4$ integrin targeting enhances gene delivery and selectivity to cancer cells, *J. Control. Release* 251 (2017) 24–36. <https://doi.org/10.1016/j.jconrel.2017.02.017>.

Introduction

[134] C.L. Modery-Pawlowski, A.S. Gupta, Heteromultivalent ligand-decoration for actively targeted nanomedicine, *Biomaterials* 35 (2014) 2568–2579. <https://doi.org/10.1016/j.biomaterials.2013.12.047>.

[135] E. Kluza, D.W.J. van der Schaft, P.A.I. Hautvast, W.J.M. Mulder, K.H. Mayo, A.W. Griffioen, G.J. Strijkers, K. Nicolay, Synergistic targeting of alphavbeta3 integrin and galectin-1 with heteromultivalent paramagnetic liposomes for combined MR imaging and treatment of angiogenesis, *Nano Letters* 10 (2010) 52–58. <https://doi.org/10.1021/nl902659g>.

[136] A. Singla, S.B. Simbassa, B. Chirra, A. Gairola, M.R. Southerland, K.N. Shah, R.E. Rose, Q. Chen, A. Basharat, J. Baeza, R. Raina, M.J. Chapman, A.M. Hassan, I. Ivanov, A. Sen, H.-J. Wu, C.L. Cannon, Hetero-Multivalent Targeted Liposomal Drug Delivery to Treat *Pseudomonas aeruginosa* Infections, *ACS Appl. Mater. Interfaces* 14 (2022) 40724–40737. <https://doi.org/10.1021/acsami.2c12943>.

[137] L. Woythe, N.B. Tito, L. Albertazzi, A quantitative view on multivalent nanomedicine targeting, *Adv. Drug Deliv. Rev.* 169 (2021) 1–21. <https://doi.org/10.1016/j.addr.2020.11.010>.

[138] C. Qiu, F. Xia, J. Zhang, Q. Shi, Y. Meng, C. Wang, H. Pang, L. Gu, C. Xu, Q. Guo, J. Wang, Advanced Strategies for Overcoming Endosomal/Lysosomal Barrier in Nanodrug Delivery, *Research (Wash D C)* 6 (2023) 148. <https://doi.org/10.34133/research.0148>.

[139] A.K. Varkouhi, M. Scholte, G. Storm, H.J. Haisma, Endosomal escape pathways for delivery of biologicals, *J. Control. Release* 151 (2011) 220–228. <https://doi.org/10.1016/j.jconrel.2010.11.004>.

[140] P. Kanjilal, K. Dutta, S. Thayumanavan, Thiol-Disulfide Exchange as a Route for Endosomal Escape of Polymeric Nanoparticles, *Angewandte Chemie (International ed. in English)* 61 (2022) e202209227. <https://doi.org/10.1002/anie.202209227>.

[141] M. Walter, M. Bresinsky, O. Zimmer, S. Pockes, A. Goepferich, Conditional Cell-Penetrating Peptide Exposure as Selective Nanoparticle Uptake Signal, *ACS Appl. Mater. Interfaces* 16 (2024) 37734–37747. <https://doi.org/10.1021/acsami.4c07821>.

[142] B.R. Liu, Y. Huang, J.G. Winiarz, H.-J. Chiang, H.-J. Lee, Intracellular delivery of quantum dots mediated by a histidine- and arginine-rich HR9 cell-penetrating peptide through the direct membrane translocation mechanism, *Biomaterials* 32 (2011) 3520–3537. <https://doi.org/10.1016/j.biomaterials.2011.01.041>.

Chapter 1

[143]J. Lin, A. Alexander-Katz, Cell membranes open "doors" for cationic nanoparticles/biomolecules: insights into uptake kinetics, *ACS Nano* 7 (2013) 10799–10808. <https://doi.org/10.1021/nn4040553>.

[144]R. Ray, S. Ghosh, A. Maity, N.R. Jana, Arginine Surface Density of Nanoparticles Controls Nonendocytic Cell Uptake and Autophagy Induction, *ACS Appl. Mater. Interfaces* 16 (2024) 5451–5461. <https://doi.org/10.1021/acsami.3c14472>.

[145]H. Lee, R.G. Larson, Lipid bilayer curvature and pore formation induced by charged linear polymers and dendrimers: the effect of molecular shape, *The Journal of Physical Chemistry B* 112 (2008) 12279–12285. <https://doi.org/10.1021/jp805026m>.

[146]I.A. Khalil, K. Kogure, H. Akita, H. Harashima, Uptake pathways and subsequent intracellular trafficking in nonviral gene delivery, *Pharmacol Rev* 58 (2006) 32–45. <https://doi.org/10.1124/pr.58.1.8>.

[147]Y.-X. Li, H.-B. Pang, Macropinocytosis as a cell entry route for peptide-functionalized and bystander nanoparticles, *J. Control. Release* 329 (2021) 1222–1230. <https://doi.org/10.1016/j.jconrel.2020.10.049>.

[148]H. Xia, G. Gu, Q. Hu, Z. Liu, M. Jiang, T. Kang, D. Miao, Q. Song, L. Yao, Y. Tu, H. Chen, X. Gao, J. Chen, Activatable cell penetrating peptide-conjugated nanoparticles with enhanced permeability for site-specific targeting delivery of anticancer drug, *Bioconjug. Chem.* 24 (2013) 419–430. <https://doi.org/10.1021/bc300520t>.

[149]L. Chen, C. Liu, Y. Xiang, J. Lyu, Z. Zhou, T. Gong, H. Gao, L. Li, Y. Huang, Exocytosis blockade of endoplasmic reticulum-targeted nanoparticle enhances immunotherapy, *Nano Today* 42 (2022) 101356. <https://doi.org/10.1016/j.nantod.2021.101356>.

[150]S. Han, R. Da Costa Marques, J. Simon, A. Kaltbeitzel, K. Koynov, K. Landfester, V. Mailänder, I. Lieberwirth, Endosomal sorting results in a selective separation of the protein corona from nanoparticles, *Nat Commun* 14 (2023) 295. <https://doi.org/10.1038/s41467-023-35902-9>.

[151]Y. Song, Y. Wu, L. Xu, T. Jiang, C. Tang, C. Yin, Caveolae-Mediated Endocytosis Drives Robust siRNA Delivery of Polymeric Nanoparticles to Macrophages, *ACS Nano* 15 (2021) 8267–8282. <https://doi.org/10.1021/acsnano.0c08596>.

[152]G. Sahay, D.Y. Alakhova, A.V. Kabanov, Endocytosis of nanomedicines, *J. Control. Release* 145 (2010) 182–195. <https://doi.org/10.1016/j.jconrel.2010.01.036>.

[153]S. Mayor, R.E. Pagano, Pathways of clathrin-independent endocytosis, *Nat. Rev. Mol. Cell Biol.* 8 (2007) 603–612. <https://doi.org/10.1038/nrm2216>.

Introduction

[154]T.F. Martens, K. Remaut, J. Demeester, S.C. de Smedt, K. Braeckmans, Intracellular delivery of nanomaterials: How to catch endosomal escape in the act, *Nano Today* 9 (2014) 344–364. <https://doi.org/10.1016/j.nantod.2014.04.011>.

[155]K.L. Douglas, Toward development of artificial viruses for gene therapy: a comparative evaluation of viral and non-viral transfection, *Biotechnology Progress* 24 (2008) 871–883. <https://doi.org/10.1021/bp070319o>.

[156]M.J. Mehta, H.J. Kim, S.B. Lim, M. Naito, K. Miyata, Recent Progress in the Endosomal Escape Mechanism and Chemical Structures of Polycations for Nucleic Acid Delivery, *Macromolecular Bioscience* (2024) e2300366. <https://doi.org/10.1002/mabi.202300366>.

[157]Da Ma, Enhancing endosomal escape for nanoparticle mediated siRNA delivery, *Nanoscale* 6 (2014) 6415–6425. <https://doi.org/10.1039/C4NR00018H>.

[158]S.A. Smith, L.I. Selby, A.P.R. Johnston, G.K. Such, The Endosomal Escape of Nanoparticles: Toward More Efficient Cellular Delivery, *Bioconjug. Chem.* 30 (2019) 263–272. <https://doi.org/10.1021/acs.bioconjchem.8b00732>.

[159]R. Sakhtianchi, R.F. Minchin, K.-B. Lee, A.M. Alkilany, V. Serpooshan, M. Mahmoudi, Exocytosis of nanoparticles from cells: role in cellular retention and toxicity, *Advances in Colloid and Interface Science* 201-202 (2013) 18–29. <https://doi.org/10.1016/j.cis.2013.10.013>.

[160]B.D. Chithrani, W.C.W. Chan, Elucidating the mechanism of cellular uptake and removal of protein-coated gold nanoparticles of different sizes and shapes, *Nano Letters* 7 (2007) 1542–1550. <https://doi.org/10.1021/nl070363y>.

[161]R.E. Serda, A. Mack, A.L. van de Ven, S. Ferrati, K. Dunner, B. Godin, C. Chiappini, M. Landry, L. Brousseau, X. Liu, A.J. Bean, M. Ferrari, Logic-embedded vectors for intracellular partitioning, endosomal escape, and exocytosis of nanoparticles, *Small* 6 (2010) 2691–2700. <https://doi.org/10.1002/smll.201000727>.

[162]C. Kim, G.Y. Tonga, B. Yan, C.S. Kim, S.T. Kim, M.-H. Park, Z. Zhu, B. Duncan, B. Creran, V.M. Rotello, Regulating exocytosis of nanoparticles via host-guest chemistry, *Organic & Biomolecular Chemistry* 13 (2015) 2474–2479. <https://doi.org/10.1039/C4OB02433H>.

[163]R. Sakhtianchi, R.F. Minchin, K.-B. Lee, A.M. Alkilany, V. Serpooshan, M. Mahmoudi, Exocytosis of nanoparticles from cells: role in cellular retention and toxicity, *Advances in Colloid and Interface Science* 201-202 (2013) 18–29. <https://doi.org/10.1016/j.cis.2013.10.013>.

Chapter 1

[164]R.E. Yanes, D. Tarn, A.A. Hwang, D.P. Ferris, S.P. Sherman, C.R. Thomas, J. Lu, A.D. Pyle, J.I. Zink, F. Tamanoi, Involvement of lysosomal exocytosis in the excretion of mesoporous silica nanoparticles and enhancement of the drug delivery effect by exocytosis inhibition, *Small* 9 (2013) 697–704. <https://doi.org/10.1002/smll.201201811>.

[165]S. Kralj, M. Rojnik, R. Romih, M. Jagodič, J. Kos, D. Makovec, Effect of surface charge on the cellular uptake of fluorescent magnetic nanoparticles, *J Nanopart Res* 14 (2012) 1–14. <https://doi.org/10.1007/s11051-012-1151-7>.

[166]A. Nan, X. Bai, S.J. Son, S.B. Lee, H. Ghandehari, Cellular uptake and cytotoxicity of silica nanotubes, *Nano Letters* 8 (2008) 2150–2154. <https://doi.org/10.1021/nl0802741>.

[167]Q. Dai, Z. Du, L. Jing, R. Zhang, W. Tang, Enzyme-Responsive Modular Peptides Enhance Tumor Penetration of Quantum Dots via Charge Reversal Strategy, *ACS Appl. Mater. Interfaces* 16 (2024) 6208–6220. <https://doi.org/10.1021/acsami.3c11500>.

[168]H. Cho, K.M. Huh, M.S. Shim, Y.-Y. Cho, J.Y. Lee, H.S. Lee, H.C. Kang, Beyond Nanoparticle-based Intracellular Drug Delivery: Cytosol/Organelle-Targeted Drug Release and Therapeutic Synergism, *Macromolecular Bioscience* (2024) e2300590. <https://doi.org/10.1002/mabi.202300590>.

[169]X.-R. Shao, X.-Q. Wei, X. Song, L.-Y. Hao, X.-X. Cai, Z.-R. Zhang, Q. Peng, Y.-F. Lin, Independent effect of polymeric nanoparticle zeta potential/surface charge, on their cytotoxicity and affinity to cells, *Cell Prolif.* 48 (2015) 465–474. <https://doi.org/10.1111/cpr.12192>.

[170]Y. Zhang, L. Liu, T. Wang, C. Mao, P. Shan, C.S. Lau, Z. Li, W. Guo, W. Wang, Reactive Oxygen Species-Responsive Polymeric Prodrug Nanoparticles for Selective and Effective Treatment of Inflammatory Diseases, *Advanced healthcare materials* 12 (2023) e2301394. <https://doi.org/10.1002/adhm.202301394>.

[171]Y. Wu, W. Chen, F. Meng, Z. Wang, R. Cheng, C. Deng, H. Liu, Z. Zhong, Core-crosslinked pH-sensitive degradable micelles: A promising approach to resolve the extracellular stability versus intracellular drug release dilemma, *J. Control. Release* 164 (2012) 338–345. <https://doi.org/10.1016/j.jconrel.2012.07.011>.

[172]M. Chen, F. Song, Y. Liu, J. Tian, C. Liu, R. Li, Q. Zhang, A dual pH-sensitive liposomal system with charge-reversal and NO generation for overcoming multidrug resistance in cancer, *Nanoscale* 11 (2019) 3814–3826. <https://doi.org/10.1039/C8NR06218H>.

[173]C.Y. Zhang, W. Lin, J. Gao, X. Shi, M. Davaritouchaee, A.E. Nielsen, R.J. Mancini, Z. Wang, pH-Responsive Nanoparticles Targeted to Lungs for Improved Therapy of Acute

Introduction

Lung Inflammation/Injury, *ACS Appl. Mater. Interfaces* 11 (2019) 16380–16390. <https://doi.org/10.1021/acsami.9b04051>.

[174] S. Li, P.E. Saw, C. Lin, Y. Nie, W. Tao, O.C. Farokhzad, L. Zhang, X. Xu, Redox-responsive polyprodrug nanoparticles for targeted siRNA delivery and synergistic liver cancer therapy, *Biomaterials* 234 (2020) 119760. <https://doi.org/10.1016/j.biomaterials.2020.119760>.

[175] X. Ji, Y. Meng, Q. Wang, T. Tong, Z. Liu, J. Lin, B. Li, Y. Wei, X. You, Y. Lei, M. Song, L. Wang, Y. Guo, Y. Qiu, Z. Chen, B. Mai, S. Xie, J. Wu, N. Cao, Cysteine-Based Redox-Responsive Nanoparticles for Fibroblast-Targeted Drug Delivery in the Treatment of Myocardial Infarction, *ACS Nano* 17 (2023) 5421–5434. <https://doi.org/10.1021/acsnano.2c10042>.

[176] X. Xu, P.E. Saw, W. Tao, Y. Li, X. Ji, S. Bhasin, Y. Liu, D. Ayyash, J. Rasmussen, M. Huo, J. Shi, O.C. Farokhzad, ROS-Responsive Polyprodrug Nanoparticles for Triggered Drug Delivery and Effective Cancer Therapy, *Adv. Mater.* 29 (2017). <https://doi.org/10.1002/adma.201700141>.

[177] F. Luo, M. Li, Y. Chen, S. Song, H. Yu, P. Zhang, C. Xiao, G. Lv, X. Chen, Immunosuppressive enzyme-responsive nanoparticles for enhanced accumulation in liver allograft to overcome acute rejection, *Biomaterials* 306 (2024) 122476. <https://doi.org/10.1016/j.biomaterials.2024.122476>.

[178] J. Liu, B. Zhang, Z. Luo, X. Ding, J. Li, L. Dai, J. Zhou, X. Zhao, J. Ye, K. Cai, Enzyme responsive mesoporous silica nanoparticles for targeted tumor therapy in vitro and in vivo, *Nanoscale* 7 (2015) 3614–3626. <https://doi.org/10.1039/C5NR00072F>.

[179] G. He, M. He, R. Wang, X. Li, H. Hu, D. Wang, Z. Wang, Y. Lu, N. Xu, J. Du, J. Fan, X. Peng, W. Sun, A Near-Infrared Light-Activated Photocage Based on a Ruthenium Complex for Cancer Phototherapy, *Angewandte Chemie (International ed. in English)* 62 (2023) e202218768. <https://doi.org/10.1002/anie.202218768>.

[180] H. Yu, N. Ingram, J.V. Rowley, S. Parkinson, D.C. Green, N.J. Warren, P.D. Thornton, Thermoresponsive polysarcosine-based nanoparticles, *J. Mater. Chem. B* 7 (2019) 4217–4223. <https://doi.org/10.1039/C9TB00588A>.

[181] J.L. Paris, M.V. Cabañas, M. Manzano, M. Vallet-Regí, Polymer-Grafted Mesoporous Silica Nanoparticles as Ultrasound-Responsive Drug Carriers, *ACS Nano* 9 (2015) 11023–11033. <https://doi.org/10.1021/acsnano.5b04378>.

[182] H. Jeon, J. Kim, Y.M. Lee, J. Kim, H.W. Choi, J. Lee, H. Park, Y. Kang, I.-S. Kim, B.-H. Lee, A.S. Hoffman, W.J. Kim, Poly-paclitaxel/cyclodextrin-SPION nano-assembly for

Chapter 1

magnetically guided drug delivery system, *J. Control. Release* 231 (2016) 68–76. <https://doi.org/10.1016/j.jconrel.2016.01.006>.

[183]A.M. Demin, A.V. Vakhrushev, A.G. Pershina, M.S. Valova, L.V. Efimova, A.A. Syomchina, M.A. Uimin, A.S. Minin, G.L. Levit, V.P. Krasnov, V.N. Charushin, Magnetic-Responsive Doxorubicin-Containing Materials Based on Fe₃O₄ Nanoparticles with a SiO₂/PEG Shell and Study of Their Effects on Cancer Cell Lines, *Int. J. Mol. Sci.* 23 (2022) 9093. <https://doi.org/10.3390/ijms23169093>.

[184]E. Cazares-Cortes, A. Espinosa, J.-M. Guigner, A. Michel, N. Griffete, C. Wilhelm, C. Ménager, Doxorubicin Intracellular Remote Release from Biocompatible Oligo(ethylene glycol) Methyl Ether Methacrylate-Based Magnetic Nanogels Triggered by Magnetic Hyperthermia, *ACS Appl. Mater. Interfaces* 9 (2017) 25775–25788. <https://doi.org/10.1021/acsami.7b06553>.

[185]S. Maghsoudian, H. Motasadizadeh, H. Farhadnejad, Y. Fatahi, M.H. Fathian Nasab, A. Mahdieh, Z. Nouri, A. Abdollahi, M. Amini, F. Atyabi, R. Dinarvand, Targeted pH- and redox-responsive AuS/micelles with low CMC for highly efficient sonodynamic therapy of metastatic breast cancer, *Biomaterials Advances* 158 (2024) 213771. <https://doi.org/10.1016/j.bioadv.2024.213771>.

[186]Z. Liu, X. Hao, J. Qian, H. Zhang, H. Bao, Q. Yang, W. Gu, X. Huang, Y. Zhang, Enzyme/pH Dual-Responsive Engineered Nanoparticles for Improved Tumor Immuno-Chemotherapy, *ACS Appl. Mater. Interfaces* 16 (2024) 12951–12964. <https://doi.org/10.1021/acsami.3c18348>.

[187]Rong Li, Xueqing Zhang, Seunghyeon Kim, Volker Mailänder, Katharina Landfester, Calum T. J. Ferguson, Therapeutic applications of responsive organic photocatalytic polymers, enabling *in situ* drug activation, *Polymer Chemistry* 15 (2024) 3223–3228. <https://doi.org/10.1039/D4PY00493K>.

[188]B.D. White, C. Duan, H.E. Townley, Nanoparticle Activation Methods in Cancer Treatment, *Biomolecules* 9 (2019) 202. <https://doi.org/10.3390/biom9050202>.

[189]T.-G. Iversen, T. Skotland, K. Sandvig, Endocytosis and intracellular transport of nanoparticles: Present knowledge and need for future studies, *Nano Today* 6 (2011) 176–185. <https://doi.org/10.1016/j.nantod.2011.02.003>.

[190]T. Andrian, R. Riera, S. Pujals, L. Albertazzi, Nanoscopy for endosomal escape quantification, *Nanoscale Advances* 3 (2021) 10–23. <https://doi.org/10.1039/d0na00454e>.

[191]J.R. Casey, S. Grinstein, J. Orlowski, Sensors and regulators of intracellular pH, *Nat Rev Mol Cell Biol* 11 (2010) 50–61. <https://doi.org/10.1038/nrm2820>.

Introduction

[192]I.H. Madshus, Regulation of intracellular pH in eukaryotic cells, *Biochem J* 250 (1988) 1–8. <https://doi.org/10.1042/bj2500001>.

[193]G.K. Such, Y. Yan, A.P.R. Johnston, S.T. Gunawan, F. Caruso, Interfacing materials science and biology for drug carrier design, *Advanced Materials* 27 (2015) 2278–2297. <https://doi.org/10.1002/adma.201405084>.

[194]N. Deirram, C. Zhang, S.S. Kermanian, A.P.R. Johnston, G.K. Such, pH-Responsive Polymer Nanoparticles for Drug Delivery, *Macromol. Rapid Commun.* 40 (2019) e1800917. <https://doi.org/10.1002/marc.201800917>.

[195]E.S. Lee, Z. Gao, D. Kim, K. Park, I.C. Kwon, Y.H. Bae, Super pH-sensitive multifunctional polymeric micelle for tumor pH(e) specific TAT exposure and multidrug resistance, *J. Control. Release* 129 (2008) 228–236. <https://doi.org/10.1016/j.jconrel.2008.04.024>.

[196]R. Liu, Y. Zhang, X. Zhao, A. Agarwal, L.J. Mueller, P. Feng, pH-responsive nanogated ensemble based on gold-capped mesoporous silica through an acid-labile acetal linker, *J. Am. Chem. Soc.* 132 (2010) 1500–1501. <https://doi.org/10.1021/ja907838s>.

[197]W. Chen, F. Meng, F. Li, S.-J. Ji, Z. Zhong, pH-responsive biodegradable micelles based on acid-labile polycarbonate hydrophobe: synthesis and triggered drug release, *Biomacromolecules* 10 (2009) 1727–1735. <https://doi.org/10.1021/bm900074d>.

[198]S. Aryal, C.-M.J. Hu, L. Zhang, Polymer–cisplatin conjugate nanoparticles for acid-responsive drug delivery, *ACS Nano* 4 (2010) 251–258. <https://doi.org/10.1021/nn9014032>.

[199]Y. Bae, N. Nishiyama, S. Fukushima, H. Koyama, M. Yasuhiro, K. Kataoka, Preparation and biological characterization of polymeric micelle drug carriers with intracellular pH-triggered drug release property: tumor permeability, controlled subcellular drug distribution, and enhanced *in vivo* antitumor efficacy, *Bioconjug. Chem.* 16 (2005) 122–130. <https://doi.org/10.1021/bc0498166>.

[200]C. Ding, J. Gu, X. Qu, Z. Yang, Preparation of multifunctional drug carrier for tumor-specific uptake and enhanced intracellular delivery through the conjugation of weak acid labile linker, *Bioconjug. Chem.* 20 (2009) 1163–1170. <https://doi.org/10.1021/bc800563g>.

[201]Y. Jin, L. Song, Y. Su, L. Zhu, Y. Pang, F. Qiu, G. Tong, D. Yan, B. Zhu, X. Zhu, Oxime linkage: a robust tool for the design of pH-sensitive polymeric drug carriers, *Biomacromolecules* 12 (2011) 3460–3468. <https://doi.org/10.1021/bm200956u>.

[202]T. Thambi, V.G. Deepagan, C.K. Yoo, J.H. Park, Synthesis and physicochemical characterization of amphiphilic block copolymers bearing acid-sensitive orthoester linkage

Chapter 1

as the drug carrier, *Polymer* 52 (2011) 4753–4759. <https://doi.org/10.1016/j.polymer.2011.08.024>.

[203] C. Wang, P. Qi, Y. Lu, L. Liu, Y. Zhang, Q. Sheng, T. Wang, M. Zhang, R. Wang, S. Song, Bicomponent polymeric micelles for pH-controlled delivery of doxorubicin, *Drug Delivery* 27 (2020) 344–357. <https://doi.org/10.1080/10717544.2020.1726526>.

[204] L. Fang, W. Zhang, Z. Wang, X. Fan, Z. Cheng, X. Hou, D. Chen, Novel mitochondrial targeting charge-reversal polysaccharide hybrid shell/core nanoparticles for prolonged systemic circulation and antitumor drug delivery, *Drug Delivery* 26 (2019) 1125–1139. <https://doi.org/10.1080/10717544.2019.1687614>.

[205] J. Shin, P. Shum, J. Grey, S. Fujiwara, G.S. Malhotra, A. González-Bonet, S.-H. Hyun, E. Moase, T.M. Allen, D.H. Thompson, Acid-labile mPEG-vinyl ether-1,2-dioleylglycerol lipids with tunable pH sensitivity: synthesis and structural effects on hydrolysis rates, DOPE liposome release performance, and pharmacokinetics, *Mol. Pharm.* 9 (2012) 3266–3276. <https://doi.org/10.1021/mp300326z>.

[206] J.A. Boomer, M.M. Qualls, H.D. Inerowicz, R.H. Haynes, V.S. Patri, J.-M. Kim, D.H. Thompson, Cytoplasmic delivery of liposomal contents mediated by an acid-labile cholesterol-vinyl ether-PEG conjugate, *Bioconjug. Chem.* 20 (2009) 47–59. <https://doi.org/10.1021/bc800239b>.

[207] C. Ding, H. Wu, Z.-Z. Yin, J. Gao, D. Wu, Y. Qin, Y. Kong, Disulfide-cleavage- and pH-triggered drug delivery based on a vesicle structured amphiphilic self-assembly, *Mater. Sci. Eng. C Mater. Biol. Appl.* 107 (2020) 110366. <https://doi.org/10.1016/j.msec.2019.110366>.

[208] A. Meister, M.E. Anderson, Glutathione, *Annu. Rev. Biochem.* 52 (1983) 711–760. <https://doi.org/10.1146/annurev.bi.52.070183.003431>.

[209] A. Pompella, A. Visvikis, A. Paolicchi, V. de Tata, A.F. Casini, The changing faces of glutathione, a cellular protagonist, *Biochemical Pharmacology* 66 (2003) 1499–1503. [https://doi.org/10.1016/S0006-2952\(03\)00504-5](https://doi.org/10.1016/S0006-2952(03)00504-5).

[210] X. Du, L. Xiong, S. Dai, S.Z. Qiao, γ -PGA-coated mesoporous silica nanoparticles with covalently attached prodrugs for enhanced cellular uptake and intracellular GSH-responsive release, *Advanced healthcare materials* 4 (2015) 771–781. <https://doi.org/10.1002/adhm.201400726>.

[211] D. Li, R. Zhang, G. Liu, Y. Kang, J. Wu, Redox-Responsive Self-Assembled Nanoparticles for Cancer Therapy, *Advanced healthcare materials* 9 (2020) e2000605. <https://doi.org/10.1002/adhm.202000605>.

Introduction

[212] J. Wu, L. Zhao, X. Xu, N. Bertrand, W. Choi II, B. Yameen, J. Shi, V. Shah, M. Mulvale, J.L. MacLean, O.C. Farokhzad, Hydrophobic Cysteine Poly(disulfide)-based Redox-Hypersensitive Nanoparticle Platform for Cancer Theranostics, *Angewandte Chemie (International ed. in English)* 54 (2015) 9218–9223. <https://doi.org/10.1002/anie.201503863>.

[213] Y. Luo, X. Liu, K. Liang, Q. Chen, T. Liu, B. Yin, H. Chen, 2020. Disulfide Bond Reversible Strategy Enables GSH Responsive-Transferrin Nanoparticles for Precise Chemotherapy. *Adv. Ther. (Weinh)* 3, 2000064. <https://doi.org/10.1002/adtp.202000064>.

[214] Z. Xie, H. Gong, M. Liu, H. Zhu, H. Sun, The properties of mesoporous silica nanoparticles functionalized with different PEG-chain length via the disulfide bond linker and drug release in glutathione medium, *J. Biomater. Sci. Polym. Ed.* 27 (2016) 55–68. <https://doi.org/10.1080/09205063.2015.1107708>.

[215] Y. Fang, X. Lin, X. Jin, D. Yang, S. Gao, K. Shi, M. Yang, Design and Fabrication of Dual Redox Responsive Nanoparticles with Diselenide Linkage Combined Photodynamically to Effectively Enhance Gene Expression, *Int. J. Nanomedicine* 15 (2020) 7297–7314. <https://doi.org/10.2147/IJN.S266514>.

[216] T. Li, H. Xu, Selenium-Containing Nanomaterials for Cancer Treatment, *Cell Reports Physical Science* 1 (2020) 100111. <https://doi.org/10.1016/j.xcrp.2020.100111>.

[217] S. Zhai, X. Hu, Y. Hu, B. Wu, Da Xing, Visible light-induced crosslinking and physiological stabilization of diselenide-rich nanoparticles for redox-responsive drug release and combination chemotherapy, *Biomaterials* 121 (2017) 41–54. <https://doi.org/10.1016/j.biomaterials.2017.01.002>.

[218] A. Rinaldi, R. Caraffi, M.V. Grazioli, N. Oddone, L. Giardino, G. Tosi, M.A. Vandelli, L. Calzà, B. Ruozi, J.T. Duskey, Applications of the ROS-Responsive Thioketal Linker for the Production of Smart Nanomedicines, *Polymers* 14 (2022). <https://doi.org/10.3390/polym14040687>.

[219] Q. Pan, B. Zhang, X. Peng, S. Wan, K. Luo, W. Gao, Y. Pu, B. He, A dithiocarbamate-based H₂O₂-responsive prodrug for combinational chemotherapy and oxidative stress amplification therapy, *Chem. Commun. (Camb)* 55 (2019) 13896–13899. <https://doi.org/10.1039/C9CC05438C>.

[220] N. Ma, Y. Li, H. Ren, H. Xu, Z. Li, X. Zhang, Selenium-containing block copolymers and their oxidation-responsive aggregates, *Polym. Chem.* 1 (2010) 1609. <https://doi.org/10.1039/C0PY00144A>.

Chapter 1

[221]W. Cao, Y. Gu, T. Li, H. Xu, Ultra-sensitive ROS-responsive tellurium-containing polymers, *Chem. Commun. (Camb)* 51 (2015) 7069–7071. <https://doi.org/10.1039/C5CC01779C>.

[222]L. Wang, F. Fan, W. Cao, H. Xu, Ultrasensitive ROS-Responsive Coassemblies of Tellurium-Containing Molecules and Phospholipids, *ACS Appl. Mater. Interfaces* 7 (2015) 16054–16060. <https://doi.org/10.1021/acsami.5b04419>.

[223]Z. Su, M. Chen, Y. Xiao, M. Sun, L. Zong, S. Asghar, M. Dong, H. Li, Q. Ping, C. Zhang, ROS-triggered and regenerating anticancer nanosystem: an effective strategy to subdue tumor's multidrug resistance, *J. Control. Release* 196 (2014) 370–383. <https://doi.org/10.1016/j.jconrel.2014.09.020>.

[224]M. Wang, S. Sun, C.I. Neufeld, B. Perez-Ramirez, Q. Xu, Reactive Oxygen Species-Responsive Protein Modification and Its Intracellular Delivery for Targeted Cancer Therapy, *Angewandte Chemie* 126 (2014) 13662–13666. <https://doi.org/10.1002/ange.201407234>.

[225]Q. Xu, C. He, C. Xiao, X. Chen, Reactive Oxygen Species (ROS) Responsive Polymers for Biomedical Applications, *Macromolecular Bioscience* 16 (2016) 635–646. <https://doi.org/10.1002/mabi.201500440>.

[226]H. Li, M. Miteva, K.C. Kirkbride, M.J. Cheng, C.E. Nelson, E.M. Simpson, M.K. Gupta, C.L. Duvall, T.D. Giorgio, Dual MMP7-proximity-activated and folate receptor-targeted nanoparticles for siRNA delivery, *Biomacromolecules* 16 (2015) 192–201. <https://doi.org/10.1021/bm501394m>.

[227]H. He, L. Sun, J. Ye, E. Liu, S. Chen, Q. Liang, M.C. Shin, V.C. Yang, Enzyme-triggered, cell penetrating peptide-mediated delivery of anti-tumor agents, *J. Control. Release* 240 (2016) 67–76. <https://doi.org/10.1016/j.jconrel.2015.10.040>.

[228]P. Klán, T. Šolomek, C.G. Bochet, A. Blanc, R. Givens, M. Rubina, V. Popik, A. Kostikov, J. Wirz, Photoremovable protecting groups in chemistry and biology: reaction mechanisms and efficacy, *Chemical Reviews* 113 (2013) 119–191. <https://doi.org/10.1021/cr300177k>.

[229]C. Bao, L. Zhu, Q. Lin, H. Tian, Building biomedical materials using photochemical bond cleavage, *Advanced Materials* 27 (2015) 1647–1662. <https://doi.org/10.1002/adma.201403783>.

[230]D.C. Thang, Z. Wang, X. Lu, B. Xing, Precise cell behaviors manipulation through light-responsive nano-regulators: recent advance and perspective, *Theranostics* 9 (2019) 3308–3340. <https://doi.org/10.7150/thno.33888>.

Introduction

[231]G.C.R. Ellis-Davies, Caged compounds: photorelease technology for control of cellular chemistry and physiology, *Nature methods* 4 (2007) 619–628. <https://doi.org/10.1038/nmeth1072>.

[232]J. Liu, W. Kang, W. Wang, Photocleavage-based Photoresponsive Drug Delivery, *Photochem. Photobiol.* 98 (2022) 288–302. <https://doi.org/10.1111/php.13570>.

[233]J.M. Silva, E. Silva, R.L. Reis, Light-triggered release of photocaged therapeutics - Where are we now?, *J. Control. Release* 298 (2019) 154–176. <https://doi.org/10.1016/j.jconrel.2019.02.006>.

[234]P. Sánchez-Moreno, J. de Vicente, S. Nardecchia, J.A. Marchal, H. Boulaiz, Thermo-Sensitive Nanomaterials: Recent Advance in Synthesis and Biomedical Applications, *Nanomaterials* 8 (2018) 935. <https://doi.org/10.3390/nano8110935>.

[235]A. Bordat, T. Boissenot, J. Nicolas, N. Tsapis, Thermoresponsive polymer nanocarriers for biomedical applications, *Adv. Drug Deliv. Rev.* 138 (2019) 167–192. <https://doi.org/10.1016/j.addr.2018.10.005>.

[236]Y. Kotsuchibashi, Recent advances in multi-temperature-responsive polymeric materials, *Polym J* 52 (2020) 681–689. <https://doi.org/10.1038/s41428-020-0330-0>.

[237]W. Li, L. Huang, X. Ying, Y. Jian, Y. Hong, F. Hu, Y. Du, Antitumor drug delivery modulated by a polymeric micelle with an upper critical solution temperature, *Angewandte Chemie International Edition* 54 (2015) 3126–3131. <https://doi.org/10.1002/anie.201411524>.

[238]W. Maamoun, M.I. Badawi, A.A. Aly, Y. Khedr, Nanoparticles in enhancing microwave imaging and microwave Hyperthermia effect for liver cancer treatment, *REVIEWS ON ADVANCED MATERIALS SCIENCE* 60 (2021) 223–236. <https://doi.org/10.1515/ramss-2021-0014>.

[239]M. Gongalsky, G. Gvindzhiliia, K. Tamarov, O. Shalygina, A. Pavlikov, V. Solovyev, A. Kudryavtsev, V. Sivakov, L.A. Osminkina, Radiofrequency Hyperthermia of Cancer Cells Enhanced by Silicic Acid Ions Released During the Biodegradation of Porous Silicon Nanowires, *ACS Omega* 4 (2019) 10662–10669. <https://doi.org/10.1021/acsomega.9b01030>.

[240]Y. Su, X. Wei, F. Peng, Y. Zhong, Y. Lu, S. Su, T. Xu, S.-T. Lee, Y. He, Gold nanoparticles-decorated silicon nanowires as highly efficient near-infrared hyperthermia agents for cancer cells destruction, *Nano Letters* 12 (2012) 1845–1850. <https://doi.org/10.1021/nl204203t>.

Chapter 1

[241] A. Józefczak, K. Kaczmarek, T. Hornowski, M. Kubovčíková, Z. Rozynek, M. Timko, A. Skumił, 2016. Magnetic nanoparticles for enhancing the effectiveness of ultrasonic hyperthermia. *Appl. Phys. Lett.* 108, 263701. <https://doi.org/10.1063/1.4955130>.

[242] A. Jordan, R. Scholz, P. Wust, H. Fähling, R. Felix, Magnetic fluid hyperthermia (MFH): Cancer treatment with AC magnetic field induced excitation of biocompatible superparamagnetic nanoparticles, *Journal of Magnetism and Magnetic Materials* 201 (1999) 413–419. [https://doi.org/10.1016/S0304-8853\(99\)00088-8](https://doi.org/10.1016/S0304-8853(99)00088-8).

[243] I. Yıldız, B. Sızırıcı Yıldız, Applications of Thermoresponsive Magnetic Nanoparticles, *Journal of Nanomaterials* 2015 (2015) 1–12. <https://doi.org/10.1155/2015/350596>.

[244] M.A. Ward, T.K. Georgiou, Thermoresponsive Polymers for Biomedical Applications, *Polymers* 3 (2011) 1215–1242. <https://doi.org/10.3390/polym3031215>.

[245] N.S. Awad, V. Paul, N.M. AlSawaftah, G. ter Haar, T.M. Allen, W.G. Pitt, G.A. Husseini, Ultrasound-Responsive Nanocarriers in Cancer Treatment: A Review, *ACS Pharmacology & Translational Science* 4 (2021) 589–612. <https://doi.org/10.1021/acsptsci.0c00212>.

[246] S. Ibsen, C.E. Schutt, S. Esener, Microbubble-mediated ultrasound therapy: a review of its potential in cancer treatment, *Drug Design, Development and Therapy* 7 (2013) 375–388. <https://doi.org/10.2147/DDDT.S31564>.

[247] A. Kheirolomoom, L.M. Mahakian, C.-Y. Lai, H.A. Lindfors, J.W. Seo, E.E. Paoli, K.D. Watson, E.M. Haynam, E.S. Ingham, L. Xing, R.H. Cheng, A.D. Borowsky, R.D. Cardiff, K.W. Ferrara, Copper-doxorubicin as a nanoparticle cargo retains efficacy with minimal toxicity, *Mol. Pharm.* 7 (2010) 1948–1958. <https://doi.org/10.1021/mp100245u>.

[248] C. Hark, J. Chen, J. Blöck, E.M. Buhl, H. Radermacher, R. Pola, M. Pechar, T. Etrych, Q. Peña, A. Rix, N.I. Drude, F. Kiessling, T. Lammers, J.-N. May, RGD-coated polymeric microbubbles promote ultrasound-mediated drug delivery in an inflamed endothelium-pericyte co-culture model of the blood-brain barrier, *Drug Deliv. and Transl. Res.* 14 (2024) 2629–2641. <https://doi.org/10.1007/s13346-024-01561-6>.

[249] R. Cheng, H.A. Santos, Smart Nanoparticle-Based Platforms for Regulating Tumor Microenvironment and Cancer Immunotherapy, *Advanced healthcare materials* 12 (2023) e2202063. <https://doi.org/10.1002/adhm.202202063>.

[250] Q. Wang, T.R. Chan, R. Hilgraf, V.V. Fokin, K.B. Sharpless, M.G. Finn, Bioconjugation by copper(I)-catalyzed azide-alkyne 3 + 2 cycloaddition, *J. Am. Chem. Soc.* 125 (2003) 3192–3193. <https://doi.org/10.1021/ja021381e>.

[251] S.L. Scinto, D.A. Bilodeau, R. Hincapie, W. Lee, S.S. Nguyen, M. Xu, C.W. am Ende, M.G. Finn, K. Lang, Q. Lin, J.P. Pezacki, J.A. Prescher, M.S. Robillard, J.M. Fox,

Introduction

Bioorthogonal chemistry, Nat Rev Methods Primers 1 (2021) 1–23. <https://doi.org/10.1038/s43586-021-00028-z>.

[252] L. Taiariol, C. Chaix, C. Farre, E. Moreau, Click and Bioorthogonal Chemistry: The Future of Active Targeting of Nanoparticles for Nanomedicines?, Chemical Reviews 122 (2022) 340–384. <https://doi.org/10.1021/acs.chemrev.1c00484>.

[253] O. Keinänen, E.M. Mäkilä, R. Lindgren, H. Virtanen, H. Liljenbäck, V. Oikonen, M. Sarparanta, C. Molthoff, A.D. Windhorst, A. Roivainen, J.J. Salonen, A.J. Airaksinen, Pretargeted PET Imaging of trans-Cyclooctene-Modified Porous Silicon Nanoparticles, ACS Omega 2 (2017) 62–69. <https://doi.org/10.1021/acsomega.6b00269>.

[254] M. Handula, K.-T. Chen, Y. Seimbille, IEDDA: An Attractive Bioorthogonal Reaction for Biomedical Applications, Molecules 26 (2021) 4640. <https://doi.org/10.3390/molecules26154640>.

[255] K.M. Au, A.Z. Wang, S.I. Park, Pretargeted delivery of PI3K/mTOR small-molecule inhibitor-loaded nanoparticles for treatment of non-Hodgkin's lymphoma, Sci. Adv. 6 (2020) eaaz9798. <https://doi.org/10.1126/sciadv.aaz9798>.

[256] C.V.H.-H. Chen, B.P. Triana, R.K. Prud'homme, Investigation of the Local Environment of Hydrophobic End Groups on Polyethylene Glycol (PEG) Brushes Using Fluorometry: Relationship to Click Chemistry Conjugation Reactions on PEG-Protected Nanoparticles, ACS Macro Letters 4 (2015) 521–525. <https://doi.org/10.1021/acsmacrolett.5b00119>.

[257] E.J.L. Stéen, P.E. Edem, K. Nørregaard, J.T. Jørgensen, V. Shalgunov, A. Kjaer, M.M. Herth, Pretargeting in nuclear imaging and radionuclide therapy: Improving efficacy of theranostics and nanomedicines, Biomaterials 179 (2018) 209–245. <https://doi.org/10.1016/j.biomaterials.2018.06.021>.

[258] I.V.J. Feiner, K.R. Pulagam, K.B. Uribe, R. Passannante, C. Simó, K. Zamacola, V. Gómez-Vallejo, N. Herrero-Álvarez, U. Cossío, Z. Baz, M.M. Caffarel, C.H. Lawrie, D.J. Vugts, L. Rejc, J. Llop, Pre-targeting with ultra-small nanoparticles: boron carbon dots as drug candidates for boron neutron capture therapy, J. Mater. Chem. B 9 (2021) 410–420. <https://doi.org/10.1039/D0TB01880E>.

[259] S.B. Lee, H.L. Kim, H.-J. Jeong, S.T. Lim, M.-H. Sohn, D.W. Kim, Mesoporous silica nanoparticle pretargeting for PET imaging based on a rapid bioorthogonal reaction in a living body, Angewandte Chemie (International ed. in English) 52 (2013) 10549–10552. <https://doi.org/10.1002/anie.201304026>.

[260] H.J. Jeong, R.J. Yoo, J.K. Kim, M.H. Kim, S.H. Park, H. Kim, J.W. Lim, S.H. Do, K.C. Lee, Y.J. Lee, D.W. Kim, Macrophage cell tracking PET imaging using mesoporous silica

Chapter 1

nanoparticles via in vivo bioorthogonal F-18 labeling, *Biomaterials* 199 (2019) 32–39. <https://doi.org/10.1016/j.biomaterials.2019.01.043>.

[261] J. Idiago-López, E. Moreno-Antolín, J.M. de La Fuente, R.M. Fratila, Nanoparticles and bioorthogonal chemistry joining forces for improved biomedical applications, *Nanoscale Advances* 3 (2021) 1261–1292. <https://doi.org/10.1039/d0na00873g>.

[262] S. Maslanka Figueroa, D. Fleischmann, S. Beck, P. Tauber, R. Witzgall, F. Schweda, A. Goepferich, Nanoparticles Mimicking Viral Cell Recognition Strategies Are Superior Transporters into Mesangial Cells, *Adv. Sci. (Weinh)* 7 (2020) 1903204. <https://doi.org/10.1002/advs.201903204>.

[263] S. Li, C. Meng, Q. Hao, R. Zhou, L. Dai, Y. Guo, S. Zhao, X. Zhou, C. Lou, J. Xu, P. Xu, J. Yang, Y. Ding, Y. Lv, S. Han, S. Li, J. Li, H. Kang, Z. Xiao, M. Tan, X. Ma, H. Wu, "On/off"-switchable crosslinked PTX-nanoformulation with improved precise delivery for NSCLC brain metastases and restrained adverse reaction over nab-PTX, *Biomaterials* 307 (2024) 122537. <https://doi.org/10.1016/j.biomaterials.2024.122537>.

Introduction

Chapter 1

Chapter 2

Goals of the Thesis

Chapter 2

Although today's pharmaceutical research has identified promising drug candidates for a wide range of diseases, the efficacy of many active substances is limited by their unfavorable biodistribution. As a result, relevant biological effects in the organism cannot be achieved or require the administration of higher doses, frequently resulting in adverse drug effects or even the need to discontinue the therapy due to toxic effects. Drug delivery via targeted nanomaterials offers a powerful tool to overcome this drawback. By conjugating receptor ligands to the nanoparticle corona, nanoparticle-cell interactions can be precisely tailored, and particles can be addressed to a specific target tissue. In this way, drug accumulation at the site of action can be increased, preventing harmful side effects and improving therapeutic efficacy [1].

However, up to date targeted nanotherapeutics do not meet their high expectations [2]. They face several hurdles that limit their capabilities, such as the adsorption of plasma proteins [3], preliminary clearance [4], endosomal entrapment [5], premature drug release [6], or insufficient target retention time [7]. Moreover, targeting moieties such as cell surface receptors are frequently not expressed exclusively in one cell type but show a ubiquitous presence [8,9], which demands for new strategies enabling distinct discrimination between target and off-target tissue.

Viruses, as natural nanoparticles, are in contrast highly efficient in controlling their distribution in the organism and selectively infecting their host target cells. They identify specific cell types not by the presence of a single recognition motif, but by scanning the cell surface for a particular composition of multiple enzymes or receptors. To do this, the virus binds to a specific structure on the cell surface in a first step. If this initial attachment was successful, a multi-step cascade is triggered, in which the virus interacts with additional target moieties. Only if the cell surface composition exactly matches the viral recognition mechanism, internalization occurs [10,11].

Therefore, the aim of this work was the development of virus-mimetic nanoparticles as drug delivery system, exploiting the beneficial properties of their blueprints to precisely control biodistribution. Due to their excellent versatility with respect to particle size, charge, surface composition, drug loading capabilities, biodegradability, and compatibility, polymeric nanoparticles have been selected as platform for the investigations [12].

Chapter 2

Chapter 3 focuses on the development of nanoparticles targeting renal mesangial cells for the treatment of mesangial cell-associated diseases such as IgA nephropathy, diabetic nephropathy, or lupus nephritis, which frequently progress to end-stage renal disease. The particle system on which this chapter is based was previously established by our work group [13,14] and mimics the infection pathway of the human adenovirus (AV): after initial attachment to the coxsackie and adenovirus receptor (CAR), the AV together with the bound receptor moves along the cell surface via a lateral drift, presenting a previously shielded protein structure. Only if the revealed sequence binds to the $\alpha_v\beta_3$ -integrin receptor, receptor-mediated endocytosis occurs (Fig. 1) [14-16]. The studies of Fleischmann et al. (2020,2021) [13,14] focused on mimicking and *in vitro* evaluation of this targeting concept, using the angiotensin 1 receptor (AT1R) antagonist EXP-3174 for target cell attachment and the $\alpha_v\beta_3$ -integrin receptor agonist cRGD as the revealed uptake signal. Additionally, first *in vivo* experiments had been performed, evaluating the nanoparticle localization after one hour.

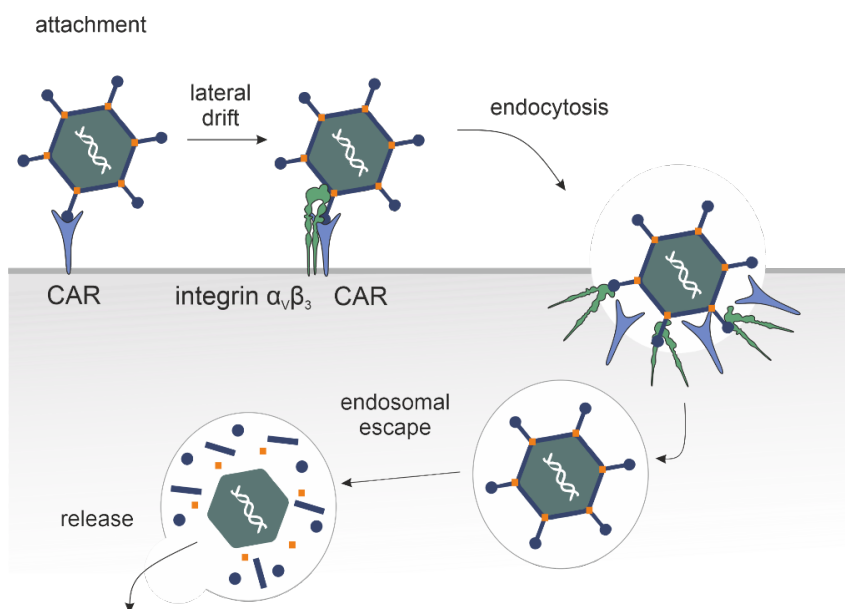


Figure 1. Simplified scheme of the target cell identification and internalization mechanism of the human adenovirus (AV). In the first step, the AV attaches to the coxsackie and adenovirus receptor (CAR) on the cell surface via button-like end linkers of fiber proteins, followed by laterally drifting motions on the cell surface. As a consequence, a previously shielded protein structure is revealed and can bind the $\alpha_v\beta_3$ -integrin receptor, which leads to receptor-mediated endocytosis. Finally, acidification of the endosome releases the viral capsid into the cytoplasm [14-16].

The current research, in contrast, aimed to evaluate the applicability of the particles by analyzing their residence time and efficacy in the renal target tissue *in vivo*. Therefore, particle distribution and accumulation in mesangial cells were assessed by intravital microscopy over 24 h and by histological sections over 10 days. Furthermore, erastin, a ferroptosis-inducing compound, was encapsulated into the particles to determine whether it is possible to deliver sufficient drug quantities to the site of action to induce a biologically relevant effect. The selection of a ferroptosis inducer, in this case, had multiple motivations: it allows the direct visualization of effects via ferroptosis-dependent histological changes in the target tissue, the erastin-loaded particles could serve as a novel, site-specific therapy for mesangial-proliferative glomerulonephritis, and the application of the particles into healthy mice could be the basis for a disease model for mesangial cell-associated diseases.

However, target cell recognition and uptake via membrane receptors can have a significant drawback: for a large number of receptors, ligand binding is directly associated with the initiation of intracellular signalling cascades [17,18]. In most cases, if the nanoparticle is intended to serve as a drug delivery system to transport an active ingredient to the site of action, this may lead to adverse drug effects. For this reason, as the second part of the project, an advanced, virus-mimetic targeting concept was developed. It is not based on the interaction with receptors such as G-protein coupled receptors (GPCRs) like the AT1R or integrin receptors, such as the $\alpha_v\beta_3$ receptor, but exclusively targets ectoenzymes, which is expected to result in a significantly lower side-effect profile (Fig. 2A).

The SARS-CoV-2 virus is a viral role model that controls both target cell recognition and uptake via the interaction with ectoenzymes [19]. In the first obligatory step, SARS-CoV-2 binds to the angiotensin-converting enzyme 2 (ACE2) for target cell identification, which induces conformational changes in the S1 subunit and exposes the S2'-cleavage site of the S2 subunit. Subsequently, there are two different potential internalization pathways, a transmembrane protease serin subtype 2 (TMPRSS2)-independent one with internalization via endosomal uptake (Fig. 2B), and a TMPRSS2-dependent one (Fig. 2C), that causes membrane fusion [19]. The fact that the virus triggered a pandemic lasting from 2020 to 2023, with over 760 million confirmed infections and at least 6.9 million deaths worldwide [20], demonstrates the effectiveness of this infection pathway. For this reason, chapters 4-6 deal with the design of a SARS-CoV-2-mimetic nanoparticle targeting concept, addressing ACE2-expressing cells, which could be utilized for the targeting of strongly ACE2-expressing compartments. These

Chapter 2

include renal tubules, gallbladder, cardiomyocytes, male reproductive cells, eyes, and vasculature [21]. Additionally, the particles could provide a platform for the direct targeting of SARS-CoV-2 host cells, enabling tracking of the virus in the human organism, which might be an innovative therapy option for acute COVID-19 disease or also post-covid symptoms.

Chapter 4 examines whether ectoenzymes are suitable cell identification structures and thus provide a viable alternative to classical ligand-receptor concepts. Therefore, the selective and potent ACE2 inhibitor MLN-4760 (MLN) was attached to the surface of polymeric nanoparticles, which should promote the attachment to ACE2-positive cells without particle internalization. The binding avidity to ACE2 and the inhibitory activity of MLN-modified particles were quantified and mono- and co-culture experiments were performed to analyze the targeting ability *in vitro*. Additionally, the localization of the nanoparticles after incubation with ACE2-positive cells was determined microscopically since particle attachment without non-specific uptake is necessary to allow the interaction with further targeting motifs.

For receptor-independent internalization, in **Chapter 5**, nanoparticles were modified with various cell-penetrating peptides (CPPs), which are small peptidic structures with highly preferential cell uptake [22]. In the first step, the correlation between CPP netto charge, resulting nanoparticle zeta potential, and the uptake-promoting properties was analyzed to identify the most suitable CPP as receptor-independent uptake signal for the virus-mimetic nanoparticle design. Subsequently, MLN-4760 was combined with a sterically shielded CPP, which is only revealed after initial binding to ACE2, mimicking the TMPRSS2-independent uptake route of SARS-CoV-2. In this way, selective uptake into ACE2-positive target cells should be achieved.

To target SARS-CoV-2 host cells and enable tracking of the virus inside the organism, it might be beneficial to further adapt the particle structure to the TMPRSS2-dependent internalization pathway. Therefore, a TMPRSS2 cleavage sequence should be implemented into the polymer chains, revealing the uptake signal exclusively after previous activation by the transmembrane protease. **Chapter 6** provides first considerations for the development of this targeting concept and describes the lentiviral transduction of HEK293 cells for the generation of an ACE2 and TMPRSS2 double-positive cell line, which is necessary for the following investigations.

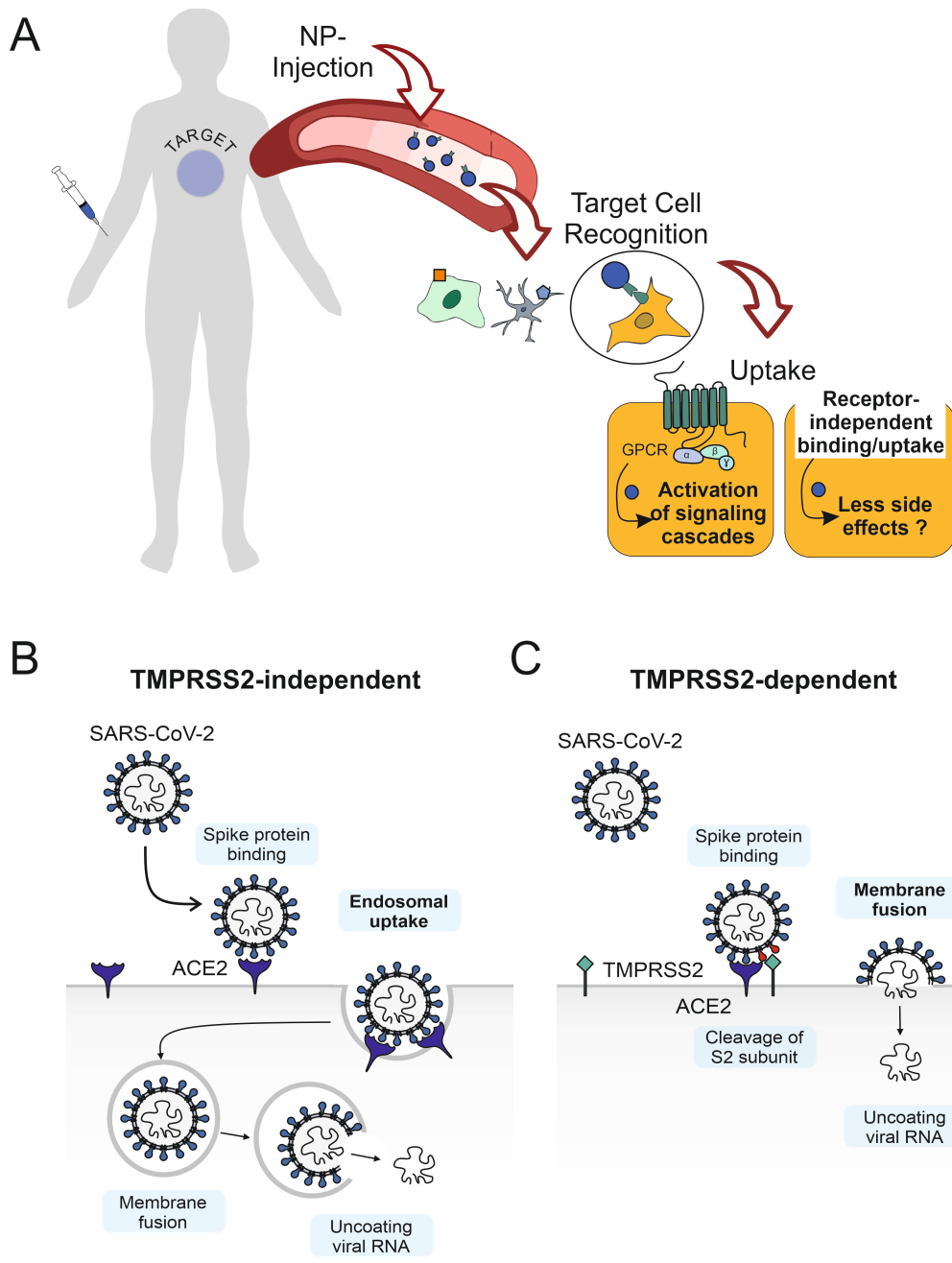


Figure 2. SARS-CoV-2 mimicry as blueprint for ectoenzyme-based nanoparticle targeting.

(A) Development of ectoenzyme-based targeting concepts as an alternative to classical receptor-based targeting approaches. **(B)** TMPRSS2-independent uptake route of SARS-CoV-2: endosomal internalization after attachment of the viral spike protein to the ACE2 enzyme. **(C)** TMPRSS2-dependent uptake route: the transmembrane protease cleaves the S2'-subunit, resulting in dramatic conformational changes that initiate membrane fusion and release of the viral RNA into the host cell cytoplasm for replication [19].

References

- [1] E. Blanco, H. Shen, M. Ferrari, Principles of nanoparticle design for overcoming biological barriers to drug delivery, *Nat Biotechnol* 33 (2015) 941–951. <https://doi.org/10.1038/nbt.3330>.
- [2] S. Wilhelm, A.J. Tavares, Q. Dai, S. Ohta, J. Audet, H.F. Dvorak, W.C.W. Chan, Analysis of nanoparticle delivery to tumours, *Nat Rev Mater* 1 (2016) 1–12. <https://doi.org/10.1038/natrevmats.2016.14>.
- [3] A. Salvati, A.S. Pitek, M.P. Monopoli, K. Prapainop, F.B. Bombelli, D.R. Hristov, P.M. Kelly, C. Åberg, E. Mahon, K.A. Dawson, Transferrin-functionalized nanoparticles lose their targeting capabilities when a biomolecule corona adsorbs on the surface, *Nat. Nanotechnol.* 8 (2013) 137–143. <https://doi.org/10.1038/nnano.2012.237>.
- [4] Z. Hussain, S. Khan, M. Imran, M. Sohail, S.W.A. Shah, M. de Matas, PEGylation: a promising strategy to overcome challenges to cancer-targeted nanomedicines: a review of challenges to clinical transition and promising resolution, *Drug Deliv. and Transl. Res.* 9 (2019) 721–734. <https://doi.org/10.1007/s13346-019-00631-4>.
- [5] D. Pei, M. Buyanova, Overcoming Endosomal Entrapment in Drug Delivery, *Bioconjug. Chem.* 30 (2019) 273–283. <https://doi.org/10.1021/acs.bioconjchem.8b00778>.
- [6] T. Miller, S. Breyer, G. van Colen, W. Mier, U. Haberkorn, S. Geissler, S. Voss, M. Weigandt, A. Goepferich, Premature drug release of polymeric micelles and its effects on tumor targeting, *International Journal of Pharmaceutics* 445 (2013) 117–124. <https://doi.org/10.1016/j.ijpharm.2013.01.059>.
- [7] L. Chen, C. Liu, Y. Xiang, J. Lyu, Z. Zhou, T. Gong, H. Gao, L. Li, Y. Huang, Exocytosis blockade of endoplasmic reticulum-targeted nanoparticle enhances immunotherapy, *Nano Today* 42 (2022) 101356. <https://doi.org/10.1016/j.nantod.2021.101356>.
- [8] Y. Shen, X. Li, D. Dong, B. Zhang, Y. Xue, P. Shang, Transferrin receptor 1 in cancer: a new sight for cancer therapy, *American Journal of Cancer Research* 8 (2018) 916–931.
- [9] M. Marti-Solano, S.E. Crilly, D. Malinverni, C. Munk, M. Harris, A. Pearce, T. Quon, A.E. Mackenzie, X. Wang, J. Peng, A.B. Tobin, G. Ladds, G. Milligan, D.E. Gloriam, M.A. Puthenveedu, M.M. Babu, Combinatorial expression of GPCR isoforms affects signalling and drug responses, *Nature* 587 (2020) 650–656. <https://doi.org/10.1038/s41586-020-2888-2>.

[10] M. Marsh, A. Helenius, Virus entry: open sesame, *Cell* 124 (2006) 729–740. <https://doi.org/10.1016/j.cell.2006.02.007>.

[11] S. Maslanka Figueroa, D. Fleischmann, A. Goepferich, Biomedical nanoparticle design: What we can learn from viruses, *J. Control. Release* 329 (2021) 552–569. <https://doi.org/10.1016/j.jconrel.2020.09.045>.

[12] S. Sur, A. Rathore, V. Dave, K.R. Reddy, R.S. Chouhan, V. Sadhu, Recent developments in functionalized polymer nanoparticles for efficient drug delivery system, *Nano-Structures & Nano-Objects* 20 (2019) 100397. <https://doi.org/10.1016/j.nanoso.2019.100397>.

[13] D. Fleischmann, S. Maslanka Figueroa, S. Beck, K. Abstiens, R. Witzgall, F. Schweda, P. Tauber, A. Goepferich, Adenovirus-Mimetic Nanoparticles: Sequential Ligand-Receptor Interplay as a Universal Tool for Enhanced In Vitro/In Vivo Cell Identification, *ACS Appl. Mater. Interfaces* 12 (2020) 34689–34702. <https://doi.org/10.1021/acsami.0c10057>.

[14] D. Fleischmann, Virus-Mimetic Nanoparticles for the Therapy of Mesangial Cells in Diabetic Nephropathy, 2021.

[15] M.M.Y. Waye, C.W. Sing, Anti-Viral Drugs for Human Adenoviruses, *Pharmaceuticals* 3 (2010) 3343–3354. <https://doi.org/10.3390/ph3103343>.

[16] S. Luisoni, U.F. Greber, 2 - Biology of Adenovirus Cell Entry: Receptors, Pathways, Mechanisms, in: D.T. Curiel (Ed.), *Adenoviral Vectors for Gene Therapy*, second. Aufl., Elsevier Reference Monographs, s.l., 2016, pp. 27–58.

[17] Z.J. Deng, M. Liang, M. Monteiro, I. Toth, R.F. Minchin, Nanoparticle-induced unfolding of fibrinogen promotes Mac-1 receptor activation and inflammation, *Nat. Nanotechnol.* 6 (2011) 39–44. <https://doi.org/10.1038/nnano.2010.250>.

[18] Q. Zhang, B.M. Reinhard, Ligand Density and Nanoparticle Clustering Cooperate in the Multivalent Amplification of Epidermal Growth Factor Receptor Activation, *ACS Nano* 12 (2018) 10473–10485. <https://doi.org/10.1021/acs.nano.8b06141>.

[19] C.B. Jackson, M. Farzan, B. Chen, H. Choe, Mechanisms of SARS-CoV-2 entry into cells, *Nat Rev Mol Cell Biol* 23 (2022) 3–20. <https://doi.org/10.1038/s41580-021-00418-x>.

[20] Coronavirus disease (COVID-19), 2024. [\(accessed 8 August 2024\)](https://www.who.int/news-room/fact-sheets/detail/coronavirus-disease-(covid-19)).

[21] F. Hikmet, L. Méar, Å. Edvinsson, P. Micke, M. Uhlén, C. Lindskog, The protein expression profile of ACE2 in human tissues, *Mol. Syst. Biol.* 16 (2020) e9610. <https://doi.org/10.15252/msb.20209610>.

Chapter 2

[22] I. Tabujew, M. Lelle, K. Peneva, Cell-penetrating peptides for nanomedicine – how to choose the right peptide, *BioNanoMaterials* 16 (2015) 59–72.
<https://doi.org/10.1515/bnm-2015-0001>.

Goals of the Thesis

Chapter 2

Chapter 3

Long-term Residence and Efficacy of Adenovirus-mimetic Nanoparticles in Renal Target Tissue

Published in *Journal of Drug Targeting*

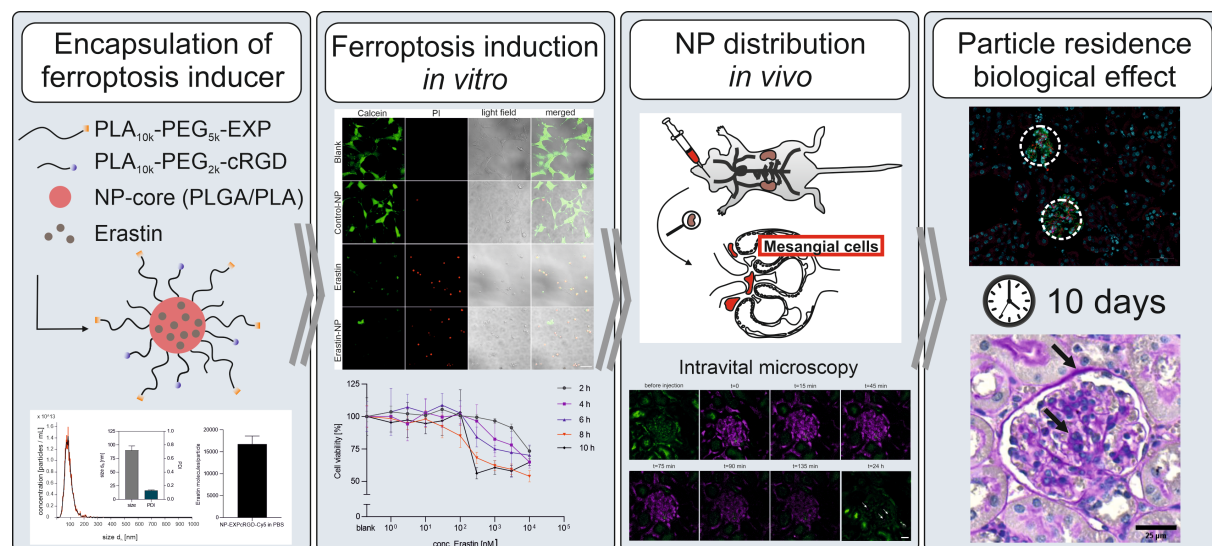
Published online 22 August 2024

This chapter was published as: M. Walter, H. Weißbach, F. Gembardt, S. Halder, K. Schorr, D. Fleischmann, V. Todorov, C. Hugo, A. Goepferich, *Journal of Drug Targeting*, 22 August 2024, doi: <https://doi.org/10.1080/1061186X.2024.2390628>. H.W. and S.H. performed the *in vivo* experiments.

Chapter 3

Abstract

A major shortcoming in the treatment of mesangial cell-associated diseases such as IgA nephropathy, diabetic nephropathy, or lupus nephritis, which frequently progress to end-stage renal disease, is poor drug availability in the glomerular mesangium. Drug delivery via active targeting of nanoparticles, using ligands attached to the particle surface for target cell recognition to increase the biodistribution to the mesangium, is a promising strategy to overcome this hurdle. However, although several glomerular tissue targeting approaches have been described, so far no study has demonstrated the particles' ability to deliver sufficient drug amounts combined with an appropriate nanoparticle target retention time to trigger relevant biological effects in the mesangium. In our study, we encapsulated erastin, a ferroptosis-inducing model compound, into adenovirus-mimetic, mesangial cell-targeting nanoparticles, enabling the direct visualization of biological effects through ferroptosis-dependent histological changes. By intravital microscopy and analysis of histological sections, we were not only able to localize the injected particles over 10 days within the target cells but also to demonstrate biological activity in the renal glomeruli. In conclusion, we have characterized adenovirus-mimetic nanoparticles as a highly suitable drug delivery platform for the treatment of mesangial cell-associated diseases and additionally provided the basis for a potential renal disease model.



Chapter 3

1 Introduction

The mesangium is a highly relevant target for drug therapy, since it plays a pivotal role in the integrity of the glomerular filter and is severely compromised in the pathogenesis of various human kidney diseases [1–3]. Besides involvement in hemolytic uremic syndrome, lupus nephritis, or diabetic nephropathy (DN) [4–6], mesangial pathophysiology is critical for progression of immunoglobulin type A nephropathy (IgAN), which is the most prevalent primary chronic glomerulonephritis worldwide [7]. Although there are numerous potential drugs to inhibit pathomechanisms such as the overproduction of extracellular matrix or mesangial cell hyperproliferation [2,8], there is no adequate causal therapy available to date. This deficiency may be due to poor availability of drugs in the target tissue or severe side effects mediated by off-target cells [6,9,10]. Therefore, all these therapeutic approaches would benefit tremendously from strategies to selectively guide drugs to the mesangium.

In this context, active nanoparticle targeting is a promising tool, since it holds the potential to effectively transport drugs to the site of action, maximizing the efficacy at the target site, while minimizing adverse drug effects in off-target tissues [11]. To this end, ligands for specific cell surface structures such as receptors [12,13] or ectoenzymes [14,15] are bound to the nanoparticle surface, enabling them to selectively identify target cells and direct them to their destination [16]. While it has already been shown that nanoparticles may reach their target tissue *in vivo* by such active targeting strategies [3,17], there is only little information on the subsequent fate of the particles. Since pharmacokinetic studies frequently focus on plasma half-life and distribution on the organ and tissue level [18,19], intracellular particle residence times that represent a critical factor are hardly known. A short retention time may result in a reduced drug release at the target site and can, therefore, become a limiting factor for pharmacological efficacy [20]. Moreover, it is essential to consider for which time period biological effects can be expected and when nanoparticles are eliminated to determine appropriate application intervals. With this study, we aimed to provide an actively targeted nanoparticulate drug delivery system that is suitable for the treatment of mesangial cell-associated diseases such as IgAN and DN in the future. We were particularly interested in the particle residence time at the target site and the particle-associated biological effect, which demonstrates successful drug delivery.

For our studies, we relied on a well-characterized and biocompatible, adenovirus-mimetic nanoparticle approach for targeting mesangial cells, which was previously established by our

Chapter 3

group [21]. The polymer-based core-shell nanoparticle system presents two ligands one after another: first, the angiotensin I receptor (AT1R) inhibitor EXP-3174 and thereafter the $\alpha_1\beta_3$ -integrin substrate cRGDfK. Hereby, EXP-3174 induces cell binding and tethers the particle to the cell surface. The successful binding reveals the previously sterically hidden integrin receptor agonist cRGDfK, which can now bind to its receptor and trigger cell uptake (Fig. 1). Therefore, after extravasation through endothelial fenestrations in mesangial areas, which have an average diameter of 60-100 nm and thus an optimal size range for the NP passage [21,22], the nanoparticles selectively recognize mesangial cell surfaces enabling a reliable and reproducible targeting *in vivo* [21].

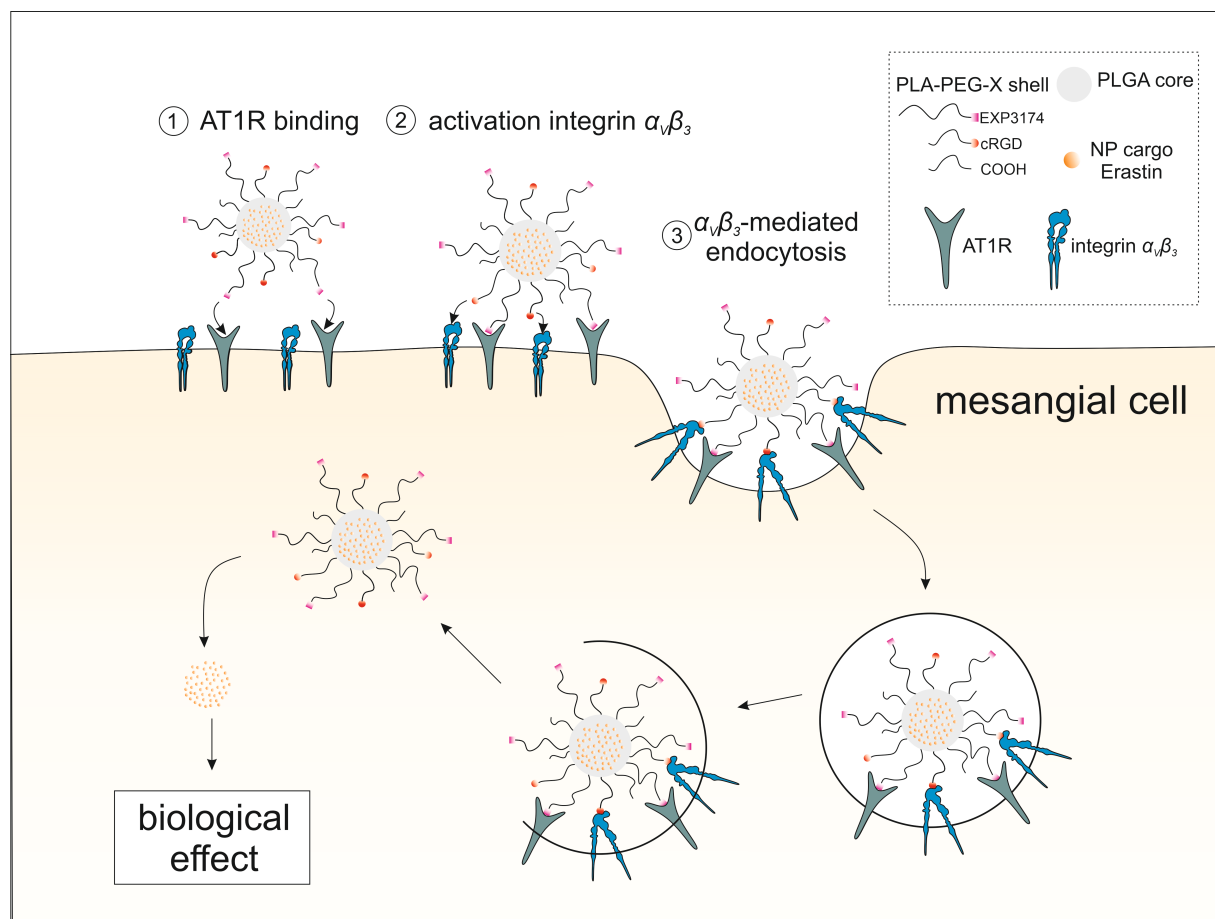


Figure 1. Illustration of the adenovirus-mimetic nanoparticle targeting concept. A sequential uptake mechanism of the drug-loaded nanoparticle is mediated by the mesangial cell attachment via EXP-3174, an inhibitor for the angiotensin I receptor (AT1R) attached to longer polymer chains in a first step and the activation of the $\alpha_1\beta_3$ integrin receptor by its substrate cRGDfK attached to shorter polymer chains as the second step [12]. The release of the transported drug triggers biological effects in the target tissue.

Adenovirus-mimetic Nanoparticles in Renal Target Tissue

To obtain nanoparticles that trigger a well detectable biological effect, erastin, a ferroptosis-inducing compound, was encapsulated as model substance for drug delivery. Erastin causes tissue damage via iron-dependent accumulation of reactive oxygen species (ROS) [23,24] (Fig. 2) and thus promotes physiological conditions related to the pathology in many kidney diseases, which are frequently associated with excessive ROS activity [25,26]. This provides direct evidence of whether sufficient drug is reaching the target site and additionally generates local conditions that may serve as the basis for a disease model to study mesangial cell-associated diseases in the future. The distribution of fluorescently labeled nanoparticles into mesangial cells was tracked *in vivo* by longitudinal intravital microscopy (IVM). Drug efficacy was investigated via histological sections.

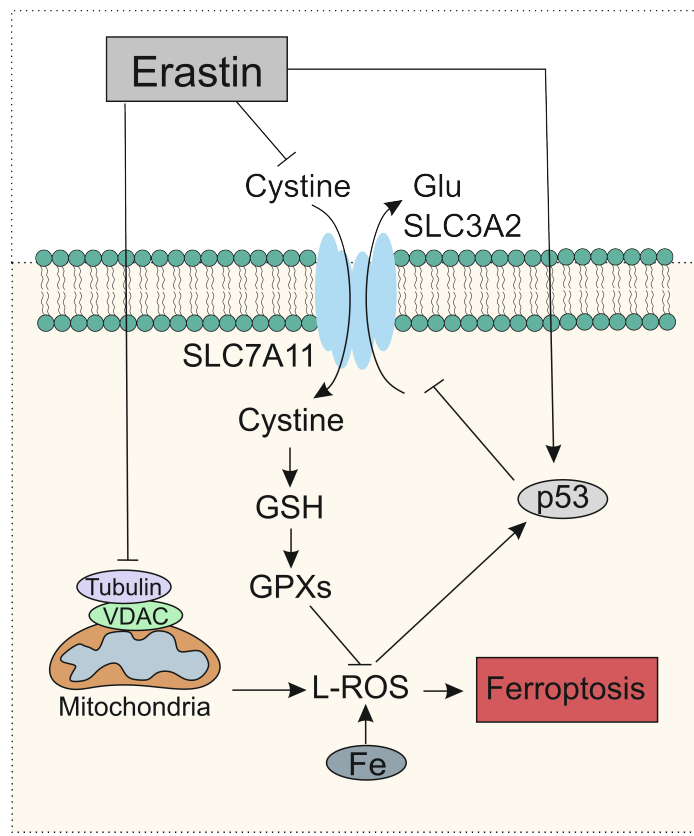


Figure 2. Ferroptosis induction by erastin. The triggering of various signaling cascades through interaction with tubulin, voltage-dependent anion channels (VDAC), p53, and the system X_C^- causes an excessive accumulation of lipid reactive oxygen species (L-ROS) and thus leads to the cell death mechanism of ferroptosis [24].

Chapter 3

2 Materials and Methods

2.1 Materials

If not otherwise declared, all reagents and chemicals were purchased from Sigma Aldrich (Taufkirchen, Germany) in analytical grade.

Ultrapure, deionized water was generated by a Milli-Q water purification system (Millipore, Schwalbach, Germany). Dulbecco's phosphate-buffered saline (PBS) was obtained from Gibco® Life Technologies (Thermo Fisher Scientific, Waltham, MA, USA).

Heterobifunctional hydroxyl poly(ethylene glycol)-carboxylic acid with a molecular mass of 2,000 g mol⁻¹ (OH-PEG_{2k}-COOH) and hydroxyl poly(ethylene glycol)Boc-amine (OH-PEG_{5k}-NH-Boc) with a molecular mass of 5,000 g mol⁻¹ were purchased from Jenkem Technology USA Inc. (Allen, TX, USA). Cyclic RGDfK (cRGD) was obtained from Synpeptide Co. (Shanghai, China).

Resomer RG 502 (PLGA; lactide:glycolide, 50:50 molecular mass, 13,400 g mol⁻¹ was purchased from Sigma Aldrich (Taufkirchen, Germany). Cyanine 5-amine (Cy5) for the fluorogenic labeling of the nanoparticles was sourced from Lumiprobe (Hannover, Germany).

The cellulose dialysis membranes for polymer purification were purchased from Spectrum Laboratories, Inc (Rancho Domingues, CA, USA). Nanoparticle solutions were concentrated with centrifugal devices with a molecular weight cut-off of 100 kDa, which were obtained from Pall Life Sciences (Portsmouth, UK).

4 % BCL Agarose Beads Fine were used as column material for size exclusion chromatography (SEC) and purchased from Agarose Bead Technologies ABT (Madrid, Spain).

SV40 MES13 cells were sourced from the American Type Culture Collection (ATCC) (Manassas, VA, USA). For the preparation of cell culture medium, fetal bovine serum (FBS) was purchased from Invivogen (Toulouse, France) and HEPES was obtained from Gibco (Thermo Fisher Scientific, Waltham, MA, USA).

For confocal scanning microscopy (CLSM) experiments the cells were seeded in 8-well microscope slides from Ibidi (Gräfelfing, Germany). The 96-well plates for cell death experiments were purchased from Greiner (Frickenhausen, Germany).

2.2 Synthesis of EXP-3174

Losartan carboxylic acid (EXP-3174) was obtained by oxidation of losartan with potassium permanganate as previously described by Abstiens et al. (2020) [27]. Therefore, losartan potassium (Santa Cruz Biotechnology, Heidelberg, Germany) (1 eq, 2 g) was dissolved in 50 mL 0.1 N sodium hydroxide solution (NaOH) and cooled down to 0 °C. 50 mL of an ice-cold aqueous solution of potassium permanganate (0.2 M) (Merck, Heidelberg, Germany) was added. The reaction mixture was stirred for 4.5 h at RT. The product was then precipitated by adjusting the pH with 1 N hydrochloric acid (HCl) until the supernatant turned pink. The reaction product was washed by centrifuging (3000 g, 4 °C, 15 min), discarding the supernatant, and resuspending the precipitate in water. This washing step was repeated twice. Afterward, the product was isolated by adjusting the pH to moderately alkaline conditions (pH 8-9) with 1 N NaOH to dissolve the product and remove manganese dioxide by centrifugation (3000 g, 15 min, 4 °C). The product was precipitated from the supernatant by acidification with 1 N HCl (pH 3-4) and then extracted with ethyl acetate in a separating funnel. Ethyl acetate was removed with a rotary evaporator. The resulting product was taken up in 13 mL ethanol, filtered with a syringe filter (0.2 µm), precipitated in a 20-fold excess of water, and freeze-dried to obtain a dry powder. The identity and purity of EXP-3174 were verified by ¹H-NMR (Bruker Avance III HD 400) and high-resolution mass spectrometry analysis (HRMS). HRMS was performed on a Q-TOF 6540 ultrahigh definition (UHD) LC/MS system by Agilent Technologies (Waldbronn, Germany) using an electrospray ionization (ESI) source.

2.3 Polymer Synthesis and Modification

Poly(lactic acid)-poly(ethylene glycol) (PLA-PEG) block-copolymers were synthesized after Qian et al. (2011) [28] via ring-opening polymerization of cyclic lactide with modifications previously described by our group [12,29]. Therefore, 3,6-dimethyl-1,4-dioxane-2,5-dione was recrystallized from ethyl acetate at 85 °C and dried under vacuum at 38 °C for 12 h before use. For the ring opening polymerization, the heterobifunctional PEG polymers OH-PEG_{5k}-NH-Boc or OH-PEG_{2k}-COOH, respectively, served as macroinitiator. One equivalent (1 eq, 0.19 mmol) was dissolved in 10 mL of anhydrous DCM in a round bottom flask and mixed with 3,6-dimethyl-1,4-dioxane-2,5-dione (70 eq, 13.3 mmol) and 1,8-diazabicyclo[5.4.0] undec-7-ene (DBU) (3 eq, 0.57 mmol). The round-bottom flask was fitted with a drying tube and the reaction mixture was stirred at RT for exactly 1 hour. Afterward, the polymerization reaction was

Chapter 3

quenched by adding benzoic acid (10 eq, 1.92 mmol). The solution was added dropwise to 100 mL ice-cold diethyl ether to precipitate the block copolymer. The suspension was centrifuged for 15 min (3000 g, 4 °C) and the supernatant was decanted. The resulting solid was dried under nitrogen flow overnight at RT. For PLA_{10k}-PEG_{5k}-NH-Boc, the polymer synthesis was followed by a cleavage reaction, to release the free amine for ligand coupling. In brief, the Boc-protected polymer was dissolved in a mixture of dichloromethane (DCM) and trifluoroacetic acid (TFA) (1:1 v/v, 10 mL) and stirred for 30 min at RT. After evaporation of DCM and TFA via a rotary evaporator, the polymer was purified by precipitation in ice-cold diethyl ether (100 mL). After centrifugation (3000 g, 15 min, 4 °C), the supernatant was decanted and the solid was again dried under nitrogen flow. The resulting polymers with 10 kDa poly(lactic acid) (PLA) content (PLA_{10k}-PEG_{2k}-COOH and PLA_{10k}-PEG_{5k}-NH₂) were characterized via ¹H-NMR (Supporting Information, Chapter 1).

The ligands EXP-3174 and cyclic RGDfK (cRGD) were coupled to PLA_{10k}-PEG_{5k}-NH₂ and PLA_{10k}-PEG_{2k}-COOH as previously described by our group [21] with slight modifications.

EXP-3174 (3.5 eq, 80 mg) was weighed in a snap cap tube and dissolved in 3 mL anhydrous *N,N*-dimethylformamide (DMF). 1-Ethyl-3-(3-dimethylaminopropyl)carbodiimide (EDC) (10 eq, 99.7 mg) and *N*-hydroxysuccinimide (NHS) (5 eq, 29.9 mg) were added, and the solution was stirred for 2 h at RT. PLA_{10k}-PEG_{5k}-NH₂ (1 eq, 800 mg) was dissolved in 2 mL anhydrous DMF and *N,N*-diisopropylethylamine (DIPEA) (17.5 eq, 179 μL) was added. The polymer solution was added dropwise to the ligand solution and stirred for further 24 h at RT.

The reaction mixture was precipitated in a mixture of ice-cold methanol and diethyl ether (1:15 v/v, 100 mL) and centrifuged at 3000 g for 15 min at 4 °C. The reaction product was dried overnight under nitrogen flow. The dried solid was dissolved in 2 mL acetonitrile (ACN) and added dropwise into vigorously stirring millipore water (20 mL). The resulting polymer micelles were stirred for 3 h at RT. The solution was dialyzed in 4 L millipore water using a 6-8 kDa molecular weight cut-off dialysis tube for 24 h (with medium change after 30 min, 2 h, and 6 h) to remove uncoupled ligand and reagents. The purified polymer solution was freeze-dried for 3 days.

For the synthesis of PLA_{10k}-PEG_{2k}-cRGD, the polymer PLA_{10k}-PEG_{2k}-COOH (1 eq, 250 mg) was dissolved in 5 mL DMF. EDC (25 eq, 100 mg) and NHS (25 eq, 60 mg) were added and the solution was stirred at RT for 2 h. The excess of EDC was quenched by the addition of β-mercaptoethanol (35 eq). The reaction mixture was stirred for 15 min before the ligand cRGD

Adenovirus-mimetic Nanoparticles in Renal Target Tissue

(3 eq, 37.9 mg) and DIPEA (10 eq, 35.6 μ L) were added and the solution was left to stir for further 24 h. The reaction product was precipitated into a mixture of ice-cold methanol and diethyl ether (1:15 v/v, 100 mL) and centrifuged at 3000 g for 15 min at 4 °C. The supernatant was decanted and the reaction product was dried under nitrogen flow overnight at RT. The dried solid was dissolved in a mixture of dimethyl sulfoxide (DMSO) and ACN (1:10 v/v, 2 mL), and the solution was added dropwise into vigorously stirring millipore water (20 mL). The resulting polymer micelles were purified and freeze-dried analogously to the coupling of EXP. For polymer synthesis, modification, and characterization refer to the supporting information (Supporting Information, Chapter 1-3).

2.4 Quantification of EXP-3174

Inverse quantification of EXP-3174 bound to the PLA_{10k}-PEG_{5k}-NH₂ polymer was performed by detecting primary amines of the unreacted polymer according to Udenfriend et al. (1972) [30]. The modified polymer was solved in 400 μ L ACN to a concentration of 10 mg/mL, added dropwise into 4 mL vigorously stirring millipore water, and stirred for 3 h at RT. For calibration, micelles with different ratios of amine- (representing unreacted) and carboxy-terminated (representing EXP-modified) polymer were prepared. 170 μ L borate buffer pH 8.5 was added into a white 96-well plate, followed by 10 μ L of the polymer micelle solution, and the mixture was shaken for 5 min at RT at 150 rpm. Subsequently, 20 μ L of a fluorescamine solution in ACN at a concentration of 0.3 mg/mL was added to the samples, and the plate was shaken for 15 min at RT at 150 rpm. The fluorescence was measured using a FluoStar Omega fluorescence microplate reader (BMG Labtech, Ortenberg, Germany) with an excitation wavelength of 390 nm and an emission wavelength of 475 nm. The degree of modification was determined and considered for particle preparation (Fig. S5).

2.5 Quantification of cRGDfK

The percentage of polymer which was successfully modified with cRGD was determined using a previously described method based on the quantification of arginine [31]. For this purpose, PLA_{10k}-PEG_{2k}-cRGD was dissolved in ACN to a concentration of 10 mg/mL, and 400 μ L of the polymer solution was added dropwise into 4 mL vigorously stirring millipore water. The micelles were stirred for 3 h under the fume hood to evaporate the organic solvent. For the

Chapter 3

quantification of the modified polymer, a calibration curve was recorded using unmodified polymer micelles with additives of free cRGD. 250 μ L of polymer micelle samples were mixed with 875 μ L of a working solution consisting of 9,10-phenanthrene quinone (150 μ M in ethanol) and 2 N NaOH (6:1 v/v) in an Eppendorf cup. After an incubation period of 3 h at 60 °C, the reaction mixture was transferred to a black 96-well plate and diluted with 1 N hydrochloric acid (HCl) in a ratio of 1:1 v/v. After incubation for 1 h at RT the fluorescence was measured at a Synergy Neo2 Multi-Mode Microplate Reader (BioTek Instrument Inc., Winooski, VT, USA) with an excitation wavelength of 312/7 nm and an emission wavelength of 395/7 nm. The degree of modification was determined and considered for particle preparation (Fig. S5).

2.6 Nanoparticle Preparation and Encapsulation of Erastin

The structure of the adenovirus-mimetic nanoparticles used as drug carrier was previously developed by our group [12]. Slight modifications in the polymer synthesis, characterization, and fluorogenic labeling of the nanoparticles were implemented to optimize drug encapsulation and nanoparticle detection *in vivo*. Ester terminated 13.4 kDa poly(lactic-co-glycolic acid) (PLGA), constituting the NP core, and the previously described PLA-PEG block-copolymers were mixed at a 30:70 mass ratio to a final concentration of 10 mg/mL in acetonitrile (ACN). The nanoparticles were prepared according to Fleischmann et al. (2020) [21] with 15 % cRGD on short polymer chains (PLA_{10k}-PEG_{2k}) and 25 % EXP-modified long polymer chains (PLA_{10k}-PEG_{5k}). The remaining nanoparticle surface was packed with unmodified PLA_{10k}-PEG_{5k}-COOH polymer chains as spacers. NPs were prepared via bulk nanoprecipitation. For the encapsulation of erastin, the drug was dissolved in ACN (10 mg/mL) and added to the organic, polymer-containing solution. The prepared polymer/erastin mixtures with polymer concentrations of 10 mg/mL and the erastin quantity specified in the corresponding experiments were added dropwise into a 10-fold excess of vigorously stirring millipore water, 10 % Dulbecco's phosphate buffered saline pH 7.4 (PBS), or 100 % PBS to a final polymer concentration of 1 mg/mL. To maximize the amount of encapsulated erastin, different drug to polymer ratios were used during particle preparation. The free erastin was separated from the prepared nanoparticles via SEC with agarose beads as column material, which was coupled to dynamic light scattering (DLS) for the detection of the eluted substances (Fig. S9). The prepared nanoparticles were analyzed for particle stability using

Adenovirus-mimetic Nanoparticles in Renal Target Tissue

DLS (Fig. S8). Furthermore, the encapsulation efficiency (EE) and the loading capacity (LC) of the particles were determined. A detailed description is provided in the supporting information (Chapter 9).

2.7 Nanoparticle Characterization and Determination of NP Concentration

The PDI and the zeta potential of the NPs were analyzed using a Malvern Zetasizer Nano ZS (Malvern, UK). The samples were analyzed with a 633 nm He-Ne laser at an angle of 173° at RT. Nanoparticle size and concentration were determined using nanoparticle tracking analysis (NanoSight NS300, Malvern, UK). Prior to measurement, the particles were diluted with millipore water to a concentration of particles per frame between 20 and 100.

2.8 Fluorescent Labeling of Nanoparticles

The fluorescent labeling of the nanoparticles was performed according to Walter et al. (2023) [14]. Carboxy-terminated PLGA was covalently linked to the fluorescent dye Cyanine5 (Cy5) to label the nanoparticle core. Therefore, carboxylic acid-terminated PLGA (1 eq), Cyanine5 amine (0.1 eq), and 3-[bis(dimethylamino)methyl]imidazol-2-yl-hexafluorophosphat (HBTU) (2 eq) were dissolved in the smallest possible amount of DMF. *N,N*-diisopropylethylamin (DIPEA) (4 eq) was added and the reaction mixture was stirred overnight at RT. Subsequently, the reaction product was precipitated in 100 mL ice-cold diethyl ether and centrifuged at 3000 g for 15 min. The supernatant was decanted, and the residue was dried under nitrogen flow. The dried precipitate was taken up in acetonitrile and the precipitation process was repeated three times as already described or at least until the supernatant was no longer bluish in color. The product was dried overnight under nitrogen. The labeled polymer was used as a replacement of plain PLGA in the preparation of fluorescent nanoparticles.

2.9 Concentration of Nanoparticles and Quantification of Encapsulated Molecules per Particle

To upscale particle concentration for *in vitro* and *in vivo* experiments, the prepared nanoparticles were concentrated and purified from free erastin using ultracentrifugal filters with a molecular

Chapter 3

weight cut-off of 100 kDa at 3000 g to separate free erastin. The centrifugation time varied between encapsulation and cell experiments (20 min) and NP preparation for *in vivo* studies (4 h). In order to avoid any entrainment, the nanoparticles were additionally purified by two washing steps with PBS before analysis or usage. After nanoparticle concentration and purification, the particle concentration was determined, and a defined number of nanoparticles was lyophilized for three days. The freeze-dried product was dissolved in DMSO and analyzed via high-performance liquid chromatography (HPLC) using a Phenomenex Gemini 3 μ M NX C18 110 \AA column (size 150 x 4.6 mm) (Phenomenex, Aschaffenburg, Germany) at an oven temperature of 40 $^{\circ}$ C during analysis. As a mobile phase, 0.05 % trifluoroacetic acid (TFA) in millipore water and 0.05 % TFA in acetonitrile were used. Absorbance was detected at 220 nm. The following linear gradient was applied: acetonitrile/TFA (0.05 %) (v/v) 0 min: 10:90, 25 min: 95:5; flow rate: 1.0 mL/min. The injection volume was 5 μ L. Erastin showed a constant retention time of 12.4 min.

2.10 Cell Culture

For cell culture experiments SV40MES13 (ATCC, CRL-1927) cells, which were stably expressing Cas9 after lentiviral transduction, were used. LentiCas9-Blast was a gift from Feng Zhang (Addgene viral prep # 52962-LV; <http://n2t.net/addgene:52692>, RRID:Addgene_52962) [32]. They were cultured in a mixture of DMEM and Ham's F-12 medium in a ratio of 3:1 to which HEPES was additionally added to a concentration of 14 mM and penicillin streptomycin solution (pen-strep) to a concentration of 100 U/mL. For the cultivation of the cells, 10 % fetal bovine serum (FBS) was added to the medium.

2.11 Cell Cytotoxicity Test

For cell death studies 20,000 cells/well were seeded in a 96-well plate. After an incubation period of 24 h at 37 $^{\circ}$ C the cell medium was aspirated, and the cells were washed with prewarmed PBS. Different amounts of free erastin or nanoparticles, respectively, were added to the cells and incubated as indicated. Afterward, the samples were aspirated and 100 μ L of MTT working reagent was added to the wells. For the preparation of MTT working reagent 3-(4,5-dimethylthiazol-2-yl)-2,5-diphenyltetrazoliumbromid was solved in a concentration of 1 mg/mL in cell culture medium. The cells were incubated for 3 h before the MTT solution was

Adenovirus-mimetic Nanoparticles in Renal Target Tissue

aspirated and 100 μ L of isopropanol was added. The 96-well plate was then sealed and incubated in the dark until all violet crystals were solved for at least 60 min. For the evaluation of the cell death assay the absorptions at 570 and 690 nm were measured at a Synergy Neo2 Multi-Mode Microplate Reader (Biotek Instrument Inc., Winooski, VT, USA). For cell viability, the difference in absorbance was evaluated and the results were normalized to untreated cells. Since free erastin was dissolved in DMSO due to its solubility and diluted with cell culture medium, the maximal applicable DMSO concentration without causing cell damage was determined in a preliminary experiment to exclude falsification of the results due to cell death triggered by DMSO (Fig. S15). Therefore, the maximum amount of DMSO was limited to 0.5 %.

2.12 Confocal Scanning Microscopy (CLSM) Analysis

To confirm the results determined via the MTT assay, CLSM experiments were performed. 6,500 cells/well were seeded in an 8-well Ibidi-slide and incubated for 24 h at 37 °C. The samples were added and incubated for further 16 h at 37 °C. Free erastin was used at a concentration of 300 nM, and the nanoparticles, prepared in millipore water, were utilized at a concentration of 51.3 pM, which corresponds to the equivalent amount of erastin. Cell medium without any additives served as blank. Nanoparticles without erastin encapsulated served as negative control. Subsequently, the cells were washed with 200 μ L PBS. 250 μ L of calcein-AM working reagent was added to the wells and incubated for 30 min at 37 °C. The calcein working reagent was prepared by solving 50 μ g calcein AM in 80 μ L DMSO and diluting 1:10,000 with DMEM medium without FBS. The supernatant was removed and 250 μ L Leibovitz medium (LM) were added. Immediately before microscopy, propidium iodide (PI) was added at a concentration of 2 μ g/mL in LM. CLSM was performed using a Zeiss LSM 710 (Carl Zeiss, Microscopy GmbH, Jena, Germany). Images were analyzed using ZEN 3.5 (blue edition) software.

2.13 Animals

Eight-week-old male C57BL/6 (Janvier Labs) mice were used in the experiments. Animals were housed at constant temperature and humidity, and with a 12:12 hour light-dark cycle. Mice had access to water and food ad libitum. All animal experiments were performed in accordance with

Chapter 3

the Federal Law on the Use of Experimental Animals in Germany and were approved by the local authorities (Landesdirektion Sachsen). Animal experiments were consistent with the National Institutes of Health (NIH) Guide for the Care and Use of Laboratory Animals (NIH Pub. No. 85-23, Revised 2011).

2.14 Intravital Microscopy

For intravital microscopy, C57BL/6 mice were anesthetized (2.5 % isoflurane, 0.8 L/min, Baxter, Unterschleißheim, Germany) and the abdominal body window was implanted for repeated kidney imaging [33]. The next day, the mouse was anesthetized and prepared for imaging with an upright Leica SP8 multiphoton laser scanning microscope as previously described [34]. Multiphoton imaging was performed with 860 to 910 nm laser excitation to visualize Cy5-labeled nanoparticles or fluorescein isothiocyanate (FITC)-conjugated dextran (150 kDa), respectively. Nanoparticle distribution was observed every half hour for 3 h immediately after injection and a second time 24 h after the first injection.

2.15 Experimental Setup

50 µL of a solution with erastin-loaded nanoparticles in a particle concentration of 174 nM, which corresponds to an erastin concentration of approximately 3 mM, were intravenously administered to the animals. Control animals received the same amount of erastin-free nanoparticles. Six days after nanoparticle injection, an unilateral nephrectomy was performed as previously described [35]. In brief, the mice were anaesthetized (2.5 % isoflurane (Baxter, Unterschleißheim, Germany) and the flank was opened to perform a ligature at the renal hylus. After separation of the kidney from the hilum, the kidney was removed, and the wound sutured. Analgetics were applied intraoperatively (0.05 mg/kg buprenorphine). 10 days after the nanoparticle injection, mice were euthanized under ketamine/xylazine anesthesia. Prior to kidney harvest, the mice were perfused with isotonic 0.9 % saline. The kidneys were cut in half and one part was fixed in zinc fixative (0.5 g calcium acetate, 5 g zinc acetate, 5 g zinc chloride dissolved in 0.1 M TRIS-buffered solution (pH 7.4)) overnight with subsequent paraffin embedding. The other half was fixed in 4 % paraformaldehyde/PBS overnight, transferred to 18 % sucrose/PBS overnight, and embedded in TissueTeK (ThermoFisher, Waltham, MA, USA) on dry ice.

2.16 Immunostaining of Histological Sections

For immunofluorescent staining, antigen-retrieval was performed on frozen sections (6 μ m) by boiling the sections in tris-EDTA buffer (pH 8.8) for 5 min. The sections were permeabilized for 10 min at RT using 0.5 % Triton-X100 and blocked with 5 % normal donkey serum for 30 min at RT. The sections were stained with primary antibodies overnight at 4 °C. Secondary antibodies were incubated for 2 h at RT. As primary antibodies alpha-8-integrin (R&D systems, #AF4076) and anti-NPHS2 (Abcam, #ab50339) were used. 555-labeled anti-goat (Invitrogen, #A-21432) and 488-labeled anti-rabbit (Thermo-Fisher, #A-21206) were used as secondary antibodies. The sections were counterstained with the nuclear marker DAPI. Confocal microscopy for representative images was performed with the Zeiss Observer Z.1 with an ApoTome as previously described [35,36]. For periodic acid-schiff (PAS)-staining, paraffin-embedded kidneys were cut into 2 μ m sections, deparaffinized, rehydrated and stained with PAS reagent. Sections were counterstained with hematoxylin.

2.17 Statistics

Statistical analysis was performed using Graphpad Prism Software 8.3.0. One-way ANOVA with a Tukey's multiple comparisons test (Fig. 3) or two-way ANOVA with a Sidak's multiple comparisons test (Fig. 4) was performed for statistical evaluation of significance. The number of performed experiments (n) and the resulting significance levels are indicated in the figure legends.

Chapter 3

3 Results

3.1 Preparation and Characterization of Drug-Loaded Adenovirus-Mimetic Nanoparticles for Mesangial Cell Targeting

As demonstrated by DLS and NTA measurements, we were able to prepare nanoparticles in good agreement with the data previously published by our work group (c7) [12].

Increasing erastin to polymer ratios were evaluated to achieve maximal drug encapsulation while maintaining particle stability. PDI and particle size characterization via DLS measurements showed a maximally applicable amount of 25 nmol erastin / mg polymer (Fig. S8). To ensure that this ratio corresponds to the maximal amount of erastin encapsulated, the encapsulation efficiency and the loading capacity of the nanoparticles were evaluated via HPLC (Fig. 3A-B, Fig. S10). EE and LC both showed a maximum for 25 nmol erastin / mg polymer (Fig. S11), which was in line with the maximally applicable amount and, therefore, this ratio was used for all further experiments.

Furthermore, the impact of the composition of the aqueous phase during particle preparation as well as particle labeling with Cy5 on drug encapsulation was analyzed. While particle labeling had no significant effect on the amount of active ingredient encapsulated, changing the aqueous phase from deionized water to PBS showed a major impact. The increased salt content during nanoparticle preparation led to a strong increase of the average encapsulated number of molecules per particle from 3555 (\pm 988) to 16742 (\pm 1854) (Fig. 3C). It was shown previously that increasing the core component PLGA compared to the shell component PLA-PEG may have beneficial effects on the EE of drugs [37,38]. However, for the encapsulation of erastin, rising PLGA concentrations led to a decrease in the amount of encapsulated drug and an increase in nanoparticle size (Fig. S13). Figure 3D summarizes our findings with respect to the EE. To maximize the amount of encapsulated erastin, a core-to-shell polymer ratio of 30:70 was used, and for *in vivo* experiments, the nanoparticle preparation was performed in PBS.

Finally, particle stability and the stability of the fluorescent labeling were examined to ensure that neither particle aggregation nor release of Cy5 could distort the study of the *in vivo* particle residence time. Since no changes could be detected for one week (Fig. S14), we concluded that the particles were stable enough to be used in the subsequent experiments.

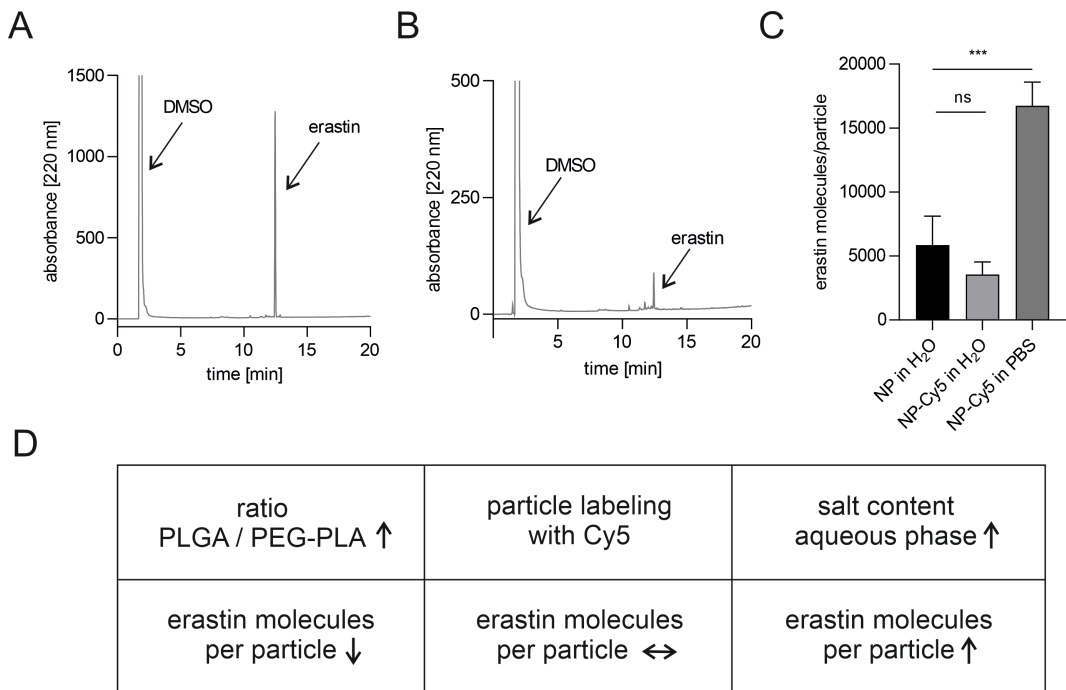


Figure 3. Determination of the amount of encapsulated erasin molecules per particle by HPLC and the influence of various preparation parameters. (A) HPLC chromatogram of free erasin. **(B)** HPLC chromatogram of freeze-dried and solubilized nanoparticles (Supporting Information, Chapter 10). **(C)** Comparison of the encapsulated drug amount after preparation in different aqueous phases and the impact of particle labeling. **(D)** Summary of the impact of particle preparation parameters on drug encapsulation. Results represent mean \pm SD ($n = 3$, levels of statistical significance are indicated as * $p \leq 0.05$, ** $p \leq 0.01$, *** $p \leq 0.001$, **** $p \leq 0.0001$).

3.2 Investigation of Ferroptosis Induction *In Vitro*

To demonstrate that a sufficient amount of drug could be encapsulated and that its application *in vivo* may cause ferroptosis, cytotoxic efficacy was tested *in vitro* using the mesangial cell line SV40MES13. MTT assays were performed to detect the resulting cytotoxicity triggered by erasin, as already described in literature [23,39,40].

Both drug-loaded adenovirus-mimetic nanoparticles and free erasin showed a concentration- and time-dependent cytotoxic response. 10 nM erasin solutions caused cytotoxic effects that could be detected after 8 h, which increased with higher erasin concentrations and incubation times (Fig. 4A). Even after a longer incubation period of up to 72 h, lower concentrations of erasin showed no cytotoxicity and cell viability remained at the level of untreated cells (Fig. 4B).

Chapter 3

The effect of drug-loaded nanoparticles, the erastin content of which was identical to the free active ingredient, was in a similar range after 10 h but occurred significantly earlier. Already after an incubation time of 4 h, a decrease in cell viability could be detected, and the difference became significant after 6 h (Fig. 4C-D). The biocompatibility of the carrier system was already demonstrated in a previous study after DIN EN ISO 10993-5:2009 with L929 cells [21], and was additionally evaluated with the mesangial cell line SV40MES13. Nanoparticles without encapsulated drug showed no or at most weak time-independent cytotoxic properties (Fig. 4E-F). Thus, the occurring cell death after treatment with erastin-loaded particles was clearly attributable to the nanoparticle cargo.

The cytotoxic properties were also confirmed by confocal scanning microscopy (Fig. 5). For this purpose, cell viability was compared after treatment with free erastin, erastin-loaded nanoparticles, or drug-free control nanoparticles, respectively, after 16 h. The treatment with control particles did not lead to any morphological changes compared to untreated cells. Furthermore, the viability staining with calcein and PI showed that the cells were calcein positive, which indicates enzymatic activity of living cells [41] and PI negative, which would stain dead cells [41]. Therefore, the control nanoparticles showed no detectable cytotoxic effects and served as negative control, which is in line with previous data on the biocompatibility of the adenovirus-mimetic particles [12]. The erastin-treated cells, in contrast, showed a spherical shape and were PI positive. The drug loaded nanoparticles exhibited a similar effect to free erastin, although a tendency towards stronger residual staining with calcein-AM was observed after treatment with free erastin. This was consistent with the MTT assay results, which showed a slower onset of cytotoxic effects for the free drug compared to erastin-loaded nanoparticles. Nevertheless, it should be noted that the quantitative survival rates determined by MTT and CLSM cannot be directly compared, since cytotoxicity is also related to cell density (Fig. S16). In conclusion, it was confirmed that a sufficient amount of erastin was encapsulated to generate a biological effect *in vitro*, suggesting that ferroptosis induction may also be possible *in vivo*.

Adenovirus-mimetic Nanoparticles in Renal Target Tissue

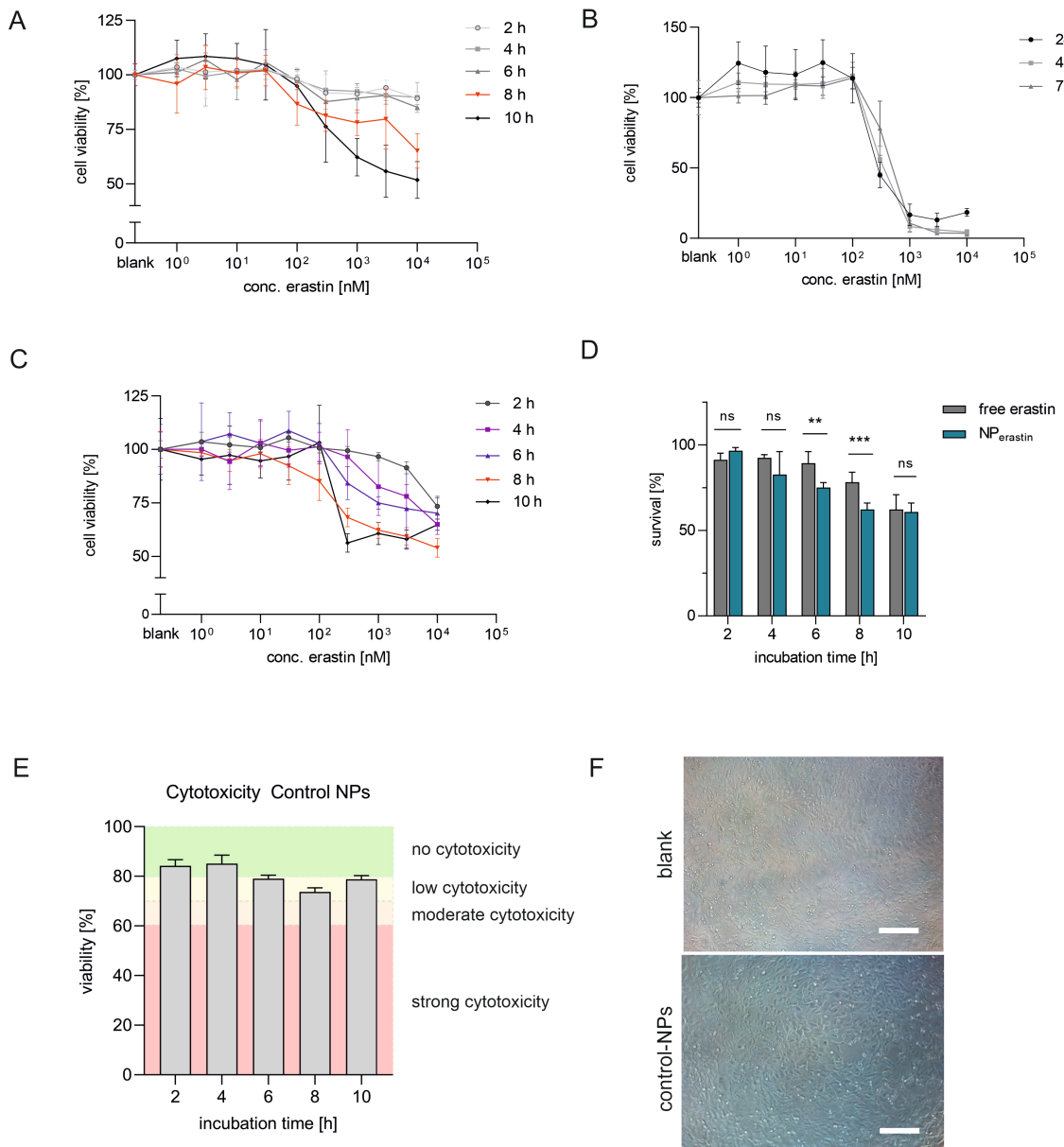


Figure 4. Biological effect of erastin-loaded nanoparticles *in vitro* via MTT-assay. (A) Effect of free erastin over 10 h of incubation. (B) Effect of free erastin for 24 to 72 h. (C) Effect of erastin-loaded NPs, concentrations represent the amount of encapsulated erastin. (D) Comparison of the effect of free and encapsulated erastin in a concentration of 1 μ M. (E) Evaluation of the cytotoxicity of drug-free control NPs (NP concentration corresponding to the NP concentration analyzed in Fig. 4D, 171 pM). (F) Evaluation of cell morphology after 10 h incubation with control-NPs or cell culture medium (blank) using transmitted light microscopy to detect cytotoxicity-dependent changes. Scale bar: 200 μ m. Results represent mean \pm SD ($n \geq 3$, levels of statistical significance are indicated as * $p \leq 0.05$, ** $p \leq 0.01$, *** $p \leq 0.001$, **** $p \leq 0.0001$).

Chapter 3

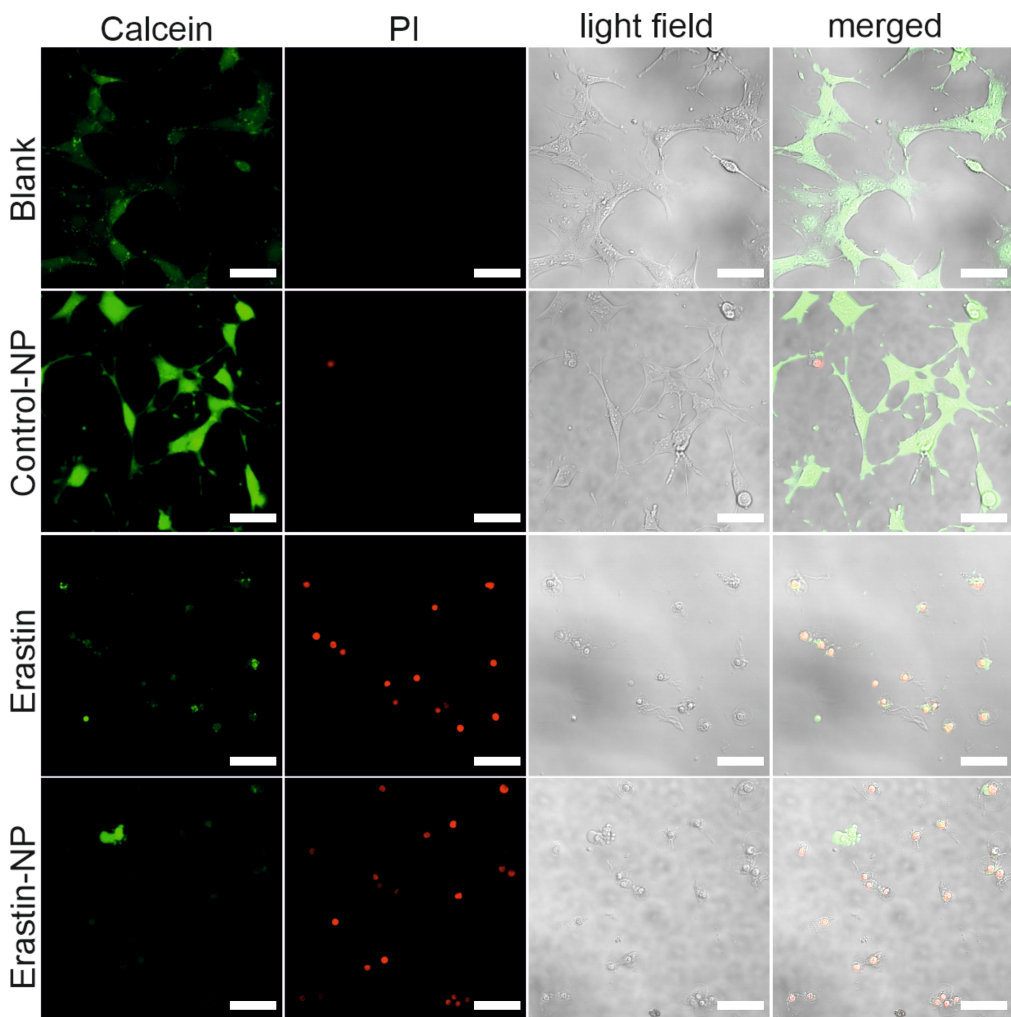


Figure 5. CLSM image of viability staining of SV40MES13 cells after treatment with erastin-loaded nanoparticles. The viability of the cells was examined after 16 h of treatment with free erastin or erastin-loaded adenovirus mimetic nanoparticles. Calcein stains living cells with esterase activity, while PI labels dead cells. Cells without treatment and treatment with control nanoparticles without erastin served as negative controls and did not show cytotoxicity, while both free erastin and erastin-loaded nanoparticles had a strong cytotoxic effect due to the ferroptosis induction. Scale bar: 50 μ m.

3.3 Nanoparticle Distribution and Residence Time *In Vivo*

As the adenovirus-mimetic nanoparticles are intended to serve as a variable, targeted drug delivery platform to the glomerular mesangium, the distribution and accumulation of drug-free particles in the target tissue was monitored by intravital microscopy (Fig. 6). Directly after particle injection, the highest fluorescence was detected in the blood vessels. Thereafter, particle fluorescence gradually decreased over time. After 135 min, the fluorescence had declined

Adenovirus-mimetic Nanoparticles in Renal Target Tissue

substantially, but was still visible. 24 h after injection, there was no residual fluorescence in the blood vessels and the nanoparticles could specifically be detected in the glomeruli.

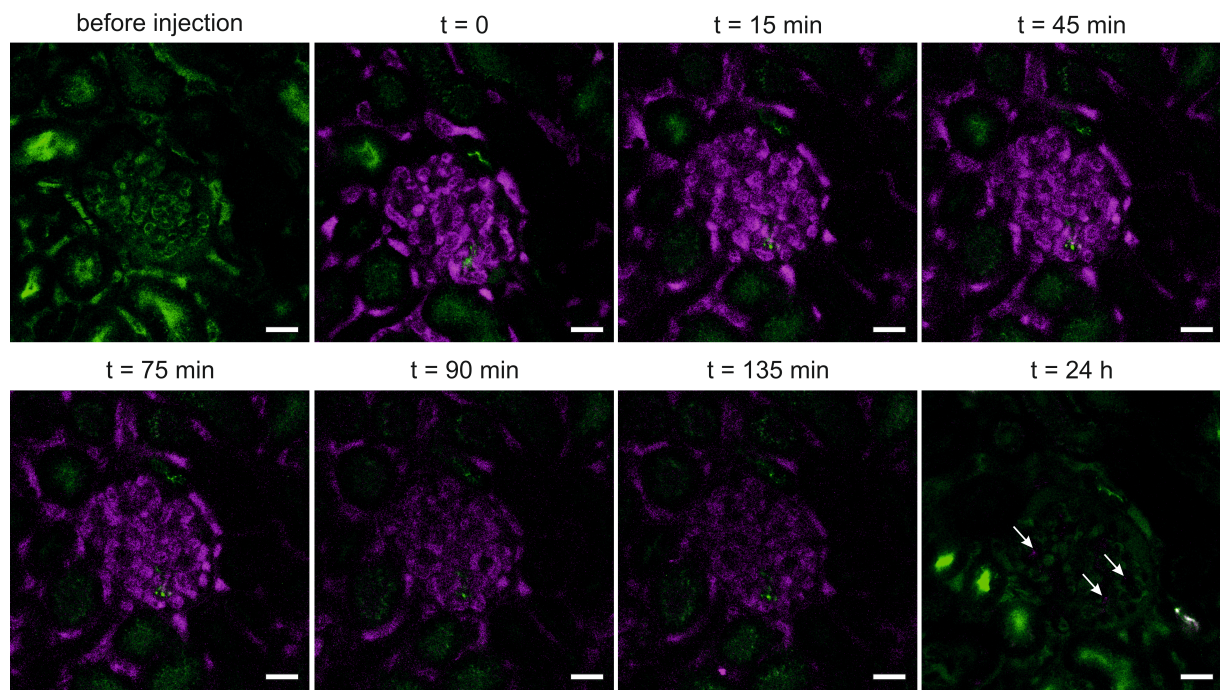


Figure 6. Distribution of nanoparticles *in vivo* via longitudinal intravital microscopy. FITC conjugated dextran (green) was injected to simplify the localization of the glomeruli prior to the injection of the nanoparticles (upper left panel). The distribution of the Cy5-labeled nanoparticles (purple) was observed over 24 h. The arrows indicate the localization of the nanoparticles after 24 h, which had been taken up by glomerular cells. Scale bar: 20 μ m.

As an orthogonal method for intravital microscopy and to enable the study of longer observation periods of particle residence time, immunostaining of histological sections was performed (Fig. 7). The generated kidney sections were stained with antibodies for NPHS2 (podocin), which visualized the glomerular slit membrane and the podocytes [42]. The antibody for α 8-integrin stained membranes of mesangial cells, the target cells of the nanoparticles [43].

After 24 h, the nanoparticles were observed specifically inside mesangial cells, as indicated by the close proximity to the α 8-integrin staining. The particles were visible in the mesangium for up to 10 days after injection.

Chapter 3

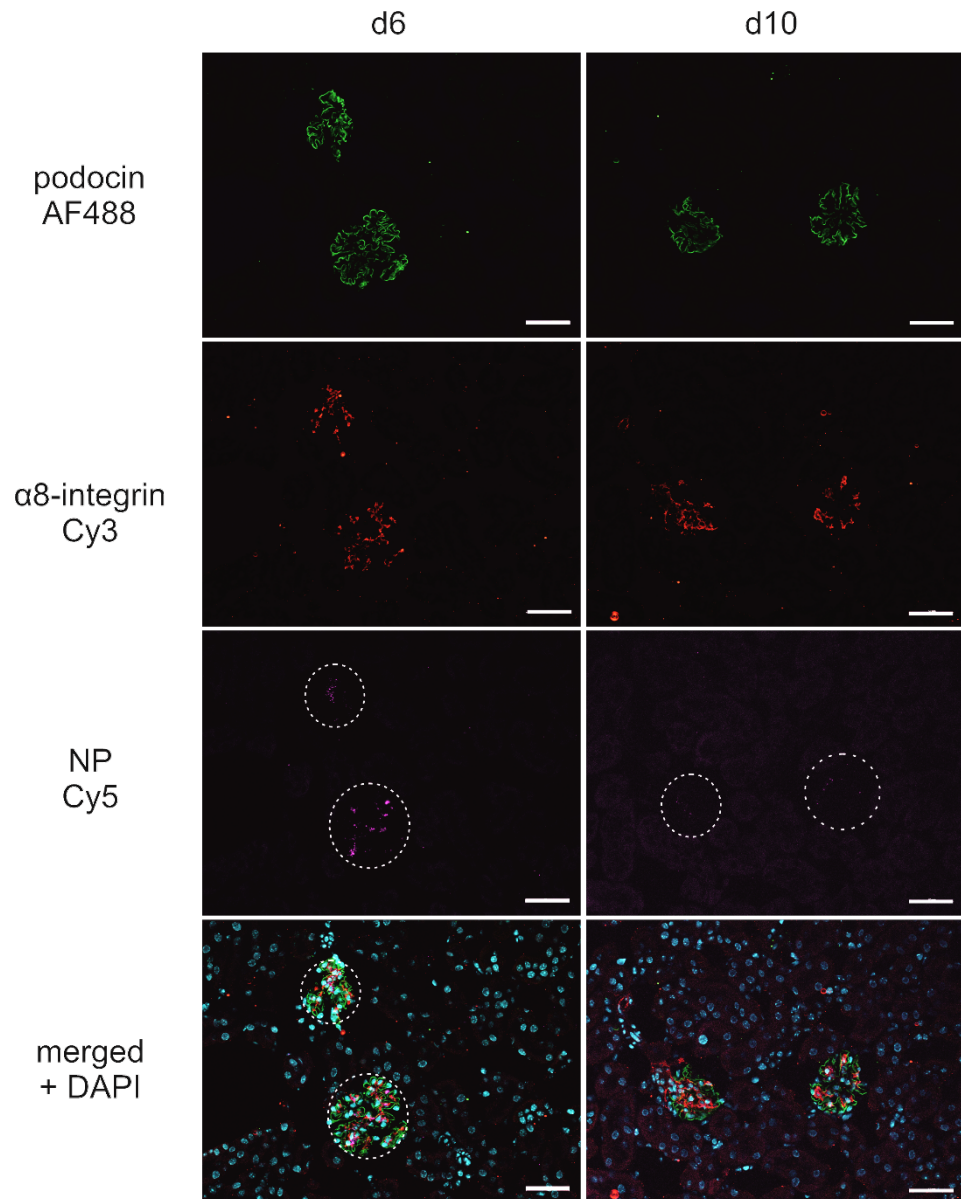


Figure 7. Immunostaining of histological sections. Localization of adenovirus-mimetic nanoparticles without erastin in the mesangium at different time points (day 6 or day 10) after particle injection for the estimation of the particle residence time *in vivo*. The dashed circles represent the location of the glomeruli. Scale bar: 50 μ m.

3.4 Biological Effect Mediated by the Nanoparticle Cargo

10 days after the injection of erastin-loaded particles, structural changes in the tissue of interest were observed. They indicate the induction of ferroptosis in mesangial cells by the release of erastin. At this point in time, several glomeruli showed distinct structural changes compared to the control group without the encapsulated drug (Fig. 8). In addition to an increase of the PAS-positive area inside the glomeruli, an increase of the total glomerular size was observed, and Bowman's capsule was more prominent.

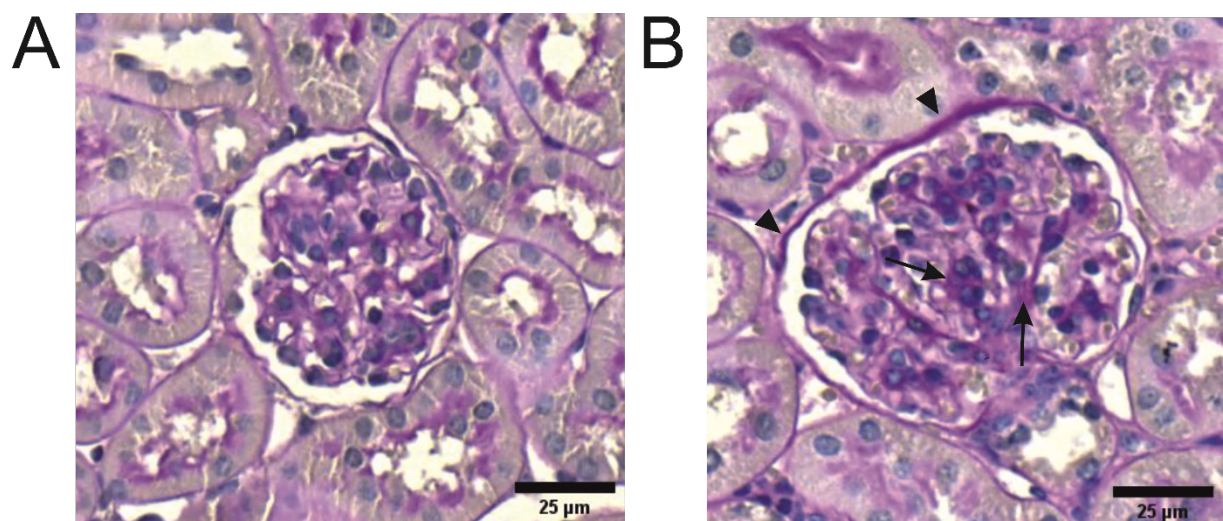


Figure 8. Structural changes in the glomerulus. PAS staining was performed on kidney sections 10 days after the injection of (A) unloaded or (B) erastin-loaded nanoparticles. Erastin-loaded nanoparticles led to a moderate increase in the PAS-positive area (open arrow) and a prominent PAS-positive Bowman's capsule (arrow head).

4. Discussion

The results presented are of relevance for the further development of therapeutics for the treatment of mesangium-associated diseases. The implementation of an actively targeted drug delivery system provides the opportunity to increase the amount of drug transported to the mesangium while minimizing adverse drug effects [44]. Three key factors play a decisive role in the development of a nanoparticle-based therapy: reaching the target site, sufficient particle retention for efficient intracellular drug release, and achieving a biological effect in the target tissue [45,46]. Many studies on actively targeted nanotherapeutics address some of these issues [3,12,47]. However, to offer a clinically applicable therapy option, all three aspects must be considered in combination, which has been a major hurdle to date. Our group previously demonstrated that after extravasation through endothelial fenestrations, adenovirus-mimetic nanoparticles accumulate in significantly higher amounts in mesangial cells than unmodified control particles [12]. However, besides the question of whether the nanoparticles allow sufficient drug transport to the mesangium, it must be clarified if the particle residence time in the target tissue is long enough to release the active substance and achieve sensible application intervals. Both questions have remained unanswered so far since the particle localization was analyzed merely after 60 min and without an encapsulated drug. A closer look into the literature reveals that there is little information available on the nanoparticle residence time in specific target tissues in the living organism, especially after active nanoparticle targeting [48]. Most available studies only describe the half-life in blood circulation [49,50], the residence time on the organ level in general [19,51], or in specific tumor tissues [52], respectively. Furthermore, the *in vivo* observation time is often not longer than 48 h [53,54]. Therefore, the residence time of nanoparticles in cells of non-malignant target tissues is frequently completely unknown. We were successful in the reproducible targeting of mesangial cells and detected intracellular nanoparticles for up to 10 days. Even if the residence time is not necessarily equivalent to the duration of drug release, a long nanoparticle retention time provides the basis for a long-acting therapeutic concept, which is a prerequisite for the applicability of a nanoparticle-based therapeutic approach. Moreover, we reliably encapsulated erastin in the nanoparticle core, which allowed the direct visualization of biological effects due to its ferroptosis-inducing properties *in vitro* and *in vivo* and thus the estimation of the time course of pharmacological effects. Simultaneously, the erastin-loaded nanoparticles may provide the basis for a disease model of mesangial cell-associated diseases and additionally may serve as a new site-specific therapeutic strategy in hypercellular mesangial-proliferative glomerulonephritis. Structural

Adenovirus-mimetic Nanoparticles in Renal Target Tissue

changes were observed in the glomeruli 10 days after the injection of erastin-loaded particles, but not after injection of control particles. This demonstrated that a sufficient drug quantity was delivered to the target tissue to induce a biological effect. This is highly promising, since by adjusting the particle concentrations or application intervals, the mediated effect could be further modified and adapted to different therapy objectives. We consider this finding an initial proof of concept, justifying further research.

Even if promising studies on targeting the glomerulus with nanoparticles are currently available, such as Wu et al. (2021) [55], using peptide-coupled CLT-phospholipid lipid nanoparticles for the targeted delivery of celastrol to the glomerular endothelium, or Li et al. (2019) [47] targeting the glomerular mesangium with targeted PLA-PEG nanoparticles, to our knowledge no study combines successful targeting with the determination of the nanoparticle retention time in the glomerulus and additionally the detection of biological effects *in vivo*.

Chapter 3

5. Conclusion

In this study, we encapsulated the ferroptosis-inducing compound erastin into adenovirus-mimetic nanoparticles, targeting the glomerular mesangium *in vivo*. Intravital microscopy and histological examinations demonstrated the successful accumulation in target cells and proved intracellular particle residence time over the entire investigation period of 10 days. By encapsulating a ferroptosis-inducing compound, we were able to visualize a biological effect induced by the nanoparticle cargo, which provides evidence for successful drug delivery to the target tissue and may serve as a basis for the development of mesangial cell-based disease models or as a site-specific novel therapeutic strategy. Our findings play a crucial role in the development of nanoparticle-based treatment options for mesangial cell-associated diseases and thus contribute to the rationale treatment of diseases such as IgA nephropathy or diabetic nephropathy.

References

- [1] A. Meguid El Nahas, A.K. Bello, Chronic kidney disease: the global challenge, *The Lancet* 365 (2005) 331–340. [https://doi.org/10.1016/S0140-6736\(05\)17789-7](https://doi.org/10.1016/S0140-6736(05)17789-7).
- [2] Y.M. Scindia, U.S. Deshmukh, H. Bagavant, Mesangial pathology in glomerular disease: targets for therapeutic intervention, *Adv. Drug Deliv. Rev.* 62 (2010) 1337–1343. <https://doi.org/10.1016/j.addr.2010.08.011>.
- [3] S. Maslanka Figueroa, D. Fleischmann, S. Beck, P. Tauber, R. Witzgall, F. Schweda, A. Goepferich, Nanoparticles Mimicking Viral Cell Recognition Strategies Are Superior Transporters into Mesangial Cells, *Adv. Sci. (Weinh)* 7 (2020) 1903204. <https://doi.org/10.1002/advs.201903204>.
- [4] S.O. Kolset, F.P. Reinholt, T. Jenssen, Diabetic nephropathy and extracellular matrix, *J. Histochem. Cytochem.* 60 (2012) 976–986. <https://doi.org/10.1369/0022155412465073>.
- [5] S. Dronavalli, I. Duka, G.L. Bakris, The pathogenesis of diabetic nephropathy, *Nat. Clin. Pract. Endocrinol. Metab.* 4 (2008) 444–452. <https://doi.org/10.1038/ncpendmet0894>.
- [6] R.E. Patzer, L.C. Plantinga, S. Paul, J. Gander, J. Krisher, L. Sauls, E.M. Gibney, L. Mulloy, S.O. Pastan, Variation in Dialysis Facility Referral for Kidney Transplantation Among Patients With End-Stage Renal Disease in Georgia, *JAMA* 314 (2015) 582–594. <https://doi.org/10.1001/jama.2015.8897>.
- [7] G. D'AMICO, The Commonest Glomerulonephritis in the World: IgA Nephropathy, *QJM* 64 (1987) 709–727. <https://doi.org/10.1093/oxfordjournals.qjmed.a068143>.
- [8] H.M. Kok, L.L. Falke, R. Goldschmeding, T.Q. Nguyen, Targeting CTGF, EGF and PDGF pathways to prevent progression of kidney disease, *Nature reviews. Nephrology* 10 (2014) 700–711. <https://doi.org/10.1038/nrneph.2014.184>.
- [9] H. Selvaskandan, J. Barratt, C.K. Cheung, Immunological drivers of IgA nephropathy: Exploring the mucosa-kidney link, *Int. J. Immunogenet.* 49 (2022) 8–21. <https://doi.org/10.1111/iji.12561>.
- [10] J. Barratt, J.A. Tumlin, Y. Suzuki, A. Kao, A. Aydemir, Y. Zima, G. Appel, 2020. MO039THE 24-WEEK INTERIM ANALYSIS RESULTS OF A RANDOMIZED, DOUBLE-BLIND, PLACEBO-CONTROLLED PHASE II STUDY OF ATACICEPT IN PATIENTS WITH IGA NEPHROPATHY AND PERSISTENT PROTEINURIA. *Nephrology Dialysis Transplantation* 35, gfaa140.MO039. <https://doi.org/10.1093/ndt/gfaa140.MO039>.

Chapter 3

[11] S. Muro, Challenges in design and characterization of ligand-targeted drug delivery systems, *J. Control. Release* 164 (2012) 125–137. <https://doi.org/10.1016/j.jconrel.2012.05.052>.

[12] D. Fleischmann, S. Maslanka Figueroa, S. Beck, K. Abstiens, R. Witzgall, F. Schweda, P. Tauber, A. Goepferich, Adenovirus-Mimetic Nanoparticles: Sequential Ligand-Receptor Interplay as a Universal Tool for Enhanced In Vitro/In Vivo Cell Identification, *ACS Appl. Mater. Interfaces* 12 (2020) 34689–34702. <https://doi.org/10.1021/acsami.0c10057>.

[13] X. Ma, Y. Xiong, L.T.O. Lee, Application of Nanoparticles for Targeting G Protein-Coupled Receptors, *Int. J. Mol. Sci.* 19 (2018) 2006. <https://doi.org/10.3390/ijms19072006>.

[14] M. Walter, F. Baumann, K. Schorr, A. Goepferich, Ectoenzymes as Promising Cell Identification Structures for the High Avidity Targeting of Polymeric Nanoparticles, *International Journal of Pharmaceutics* (2023) 123453. <https://doi.org/10.1016/j.ijpharm.2023.123453>.

[15] S. Maslanka Figueroa, A. Veser, K. Abstiens, D. Fleischmann, S. Beck, A. Goepferich, Influenza A virus mimetic nanoparticles trigger selective cell uptake, *Proc. Natl. Acad. Sci. U. S. A.* 116 (2019) 9831–9836. <https://doi.org/10.1073/pnas.1902563116>.

[16] G.T. Tietjen, L.G. Bracaglia, W.M. Saltzman, J.S. Pober, Focus on Fundamentals: Achieving Effective Nanoparticle Targeting, *Trends in Molecular Medicine* 24 (2018) 598–606. <https://doi.org/10.1016/j.molmed.2018.05.003>.

[17] Z. Zhao, A. Ukidve, J. Kim, S. Mitragotri, Targeting Strategies for Tissue-Specific Drug Delivery, *Cell* 181 (2020) 151–167. <https://doi.org/10.1016/j.cell.2020.02.001>.

[18] R.S. Kadam, D.W.A. Bourne, U.B. Kompella, Nano-advantage in enhanced drug delivery with biodegradable nanoparticles: contribution of reduced clearance, *Drug Metab. Dispos.* 40 (2012) 1380–1388. <https://doi.org/10.1124/dmd.112.044925>.

[19] J. Madan, R.S. Pandey, V. Jain, O.P. Katare, R. Chandra, A. Katyal, Poly (ethylene)-glycol conjugated solid lipid nanoparticles of noscapine improve biological half-life, brain delivery and efficacy in glioblastoma cells, *Nanomedicine* 9 (2013) 492–503. <https://doi.org/10.1016/j.nano.2012.10.003>.

[20] K.S.S. Lee, J. Yang, J. Niu, C.J. Ng, K.M. Wagner, H. Dong, S.D. Kodani, D. Wan, C. Morisseau, B.D. Hammock, Drug-Target Residence Time Affects in Vivo Target Occupancy through Multiple Pathways, *ACS Central Science* 5 (2019) 1614–1624. <https://doi.org/10.1021/acscentsci.9b00770>.

Adenovirus-mimetic Nanoparticles in Renal Target Tissue

[21] D. Fleischmann, S. Maslanka Figueroa, S. Beck, K. Abstiens, R. Witzgall, F. Schweda, P. Tauber, A. Goepferich, Adenovirus-Mimetic Nanoparticles: Sequential Ligand-Receptor Interplay as a Universal Tool for Enhanced In Vitro/In Vivo Cell Identification, *ACS Appl. Mater. Interfaces* 12 (2020) 34689–34702. <https://doi.org/10.1021/acsami.0c10057>.

[22] S.C. Satchell, F. Braet, Glomerular endothelial cell fenestrations: an integral component of the glomerular filtration barrier, *Am. J. Physiol. Renal Physiol.* 296 (2009) F947-56. <https://doi.org/10.1152/ajprenal.90601.2008>.

[23] Y.-Q. Wang, S.-Y. Chang, Q. Wu, Y.-J. Gou, L. Jia, Y.-M. Cui, P. Yu, Z.-H. Shi, W.-S. Wu, G. Gao, Y.-Z. Chang, The Protective Role of Mitochondrial Ferritin on Erastin-Induced Ferroptosis, *Front. Aging Neurosci.* 8 (2016) 308. <https://doi.org/10.3389/fnagi.2016.00308>.

[24] Y. Zhao, Y. Li, R. Zhang, F. Wang, T. Wang, Y. Jiao, The Role of Erastin in Ferroptosis and Its Prospects in Cancer Therapy, *Onco. Targets. Ther.* 13 (2020) 5429–5441. <https://doi.org/10.2147/OTT.S254995>.

[25] H. Ha, I.-A. Hwang, J.H. Park, H.B. Lee, Role of reactive oxygen species in the pathogenesis of diabetic nephropathy, *Diabetes research and clinical practice* 82 Suppl 1 (2008) S42-5. <https://doi.org/10.1016/j.diabres.2008.09.017>.

[26] S. Fakhruddin, W. Alanazi, K.E. Jackson, Diabetes-Induced Reactive Oxygen Species: Mechanism of Their Generation and Role in Renal Injury, *Journal of Diabetes Research* 2017 (2017) 8379327. <https://doi.org/10.1155/2017/8379327>.

[27] K. Abstiens, Heteromultivalent Nanoparticles for Selective Targeting of Renal Cells, 2020.

[28] H. Qian, A.R. Wohl, J.T. Crow, C.W. Macosko, T.R. Hoye, A Strategy for Control of "Random" Copolymerization of Lactide and Glycolide: Application to Synthesis of PEG-b-PLGA Block Polymers Having Narrow Dispersity, *Macromolecules* 44 (2011) 7132–7140. <https://doi.org/10.1021/ma201169z>.

[29] K. Abstiens, S. Maslanka Figueroa, M. Gregoritza, A.M. Goepferich, Interaction of functionalized nanoparticles with serum proteins and its impact on colloidal stability and cargo leaching, *Soft Matter* 15 (2019) 709–720. <https://doi.org/10.1039/C8SM02189A>.

[30] S. Udenfriend, S. Stein, P. Böhlen, W. Dairman, W. Leimgruber, M. Weigle, Fluorescamine: a reagent for assay of amino acids, peptides, proteins, and primary amines in the picomole range, *Science* 178 (1972) 871–872. <https://doi.org/10.1126/science.178.4063.871>.

[31] N. Graf, D.R. Bielenberg, N. Kolishetti, C. Muus, J. Banyard, O.C. Farokhzad, S.J. Lippard, $\alpha(V)\beta(3)$ integrin-targeted PLGA-PEG nanoparticles for enhanced anti-tumor

Chapter 3

efficacy of a Pt(IV) prodrug, ACS Nano 6 (2012) 4530–4539. <https://doi.org/10.1021/nn301148e>.

[32] N.E. Sanjana, O. Shalem, F. Zhang, Improved vectors and genome-wide libraries for CRISPR screening, Nat Methods 11 (2014) 783–784. <https://doi.org/10.1038/nmeth.3047>.

[33] I.M. Schiessl, K. Fremter, J.L. Burford, H. Castrop, J. Peti-Peterdi, Long-Term Cell Fate Tracking of Individual Renal Cells Using Serial Intravital Microscopy, Methods Mol. Biol. 2150 (2020) 25–44. https://doi.org/10.1007/7651_2019_232.

[34] H. Kroeger, F. Kessel, J. Sradnick, V. Todorov, F. Gembardt, C. Hugo, Intravital imaging of hemodynamic glomerular effects of enalapril or/and empagliflozin in STZ-diabetic mice, Front. Physiol. 13 (2022) 982722. <https://doi.org/10.3389/fphys.2022.982722>.

[35] A. Steglich, F. Kessel, L. Hickmann, M. Gerlach, P. Lachmann, F. Gembardt, M. Lesche, A. Dahl, A. Federlein, F. Schweda, C.P.M. Hugo, V.T. Todorov, Renin cells with defective G_α/cAMP signaling contribute to renal endothelial damage, Pflugers Arch - Eur J Physiol 471 (2019) 1205–1217. <https://doi.org/10.1007/s00424-019-02298-9>.

[36] F. Kessel, A. Steglich, T. Tschongov, F. Gembardt, L. Ruhnke, J. Stumpf, R. Behrendt, C. Cohrs, I. Kopaliani, V. Todorov, M. Gerlach, C. Hugo, New automatic quantification method of immunofluorescence and histochemistry in whole histological sections, Cellular Signalling 62 (2019) 109335. <https://doi.org/10.1016/j.cellsig.2019.05.020>.

[37] D. Fleischmann, M. Harloff, S. Maslanka Figueroa, J. Schlossmann, A. Goepferich, Targeted Delivery of Soluble Guanylate Cyclase (sGC) Activator Cinaciguat to Renal Mesangial Cells via Virus-Mimetic Nanoparticles Potentiates Anti-Fibrotic Effects by cGMP-Mediated Suppression of the TGF-β Pathway, Int. J. Mol. Sci. 22 (2021). <https://doi.org/10.3390/ijms22052557>.

[38] S. Maslanka Figueroa, D. Fleischmann, S. Beck, A. Goepferich, Thermodynamic, Spatial and Methodological Considerations for the Manufacturing of Therapeutic Polymer Nanoparticles, Pharm. Res. 37 (2020) 59. <https://doi.org/10.1007/s11095-020-2783-4>.

[39] H. Huo, Z. Zhou, J. Qin, W. Liu, B. Wang, Y. Gu, Erastin Disrupts Mitochondrial Permeability Transition Pore (mPTP) and Induces Apoptotic Death of Colorectal Cancer Cells, PLoS One 11 (2016) e0154605. <https://doi.org/10.1371/journal.pone.0154605>.

[40] M. Li, X. Wang, S. Lu, C. He, C. Wang, L. Wang, X. Wang, P. Ge, D. Song, Erastin triggers autophagic death of breast cancer cells by increasing intracellular iron levels, Oncol. Lett. 20 (2020) 57. <https://doi.org/10.3892/ol.2020.11918>.

Adenovirus-mimetic Nanoparticles in Renal Target Tissue

[41] S. V S, M. P V, Degradation of Poly(ϵ -caprolactone) and bio-interactions with mouse bone marrow mesenchymal stem cells, *Colloids Surf. B Biointerfaces* 163 (2018) 107–118. <https://doi.org/10.1016/j.colsurfb.2017.12.039>.

[42] S.-Y. Zhang, A. Marlier, O. Gribouval, T. Gilbert, L. Heidet, C. Antignac, M.C. Gubler, In vivo expression of podocyte slit diaphragm-associated proteins in nephrotic patients with NPHS2 mutation, *Kidney international* 66 (2004) 945–954. <https://doi.org/10.1111/j.1523-1755.2004.00840.x>.

[43] B. Bieritz, P. Spessotto, A. Colombatti, A. Jahn, F. Prols, A. Hartner, Role of alpha8 integrin in mesangial cell adhesion, migration, and proliferation, *Kidney international* 64 (2003) 119–127. <https://doi.org/10.1046/j.1523-1755.2003.00057.x>.

[44] H. Tian, T. Zhang, S. Qin, Z. Huang, L. Zhou, J. Shi, E.C. Nice, N. Xie, C. Huang, Z. Shen, Enhancing the therapeutic efficacy of nanoparticles for cancer treatment using versatile targeted strategies, *J Hematol Oncol* 15 (2022) 132. <https://doi.org/10.1186/s13045-022-01320-5>.

[45] R.C. Popescu, D. Savu, I. Dorobantu, B.S. Vasile, H. Hosser, A. Boldeiu, M. Temelie, M. Straticiuc, D.A. Iancu, E. Andronescu, F. Wenz, F.A. Giordano, C. Herskind, M.R. Veldwijk, Efficient uptake and retention of iron oxide-based nanoparticles in HeLa cells leads to an effective intracellular delivery of doxorubicin, *Sci Rep* 10 (2020) 10530. <https://doi.org/10.1038/s41598-020-67207-y>.

[46] J. Yoo, C. Park, G. Yi, D. Lee, H. Koo, Active Targeting Strategies Using Biological Ligands for Nanoparticle Drug Delivery Systems, *Cancers* 11 (2019) 640. <https://doi.org/10.3390/cancers11050640>.

[47] S. Li, Y.-C. Zeng, K. Peng, C. Liu, Z.-R. Zhang, L. Zhang, Design and evaluation of glomerulus mesangium-targeted PEG-PLGA nanoparticles loaded with dexamethasone acetate, *Acta Pharmacol Sin* 40 (2019) 143–150. <https://doi.org/10.1038/s41401-018-0052-4>.

[48] M.M. Nguyen, A.S. Carlini, M.-P. Chien, S. Sonnenberg, C. Luo, R.L. Braden, K.G. Osborn, Y. Li, N.C. Gianneschi, K.L. Christman, Enzyme-Responsive Nanoparticles for Targeted Accumulation and Prolonged Retention in Heart Tissue after Myocardial Infarction, *Advanced Materials* 27 (2015) 5547–5552. <https://doi.org/10.1002/adma.201502003>.

[49] A.G. Próspero, C.C. Quini, A.F. Bakuzis, P. Fidelis-de-Oliveira, G.M. Moretto, F.P.F. Mello, M.F.F. Calabresi, R.V.R. Matos, E.A. Zandoná, N. Zufelato, R.B. Oliveira, J.R.A. Miranda, Real-time in vivo monitoring of magnetic nanoparticles in the bloodstream by

Chapter 3

AC biosusceptometry, *J Nanobiotechnol* 15 (2017) 22. <https://doi.org/10.1186/s12951-017-0257-6>.

[50] N. Hoshyar, S. Gray, H. Han, G. Bao, The effect of nanoparticle size on in vivo pharmacokinetics and cellular interaction, *Nanomedicine (Lond)* 11 (2016) 673–692. <https://doi.org/10.2217/nmm.16.5>.

[51] Q. Li, Z. Yan, F. Li, W. Lu, J. Wang, C. Guo, Corrigendum: The improving effects on hepatic fibrosis of interferon- γ liposomes targeted to hepatic stellate cells, *Nanotechnology* 25 (2014) 79501. <https://doi.org/10.1088/0957-4484/25/7/079501>.

[52] L. Shi, C. Tang, C. Yin, Glycyrrhizin-modified O-carboxymethyl chitosan nanoparticles as drug vehicles targeting hepatocellular carcinoma, *Biomaterials* 33 (2012) 7594–7604. <https://doi.org/10.1016/j.biomaterials.2012.06.072>.

[53] M.M. Khan, A. Madni, V. Torchilin, N. Filipczak, J. Pan, N. Tahir, H. Shah, Lipid-chitosan hybrid nanoparticles for controlled delivery of cisplatin, *Drug Delivery* 26 (2019) 765–772. <https://doi.org/10.1080/10717544.2019.1642420>.

[54] M.K. Anwer, M. Mohammad, E. Ezzeldin, F. Fatima, A. Alalaiwe, M. Iqbal, Preparation of sustained release apremilast-loaded PLGA nanoparticles: in vitro characterization and in vivo pharmacokinetic study in rats, *Int. J. Nanomedicine* 14 (2019) 1587–1595. <https://doi.org/10.2147/IJN.S195048>.

[55] Q. Wu, J. Wang, Y. Wang, L. Xiang, Y. Tan, J. Feng, Z. Zhang, L. Zhang, Targeted delivery of celastrol to glomerular endothelium and podocytes for chronic kidney disease treatment, *Nano Res.* 15 (2022) 3556–3568. <https://doi.org/10.1007/s12274-021-3894-x>.

Adenovirus-mimetic Nanoparticles in Renal Target Tissue

Chapter 3

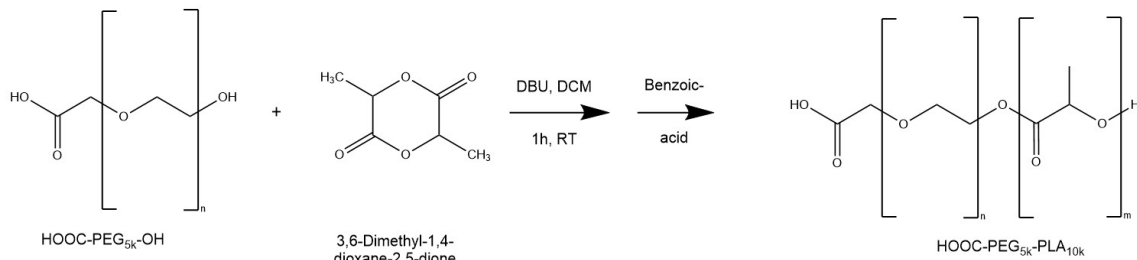
Chapter 3

Supporting Information

Chapter 3 – Supporting Information

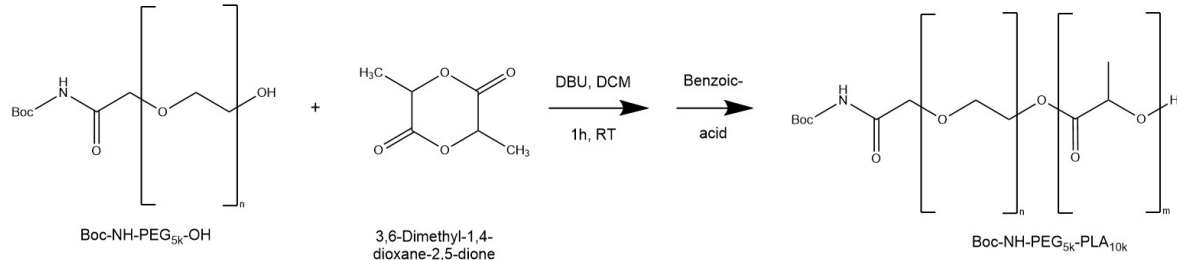
1 Synthesis and Characterization of PLA-PEG Block Copolymers

A

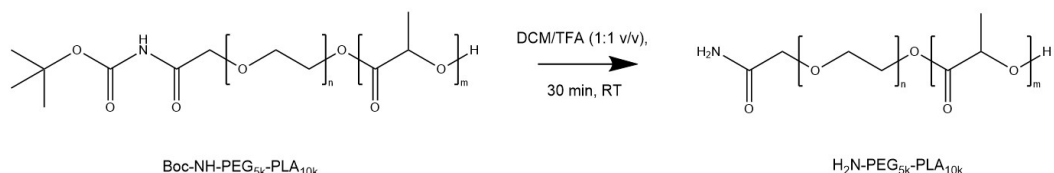


B

1)



2) Boc-deprotection



Scheme S1. Block copolymer synthesis via ring-opening polymerization of cyclic lactide. **(A)** Synthesis of PLA_{10k}-PEG_{2k}-COOH. **(B)** Synthesis of PLA_{10k}-PEG_{5k}-NH-Boc and cleavage of the protection group. For the ring opening polymerization, which was performed in dichloromethane (DCM), OH-PEG_{5k}-NH-Boc or OH-PEG_{2k}-COOH served as a macroinitiator. 1,8-diazabicyclo[5.4.0]undec-7-ene (DBU) was used as a catalyst for the reaction. After 1 h of stirring at RT the reaction was quenched by the addition of benzoic acid. The Boc-protection group of the amino-functionalized polymer was initially cleaved by stirring in a mixture of dichloromethane (DCM) and trifluoroacetic acid (TFA) (1:1 v/v) for 30 min.

Chapter 3 – Supporting Information

^1H -NMR Spectra Polymers

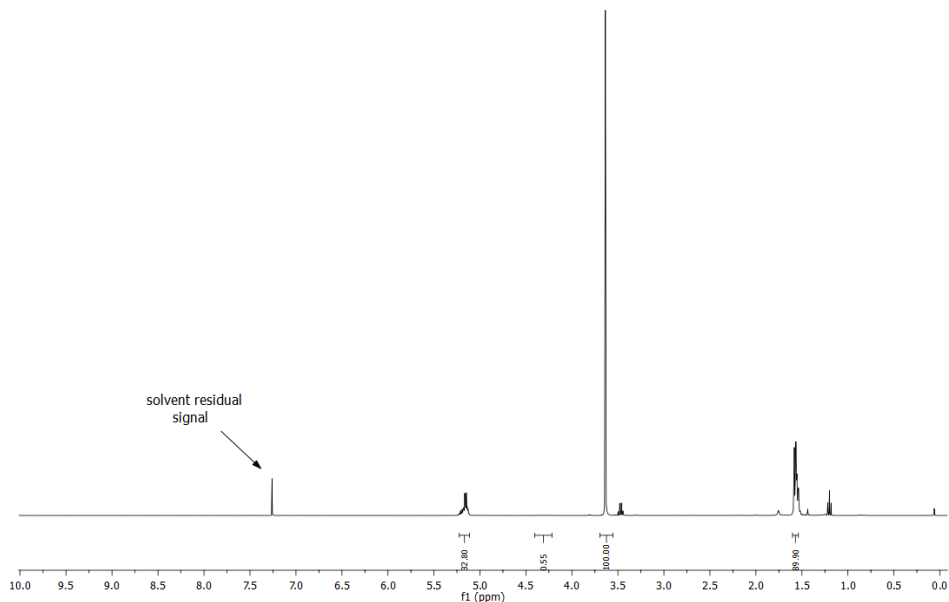


Figure S1. ^1H -NMR spectrum of PLA_{10k}-PEG_{5k}-NH₂. ^1H -NMR (400 MHz, CDCl_3) δ 5.23 – 5.10 (m, 33H) $\text{(-(CH}_3\text{)H-}$; 4.38 – 4.19 (m, 1H), $\text{(-OCH}_2\text{CH}_2\text{-O(CO)-}$); 3.64 (s, 100H), $\text{(-OCH}_2\text{CH}_2\text{-)}$; 1.61 – 1.53 (m, 90H) $\text{(-C(CH}_3\text{)H-}$). PEG (5000 Da) normalized to an integral area of 100. Integrating the PLA peaks resulted in a total molecular weight of the polymer of 15084 Da.

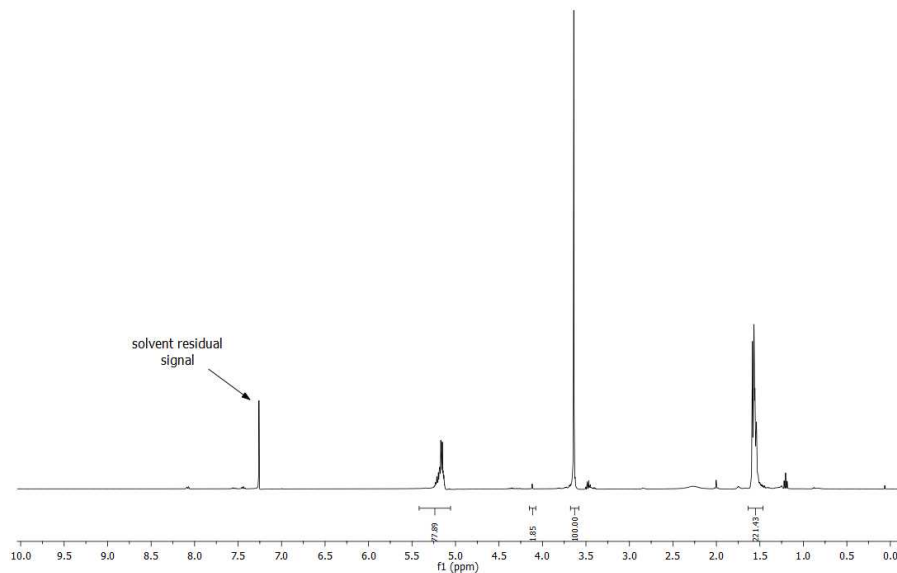
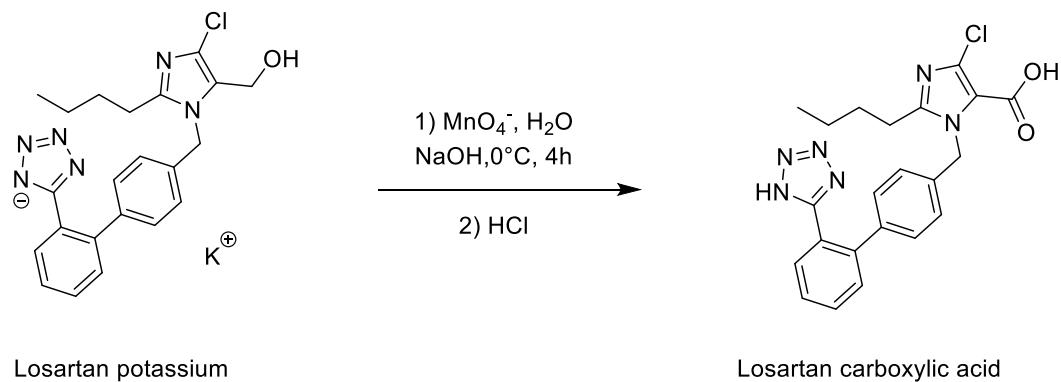


Figure S2. ^1H -NMR spectrum of PLA_{10k}-PEG_{2k}-COOH. ^1H -NMR (400 MHz, CDCl_3) δ 5.39 – 5.06 (m, 78H) $\text{(-(CH}_3\text{)H-}$; 4.13 (s, 4H) $\text{(-OCH}_2\text{CH}_2\text{-O(CO)-}$); 3.64 (s, 100H) $\text{(-OCH}_2\text{CH}_2\text{-)}$; 1.65 – 1.45 (m, 3H) $\text{(-C(CH}_3\text{)H-}$). PEG (2000 Da) signal normalized to an integral area of 100. Integrating the PLA peaks resulted in a total molecular weight of the polymer of 11856 Da.

2 Synthesis EXP-3174



Scheme S2. Synthesis of EXP-3174 via oxidation of losartan potassium.

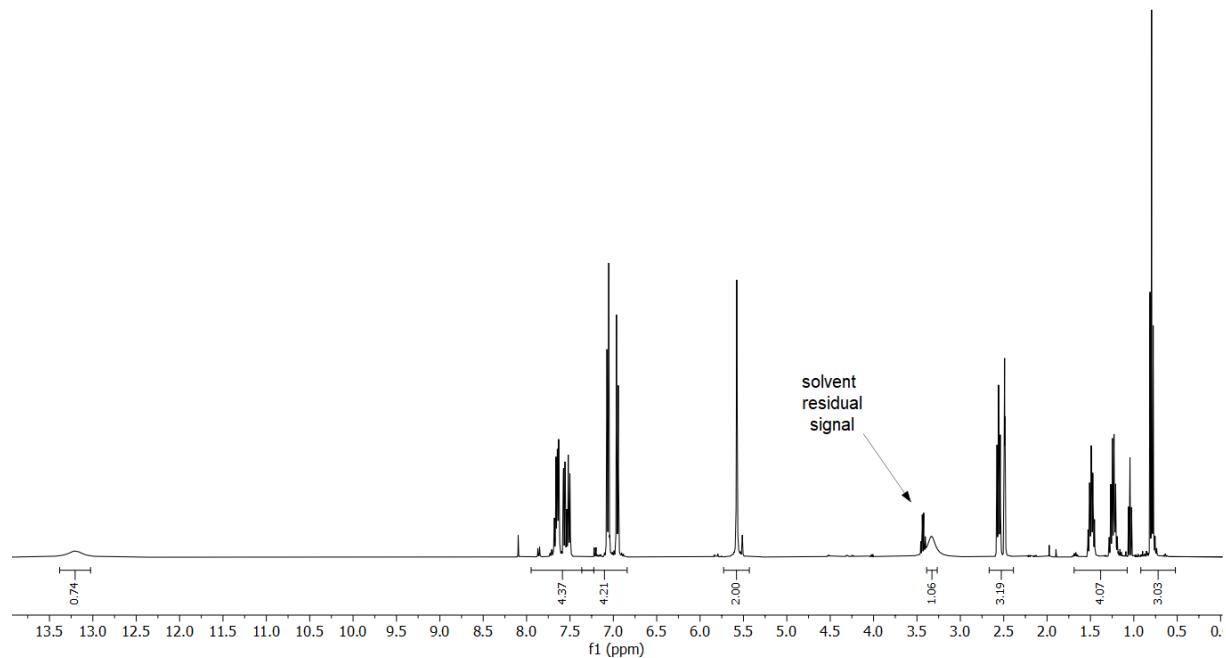
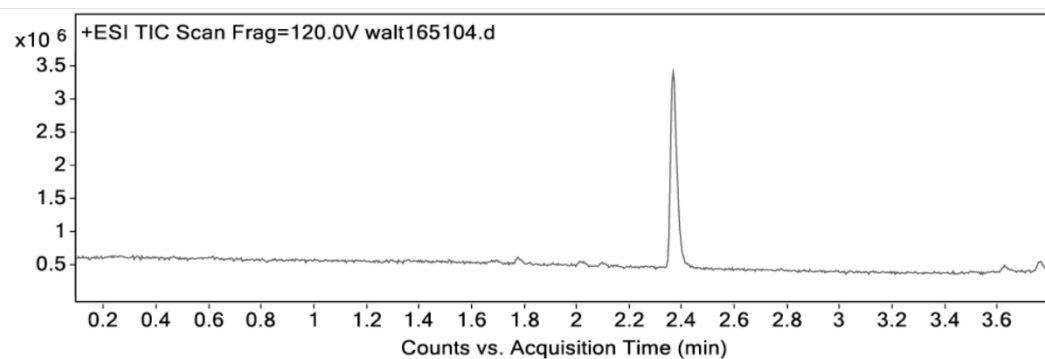


Figure S3. $^1\text{H-NMR}$ spectrum of EXP-3174. $^1\text{H-NMR}$ (400 MHz, DMSO-d6) δ 13.20 (s, 1H), 7.89 – 7.36 (m, 4H), 7.31 – 6.79 (m, 4H), 5.58 (s, 2H), 3.33 (s, 1H), 2.77 – 2.30 (m, 3H), 1.73 – 0.97 (m, 4H), 0.79 (t, J = 7.3 Hz, 3H).

Chapter 3 – Supporting Information

Chromatogramm



Spectrum

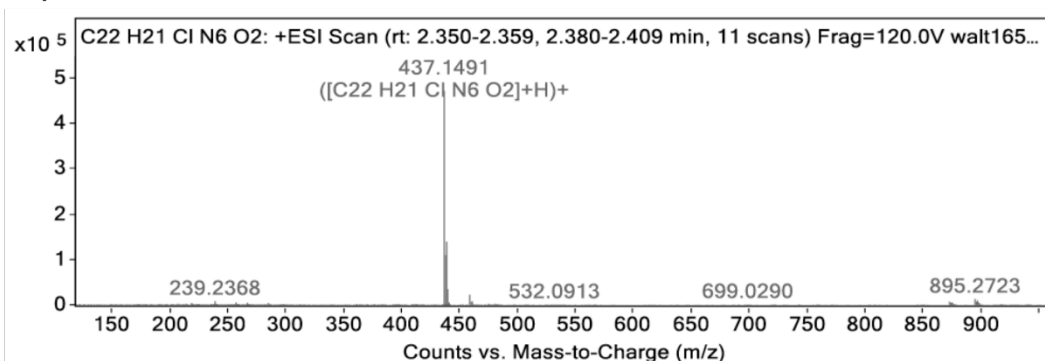
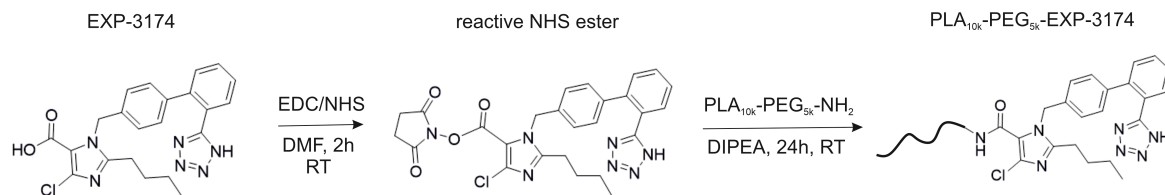
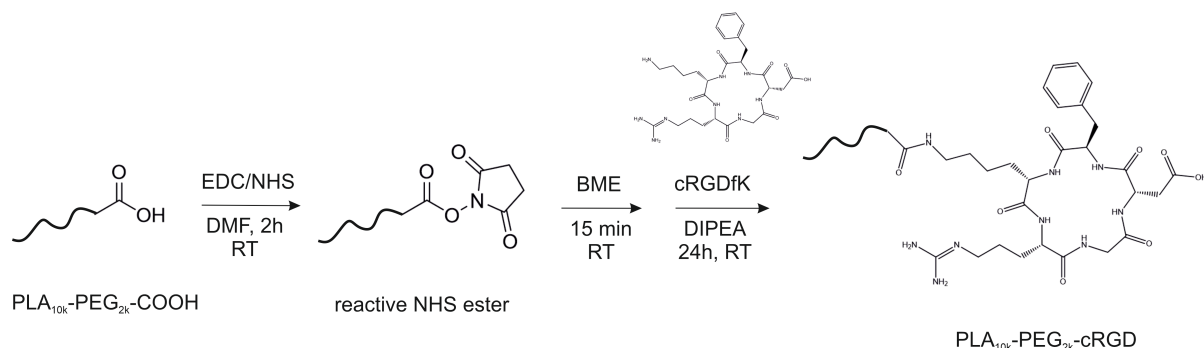


Figure S4. Mass spectrometric analysis of EXP-3174.

3 Polymer Modification and Characterization



Scheme S3. Synthesis of EXP3174-modified polymer. The ligand EXP3174 was coupled to PLA_{10k}-PEG_{5k}-NH₂ via the carboxylic acid residue of the imidazole component. To enable this, EXP was first activated with 1-ethyl-3-(3-dimethylaminopropyl)carbodiimide (EDC) and *N*-hydroxysuccinimide (NHS) for 2 h at RT in *N,N*-dimethylformamide (DMF). PLA_{10k}-PEG_{5k}-NH₂ and *N,N*-diisopropylethylamine (DIPEA) were added to the solution and the reaction was stirred for further 24 h at RT.



Scheme S4. Synthesis of cRGD-modified polymer. PLA_{10k}-PEG_{2k}-COOH was activated with 1-ethyl-3-(3-dimethylaminopropyl)carbodiimide (EDC) and *N*-hydroxysuccinimide (NHS) for 2 h at RT in *N,N*-dimethylformamide (DMF). The excess of EDC was quenched by the edition of β -mercaptoethanol (BME) to avoid the activation of the free carboxy group of cyclo-RGDfK (cRGD) and thus of undesired side reactions. After 15 min of incubation time at RT the ligand cRGD, together with DIPEA, was added to the reaction mixture and stirred for 24 h at RT.

Chapter 3 – Supporting Information

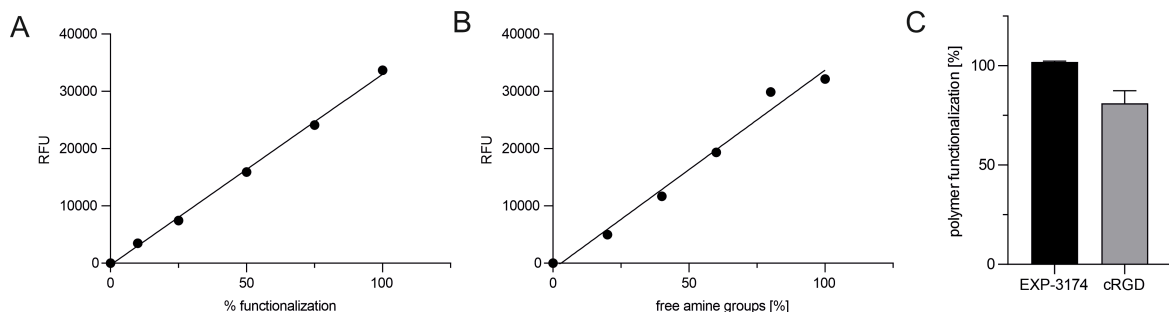


Figure S5. Determination of the degree of functionalization of the modified polymers. (A) Calibration curve for the determination of the amount of cRGD bound to PLA_{10k}-PEG_{2k} polymer via PCA Assay. (B) Calibration curve for the determination of the amount of EXP-3174 bound to PLA_{10k}-PEG_{5k} polymer (RFU = relative fluorescence units).

4 Nanoparticle Preparation via Nanoprecipitation

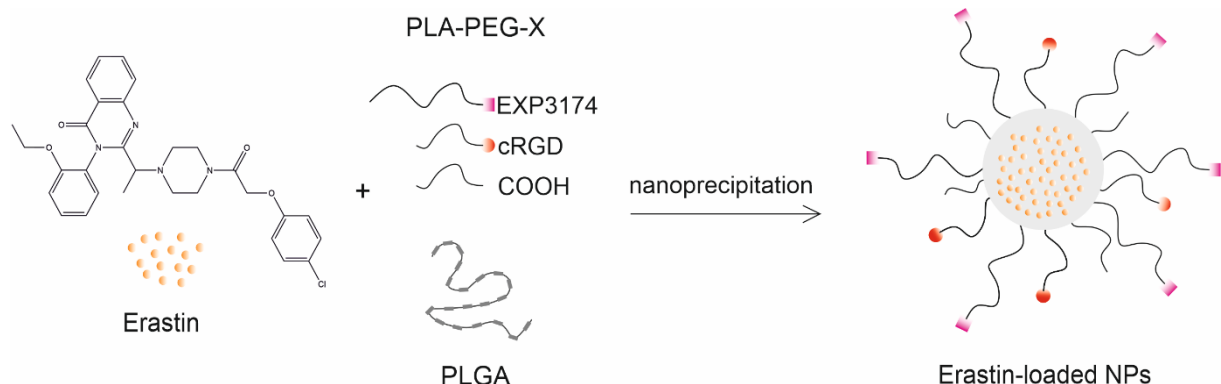


Figure S6. Nanoparticle preparation via nanoprecipitation. Erastin was co-solved with the polymers in the organic phase and added dropwise to vigorously stirring millipore water. Due to the high lipophilicity of erastin, we suspect an encapsulation in the PLGA-containing nanoparticle core.

5 Nanoparticle Characterization

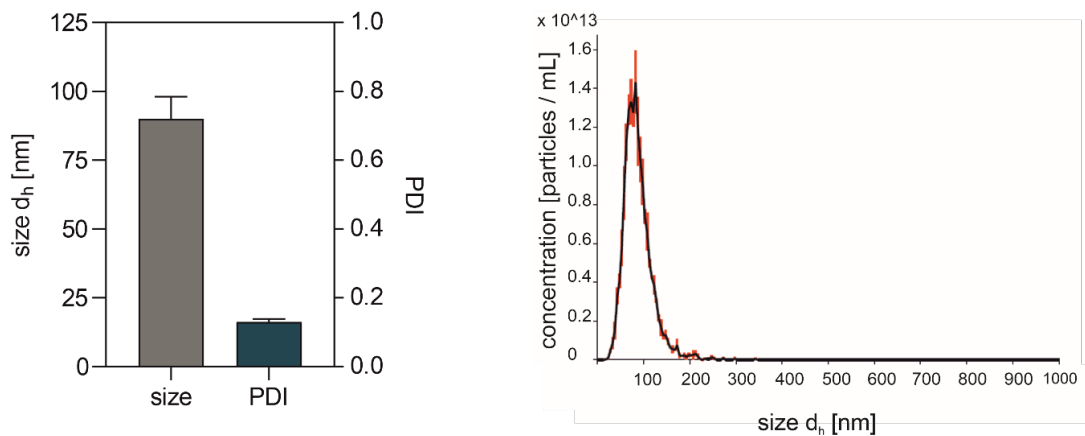


Figure S7. Nanoparticle characterization. Characterization of nanoparticle size and polydispersity index (PDI) via DLS. Determination of nanoparticle size distribution and concentration via NTA.

6 Determination of the Maximal Applicable Amount of Erastin for Particle Preparation

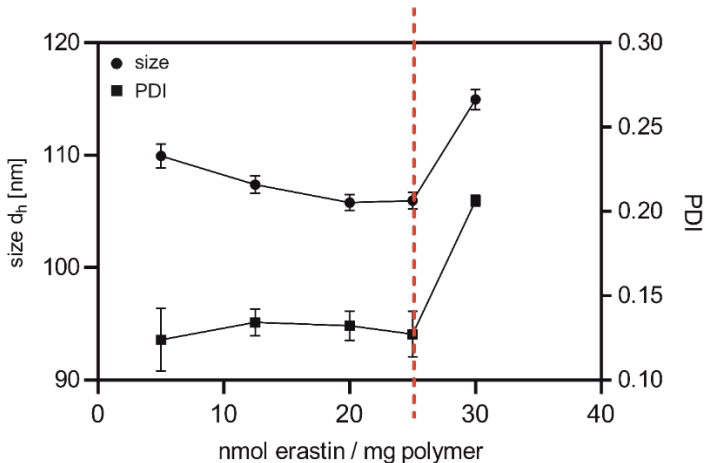


Figure S8. Determination of the maximal applicable amount of erastin during NP preparation. Increase of particle size and PDI value at higher amounts than 25 nmol erastin / mg polymer. Values determined via dynamic light scattering (DLS).

7 Proof of Concept for the Successful Encapsulation of Erastin – Separation of NP Fraction and Free Erastin via Size Exclusion Chromatography (SEC)

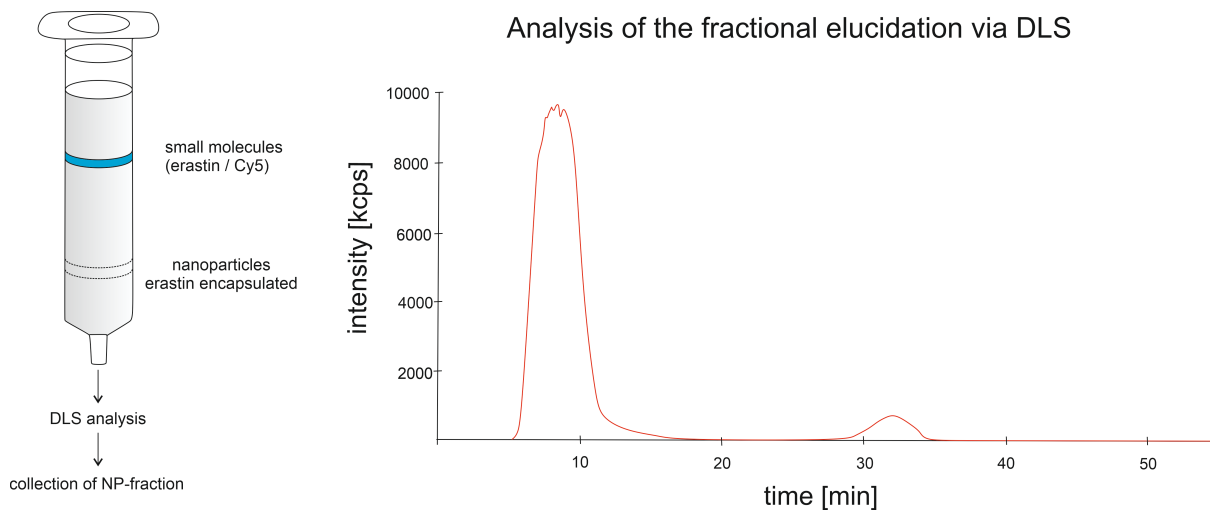


Figure S9. Proof of concept of the encapsulation of erastin via size exclusion chromatography (SEC) and monitoring via dynamic light scattering (DLS). After particle preparation, free erastin was separated from the encapsulated erastin by SEC. DLS tracked the elution of particles at about 8 min and the elution of small molecules like erastin ($M_w = 547.04$ Da) at about 32 min. The range of small molecule elution was visualized by the addition of free Cyanine 5 (Cy5), which has a comparable molecular weight to erastin ($M_w(Cy5) = 653.77$ Da.) Clear baseline separation over a range of almost 15 min allowed separation of free and encapsulated erastin. The eluted solution in the nanoparticle range was collected, freeze-dried and subsequently analyzed by HPLC.

8 HPLC Analysis for the Quantification of Encapsulated Erastin

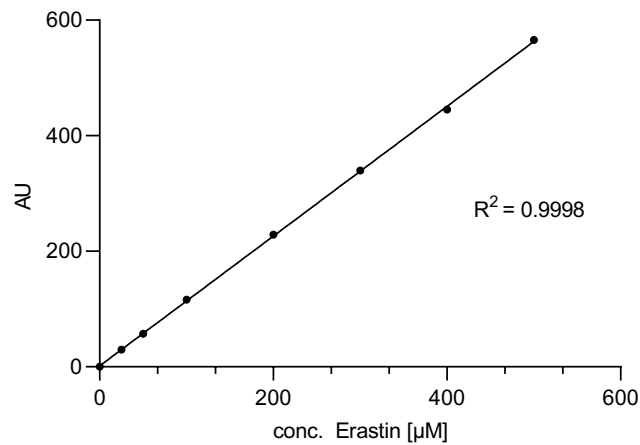


Figure S10. Calibration curve for the quantification of erastin via HPLC. Freeze-dried nanoparticle fractions were resolved in DMSO and analyzed via HPLC. Free erastin solved in DMSO served as calibration for the determination of the amount of encapsulated drug in the purified nanoparticle fraction. Absorbance was detected at 220 nm.

9 Investigation of the Highest Encapsulation Efficiency (EE) and Loading Capacity (LC) for Different Amounts of Initially Added Erastin

The fraction of the eluted particles was freeze-dried for three days, weighed, dissolved in dimethylsulfoxide (DMSO), and analyzed via high performance liquid chromatography (HPLC). The analysis was performed using a Phenomenex Gemini 3 μ M NX C18 110 \AA column (size 150 x 4.6 mm) (Phenomenex, Aschaffenburg, Germany) at an oven temperature of 40 $^{\circ}$ C during analysis. As a mobile phase, 0.05 % trifluoracetic acid (TFA) in millipore water and 0.05 % TFA in acetonitrile were used. Absorbance was detected at 220 nm. The following linear gradient was applied: acetonitrile/TFA (0.05 %) (v/v) 0 min: 10:90, 25 min: 95:5; flow rate: 1.0 mL/min. The injection volume was 5 μ L. Erastin showed a constant retention time of 12.4 min. The EE was calculated via equation (Eq) 1, the LC via Eq 2, where m_E is the quantified mass of entrapped drug, m_T is the total mass of drug added to the formulation, and M_T is the total mass of the particle formulation [1,2].

$$Eq\ 1 \quad EE\ (\%) = \frac{m_E}{m_T} \times 100$$

$$Eq\ 2 \quad LC\ (\%) = \frac{m_E}{M_T} \times 100$$

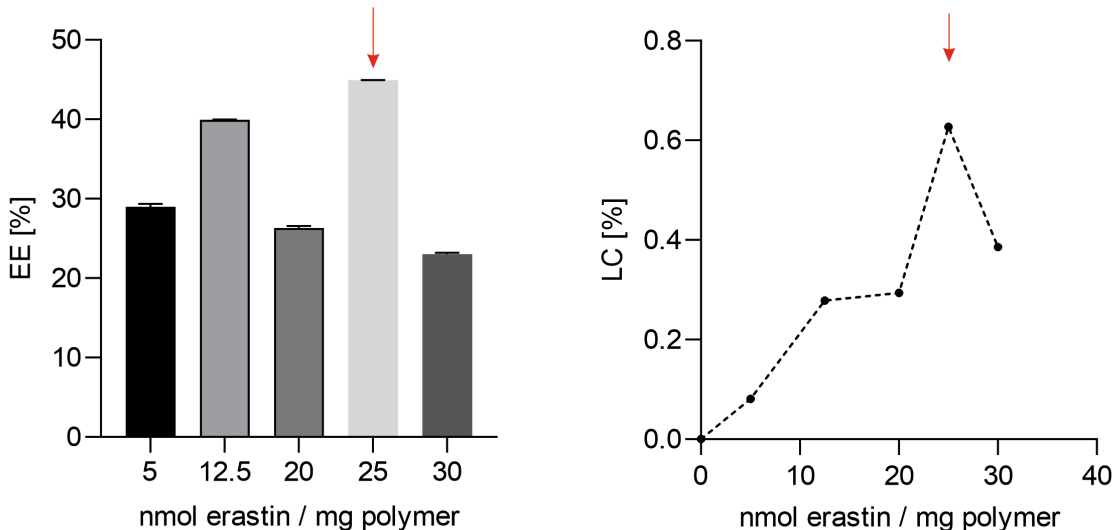


Figure S11. Investigation of the maximal encapsulation efficiency (EE) and loading capacity (LC) after addition of different amounts of erastin during NP preparation.

10 Determination of Erastin Molecules per Particle

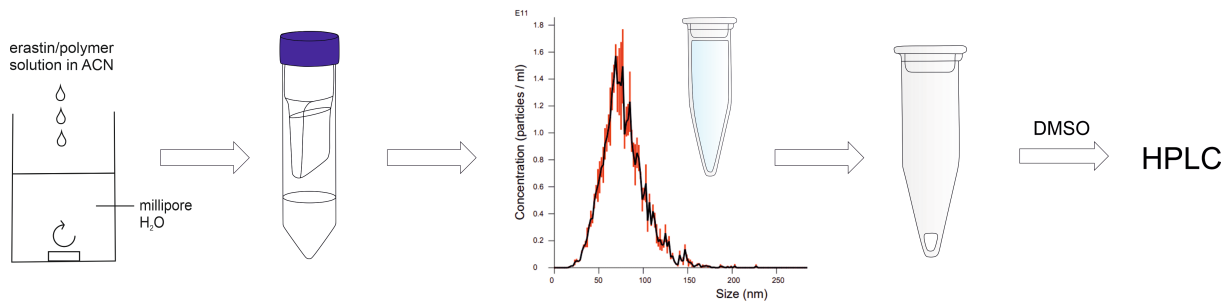


Figure. S12 Scheme of the determination of erastin molecules per particle. After nanoparticle preparation via nanoprecipitation, free erastin was separated from encapsulated erastin via centrifugation in ultracentrifugal devices with a molecular weight cut-off of 100 kDa ($M_w(\text{Erastin}) = 547.04 \text{ Da}$). Particle up-concentration in ultracentrifugal devices with a molecular weight cut-off of 100 kDa also obviates the need for separation of free erastin by size exclusion chromatography, since free erastin with a molecular weight of 547.04 Da was quantitatively filtered (ratio of molecular weight cut off to molecular weight of free drug approx. 1:183). The NP concentration was determined via nanoparticle tracking analysis (NTA) and a defined number of NPs was freeze-dried for three days. The freeze-dried NPs were solved in dimethyl sulfoxide (DMSO) and analyzed via high-performance liquid chromatography (HPLC).

11 Determination of the Impact of Different PLGA Contents on the Number of Encapsulated Erastin Molecules per Particle and Particle Size

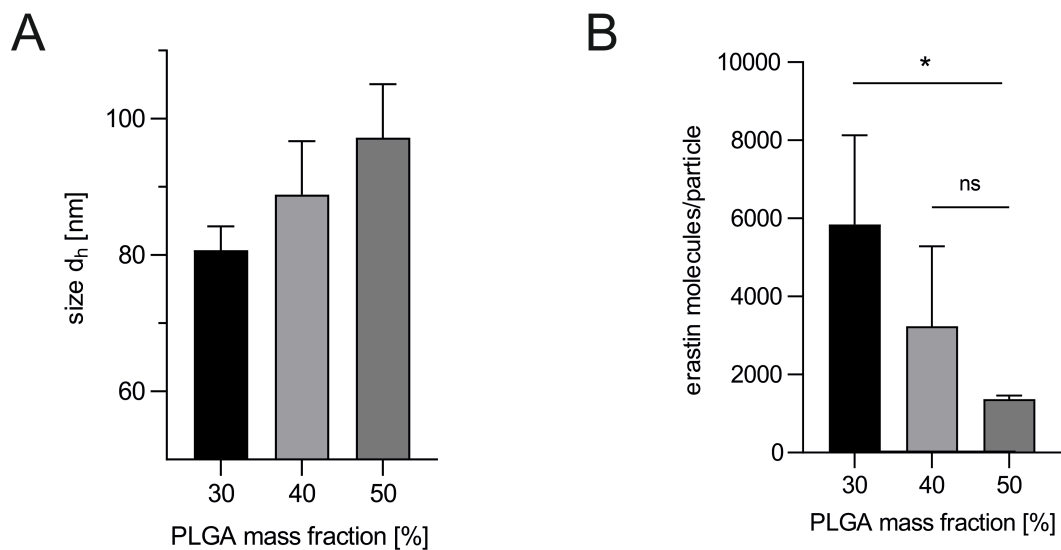


Figure S13. Impact of PLGA content on (A) NP size and (B) encapsulated amount of erastin. Rising amounts of PLGA content led to a higher nanoparticle size and to a decrease in the number of erastin molecules which were encapsulated per nanoparticle.

12 Analysis of Particle Stability and Labeling

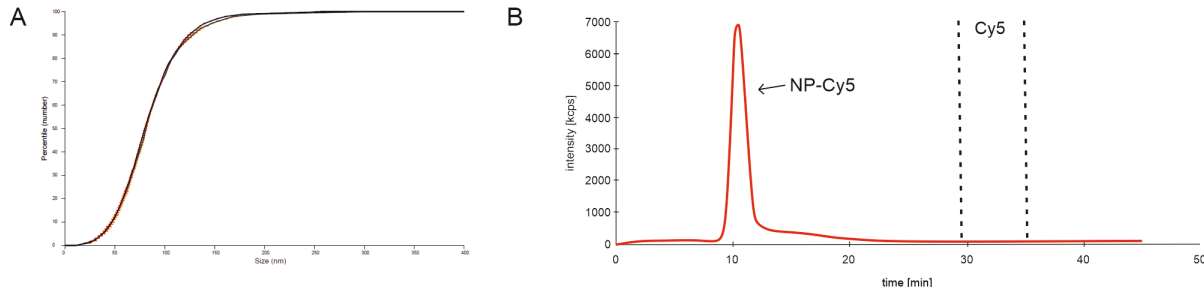


Figure S14. Particle stability determined via NTA and DLS after 7 days. (A) No changes in size distribution were detected after an incubation period of 7 days via NTA. **(B)** DLS analysis showed no free Cy5 after one week of incubation time, which confirms the stability of particle labeling.

13 Pretest DMSO Resistance of Target Cells for the MTT Assay

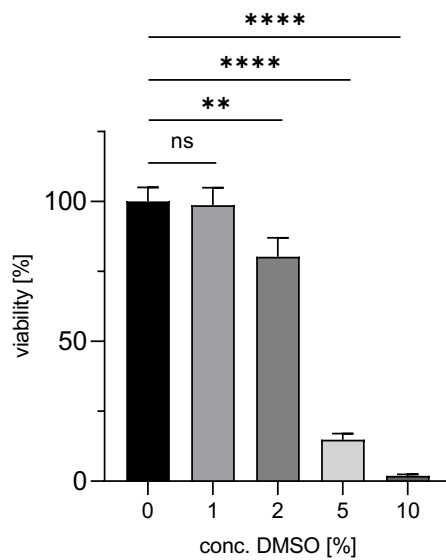


Figure S15. Pretest DMSO resistance of SV40MES13 cells. 15,000 cells/well were seeded in a 96-well plate and incubated for 24 h at 37 °C. The medium was aspirated and medium with different amounts of DMSO was added to test the DMSO resistance of the cell line. After an incubation period of 24 h at 37 °C, the MTT Assay was performed as described in chapter 2.11. The residual viability of the cells was evaluated. Untreated cells served as 100 % reference value. Results represent mean ± SD (n = 3, levels of statistical significance are indicated as *p ≤ 0.05, **p ≤ 0.01, ***p ≤ 0.001, ****p ≤ 0.0001).

14 Cytotoxicity Dependence on Cell Density

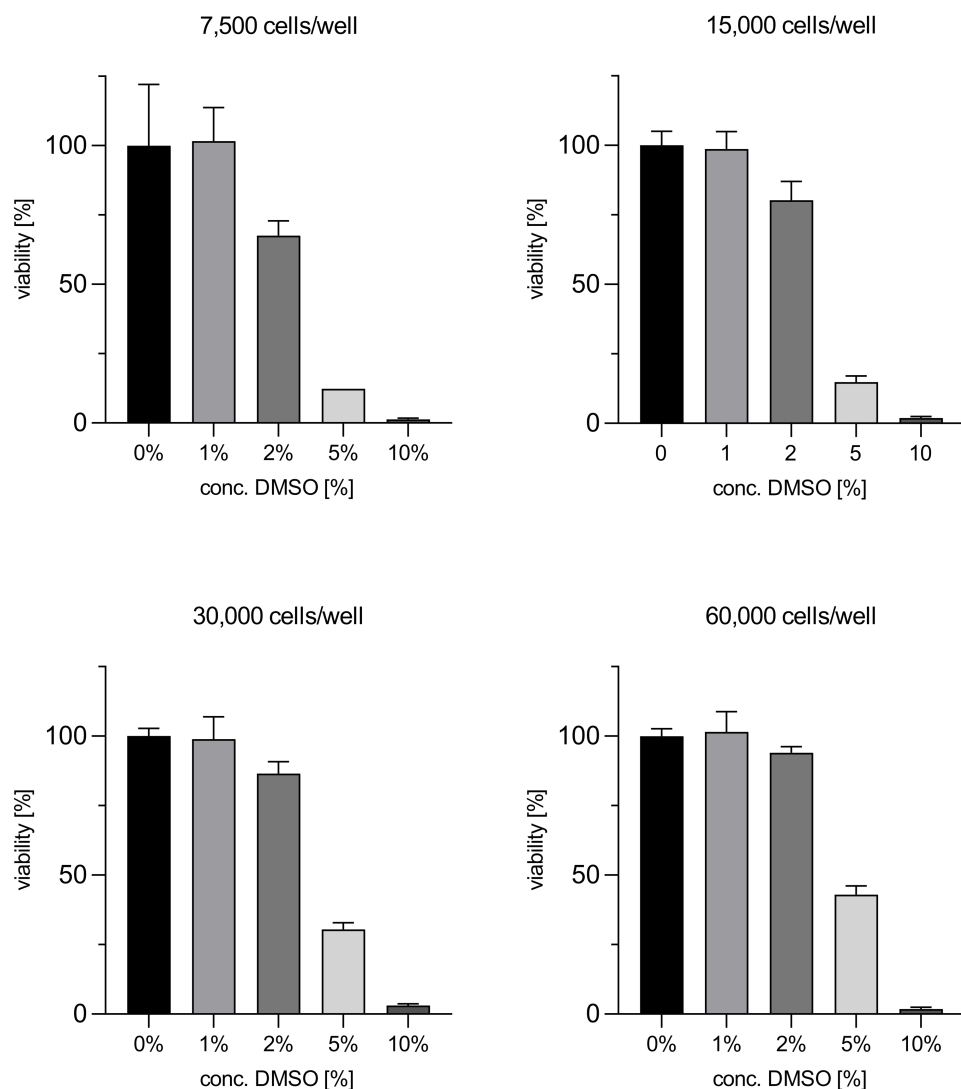


Figure S16. Pretest DMSO resistance of SV40MES13 cells – impact of cell density. Different cell densities (7,500-60,000 cells/well) were seeded in a 96-well plate and incubated for 24 h at 37 °C. The medium was aspirated and medium with different amounts of DMSO was added. After an incubation period of 24 h at 37 °C, the MTT Assay was performed as described in chapter 2.11. The rest viability of the cells was evaluated. Untreated cells served as 100 % reference value.

Supporting Information - Adenovirus-mimetic Nanoparticles in Renal Target Tissue

Chapter 3 – Supporting Information

Chapter 4

Ectoenzymes as Promising Cell Identification Structures for the High Avidity Targeting of Polymeric Nanoparticles

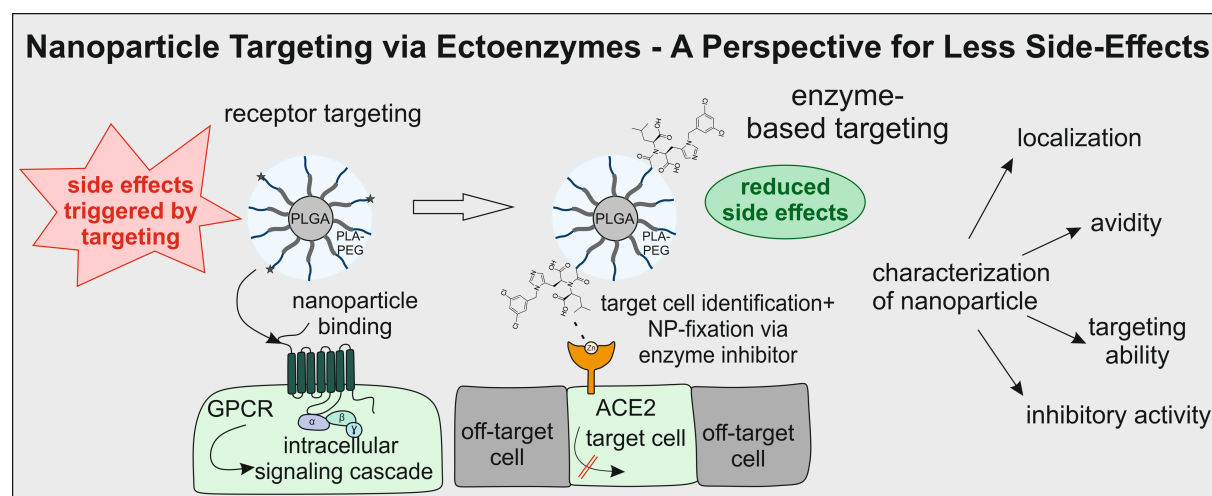
Published in *International Journal of Pharmaceutics*

2023, Volume 647, 25 November 2023, 123453

Chapter 4

Abstract

Pharmacotherapy is often limited by undesired side effects while insufficient drug reaches the site of action. Active nanoparticle targeting should provide a solution to this problem by using ligands attached to the nanoparticle corona for the identification of receptors on the target cell surface. However, since receptor binding is directly associated with pharmacological responses, today's targeting concepts must be critically evaluated. We hypothesized that addressing ectoenzymes would help to overcome this problem, but it was not clear if particles would show sufficiently high avidity to provide us with a viable alternative to classical ligand-receptor targeting concepts. We scrutinized this aspect by immobilizing the highly selective angiotensin-converting enzyme 2 (ACE2) inhibitor MLN-4760 in the corona of block-copolymer nanoparticles and investigated enzyme binding by microscale thermophoresis and flow cytometry. Excellent avidities with K_d values as low as 243 pM for soluble ACE2 and 306 pM for ACE2-positive cells were obtained. In addition, the inhibitory activity had an IC_{50} value of 2.88 nM and reliable target cell identification could be proven in co-culture experiments. High avidity is the basis for minimizing material loss to off-target sites and paves the way for a paradigm shift in nanoparticle targeting which does not trigger unintended side effects following target cell identification.



Chapter 4

1 Introduction

Drug application often shows the problem of insufficient drug transport to the site of action with pronounced adverse drug effects. In such cases, drug delivery via active nanoparticle (NP) targeting offers a beneficial alternative [1]. For this reason, new targeting approaches to selectively address specific cell types or tissues [2,3] are constantly being developed [4]. However, one aspect has largely been ignored so far: if a ligand is attached to the surface of a nanoparticle to selectively identify its target cell, ligand binding to its receptor on the target cell surface might induce a pharmacological effect separate from the payload [5,6]. In most applications such a pharmacological response resulting from cell identification is highly undesirable. Unfortunately this is also true for the most popular structures reported in the literature for addressing nanoparticles to target cells, such as G-protein coupled receptors (GPCRs) [7,8], integrin receptors [9,10], and transferrin receptors (TfRs) [11,12].

GPCRs allow for the identification of a wide range of different cells in the human body [7] since they are the largest family of cell surface receptors [13]. Thus, there are many concepts based on GPCRs as recognition structures [6,14,15]. Uptake into the target cells can be mediated by the receptor binding of a GPCR agonist [16], which leads to the initiation of an intracellular signaling cascade via the G-proteins of the receptor [17]. Even the recognition of target cells by antagonists is not without consequences as blocking signaling cascades exhibits direct pharmacological effects on the cell [18]. Since GPCRs play an important role in various physiological and pathological processes, such as cell proliferation, differentiation, or communication [19], it is almost impossible not to interfere with relevant signaling pathways during target cell recognition [13].

Integrin receptors seem to be more advantageous as recognition structures since their main task is linking the cell cytoskeleton to the extracellular matrix and controlling the communication of the intra- and extracellular environment [20]. Integrins are heterodimeric cell surface anchor proteins consisting of α - and β -chains [13] and, like GPCRs, widely expressed on cell surfaces [10,21]. However, also integrin receptors are subject to outside-in signaling cascades that trigger biological effects upon receptor activation [22–24]. In addition to short-term effects such as the reorganization of the actin cytoskeleton, long-term effects such as cell proliferation, survival pathways, or the control of cell morphology are also regulated [24–27]. Consequently, they are not unrestrictedly suitable as targeting moieties.

Chapter 4

Another type of target structure that has frequently been used to identify cells with nanoparticles are transferrin receptors, which support iron uptake into cells via an endo- and exocytosis cycle of transferrin [28]. Targeting concepts via TfRs initially appear beneficial compared to GPCRs or integrins regarding possible side effects but reveal an additional problem. Since transferrin receptors are ubiquitously expressed in mammalian tissues, their potential use is limited to cancer cells in which the receptor is overexpressed [29].

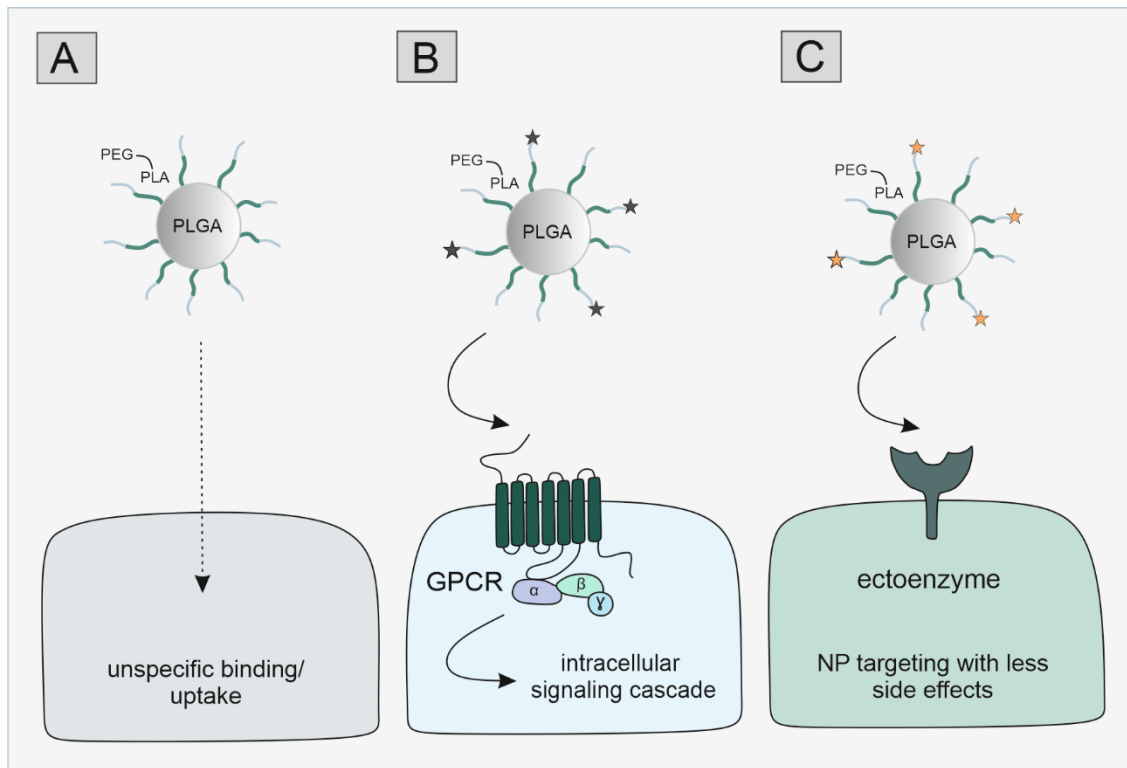


Figure 1. Illustration of the evolution of nanoparticle design concepts toward targeting strategies with minimized side effects. (A) Non-targeted control NPs with only non-specific binding and uptake. **(B)** Receptor-based targeting concept using the example of the interaction with a GPCR. Receptor-mediated nanoparticle uptake triggers a biological signaling cascade. **(C)** Targeting exclusively via ectoenzymes leads to minimized side effects. Nanoparticle cell attachment via an enzyme-inhibiting ligand presented by the NP.

In summary, today's predominant targeting concepts do not provide a satisfactory basis for nanotherapy in which solely the transported cargo is supposed to mediate a biological effect. We hypothesized that making use of nanoparticle cell interactions via ectoenzymes that interact with their substrates outside the cell [30] would allow to overcome this massive drawback (Fig. 1). Since they are widespread, ectoenzymes would enable the targeting of a

Ectoenzymes as Cell Identification Structures

large variety of different cells [31]. Moreover, there is a multitude of high-affinity ligands for ectoenzymes with affinities comparable to ligand-receptor pairs currently used for targeted nanotherapy [32,33].

To test our hypothesis, we developed nanoparticles targeting ACE2. This ectoenzyme was first described in the year 2000 as a homolog of the angiotensin-converting enzyme (ACE). In protein expression studies, Hikmet et al. (2020) reported the expression of ACE2 in more than 150 different cell types based on mRNA and protein level analysis [34–36]. Recently, this enzyme has received special attention as it serves as a recognition structure for the coronavirus SARS-CoV-2 and is involved in its uptake [37]. We focused our nanoparticle design on a high-avidity target cell identification and mimicked the first contact between the virus and its target cells through small molecule-protein interactions. To this end, we covalently coupled the potent small molecule ACE2 inhibitor MLN-4760 (MLN) to the nanoparticle surface using a modified version described by Sanna et al. (2022) [38]. NP avidity was assessed for the soluble enzyme and in a cell-based model by microscale thermophoresis and flow cytometric analysis. The inhibitory activity of the MLN-modified nanoparticles was evaluated in a fluorogenic ACE2 activity assay. Furthermore, the target cell specificity of the nanoparticles was tested in mono- and co-cultures of ACE2-positive and -negative cells by flow cytometry.

Chapter 4

2 Materials and Methods

2.1 Materials

Millipore water was generated by a Milli-Q water purification system (Millipore, Schwalbach, Germany). Dulbecco's phosphate-buffered saline (PBS) was obtained from Gibco® Life Technologies (Thermo Fisher Scientific, Waltham, MA, USA). If not stated otherwise, all reagents and chemicals were analytical grade and purchased from Sigma Aldrich (Taufkirchen, Germany).

Poly(ethylene glycol)(PEG)-carboxylic acid with a molecular mass of 5,000 g mol⁻¹ (OH-PEG_{5k}-COOH) was purchased from Jenkem Technology USA Inc. (Allen, TX, USA). Poly(ethylene glycol)-methylether with a molecular mass of 5,000 g mol⁻¹ (OH-PEG_{5k}-MeO) as well as Resomer® RG 502, Poly(D,L-lactide-co-glycolide; lactide:glycolide 50:50, ester terminated or acid terminated (M_w 7000-17,000 Da)) (PLGA) were sourced from Sigma Aldrich (Taufkirchen, Germany). MLN-4760 was obtained from MedChemExpress (Monmouth Junction, NJ, USA). The fluorescent dyes were purchased from Lumiprobe (Hannover, Germany).

The cellulose dialysis membranes used for purification during polymer modification were obtained from Spectrum Laboratories, Inc. (Rancho Domingues, CA, USA). Nanoparticle solutions were concentrated with centrifugal devices with a molecular weight cut-off of 30 kDa, which were purchased from Pall Life Sciences (Portsmouth, UK).

HEK293T cells which are stably expressing ACE2 (HEK293T-ACE2) and the Alexa Fluor 647-labeled ACE2 enzyme were a kind gift from Prof. Dr. Ralf Wagner (Institute of Clinical Microbiology and Hygiene, University Hospital Regensburg). Untransfected HEK293 cells were obtained from the German Collection of Microorganisms and Cell Cultures GmbH, DSMZ (Göttingen, Germany).

For the preparation of cell culture medium, fetal bovine serum (FBS) was sourced from Biowest (Nuillé, France) and blasticidin was purchased from Invivogen (Toulouse, France). CellTracker™ green (CTG) for target cell labeling was purchased from Fisher Scientific GmbH (Schwerte, Germany). For all microscope experiments, the cells were seeded in 8-well microscope slides from Ibidi (Gräfelfing, Germany). The Dako Faramount Mounting Medium for the preparation of the microscope slides was obtained from Agilent Technologies (Santa

Clara, CA, USA). The 96-well plates for flow cytometry experiments, or the fluorogenic enzyme assay were obtained from Greiner (Frickenhausen, Germany).

For the determination of the inhibitory activity of the MLN-NPs, an ACE2 activity assay kit was obtained from Abcam (Cambridge, UK). The antibodies used to analyze the expression of ACE2 on the cell surface, Human ACE-2 Alexa Fluor ® 647-conjugated Antibody and Mouse IgG2A Alexa Fluor ® 647-conjugated Isotype Control, were purchased from R&D Systems (Minneapolis, MA, USA).

2.2 Polymer Synthesis and Ligand Coupling

Poly(lactic acid)-poly(ethylene glycol) (PLA-PEG) block-copolymers were synthesized via ring-opening polymerization of cyclic lactide as described by Qian et al. (2011) [39] with modifications previously described by our group [40]. For the ring-opening polymerization OH-PEG_{5k}-COOH or OH-PEG_{5k}-MeO, respectively, served as macroinitiator. 1,8-Diazabicyclo[5.4.0]undec-7-ene (DBU) was used as a catalyst for the reaction. The polymerization was quenched with benzoic acid after 1h (Scheme S1). The resulting polymers with 10 kDa poly(lactic acid) (PLA) content (PLA_{10k}-PEG_{5k}-COOH and PLA_{10k}-PEG_{5k}-MeO) were characterized via ¹H-NMR (Fig. S1, S2) (Supporting Information, Chapter 1).

PLA_{10k}-PEG_{5k}-MLN-4760 was synthesized by activating PLA_{10k}-PEG_{5k}-COOH (1 eq) with 1-ethyl-3-(3-dimethylaminopropyl)carbodiimide (EDC) (25 eq) and *N*-hydroxysuccinimide (NHS) (25 eq) in *N,N*-dimethylformamide (DMF) for 2 h under stirring at room temperatur. Afterward, the reaction was quenched by the addition of β -mercaptoethanol (BME) (35 eq), and the reaction mixture was stirred for 15 min before adding the ligand. This quenching step prevented the unintended activation of the carboxy group of MLN, which could lead to undesired side reactions. The ligand MLN-4760 (3.5 eq) was dissolved in dimethyl sulfoxide (DMSO) and added to the activated polymer solution followed by *N,N*-diisopropylethylamine (DIPEA) (10 eq). Subsequently, the solution was stirred for 24 h at room temperature to couple the NHS-ester to the secondary amine of MLN-4760. The reaction mixture was precipitated in ice-cold diethyl ether and centrifuged at 3000 rpm for 15 min. The supernatant was decanted, and the reaction product was dried overnight under nitrogen (N₂) flow. The dried solid was solved in a mixture of acetonitrile (ACN) and DMSO (10:1 v/v) and added dropwise to vigorously stirring millipore water. The resulting polymer micelles were stirred for 3 h at room

Chapter 4

temperature until the organic solvent was completely evaporated. The solution was dialyzed in millipore water using a 3.5 kDa molecular weight cut-off dialysis tube for 24 h (with medium change after 30 min, 2 h, and 6 h) to remove the uncoupled ligand and reagents. The purified polymer solution was freeze-dried for 3 days. The concept of the synthesis was also verified by coupling MLN-4760 to 2-[2-(2-methoxyethoxy)ethoxy]acetic acid (Scheme S2) to enable the analysis of the synthesis by high-resolution mass spectrometry (HRMS) and ¹H-NMR (Fig. S3). The stability of the product was examined via high-performance liquid chromatography (HPLC) (Fig. S4). In addition, the modified polymer was analyzed via UV/Vis and by HRMS after polymer hydrolysis (Supporting Information, Chapter 2).

2.3 Nanoparticle Preparation

End-capped 13.4 kDa PLGA, constituting the NP core, and the previously described PLA-PEG block-copolymer as shell component were mixed at a 30:70 mass ratio to a final concentration of 10 mg/mL in ACN. For ligand-modified particles, PLA_{10k}-PEG_{5k}-COOH and PLA_{10k}-PEG_{5k}-MLN-4760 were mixed in various ratios, if not mentioned otherwise 25 % MLN-modified polymer and 75 % unmodified polymer. NPs were prepared via bulk nanoprecipitation. Therefore, the prepared polymer mixtures were added dropwise to vigorously stirring 10 % PBS to a final polymer concentration of 1 mg/mL. The particle preparation was stirred for 3 h and afterward concentrated by centrifugal ultrafiltration for 20 min at 3000 rpm.

2.4 Nanoparticle Characterization and Determination of NP Concentration

The polydispersity index (PDI) and the zeta potential of the NPs were evaluated prior to the concentration step using a Malvern Zetasizer Nano ZS (Malvern, UK). The samples were analyzed with a 633 nm He-Ne laser at an angle of 173° at RT. Nanoparticle size and concentration were determined after the concentration step using nanoparticle tracking analysis (NTA, NanoSight NS300, Malvern, UK). Before measurement, the particles were diluted with millipore water to a concentration of 20 to 100 particles per frame (dilution 1:10,000 - 1:40,000).

2.5 Nanoparticle Labeling with Fluorescent Dyes

The nanoparticles were fluorescently labeled for flow cytometry and confocal scanning microscopy (CLSM) experiments. Carboxy-terminated PLGA was covalently linked to the fluorescent dyes Cyanine5 (Cy5) or tetramethylrhodamine (TAMRA), respectively, for the usage as labeled nanoparticle core material. Carboxylic acid-terminated PLGA (1 eq), Cy5-amine (0.1 eq), and 3-[bis(dimethylamino)methyl]imidazol-1-oxido-hexafluorophosphate (HBTU) (2 eq) were dissolved in the smallest possible amount of DMF. DIPEA (4 eq) was added, and the reaction mixture was stirred overnight at room temperature (RT). Subsequently, the reaction product was precipitated in ice-cold diethyl ether and centrifuged at 3000 rpm for 15 min. The supernatant was decanted, and the product was dried under nitrogen flow. The dried precipitate was taken up in acetonitrile and the precipitation process was repeated three times as already described or at least until the supernatant was no longer bluish in color. The product was dried overnight under nitrogen flow. Characterization was performed by $^1\text{H-NMR}$ in deuterated chloroform (CDCl_3).

The labeling with TAMRA was carried out by activating carboxylic acid-terminated PLGA using 4-(4,6-dimethoxy-1,3,5-triazin-2-yl)-4-methylmorpholinium chloride (DMTMM) as coupling reagent as previously described by our group [41]. PLGA was used in a 5-fold excess. To remove the unbound dye, the polymer was dialyzed in a 6-8 kDa tube for 24 h.

The labeled polymer was used as a replacement for plain PLGA in the preparation of fluorescent nanoparticles.

2.6 Microscale Thermophoresis Measurements

The binding affinities of the MLN-modified NPs to the soluble ACE2 enzyme were investigated using microscale thermophoresis measurements (MST). All measurements were performed in PBS with 0.05 % polysorbate 20. A serial dilution of each NP sample with 16 dilution steps (1:1 v/v) was performed, starting with the highest NP concentration of 6 nM. Afterward, an equal volume of the labeled enzyme was added to each dilution. The final enzyme concentration in all samples was 0.5 nM. All the resulting dilutions were mixed by pipetting up and down and afterward absorbed into Monolith NT 115 standard capillaries. The measurements were performed at RT using the MST device Monolith NT 115 pico (Nanotemper Technologies,

Chapter 4

Munich, Germany). The LED power was set to 35 % and the MST power was set to 80 %. Control NPs served as a negative control. Changes in the fluorescence signal resulting from a binding event of nanoparticles to the fluorogenic ACE2 enzyme were recorded and normalized to the fraction bound (0 = unbound, 1 = bound) [42]. The curve fits and the resulting nanoparticle dissociation constants (K_d) were determined by MO.Affinity Analysis software version 2.3 (Nanotemper).

2.7 Cell Culture

The target cells, HEK293T cells which are stably expressing the ACE2 enzyme, were cultivated in Dulbecco's Modified Eagle Medium (DMEM) supplemented with 10 % fetal bovine serum and 10 μ g/mL blasticidin. Untransfected HEK293 cells served as control cells in all experiments. They were cultivated in DMEM medium with 10 % FBS but without additional antibiotics.

2.8 Confocal Scanning Microscopy Analysis

To investigate the concrete interaction of the NPs with their target cells, confocal scanning microscopy was performed using a Zeiss LSM 710 (Carl Zeiss Microscopy GmbH, Jena, Germany). Images were analyzed using ZEN 3.5 (blue edition) software. For CLSM analysis 50,000 cells/well were seeded in an Ibidi 8-well chamber and incubated for 24 h at 37 °C. Afterward, the cells were washed with 200 μ L prewarmed PBS. 200 μ L of TAMRA-labeled nanoparticles in a concentration of 500 pM (Fig. 2A, 2B) or 3 nM (Fig. 2C) in Leibovitz L-15 medium (LM) were added and incubated for one hour at 37 °C. Nanoparticles were aspirated followed by two washing steps with PBS. The cells were fixed using a 4 % paraformaldehyde (PFA) solution for 10 min at RT. After fixation and two washing steps with PBS, the cells were incubated with a DAPI staining solution (1 μ g/mL in 0.1 M PBS) for 10 min for cell nucleus labeling. After one more washing step, the cells were incubated with the hACE-antibody solution diluted 1:100 with 0.1 M PBS for one hour at RT in the dark. After removal of the unbound antibody, the cells were mounted using Dako Faramount Mounting Medium and stored in the fridge (4 °C) until measurement.

2.9 Flow Cytometry

2.9.1 Determination of a Cell-based K_d Value

HEK293T-ACE2 cells were seeded into 96-well plates at a concentration of 60,000 cells/well and incubated for 24 h at 37 °C. NPs were manufactured using Cy5-labeled PLGA and the concentration was adjusted with LM. The cells were incubated with different concentrations of MLN-NPs or control nanoparticles for 1 h at 37 °C. After removal of the NP samples, the cells were washed twice with PBS and detached using trypsin (0.05%). The samples were analyzed using a FACS Canto II (Becton Dickinson, Franklin Lakes, NJ, USA). NP fluorescence was excited at 633 nm and the emission was recorded using a 661/16 nm bandpass filter.

The fluorescence signal resulting from the binding of control particles was subtracted as unspecific binding from the fluorescence resulting from the binding of MLN-NP to ACE2-expressing target cells. The cell-based K_d value was calculated via a specific binding fit. Fraction bound = 1 represents the maximal specific binding, i.e. the maximum binding capacity (B_{max}) of the fitted curve, fraction bound = 0 represents no binding event. Calculations were performed using GraphPad Prism Software 8.3.0.

2.9.2 Targeting Ability of MLN-NPs

The binding of MLN-NPs and control nanoparticles to ACE2-expressing target cells was compared by flow cytometry. Furthermore, co-culture experiments with target and off-target cells were performed.

For monoculture experiments, HEK293T-ACE2 cells were seeded into 96-well plates at a concentration of 60,000 cells/well and incubated for 24 h at 37 °C. For co-culture experiments, the target cells were stained with CTG prior to seeding and co-seeded with unstained HEK293 off-target cells in a 96-well plate at a ratio of 50/50, or 10/90, respectively. For the staining process target cells were incubated for 45 min at 37 °C in a 15 µM solution of CTG in serum-free DMEM. Both cell types were differentiated during measurements using the fluorescein (FITC) channel.

NPs were manufactured using Cy5-labeled PLGA and the concentration was adjusted with LM. To confirm the ACE2-dependence of NP binding, 100 µL of free MLN-4760 (200 µM) was

Chapter 4

added to the relevant cell samples 15 min before NP incubation. 100 μ L of LM was added to the other wells instead. 200 μ M MLN-4760 solution was diluted from a 20 mM solution of MLN-4760 in DMSO with LM.

The nanoparticles were added to the target cells at various time points to analyze the time-dependence of binding and uptake. After the incubation periods, the cells were washed with PBS and subsequently detached with 200 μ L trypsin (0.05%) at 37 °C. The samples were analyzed using a FACS Canto II (Becton Dickinson, Franklin Lakes, NJ, USA). The NP fluorescence was excited at 633 nm and the emission was recorded using a 661/16 nm bandpass filter. The fluorescence of HEK293T-ACE2 cells due to staining with CTG was excited at 488 nm and recorded using a 530/30 nm bandpass filter. The results were analyzed using Flowing software 2.5.1 (Turku Centre for Biotechnology, Finland). The geometric mean or the median of the NP-associated fluorescence was determined after gating the viable cell population and excluding cell doublets.

2.10 Determination of the Inhibitory Activity of MLN-NP towards ACE2

For the determination of the inhibitory activity of MLN-NPs towards ACE2 and the calculation of the half-maximal inhibitory concentration (IC₅₀), a fluorometric ACE2 activity assay kit was used. To evaluate the residual activity of the ACE2 enzyme after treatment with MLN-NPs at different concentrations, the cells were first washed with serum-free DMEM and aliquoted to 250,000 cells in Eppendorf cups. After a centrifugation step (5 min, 300 g), the supernatant was aspirated, and the cells were resuspended in 100 μ L of the nanoparticle samples diluted in serum-free medium and incubated for one hour at 37 °C. Subsequently, the samples were centrifuged one more time (5 min, 300 g), the supernatant was aspirated, and the cells were resuspended in lysis buffer. Thereafter, the cells were stored on ice and digested using a Dounce homogenizer. After 10 min of incubation on ice, the cells were vortexed and incubated for 10 min. The samples were centrifuged at 16,000 g for 10 min at 4 °C to remove the cell pellet. The supernatant was transferred to a black 96-well plate and incubated for 15 min at RT. The residual activity of the enzyme was analyzed using a quenched fluorogenic substrate. The 7-methoxycoumarin-4-acetic acid (MCA)-based substrate diluted in assay buffer (48 μ L ACE2 assay buffer and 2 μ L ACE2 substrate) was added and the samples were mixed by shaking. The fluorescence was measured with a Synergy Neo2 Multi-Mode Microplate Reader (Biotek

Ectoenzymes as Cell Identification Structures

Instrument Inc., Winooski, VT, USA) with an excitation wavelength of 320 nm and an emission wavelength of 420 nm at RT in the kinetic mode for 90 min with measurement steps of 2 min. The active enzyme cleaved the substrate, releasing the free fluorophore, which leads to an increase in fluorescence over time (Fig. S15). For the evaluation of the results, the slope in the linear range at the beginning of the measurement, when the substrate was still present in high excess, was considered (Supporting Information, Chapter 7). Thus, the percentage decrease in slope can be used for the calculation of the residual enzyme activity.

2.11 Statistics

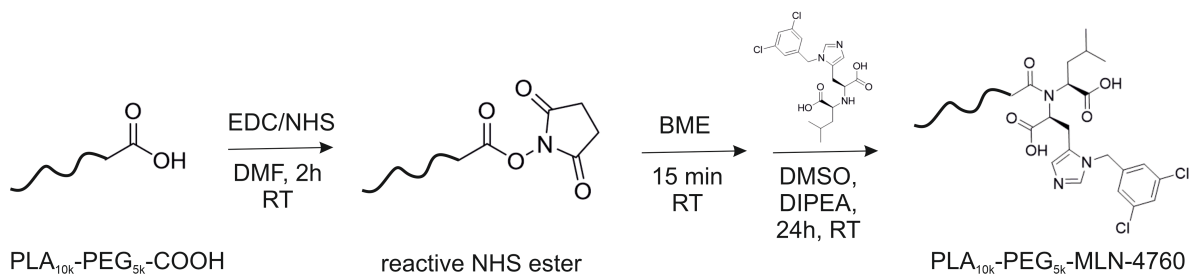
Statistical analysis was performed using GraphPad Prism Software 8.3.0. Two-way ANOVA with a Tukey's (Fig. 5A) or a Sidak's (Fig. 4A, 5B) multiple comparison test was performed for statistical evaluation of significance. The number of performed experiments (n) and the resulting significance levels are indicated in the figure legends.

3 Results and Discussion

3.1 Development and Characterization of ACE2-Targeting NPs

When selecting polymers for nanoparticle preparation, we relied on a well-established system with high reproducibility and biocompatibility [41,43]. The nanoparticle design was based on a core-shell system where PLGA formed the nanoparticle core and the shell consisted of an amphiphilic PLA-PEG block copolymer [44]. Hydrophobic PLGA stabilizes the micellar particles against dissociation and guarantees structural integrity in aqueous media [45]. Furthermore, using PLGA as core material facilitates the visualization of nanoparticles by specifically labeling the nanoparticle core by tethering TAMRA [41] and Cy5 as fluorescent dyes to the carboxylic end groups.

PLA-PEG, as the second component, offers structural flexibility and has favorable traits regarding encapsulation, controlled drug release, and targeting [46]. For ligand coupling, the copolymer was activated to an NHS-ester and coupled to the secondary amine of the selective and high-affinity ACE2-inhibitor MLN-4760 (Scheme 1).



Scheme 1. Polymer modification with MLN-4760. The carboxy group of the prior synthesized PLA_{10k}-PEG_{5k}-COOH block copolymer was activated via EDC and NHS under stirring for 2 h at room temperature (RT) in DMF. After quenching the activation reaction with β -mercaptoethanol (BME), MLN-4760 dissolved in DMSO and *N,N*-diisopropylethylamine (DIPEA) were added to the reaction mixture. The batch was stirred for another 24 h at RT.

To characterize the interaction of MLN-NPs with ACE2, particles with different ratios of modified polymer and unfunctionalized carboxy-terminated polymer chains, referred to as different degrees of modification, were prepared. The negative charge of the carboxy group was expected to stabilize the zeta potential in the negative range, thus reducing nonspecific

electrostatic adsorption to the negative cell membranes [47] and preventing nanoparticle aggregation.

For the preparation of control nanoparticles, methoxy-terminated PLA_{10k}-PEG_{5k} block copolymer was used to obtain a comparable nanoparticle size. Targeted nanoparticles (MLN-NPs) and ligand-free control nanoparticles were prepared via nanoprecipitation (Fig. S7). The particles were characterized via dynamic light scattering (DLS) and nanoparticle tracking analysis (NTA) (Fig. S8-S10).

The two particle types showed a comparable size of about 93.3 ± 4.3 nm for MLN-modified nanoparticles and 92.0 ± 1.9 nm for control nanoparticles, determined via NTA, and a narrow size distribution with polydispersity indexes of 0.135 ± 0.014 and 0.132 ± 0.019 , measured via DLS. Particle size was also investigated by DLS as an orthogonal method and showed similar results. Stability analysis under experimental conditions showed no tendency toward aggregation, which was expected due to the negative zeta potential of -18.7 ± 0.7 mV (Supporting Information, Chapter 3).

3.2 Nanoparticle Binding to the Cell Surface

CLSM was performed to characterize the interactions of MLN-modified nanoparticles with their target cells and prove the attachment to ACE2. The binding experiments demonstrated that most of the NPs remained on the cell membrane and were not taken up unspecifically by the cells (Fig. 2A-C, Fig. S12). This could be expected since ACE2 is expressed on the cell surface [48,49], which was demonstrated by antibody staining (Fig. 2C). MLN-4760, as an inhibitor, should mediate binding but not uptake into the cells [7]. Control nanoparticles without the ligand showed no specific accumulation on the surface of HEK cells, thus attributing this effect to the interaction of MLN and ACE2 (Fig. S13). This was also supported by the fact that areas on the cell surface that showed a strong ACE2 antibody signal showed a weak nanoparticle signal and vice versa, which suggests a competitive behavior at the ectoenzyme (Fig. 2C).

Chapter 4

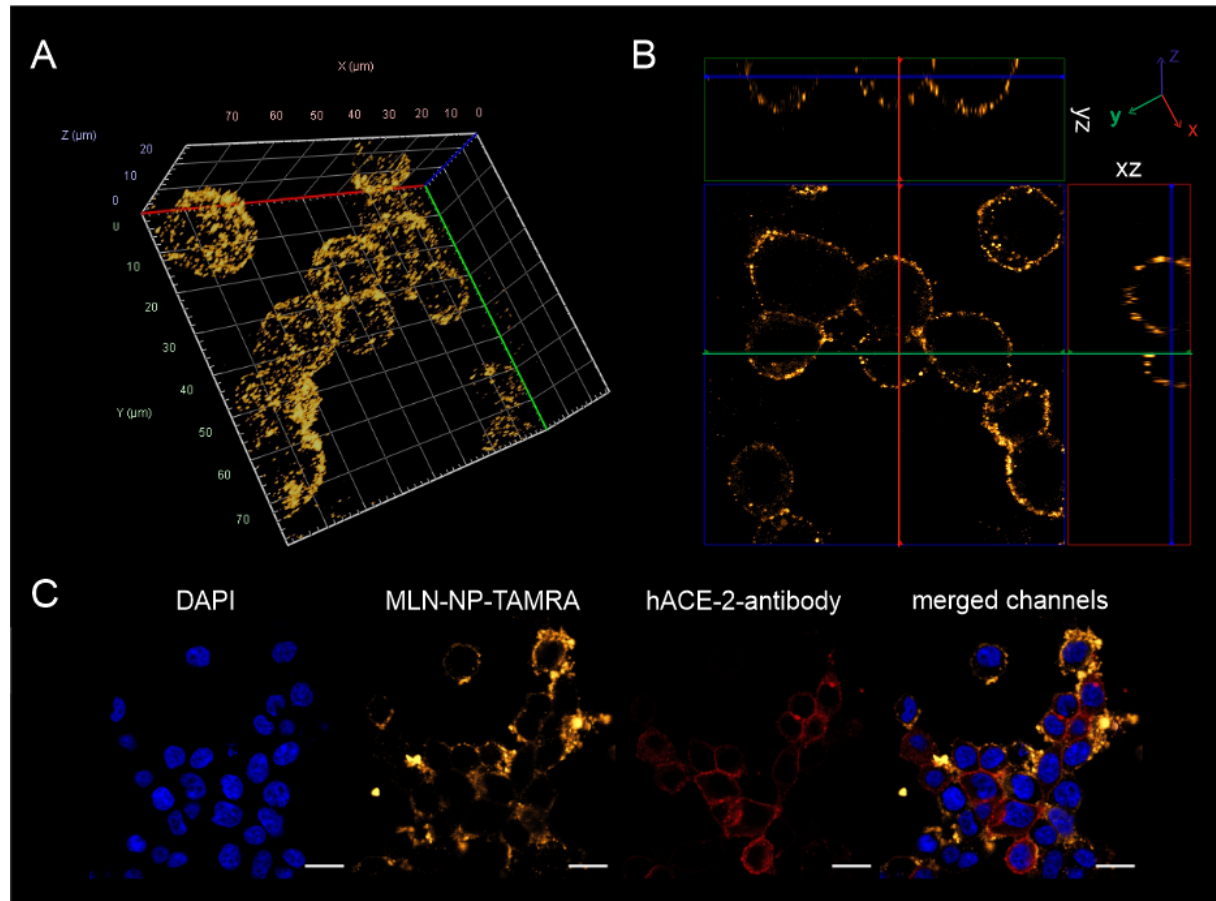


Figure 2. Cellular localization of MLN-NPs and ACE2 enzyme. (A) 3D-image of nanoparticle distribution. (B) Orthogonal view. (C) The localization of ACE2 on the cell surface was determined via staining with Alexa Fluor 647-labeled antibodies for hACE2 (red). Cell nuclei were stained with DAPI (blue) and MLN-NPs were core-labeled with TAMRA dye (yellow). The MLN-NPs were mainly localized on the cell membrane. Scale bar: 20 μ m.

3.3 Quantification of Nanoparticle Avidity

To quantitatively describe the interaction of MLN-NPs with ACE2, binding studies were performed with the soluble enzyme and additionally in a cell-based experiment with HEK293T cells stably expressing the enzyme of interest. We expected that nanoparticles are capable of multivalent binding, as they can interact with several enzymes simultaneously via multiple ligands coupled to their surface, the intensity of which is described as nanoparticle avidity [50]. Since the ligand surface density may have an impact on particle binding to the target enzyme, nanoparticles with different degrees of MLN-4760 modification were investigated via

Ectoenzymes as Cell Identification Structures

microscale thermophoresis measurements. To test particle effects like nonspecific binding or aggregation, unmodified nanoparticles served as a negative control.

A ligand density-dependent avidity of the MLN-NPs for the target enzyme was demonstrated (Fig. 3A-C). In contrast, the control nanoparticles showed no fluorescence change and thus no binding event (Fig. 3D). The more ligands were attached to the NP surface, the lower the K_d value and thus the higher the avidity of the nanoparticles for ACE2. The reduction of the ligand density on the NP surface by fifty percent was roughly accompanied by a 4-fold increase of the K_d value (50 %, 243 ± 96 pM; 25 % 1.06 ± 0.28 nM; 12.5 %, 3.85 ± 1.11 nM) (Fig. 3E).

The results are in line with reports in the literature regarding an optimal ligand density for nanoparticle binding and uptake, which can either increase with rising ligand density and plateau or decrease after exceeding the maximum [51]. The described effect and the obtained low K_d values can be attributed to nanoparticle multivalency, which counterbalances the affinity loss of a single ligand upon PEGylation [52]. Since several ligands are coupled to its surface, a nanoparticle can interact with several ACE2 enzymes. This is promoted by increasing the number of ligands. In addition, the probability of a ligand to encounter an enzyme is the higher, the more ligands are available for binding [52,53]. Too high ligand densities, however, can result in a steric hindrance, which decreases target recognition and binding [51]. Since MLN-4760 is a small molecule inhibitor this plays a minor role compared to proteins or other spacious ligands, which is consistent with the observation that higher ligand densities were consequently associated with a higher target avidity.

A compromise between nanoparticle avidity and the capacity of the corona leaves room for outfitting nanoparticles with additional ligands for the future. Since target cell identification via an enzyme inhibitor leads to cell binding but not cell uptake, additional uptake signals could be accommodated. Particle binding may thus represent the first step of a sequential uptake cascade. Another argument against excessively high ligand densities is that it may result in binding too many ectoenzymes per nanoparticle. The diminished availability of target structures for other nanoparticles could result in an overall reduced number of bound nanoparticles. Therefore, the following experiments were performed with a modification level of 25 %. This ensures high avidity, opens the possibility of coupling further ligands for a hetero-multivalent uptake process, and considers the aspect of multiple enzyme occupation by a single nanoparticle.

Chapter 4

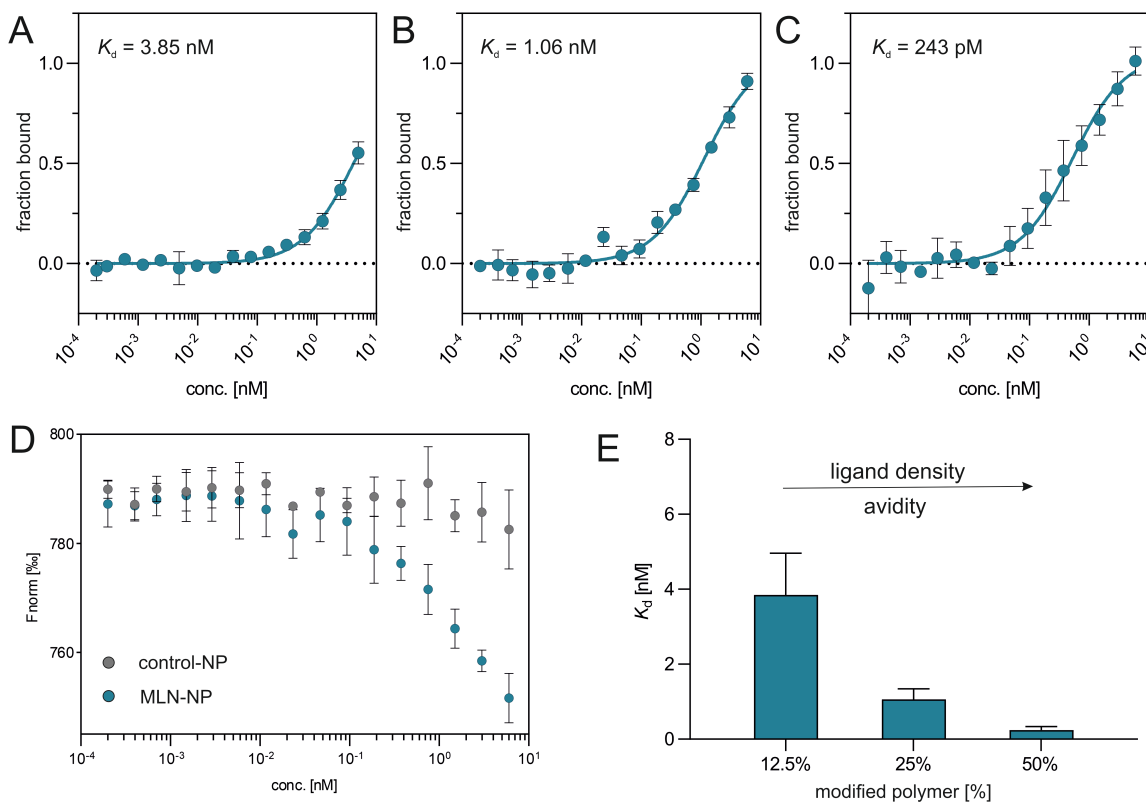


Figure 3. Microscale thermophoresis (MST) measurements of MLN-NPs and soluble ACE2 enzyme. (A-C) Show different ratios of modified to unmodified polymer: A 12.5 %; B 25 %; C 50 % modified polymer. The K_d values calculated are shown in the corresponding figures. **(D)** Control nanoparticles as negative control show no change in fluorescence intensity and thus no binding event. **(E)** K_d values calculated and relation between ligand density and particle avidity. Results are presented as mean \pm SD ($n = 3$).

Flow cytometry was used to quantify the avidity of MLN-modified nanoparticles for ACE2 on the target cell surface and thus to determine a cell-based K_d value. The binding of MLN-NPs to HEK293T-ACE2 cells was significantly higher than that of control particles (Fig. 4A). The evaluation of the MLN-NP binding under consideration of the nonspecific binding of nanoparticles to the cell surface resulted in a K_d value of 306.2 pM (Fig. 4B), which was in a similar range as the K_d value determined by MST for binding to the soluble enzyme. Thus, it can be concluded that the nanoparticles have high avidity for the soluble enzyme as well as for the respective enzyme-positive target cells and that the binding strength of nanoparticles targeting ectoenzymes is not inferior to particle-receptor interactions.

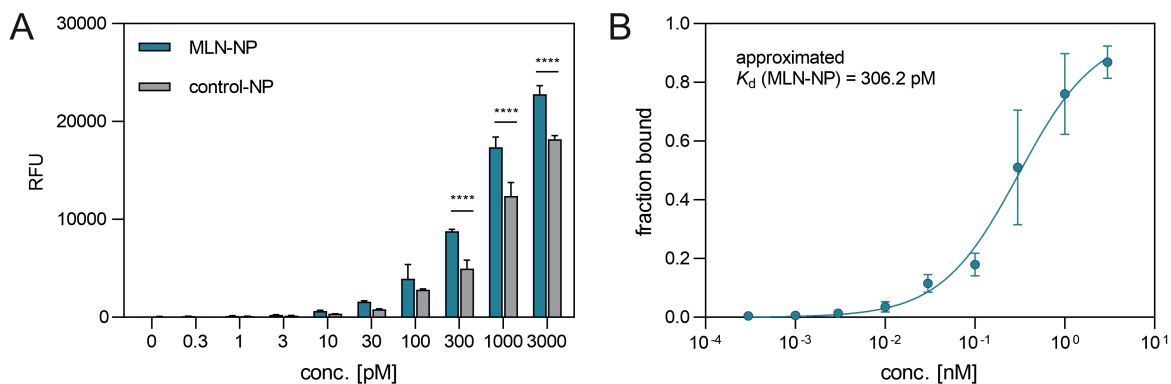


Figure 4. Determination of a cell-based dissociation constant. (A) Comparison binding activity of MLN-NPs and control-NPs after 30 min of incubation. (B) Binding curve of MLN-NPs to HEK293T-ACE2 cells under consideration of nonspecific nanoparticle binding. Results represent mean \pm SD ($n = 3$, levels of statistical significance are indicated as * $p \leq 0.05$, ** $p \leq 0.01$, *** $p \leq 0.001$, **** $p \leq 0.0001$) (RFU = relative fluorescence units).

3.4 Targeting Ability of MLN-modified Nanoparticles

To demonstrate that the MLN-modified nanoparticles not only exhibit high avidity for ACE2 but are also suitable for effective and reproducible target cell recognition, several cell experiments were performed to analyze the superiority over non-specific control particles.

In a first experiment, the time-dependence of the binding of MLN-NPs to HEK293T-ACE2 cells compared to control particles was analyzed by flow cytometry. The results showed that the fluorescence signal resulting from nanoparticle binding increased significantly faster for the MLN-4760 particles. A marked superiority of the MLN-NP binding was observed during the first 45 min. After 30 min of incubation, the fluorescence intensity was approximately 1.4-fold higher than the fluorescence of the control nanoparticles (Fig. 5A). While the signal increase for the targeted nanoparticles leveled off after 30 min, the fluorescence of the control particles rose in a linear manner over the entire investigation period of 120 min (Fig. 5A). Most likely, the control particles were subject to nonspecific uptake over time, while the targeted nanoparticles stayed tethered to ACE2 on the cell membrane, resulting in reduced nonspecific uptake. This hypothesis was supported by the fact that the effect vanished when cells were pre- and co-incubated with an excess of free MLN-4760. In this case, the ACE2 enzyme was blocked and no longer available as an anchoring protein. Thus, the fluorescence signal intensities between MLN-NPs and control nanoparticles were equalized.

Chapter 4

The reduced nonspecific uptake compared to control particles could also be confirmed by confocal scanning microscopy (Fig. S14). An incubation time of 30 min was chosen to compare the binding parameters of MLN-NPs with those of control particles to avoid an excessive effect of nonspecific uptake. To further confirm the target cell selectivity of the MLN-NPs, co-culture experiments were performed with ACE2-positive HEK293T cells and ACE2-negative HEK293 cells as off-target cells. A clear superiority of the MLN-modified NPs over the control particles was demonstrated for target cell recognition. This effect was observable for co-cultures with equal amounts of both cell types (50/50), as well as with a 90 % excess of off-target cells (10/90) (Fig. 5B).

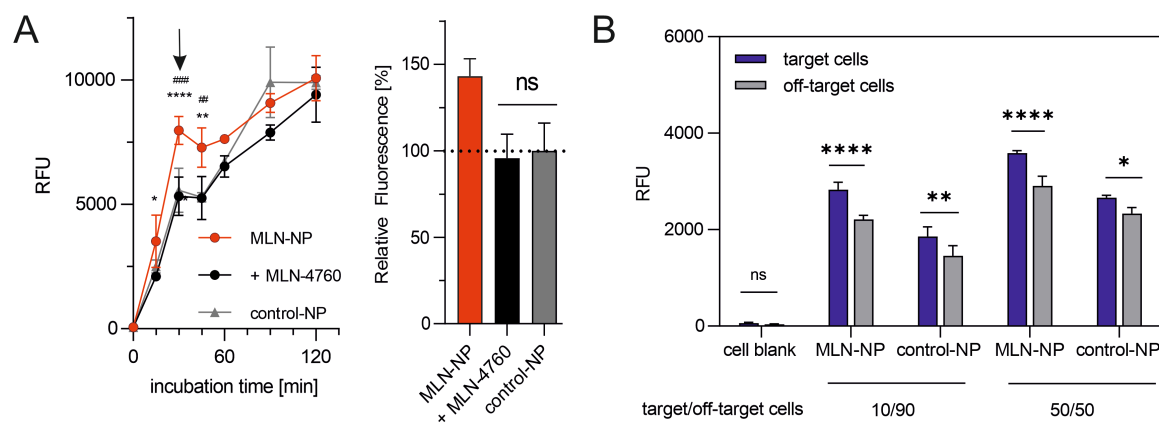


Figure 5. Flow cytometric measurements of MLN-NPs with HEK293T-ACE2 target cells and in co-culture with untransfected HEK cells as off-target cells. (A) Nanoparticle binding/uptake over time. (B) Comparison of NP binding behavior in co-culture experiments with target cells (HEK293T-ACE2) and off-target cells (HEK293). Results represent mean \pm SD ($n = 3$, levels of statistical significance are indicated as (A) * $p \leq 0.05$, ** $p \leq 0.01$, *** $p \leq 0.001$, **** $p \leq 0.0001$ compared to untargeted control NPs and # $p \leq 0.05$, ## $p \leq 0.01$, ### $p \leq 0.001$, ##### $p \leq 0.0001$ compared to target cells pre- and co-incubated with an excess of free MLN-4760 and (B) * $p \leq 0.05$, ** $p \leq 0.01$, *** $p \leq 0.001$, **** $p \leq 0.0001$ binding to target cells HEK293T-ACE2 cells compared to HEK293 control cells (RFU = relative fluorescence units).

3.5 Determination of the IC_{50} Value of MLN-NPs

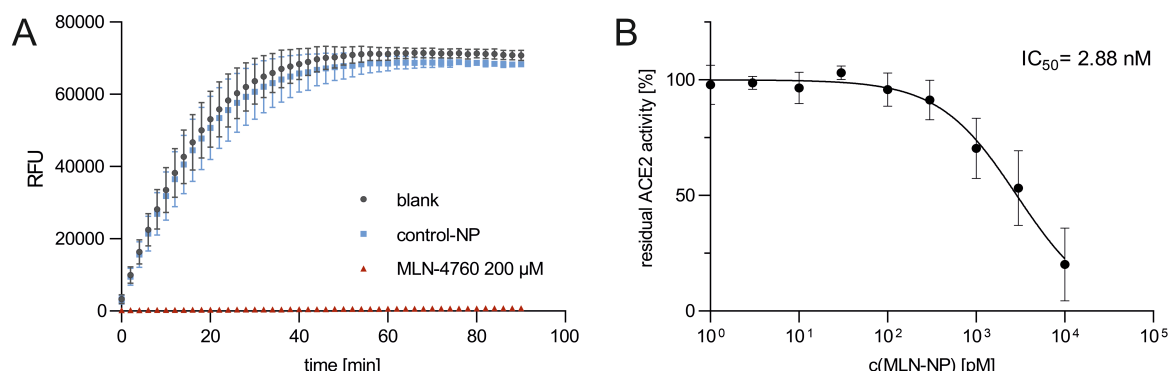


Figure 6. Determination of the IC_{50} value of MLN-NPs via an ACE2 activity assay with HEK293T-ACE2 cells. The residual enzyme activity after incubation with different NP concentrations was determined by the decrease in cleavage activity for a fluorogenic substrate of ACE2. An IC_{50} value of 2.88 nM was calculated. **(A)** An excess of free inhibitor (200 μ M) served as positive control for the enzyme inhibition and control-NPs served as negative control. **(B)** Curve fitted for the determination of the IC_{50} value. Results are presented as mean \pm SD of $n = 3$ experiments; (RFU = relative fluorescence units).

An ACE2 activity assay was performed to assess the inhibitory activity of MLN-NPs on target cells and as additional proof of the ligand activity on the nanoparticle surface (Fig. 6). For this purpose, ACE2-expressing cells were incubated with MLN-NPs for 1 hour. Control-NPs served as negative control and showed no enzyme inhibition. Free MLN-4760 in excess (200 μ M) served as positive control for the enzyme inhibition. The resulting IC_{50} value was 2.88 nM. The calculated value was higher than that of the free ligand, which has an IC_{50} value of 440 pM [54] but was in a comparable range. Overall, particle avidity, and thus the correlated activity, is the result of two counteracting effects: first, there is a loss of affinity of the ligand due to PEGylation as the spatial structure was changed and the ligand by itself fits less well into the binding pocket of the enzyme. Then, the multivalent binding of nanoparticles compensates the affinity loss and increases particle avidity [52]. The determined IC_{50} value was also in agreement with previously published studies on values for nanoparticles with similarly potent small molecule inhibitors covalently bound to the nanoparticle surface [55].

Considering that MLN-NPs have an inhibitory effect on ACE2, the enzyme targeting does not directly trigger a signaling cascade but may result in decreased substrate cleavage and therefore

Chapter 4

lead to indirect effects. ACE2 interacts in the renin-angiotensin-aldosterone system (RAAS) as a counterbalance to the ACE enzyme. Its task is to cleave the vasoconstrictive angiotensin II and its precursor angiotensin I to degrade it. Therefore, vasodilatory effects can be attributed to ACE2 [56]. Since the blockade due to nanoparticle interaction is temporary and of limited extent, it can be assumed that substrate cleavage can be compensated by non-blocked enzymes. Biological effects are therefore not expected. Furthermore, the long-term effects of low-dose therapy with MLN have been studied by Berenyiova et al. (2021) [57]. They concluded that even though MLN has pro-obesogenic effects on small arteries, there are compensatory mechanisms of larger arteries and probably other tissues. It was observed that even chronic low-dose treatment does not lead to an overall reduced ACE2 activity and an increase in blood pressure and that there were even significant NO and H₂S-mediated beneficial cardiovascular mechanisms [57]. Thus, it can be assumed that the application of MLN as a targeting structure on the nanoparticle surface is unproblematic and any indirect effects can be reversed by endogenous counter-regulation mechanisms. However, since there are only limited data available, further *in vivo* studies are necessary to evaluate the long-term effects of ACE2 inhibition by nanoparticles.

Finally, we want to mention a previous study by Sanna et al. who developed targeted nanoparticles for antiviral therapy against SARS-CoV-2 [38]. They tethered various ACE2 ligands to the corona of polymer nanoparticles to develop a drug delivery system. In contrast, our goal was to quantify the multivalent binding of MLN-4760-modified nanoparticles to target cells carrying the ectoenzyme. The picomolar particle avidities unequivocally demonstrate that ACE2 is a highly attractive target for cell identification beyond antiviral therapy that promises high target cell specificity.

4 Conclusion

The investigated nanoparticles showed excellent avidity for soluble ACE2 and ACE2-positive target cells, thus providing a promising system for selective drug delivery without triggering adverse effects through target cell identification via ligand-receptor interactions. The covalent coupling of MLN-4760 to the nanoparticle corona enabled selective target cell identification even in the presence of an excess of off-target cells.

The inhibitory activity of MLN-NPs on the target enzyme was quantified using a fluorogenic assay. Since the inhibition of ACE2 is limited in time and cell number, it can be assumed that biological effects resulting from the usage of ACE2 as a targeting structure can be compensated by endogenous mechanisms and are thus negligible.

These findings strongly support that ectoenzymes are highly suitable for target cell recognition and enable cell identification in active nanoparticle targeting with fewer side effects. Not only particle binding but also uptake could be mediated via the introduction of additional ligands that interact with ectoenzymes via sequential uptake mechanisms.

Thus, the described concept represents a viable alternative to current targeting strategies addressing receptors such as GPCRs or integrins and allows for selective and side effect-free active nanoparticle targeting.

Chapter 4

References

- [1] T.M. Allen, P.R. Cullis, Drug delivery systems: entering the mainstream, *Science* 303 (2004) 1818–1822. <https://doi.org/10.1126/science.1095833>.
- [2] G.T. Tietjen, L.G. Bracaglia, W.M. Saltzman, J.S. Pober, Focus on Fundamentals: Achieving Effective Nanoparticle Targeting, *Trends in Molecular Medicine* 24 (2018) 598–606. <https://doi.org/10.1016/j.molmed.2018.05.003>.
- [3] M. Sousa de Almeida, E. Susnik, B. Drasler, P. Taladriz-Blanco, A. Petri-Fink, B. Rothen-Rutishauser, Understanding nanoparticle endocytosis to improve targeting strategies in nanomedicine, *Chemical Society Reviews* 50 (2021) 5397–5434. <https://doi.org/10.1039/D0CS01127D>.
- [4] J. Yoo, C. Park, G. Yi, D. Lee, H. Koo, Active Targeting Strategies Using Biological Ligands for Nanoparticle Drug Delivery Systems, *Cancers* 11 (2019) 640. <https://doi.org/10.3390/cancers11050640>.
- [5] Z.J. Deng, M. Liang, M. Monteiro, I. Toth, R.F. Minchin, Nanoparticle-induced unfolding of fibrinogen promotes Mac-1 receptor activation and inflammation, *Nature Nanotech* 6 (2011) 39–44. <https://doi.org/10.1038/nnano.2010.250>.
- [6] Q. Zhang, B.M. Reinhard, Ligand Density and Nanoparticle Clustering Cooperate in the Multivalent Amplification of Epidermal Growth Factor Receptor Activation, *ACS Nano* 12 (2018) 10473–10485. <https://doi.org/10.1021/acsnano.8b06141>.
- [7] W. Hild, K. Pollinger, A. Caporale, C. Cabrele, M. Keller, N. Pluym, A. Buschauer, R. Rachel, J. Tessmar, M. Breunig, A. Goepferich, G protein-coupled receptors function as logic gates for nanoparticle binding and cell uptake, *Proc. Natl. Acad. Sci. U. S. A.* 107 (2010) 10667–10672. <https://doi.org/10.1073/pnas.0912782107>.
- [8] R. Hennig, K. Pollinger, J. Tessmar, A. Goepferich, Multivalent targeting of AT1 receptors with angiotensin II-functionalized nanoparticles, *Journal of Drug Targeting* 23 (2015) 681–689. <https://doi.org/10.3109/1061186X.2015.1035276>.
- [9] P.-H. Wu, Y. Onodera, Y. Ichikawa, E.B. Rankin, A.J. Giaccia, Y. Watanabe, W. Qian, T. Hashimoto, H. Shirato, J.-M. Nam, Targeting integrins with RGD-conjugated gold nanoparticles in radiotherapy decreases the invasive activity of breast cancer cells, *Int. J. Nanomedicine* 12 (2017) 5069–5085. <https://doi.org/10.2147/IJN.S137833>.
- [10] T.-M. Cheng, W.-J. Chang, H.-Y. Chu, R. de Luca, J.Z. Pedersen, S. Incerpi, Z.-L. Li, Y.-J. Shih, H.-Y. Lin, K. Wang, J. Whang-Peng, Nano-Strategies Targeting the Integrin $\alpha v\beta 3$

Ectoenzymes as Cell Identification Structures

Network for Cancer Therapy, Cells 10 (2021) 1684. <https://doi.org/10.3390/cells10071684>.

[11] G. Liu, J. Mao, Z. Jiang, T. Sun, Y. Hu, Z. Jiang, C. Zhang, J. Dong, Q. Huang, Q. Lan, Transferrin-modified Doxorubicin-loaded biodegradable nanoparticles exhibit enhanced efficacy in treating brain glioma-bearing rats, *Cancer Biother. Radiopharm.* 28 (2013) 691–696. <https://doi.org/10.1089/cbr.2013.1480>.

[12] M. Luo, G. Lewik, J.C. Ratcliffe, C.H.J. Choi, E. Mäkilä, W.Y. Tong, N.H. Voelcker, Systematic Evaluation of Transferrin-Modified Porous Silicon Nanoparticles for Targeted Delivery of Doxorubicin to Glioblastoma, *ACS Appl. Mater. Interfaces* 11 (2019) 33637–33649. <https://doi.org/10.1021/acsami.9b10787>.

[13] W. Wang, Y. Qiao, Z. Li, New Insights into Modes of GPCR Activation, *Trends in Pharmacological Sciences* 39 (2018) 367–386. <https://doi.org/10.1016/j.tips.2018.01.001>.

[14] P.D. Ramírez-García, J.S. Retamal, P. Shenoy, W. Imlach, M. Sykes, N. Truong, L. Constandil, T. Pelissier, C.J. Nowell, S.Y. Khor, L.M. Layani, C. Lumb, D.P. Poole, T. Lieu, G.D. Stewart, Q.N. Mai, D.D. Jensen, R. Latorre, N.N. Scheff, B.L. Schmidt, J.F. Quinn, M.R. Whittaker, N.A. Veldhuis, T.P. Davis, N.W. Bennett, A pH-responsive nanoparticle targets the neurokinin 1 receptor in endosomes to prevent chronic pain, *Nat. Nanotechnol.* 14 (2019) 1150–1159. <https://doi.org/10.1038/s41565-019-0568-x>.

[15] R. Hennig, A. Ohlmann, J. Staffel, K. Pollinger, A. Haunberger, M. Breunig, F. Schweda, E.R. Tamm, A. Goepferich, Multivalent nanoparticles bind the retinal and choroidal vasculature, *J. Control. Release* 220 (2015) 265–274. <https://doi.org/10.1016/j.jconrel.2015.10.033>.

[16] A.C. Hanyaloglu, M. von Zastrow, Regulation of GPCRs by endocytic membrane trafficking and its potential implications, *Annu. Rev. Pharmacol. Toxicol.* 48 (2008) 537–568. <https://doi.org/10.1146/annurev.pharmtox.48.113006.094830>.

[17] C. Williams, S.J. Hill, GPCR Signaling: Understanding the Pathway to Successful Drug Discovery, in: G Protein-Coupled Receptors in Drug Discovery, Humana Press, Totowa, NJ, 2009, pp. 39–50.

[18] H. Kurose, S.G. Kim, Pharmacology of Antagonism of GPCR, *Biol. Pharm. Bull.* 45 (2022) 669–674. <https://doi.org/10.1248/bpb.b22-00143>.

[19] W. Wang, Y. Qiao, Z. Li, New Insights into Modes of GPCR Activation, *Trends in Pharmacological Sciences* 39 (2018) 367–386. <https://doi.org/10.1016/j.tips.2018.01.001>.

Chapter 4

[20] B. Geiger, A. Bershadsky, R. Pankov, K.M. Yamada, Transmembrane crosstalk between the extracellular matrix--cytoskeleton crosstalk, *Nat. Rev. Mol. Cell Biol.* 2 (2001) 793–805. <https://doi.org/10.1038/35099066>.

[21] M.H. Ginsberg, Integrin activation, *BMB Rep.* 47 (2014) 655–659. <https://doi.org/10.5483/BMBRep.2014.47.12.241>.

[22] R.O. Hynes, Integrins: bidirectional, allosteric signaling machines, *Cell* 110 (2002) 673–687. [https://doi.org/10.1016/S0092-8674\(02\)00971-6](https://doi.org/10.1016/S0092-8674(02)00971-6).

[23] F.G. Giancotti, E. Ruoslahti, Integrin signaling, *Science* 285 (1999) 1028–1032. <https://doi.org/10.1126/science.285.5430.1028>.

[24] K.R. Legate, S.A. Wickström, R. Fässler, Genetic and cell biological analysis of integrin outside-in signaling, *Genes Dev.* 23 (2009) 397–418. <https://doi.org/10.1101/gad.1758709>.

[25] D.J. Webb, K. Donais, L.A. Whitmore, S.M. Thomas, C.E. Turner, J.T. Parsons, A.F. Horwitz, FAK-Src signalling through paxillin, ERK and MLCK regulates adhesion disassembly, *Nat Cell Biol* 6 (2004) 154–161. <https://doi.org/10.1038/ncb1094>.

[26] J.L. Walker, A.K. Fournier, R.K. Assoian, Regulation of growth factor signaling and cell cycle progression by cell adhesion and adhesion-dependent changes in cellular tension, *Cytokine & growth factor reviews* 16 (2005) 395–405. <https://doi.org/10.1016/j.cytogfr.2005.03.003>.

[27] H.C. Chen, P.A. Appeddu, H. Isoda, J.L. Guan, Phosphorylation of tyrosine 397 in focal adhesion kinase is required for binding phosphatidylinositol 3-kinase, *The Journal of biological chemistry* 271 (1996) 26329–26334. <https://doi.org/10.1074/jbc.271.42.26329>.

[28] E. Gammella, P. Buratti, G. Cairo, S. Recalcati, The transferrin receptor: the cellular iron gate, *Metallomics*. 9 (2017) 1367–1375. <https://doi.org/10.1039/c7mt00143f>.

[29] Y. Shen, X. Li, D. Dong, B. Zhang, Y. Xue, P. Shang, Transferrin receptor 1 in cancer: a new sight for cancer therapy, *American Journal of Cancer Research* 8 (2018) 916–931.

[30] K.K. Stanley, A.C. Newby, J.P. Luzio, What do ectoenzymes do?, *Trends in Biochemical Sciences* 7 (1982) 145–147. [https://doi.org/10.1016/0968-0004\(82\)90207-9](https://doi.org/10.1016/0968-0004(82)90207-9).

[31] S.E. Henson, T.C. Nichols, V.M. Holers, D.R. Karp, The Ectoenzyme γ -Glutamyl Transpeptidase Regulates Antiproliferative Effects of S -Nitrosoglutathione on Human T and B Lymphocytes, *The Journal of Immunology* 163 (1999) 1845–1852. <https://doi.org/10.4049/jimmunol.163.4.1845>.

Ectoenzymes as Cell Identification Structures

[32] N.A. Dales, A.E. Gould, J.A. Brown, E.F. Calderwood, B. Guan, C.A. Minor, J.M. Gavin, P. Hales, V.K. Kaushik, M. Stewart, P.J. Tummino, C.S. Vickers, T.D. Ocain, M.A. Patane, Substrate-based design of the first class of angiotensin-converting enzyme-related carboxypeptidase (ACE2) inhibitors, *J. Am. Chem. Soc.* 124 (2002) 11852–11853. <https://doi.org/10.1021/ja0277226>.

[33] M. Andújar-Sánchez, V. Jara-Pérez, A. Cámara-Artigas, Thermodynamic determination of the binding constants of angiotensin-converting enzyme inhibitors by a displacement method, *FEBS Lett.* 581 (2007) 3449–3454. <https://doi.org/10.1016/j.febslet.2007.06.048>.

[34] C.B. Jackson, M. Farzan, B. Chen, H. Choe, Mechanisms of SARS-CoV-2 entry into cells, *Nat Rev Mol Cell Biol* 23 (2022) 3–20. <https://doi.org/10.1038/s41580-021-00418-x>.

[35] F. Hikmet, L. Méar, Å. Edvinsson, P. Micke, M. Uhlén, C. Lindskog, The protein expression profile of ACE2 in human tissues, *Mol. Syst. Biol.* 16 (2020) e9610. <https://doi.org/10.15252/msb.20209610>.

[36] T. Unger, U.M. Steckelings, R.A.S.d. Santos (Eds.), *The Protective Arm of the Renin Angiotensin System (RAS): Functional Aspects and Therapeutic Implications*, 1st ed., Elsevier Reference Monographs, s.l., 2015.

[37] Y. Li, W. Zhou, L. Yang, R. You, Physiological and pathological regulation of ACE2, the SARS-CoV-2 receptor, *Pharmacological Research* 157 (2020) 104833. <https://doi.org/10.1016/j.phrs.2020.104833>.

[38] V. Sanna, S. Satta, T. Hsiai, M. Sechi, Development of targeted nanoparticles loaded with antiviral drugs for SARS-CoV-2 inhibition, *Eur. J. Med. Chem.* 231 (2022) 114121. <https://doi.org/10.1016/j.ejmech.2022.114121>.

[39] H. Qian, A.R. Wohl, J.T. Crow, C.W. Macosko, T.R. Hoye, A Strategy for Control of "Random" Copolymerization of Lactide and Glycolide: Application to Synthesis of PEG-b-PLGA Block Polymers Having Narrow Dispersity, *Macromolecules* 44 (2011) 7132–7140. <https://doi.org/10.1021/ma201169z>.

[40] K. Abstiens, S. Maslanka Figueroa, M. Gregoritza, A.M. Goepferich, Interaction of functionalized nanoparticles with serum proteins and its impact on colloidal stability and cargo leaching, *Soft Matter* 15 (2019) 709–720. <https://doi.org/10.1039/C8SM02189A>.

[41] K. Abstiens, M. Gregoritza, A.M. Goepferich, Ligand Density and Linker Length are Critical Factors for Multivalent Nanoparticle-Receptor Interactions, *ACS Appl. Mater. Interfaces* 11 (2019) 1311–1320. <https://doi.org/10.1021/acsami.8b18843>.

Chapter 4

[42] M. Jerabek-Willemsen, T. André, R. Wanner, H.M. Roth, S. Duhr, P. Baaske, D. Breitsprecher, MicroScale Thermophoresis: Interaction analysis and beyond, *Journal of Molecular Structure* 1077 (2014) 101–113. <https://doi.org/10.1016/j.molstruc.2014.03.009>.

[43] S. Maslanka Figueroa, A. Veser, K. Abstiens, D. Fleischmann, S. Beck, A. Goepferich, Influenza A virus mimetic nanoparticles trigger selective cell uptake, *Proc. Natl. Acad. Sci. U. S. A.* 116 (2019) 9831–9836. <https://doi.org/10.1073/pnas.1902563116>.

[44] H.K. Makadia, S.J. Siegel, Poly Lactic-co-Glycolic Acid (PLGA) as Biodegradable Controlled Drug Delivery Carrier, *Polymers* 3 (2011) 1377–1397. <https://doi.org/10.3390/polym3031377>.

[45] S.C. Owen, D.P. Chan, M.S. Shoichet, Polymeric micelle stability, *Nano Today* 7 (2012) 53–65. <https://doi.org/10.1016/j.nantod.2012.01.002>.

[46] R.Z. Xiao, Z.W. Zeng, G.L. Zhou, J.J. Wang, F.Z. Li, A.M. Wang, Recent advances in PEG-PLA block copolymer nanoparticles, *Int. J. Nanomedicine* 5 (2010) 1057–1065. <https://doi.org/10.2147/IJN.S14912>.

[47] A. Verma, F. Stellacci, Effect of surface properties on nanoparticle-cell interactions, *Small* 6 (2010) 12–21. <https://doi.org/10.1002/smll.200901158>.

[48] A.J. Turner, N.N. Nalivaeva, Angiotensin-converting enzyme 2 (ACE2): Two decades of revelations and re-evaluation, *Peptides* 151 (2022) 170766. <https://doi.org/10.1016/j.peptides.2022.170766>.

[49] K.K. Stanley, A.C. Newby, J.P. Luzio, What do ectoenzymes do?, *Trends in Biochemical Sciences* 7 (1982) 145–147. [https://doi.org/10.1016/0968-0004\(82\)90207-9](https://doi.org/10.1016/0968-0004(82)90207-9).

[50] S. Hong, P.R. Leroueil, I.J. Majoros, B.G. Orr, J.R. Baker, M.M. Banaszak Holl, The binding avidity of a nanoparticle-based multivalent targeted drug delivery platform, *Chemistry & biology* 14 (2007) 107–115. <https://doi.org/10.1016/j.chembiol.2006.11.015>.

[51] A.M. Alkilany, L. Zhu, H. Weller, A. Mews, W.J. Parak, M. Barz, N. Feliu, Ligand density on nanoparticles: A parameter with critical impact on nanomedicine, *Adv. Drug Deliv. Rev.* 143 (2019) 22–36. <https://doi.org/10.1016/j.addr.2019.05.010>.

[52] R. Hennig, K. Pollinger, A. Veser, M. Breunig, A. Goepferich, Nanoparticle multivalency counterbalances the ligand affinity loss upon PEGylation, *J. Control. Release* 194 (2014) 20–27. <https://doi.org/10.1016/j.jconrel.2014.07.062>.

Ectoenzymes as Cell Identification Structures

[53] X. Montet, M. Funovics, K. Montet-Abou, R. Weissleder, L. Josephson, Multivalent effects of RGD peptides obtained by nanoparticle display, *J. Med. Chem.* 49 (2006) 6087–6093. <https://doi.org/10.1021/jm060515m>.

[54] Vincent Dive, Cheng-Fu Chang, Athanasios Yiotakis, Edward D. Sturrock, Inhibition of Zinc Metallopeptidases in Cardiovascular Disease - From Unity to Trinity, or Duality?, *Current Pharmaceutical Design* 15 3606–3621.

[55] D. Fleischmann, S. Maslanka Figueroa, S. Beck, K. Abstiens, R. Witzgall, F. Schweda, P. Tauber, A. Goepferich, Adenovirus-Mimetic Nanoparticles: Sequential Ligand-Receptor Interplay as a Universal Tool for Enhanced In Vitro/In Vivo Cell Identification, *ACS Appl. Mater. Interfaces* 12 (2020) 34689–34702. <https://doi.org/10.1021/acsami.0c10057>.

[56] M. Gheblawi, K. Wang, A. Viveiros, Q. Nguyen, J.-C. Zhong, A.J. Turner, M.K. Raizada, M.B. Grant, G.Y. Oudit, Angiotensin-Converting Enzyme 2: SARS-CoV-2 Receptor and Regulator of the Renin-Angiotensin System: Celebrating the 20th Anniversary of the Discovery of ACE2, *Circ. Res.* 126 (2020) 1456–1474. <https://doi.org/10.1161/CIRCRESAHA.120.317015>.

[57] A. Berenyiova, I. Bernatova, A. Zemancikova, M. Drobna, M. Cebova, S. Golas, P. Balis, S. Liskova, Z. Valaskova, K. Krskova, S. Zorad, E. Dayar, S. Cacanyiova, Vascular Effects of Low-Dose ACE2 Inhibitor MLN-4760-Benefit or Detriment in Essential Hypertension?, *Biomedicines* 10 (2021). <https://doi.org/10.3390/biomedicines10010038>.

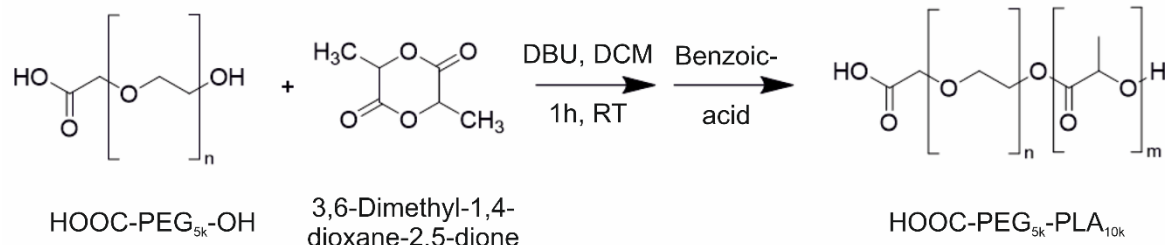
Chapter 4

Chapter 4

Supporting Information

Chapter 4 – Supporting Information

1 Synthesis and Characterization of PLA-PEG Block Copolymers



Scheme S1. Synthesis of PLA-PEG block copolymers via ring-opening polymerization. Synthesis of PLA-PEG-MeO block copolymer for control-NPs analog with methoxy polyethylene glycol 5000 Da as macroinitiator. The synthesis was performed after Qian et al. (2011) [3] with slight modifications previously described by our group [4].

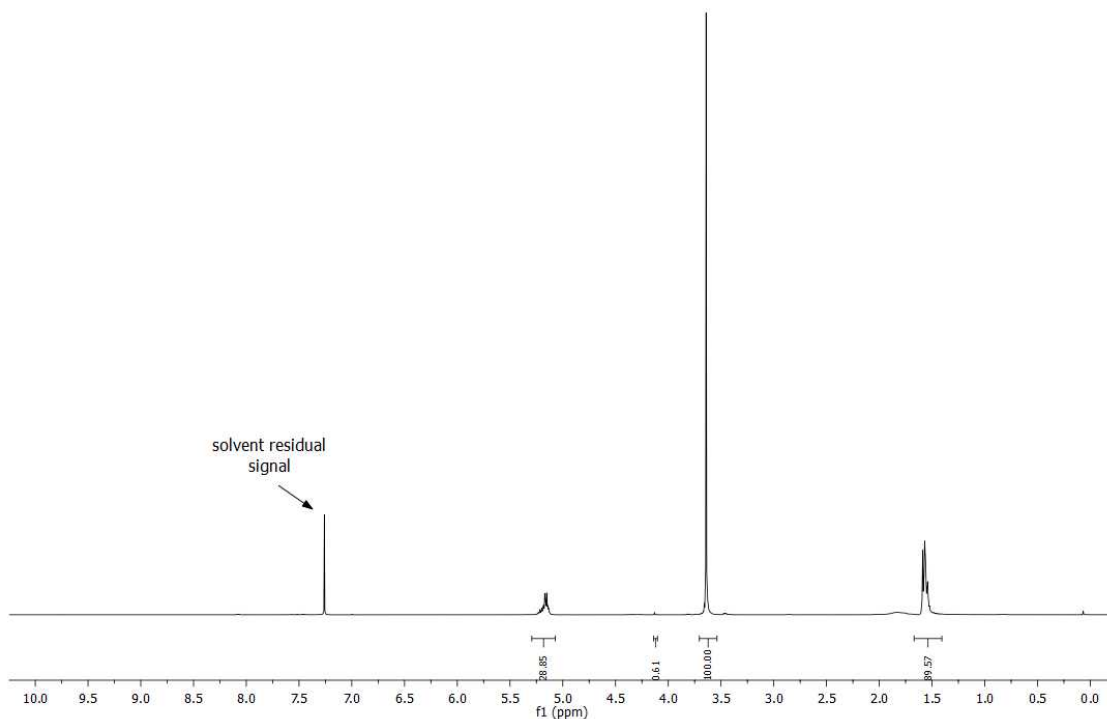


Figure S1. $^1\text{H-NMR}$ spectrum of $\text{PLA}_{10k}\text{-PEG}_{5k}\text{-COOH}$. $^1\text{H-NMR}$ (400 MHz, CDCl_3) δ (ppm) 5.30 - 5.06 (m, 29H) ($-\text{CH}_3\text{H}-$); 4.13 (s, 1H) ($-\text{OCH}_2\text{CH}_2\text{-O}(\text{CO})-$); 3.64 (s, 100H) ($-\text{OCH}_2\text{CH}_2-$); 1.60 - 1.37 (m, 90H) ($-\text{C}(\text{CH}_3)\text{H}-$). PEG (5000 Da) signal normalized to an integral area of 100. Integrating the PLA peaks resulted in a total molecular weight of the polymer of 14989 Da.

Chapter 4 – Supporting Information

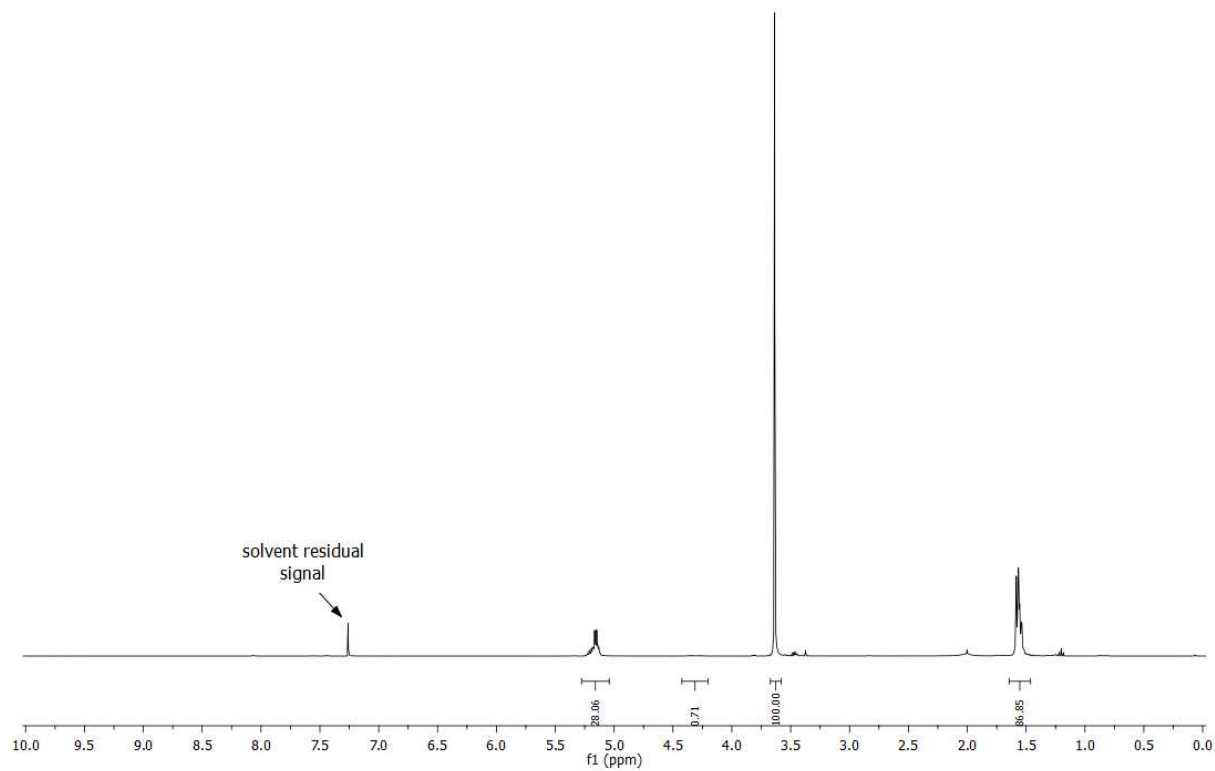


Figure S2. ^1H -NMR spectrum of $\text{PLA}_{10\text{k}}\text{-PEG}_{5\text{k}}\text{-MeO}$. ^1H -NMR (400 MHz, CDCl_3) δ (ppm): 5.31 – 5.02 (m, 28H) $(-\text{CH}_3\text{H}-)$; 4.44 – 4.18 (m, 1H) $(-\text{OCH}_2\text{CH}_2\text{-O}(\text{CO})-)$; 3.64 (s, 100H) $(-\text{OCH}_2\text{CH}_2-)$; 1.65 – 1.45 (m, 87H) $(-\text{C}(\text{CH}_3)\text{H}-)$. PEG (5000 Da) signal normalized to an integral area of 100. Integrating the PLA peaks resulted in a total molecular weight of the polymer of 14706 Da.

2 Proof of Concept for Coupling the ACE2 Inhibitor MLN-4760 to the Block-Copolymer

2.1 Coupling of MLN-4760 to an Oligoethylene Glycole (OEG)

2-[2-(2-Methoxyethoxy)ethoxy]acetic acid (oligoethylene glycole, OEG) was obtained from TCI chemicals (Tokyo, Japan).

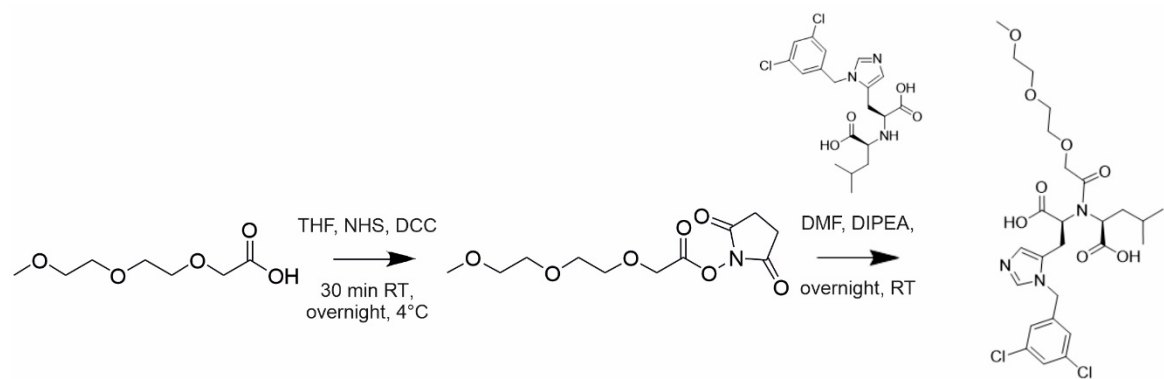
In the first step, OEG was activated to *N*-hydroxysuccinimidyl 2-[2-(2-methoxyethoxy)ethoxy]acetate (OEG-OSu) after Meißler et al. (2016) [5]. OEG-OSu (278 mg, 1.56 mmol) and *N*-hydroxysuccinimid (NHS) (205 mg, 1.78 mmol) were dissolved in tetrahydrofuran (THF) (10 mL) in a round-bottom flask and cooled in an ice water bath (0 °C). *N,N*'-Dicyclohexylcarbodiimid (DCC) (333 mg, 1.61 mmol) was added under stirring and the reaction was stirred for 30 min at RT. Afterward, the round-bottom flask was stored in the refrigerator overnight (4 °C). The formed precipitate *N,N*'-dicyclohexylurea was removed by filtration. The clear solution was evaporated on the rotary evaporator under reduced pressure, resulting in a colorless oil. This oil was dissolved in THF, resulting in a suspension. The precipitate was removed by filtration and the process described was repeated until the solution remains clear after the addition of THF. The solvent was evaporated, and the reaction product was dried overnight under vacuum.

The resulting product **OEG-OSu** was a colorless oil. (133.6 mg, 27.7 %) ¹H-NMR (300 MHz, CDCl₃) δ (ppm) 4.45 (s, 2H), 3.76 – 3.69 (m, 2H), 3.65 – 3.56 (m, 4H), 3.52 – 3.46 (m, 2H), 3.31 (s, 3H), 2.79 (s, 4H). *m/z* [M+H⁺] calculated for C₁₁H₁₇NO₇⁺ (OEG-OSu): 276.1078, found 276.1080.

For ligand coupling, MLN-4760 (0.33 mg, 0.77 μmol) was dissolved in DMF (193 μL) with a 10-fold excess of OEG-OSu. DIPEA was diluted 1:10 in DMF and added to the reaction together with 100 μL of DMF (13.5 μL). After shaking overnight at RT, the synthesis was quenched by adding 50 μL of 10 % TFA. Shaking was continued for further 15 min. The purification was carried out by preparative high-performance liquid chromatography (HPLC). Preparative HPLC was performed with a system from Waters (Eschborn, Germany) consisting of a Waters 2545 binary gradient module, a Waters 2489 UV/Vis-detector, a Waters Fraction Collector 3, and the column was a Phenomenex Gemini (250 × 21 mm, 5 μm) (Phenomenex, Aschaffenburg, Germany) at a flow rate of 20 mL/min. As a mobile phase, 0.1 % aqueous (aq.) TFA was used. The UV detection was carried out at 220 nm.

Chapter 4 – Supporting Information

The title compound **OEG-MLN** was analyzed via ¹H-NMR (Fig. S5) and high-resolution mass spectrometry (HRMS). ¹H-NMR (600 MHz, CD₃OD) δ 8.67 (s, 2H), 7.51 – 7.38 (m, 3H), 7.29 - 7.23 (m, 2H), 5.51 (s, 2H), 4.42 - 4.38 (m, 1H), 4.02 (d, *J* = 13.7 Hz, 1H), 3.75 - 3.43 (m, 13H), 3.42 - 3.41 (m, 1H), 3.19 - 3.17 (m, 1H), 1.61 - 1.55 (m, 2H), 1.17 (t, *J* = 7.0 Hz, 1H), 0.91 - 0.81 (m, 6H). *m/z* [M-H⁻] calculated for C₂₆H₃₅Cl₂N₃O₈⁻ (OEG-MLN): 586.1728, found 586.1735.



Scheme S2. Coupling of MLN-4760 to OEG. Activation of the carboxylic acid to an NHS ester (OEG-OSu) with subsequent coupling of the ligand (OEG-MLN).

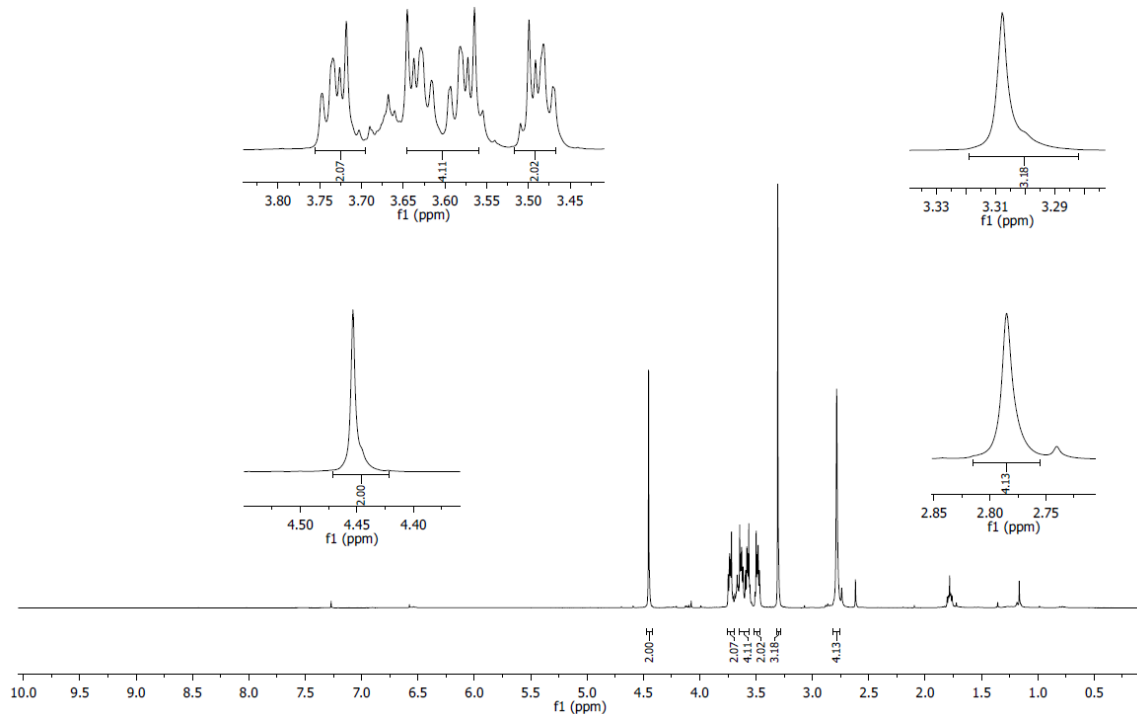


Figure S3. ^1H -NMR spectrum of OEG-OSu. ^1H -NMR (300 MHz, CDCl_3) δ (ppm) 4.45 (s, 2H), 3.76 - 3.69 (m, 2H), 3.65 - 3.56 (m, 4H), 3.52 - 3.46 (m, 2H), 3.31 (s, 3H), 2.79 (s, 4H).

The reaction product was dissolved in DMSO and transferred into HPLC vials. The stability was checked via purity measurements at different points in time: day 1, 7, 14, 28, 42, and 60 for nanoparticle storage conditions (4°C) and at room temperature (25°C). The analytical purity control was performed with a 1100 HPLC system from Agilent Technologies (Waldbronn, Germany) equipped with an instant pilot controller, a G1212A binary pump, a G1239A ALS autosampler, a G1279A vacuum degasser, a G1216A column compartment, and a G1215b diode array detector. The column was a Phenomenex Gemini NX-C18 column (250 x 4.6 mm 2.5 μM) (Phenomenex, Aschaffenburg, Germany). The oven temperature during HPLC analysis was 30°C . As a mobile phase, 0.05 % trifluoracetic acid (TFA) in millipore water and acetonitrile were used. Absorbance was detected at 220 nm. The following linear gradient was applied: acetonitrile/TFA (0.05 %) (v/v) 0 min: 10:90, 25 min: 95:5; flow rate: 1.0 mL/min. OEG-MLN showed a constant retention time of 12.7 min. The product showed first small degradations at room temperature after 14 days. Under nanoparticle storage conditions (4°C), OEG-MLN was stable until the end of the stability study on day 60. Thus, it can be

Chapter 4 – Supporting Information

concluded that MLN remains stably covalently bound to the nanoparticle surface under storage condition and no release of free ligand occurs.

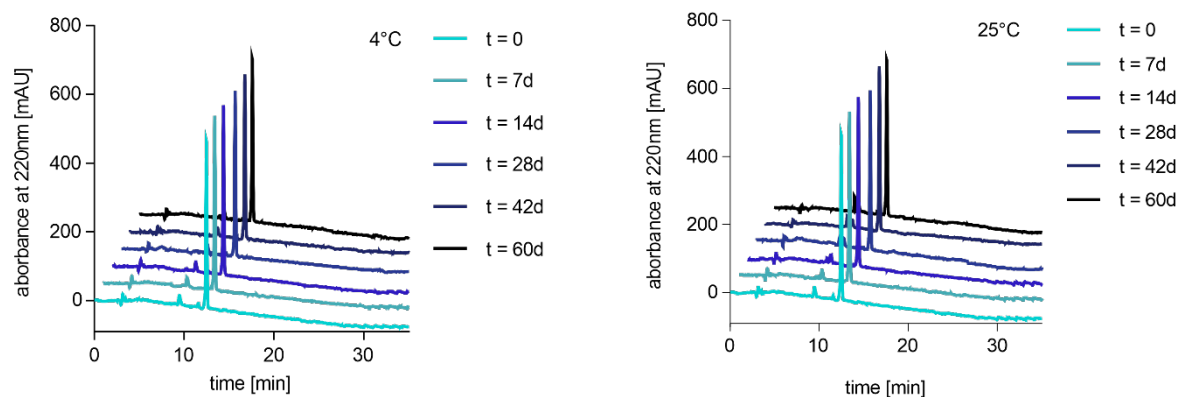


Figure S4. Stability measurements of OEG-MLN. Stability of the reaction product was determined via HPLC under storage conditions (4 °C) and at room temperature (25 °C) for a time period of two months.

Supporting Information - Ectoenzymes as Cell Identification Structures

2.2 Characterization of PLA_{10k}-PEG_{5k}-MLN

Since the analysis of the small molecule coupled to the polymer could not be performed directly, the polymer was hydrolyzed, and the hydrolysis-stable ligand was detected by mass spectrometry. UV spectroscopy was used to detect the presence of MLN-4760 bound to the polymer before hydrolysis and to monitor the success of the hydrolysis of the polymer before mass spectrometry. UV/Vis spectra were recorded using a NanoDrop 1000 UV/Vis Spectrophotometer (Thermo Fisher, Waltham, MA, USA).

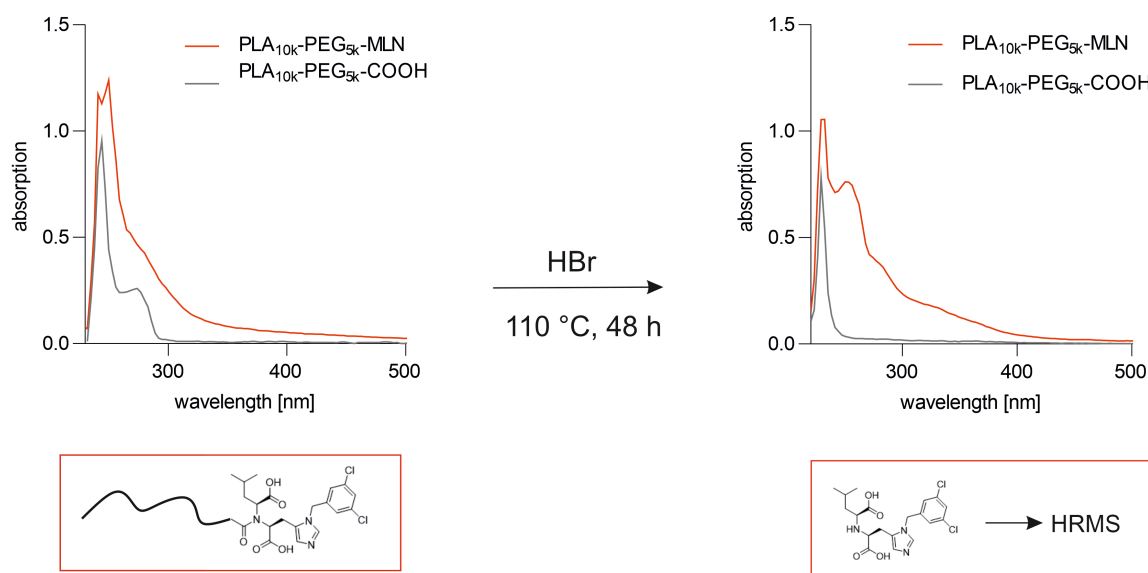


Figure S5. Absorption spectrum of modified and unmodified polymer pre- and post-hydrolysis with hydrobromic acid (HBr) at 110 °C for 48 h.

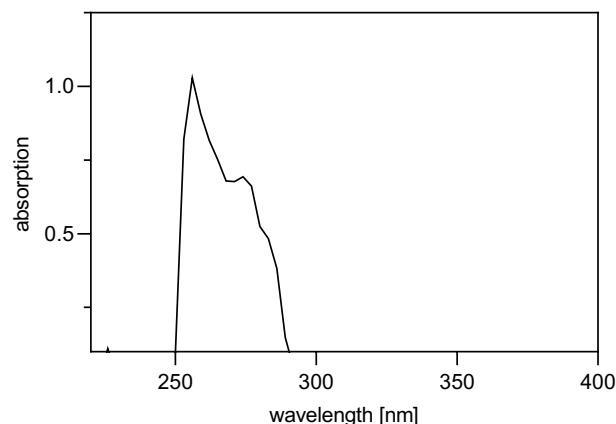


Figure S6. Absorption spectrum of MLN-4760 with DMSO blank subtracted.

Chapter 4 – Supporting Information

The UV spectra of both the hydrolyzed and the unhydrolyzed polymers showed clear differences compared to the control polymer. While the absorption spectrum of the unmodified polymer showed a clear peak at approximately 250 nm and a distinct shoulder at approximately 280 nm, the absorption spectrum of the MLN-modified polymer showed a double peak at 250 nm and no shoulder was visible. Instead, the absorption decreased at higher wavelengths. After the hydrolysis reaction, the absorption spectrum of the unmodified polymer showed a single peak that shifted to lower wavelengths (approx. 220 nm) compared to the absorption maximum of the unhydrolyzed polymer. In addition to the peak of the hydrolyzed polymer at approx. 220 nm, a second peak at around 250 nm was visible for the hydrolyzed MLN-modified polymer, corresponding to the absorption maximum of MLN-4760 at 256 nm (Fig. S5, Fig. S6). The presence of free MLN after polymer hydrolysis was further confirmed by mass spectrometry.

HRMS analysis of hydrolyzed polymer

Analysis of MLN-4760 (coupled ligand): (M-H)⁻ *m/z* calculated: 426.0993, found: 426.0992.

3 Nanoparticle Preparation and Characterization

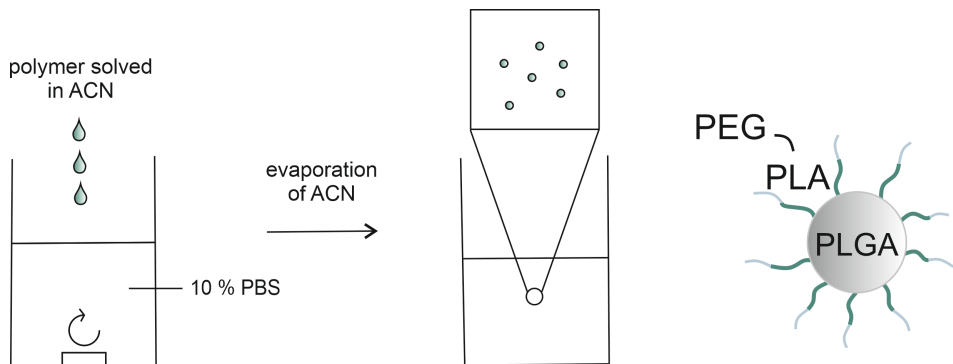


Figure S7. Scheme of nanoparticle preparation via nanoprecipitation. Core and shell polymers were solved in acetonitrile (ACN) and added dropwise into stirring 10 % PBS. After evaporation of the organic solvent, the nanoparticles were dispersed in the aqueous phase.

The MLN-modified nanoparticles and the control particles (Fig. S8A) showed a comparable size of about 100 nm (Fig. S8D, Fig. S9) and a polydispersity index (PDI) between 0.1 and 0.2, determined via dynamic light scattering (DLS). To confirm the nanoparticle sizes analyzed by DLS, nanoparticle tracking analysis (NTA) was performed as an orthogonal method, resulting in 93.3 nm for MLN-NPs and 92.0 nm for control nanoparticles (Fig. S8B, Fig. S10). The slight differences in nanoparticle size resulted from the differences in the analysis methods. While the NTA provides a number-weighted distribution, the DLS analysis is intensity-weighted. Therefore, larger particles are considered to a higher extent [6]. Since the size measurements of DLS and NTA hardly differ from each other, a narrow size distribution without aggregates can be assumed. This is also supported by the low polydispersity index (0.1-0.2) measured by DLS.

Stability analysis in PBS and Leibovitz medium for cell culture experiments showed no tendency toward aggregation under experimental conditions (Fig. S8D), which was expected due to the negative zeta potential of -18.7 mV (Fig. S8C).

Chapter 4 – Supporting Information

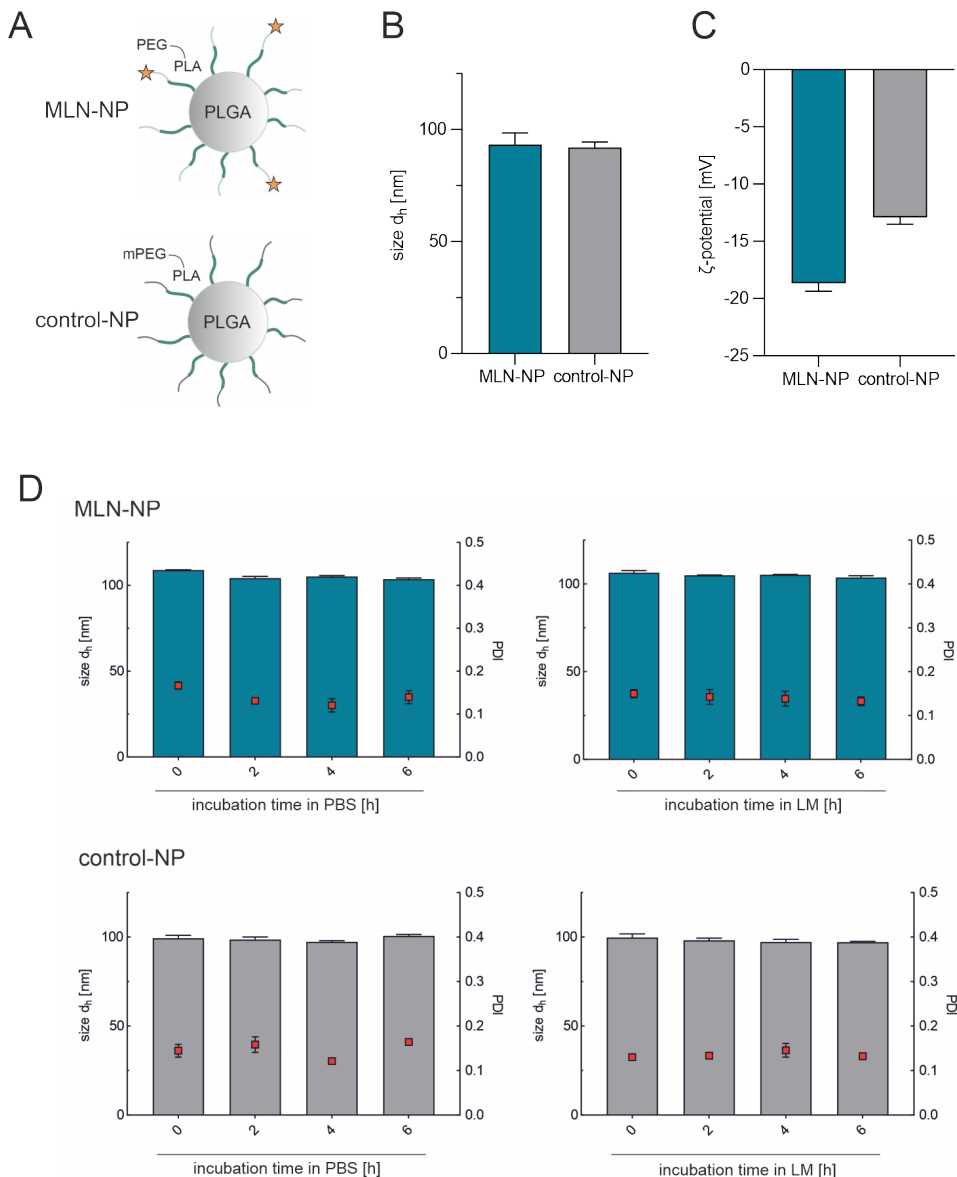
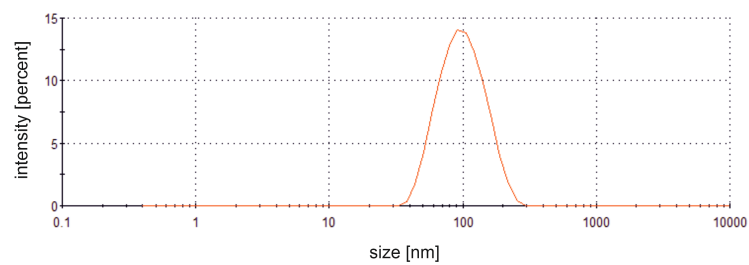


Figure S8. NP characterization. **(A)** Schematic illustration of the nanoparticle structure. **(B)** NP size measured via nanoparticle tracking analysis (NTA). **(C)** Zeta potential determined via dynamic light scattering (DLS) measurements. **(D)** Determination of particle size and stability under experimental conditions (37 °C in phosphate buffer (PBS) or Leibovitz medium (LM) for 6 h) via DLS. Results represent mean \pm SD ($n = 3$).

Supporting Information - Ectoenzymes as Cell Identification Structures

MLN-NP



control NP

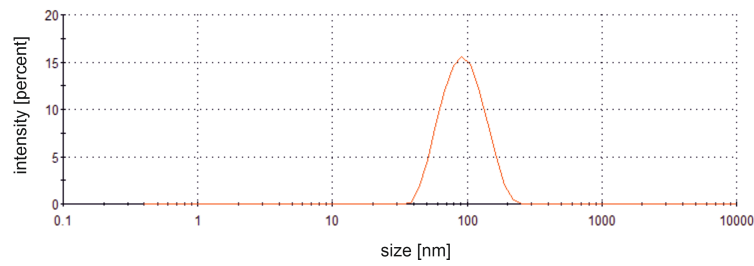


Figure S9. Size distribution determined via DLS.

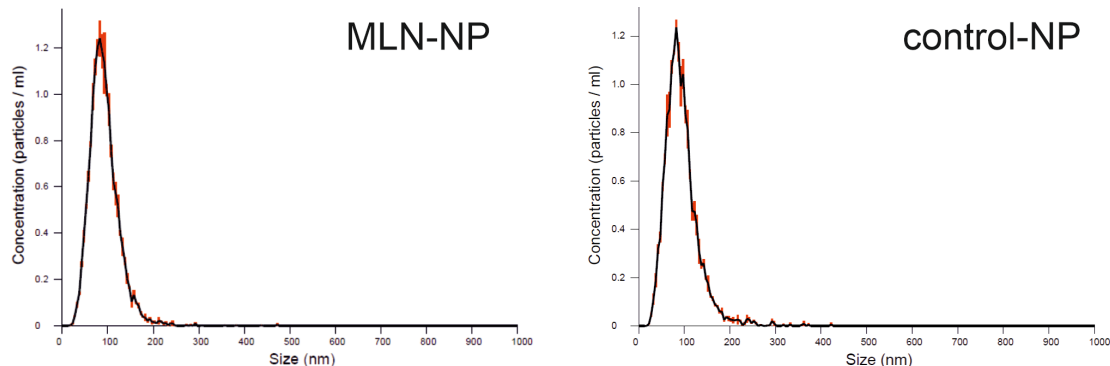


Figure S10. Size distribution determined via nanotracking analysis (NTA).

Chapter 4 – Supporting Information

4 Characterization of the HEK293T-ACE2 Target Cell Line

To characterize the target cells (HEK293T-ACE2) and verify the expression of human ACE2, hACE2 Alexa Fluor 647 conjugated antibody as well as its isotype control mouse IgG2A Alexa Fluor 647 conjugated antibody and Flow Cytometry Staining Buffer (1X) were purchased from Biotechne (R&D Systems, Minneapolis, MA, USA). Immunocytochemistry experiments were analyzed via flow cytometry and CLSM. Untransfected HEK293 cells and an isotype control served as negative controls for the staining experiment.

For flow cytometry experiments the cells in the culture flask were washed with PBS. Afterward, 10 mL of PBS were added and pipetted up and down to detach the cells. The cells were aliquoted up to 1×10^6 cells into protein low bind Eppendorf cups. 5 μ L of the hACE2 AlexaFluor 647 labeled antibody or its isotype control, respectively, were added and the mixture was incubated for 30 min at RT in the dark. After expiration of the incubation period any unbound antibody was removed by centrifugation of the cells for 5 min at 300 g. The supernatant was decanted, and the cells were resuspended in 2 mL flow cytometry staining buffer. This purification step was repeated two times. The centrifuged cell pellet was resuspended in 500 μ L of flow cytometry staining buffer for flow cytometric analysis. Cells were analyzed using FACS Canto II as described in chapter 2.9.

Flow cytometry (Fig. S11A) and CLSM (Fig. S11B) demonstrated the attachment of the hACE2 antibody to the target cell surface, thus verifying the expression of the target ectoenzyme ACE2.

Supporting Information - Ectoenzymes as Cell Identification Structures

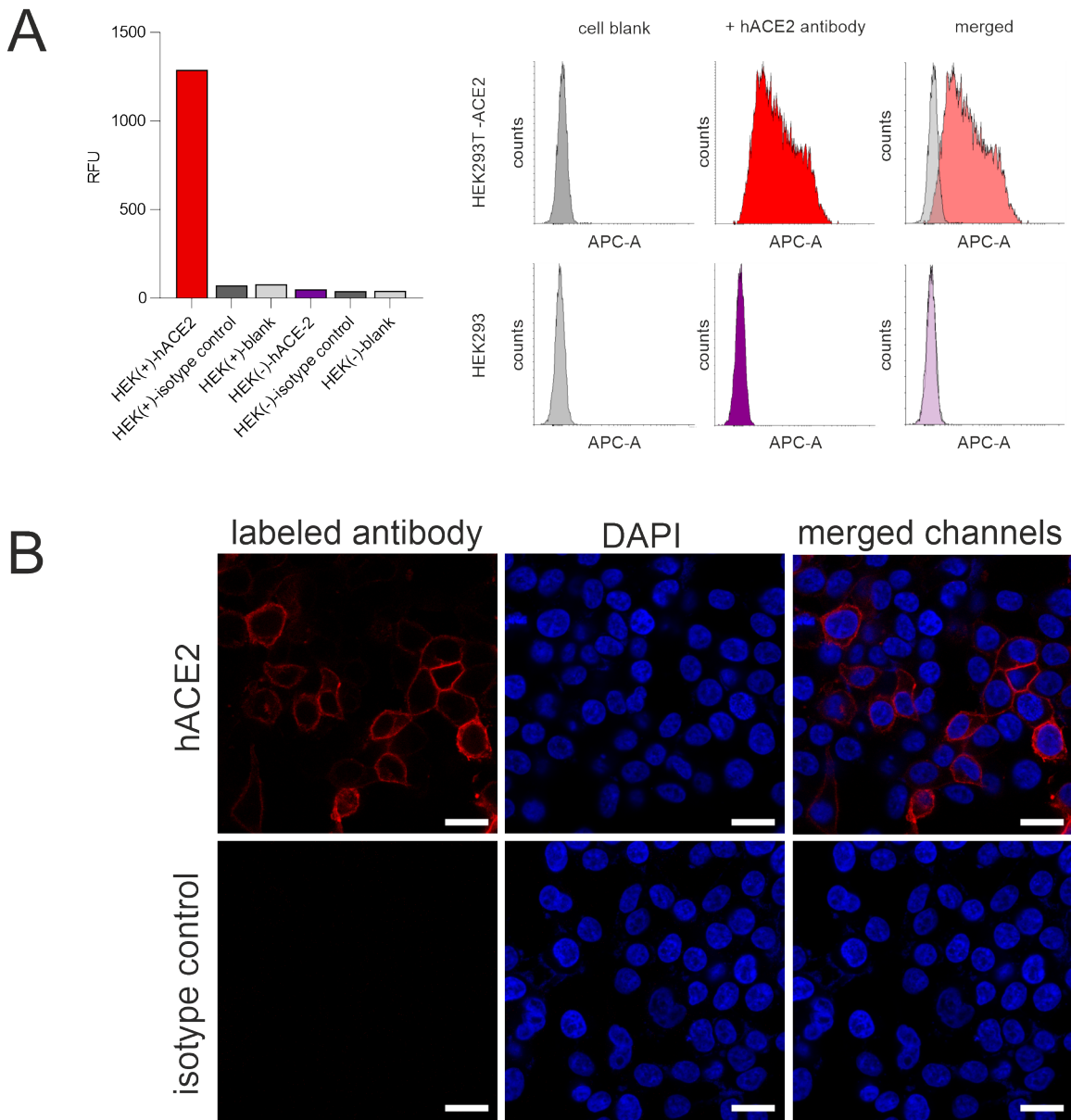


Figure S11. Demonstration of stable hACE2-expression by the target cells using antibody staining. (A) Flow cytometric analysis. HEK(+) = HEK293T-ACE2 cells; HEK(-) = HEK293 cells; hACE2 = addition of labeled antibody for hACE2; isotype control = addition of labeled isotype control antibody; blank = no addition of antibody; RFU = relative fluorescence units; APC-A = fluorescence channel for the detection of AlexaFluor647-labeled antibodies. **(B)** CLSM analysis. Scale bar: 20 μ m.

5 Characterization of Nanoparticle Localization and Binding/Uptake Behavior

The target cells were incubated with MLN-NPs in a concentration of 3 nM in Leibovitz medium for 60 min at 37 °C. Cell fixation and DAPI staining were performed according to chapter 2.8. For visualization of the cell membrane, HEK293T-ACE2 stable cells were additionally incubated with a 5 μ M staining solution of DiO for 15 min at RT. The staining solution was diluted from a stock solution (2 mM) of DMSO and EtOH (1:1 v/v). After the staining procedure, the cells were washed twice with prewarmed PBS before mounting.

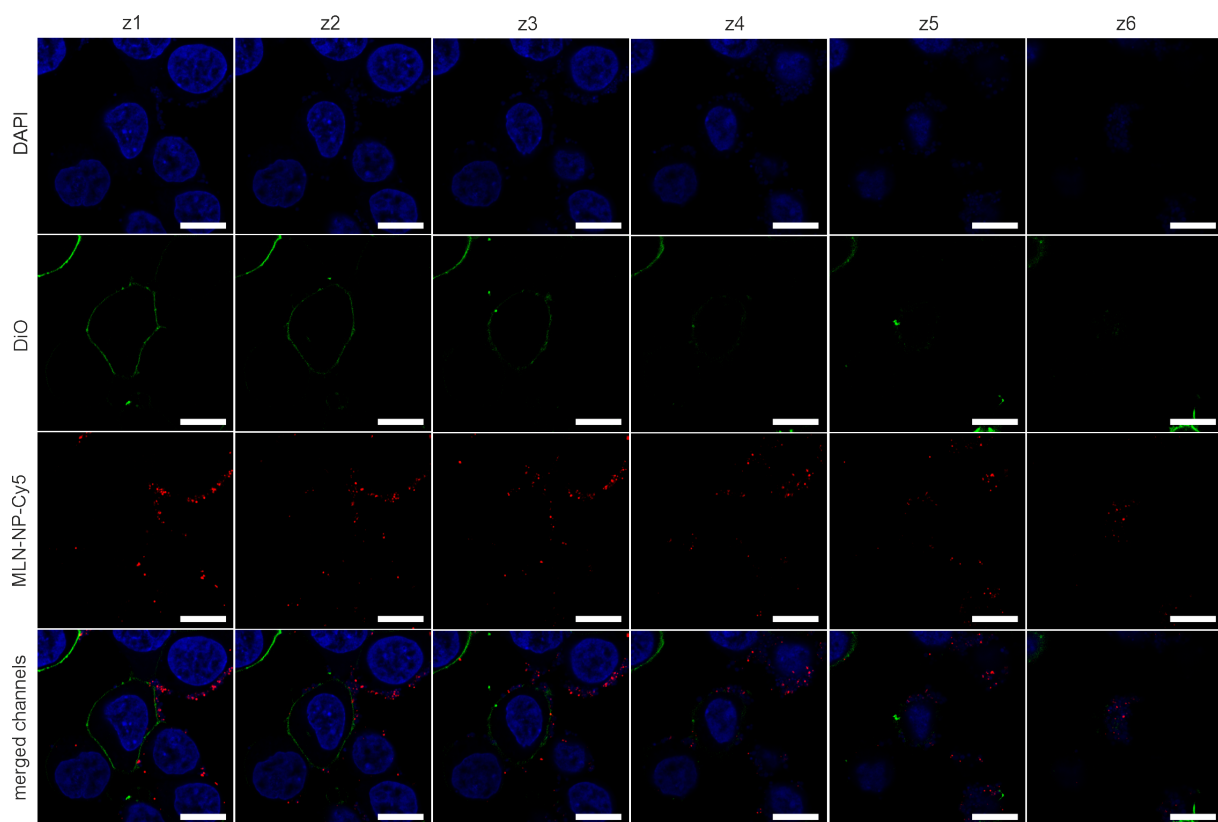


Figure S12. Cellular localization of MLN-NPs. Z-stack of HEK293T-ACE2 cells incubated with MLN-NPs labeled with Cy5 (red). Cell membrane staining with DiO dye (green). Cell nuclei were stained with DAPI (blue) NPs were mainly localized on the cell surface. (z1) cross-section – (z5) top view. Scale bar: 10 μ m.

Supporting Information - Ectoenzymes as Cell Identification Structures

HEK293 cells were incubated with NPs with 0 % modification and 100 % carboxy spacers in a concentration of 100 pM in Leibovitz medium for 60 min at 37 °C. Cell fixation and DAPI staining were performed according to chapter 2.8. After the staining procedure cells were washed twice with prewarmed PBS before mounting.

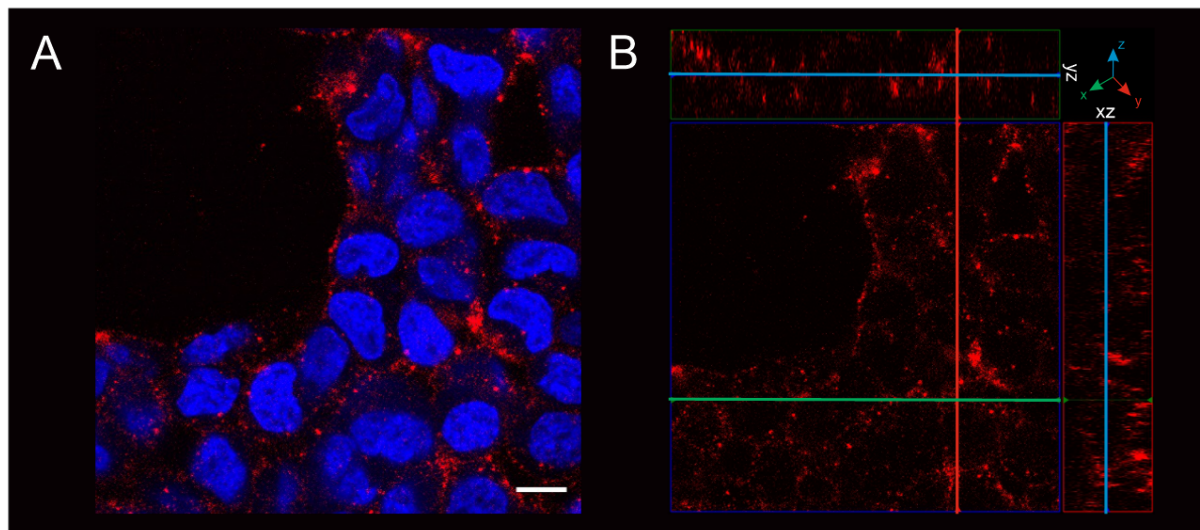


Figure S13. Cellular localization of NPs with 0 % modification / 100 % carboxy spacers. (A) 2D-Image of unspecific particle uptake. (B) Orthogonal view. In both views no specific accumulation at the cell membrane was visible. Scale bar: 10 μ m.

6 Quantification of Particle Avidity and Selectivity – Evaluation of Experimental Parameters

The target cells were incubated with control nanoparticles in a concentration of 3 nM in Leibovitz medium for 60 min at 37 °C. Cell fixation and DAPI staining were performed according to chapter 2.8. For visualization of the cell membrane, the HEK293T-ACE2 cells were additionally incubated with a 5 µM staining solution of DiO for 15 min at RT. After the staining procedure cells were washed twice with prewarmed PBS before mounting.

Compared to MLN-NPs control nanoparticles showed a higher unspecific uptake. No specific accumulation at the cell membrane was visible. The experimental conditions of the cell-based experiments were set to an incubation time of 30 min to minimize the effect of the unspecific uptake of the control group.

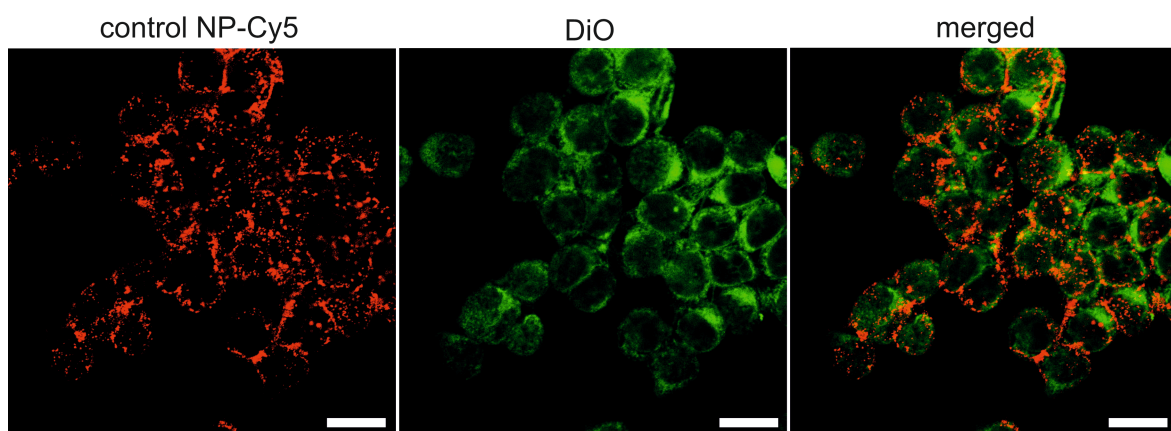


Figure S14. CLSM binding/uptake of control nanoparticles. No specific accumulation at the cell membrane was observed. Particles were unspecifically taken up over time. Scale bar: 20 µm.

7 Evaluation of the Biological Activity of MLN-NPs

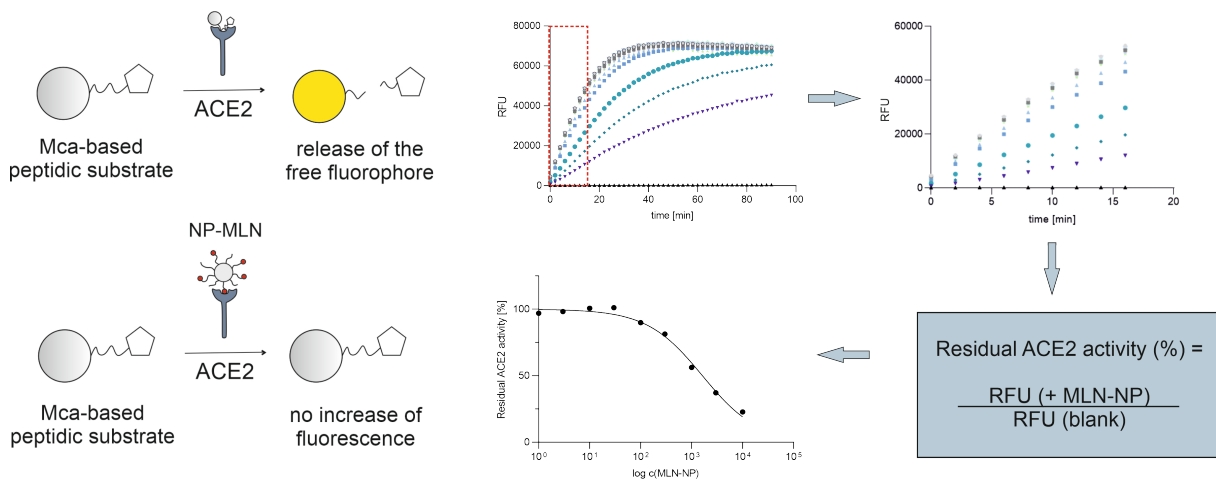


Figure S15. Concept and evaluation of the ACE2 inhibitor assay. In the range of substrate excess, the cleavage of the Mca-based substrate and thus the release of the free fluorophore is proportional to time. In this range, the decrease in enzyme activity can be determined by the decrease in the slope of the regression line. The corresponding residual activity is plotted against the inhibitor concentration to fit an IC_{50} value (RFU = relative fluorescence units).

Chapter 5

Chapter 5

Conditional Cell-Penetrating Peptide Exposure as Selective Nanoparticle Uptake Signal

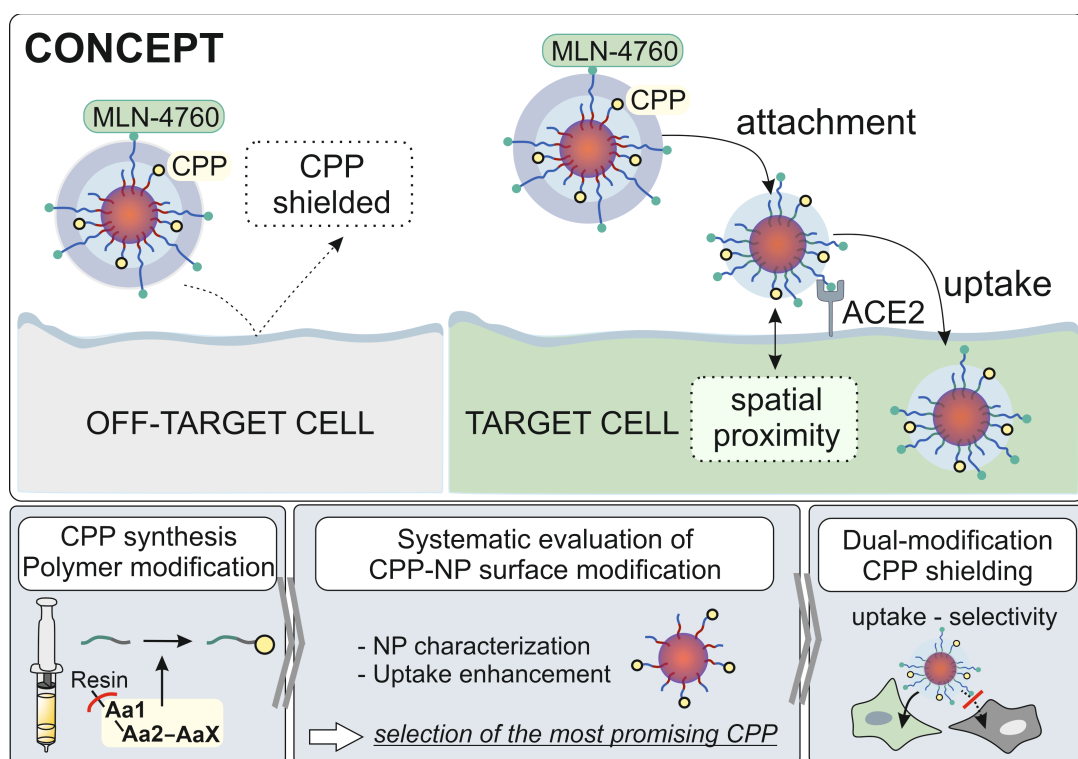
Published in *ACS Applied Materials & Interfaces*

2024, 16, 29, 37734–37747

Chapter 5

Abstract

A major bottleneck diminishing the therapeutic efficacy of various drugs is that only small proportions of the administered dose reach the site of action. One promising approach to increase the drug amount in the target tissue is the delivery via nanoparticles (NPs) modified with ligands of cell surface receptors for the selective identification of target cells. However, since receptor binding can unintentionally trigger intracellular signaling cascades, our objective was to develop a receptor-independent way of NP uptake. Cell-penetrating peptides (CPPs) are an attractive tool since they allow efficient cell membrane crossing. So far, their applicability is severely limited as their uptake-promoting ability is non-specific. Therefore, we aimed to achieve a conditional CPP-mediated NP internalization exclusively into target cells. We synthesized different CPP candidates and investigated their influence on nanoparticle stability, zeta potential, and uptake characteristics in a core-shell nanoparticle system consisting of poly(lactid-co-glycolid) (PLGA) and poly(lactic acid)-poly(ethylene glycole) (PLA_{10k}-PEG_{2k}) block copolymers with CPPs attached to the PEG part. We identified TAT47-57 (TAT) as the most promising candidate and subsequently combined the TAT-modified PLA_{10k}-PEG_{2k} polymer with longer PLA_{10k}-PEG_{5k} polymer chains, modified with the potent angiotensin-converting enzyme 2 (ACE2) inhibitor MLN-4760. While MLN-4760 enables selective target cell identification, the additional PEG length hides the CPP during a first unspecific cell contact. Only after the previous selective binding of MLN-4760 to ACE2, the established spatial proximity exposes the CPP, triggering cell uptake. We found an 18-fold uptake improvement in ACE2-positive cells compared to unmodified particles. In summary, our work paves the way for a conditional and thus highly selective receptor-independent nanoparticle uptake, which is beneficial in terms of avoiding side effects.



1 Introduction

Cell-penetrating peptides (CPPs) are molecules of 4 to 40 mostly cationic amino acids and possess unique abilities for crossing biological barriers, including cell membranes [1,2]. Therefore, they find broad application to promote the cell internalization of various cargos [3-6]. Their membrane-penetrating properties not only enable direct cell uptake via multiple pathways but are also considered to support endosomal escape (Fig. 1) [7,8]. Thus, CPPs are a promising delivery system for drugs with intracellular targets and are attracting great interest as a tool for nanoparticle surface modification [9–11]. However, the application of CPPs in case of selective nanotherapy comes along with severe challenges.

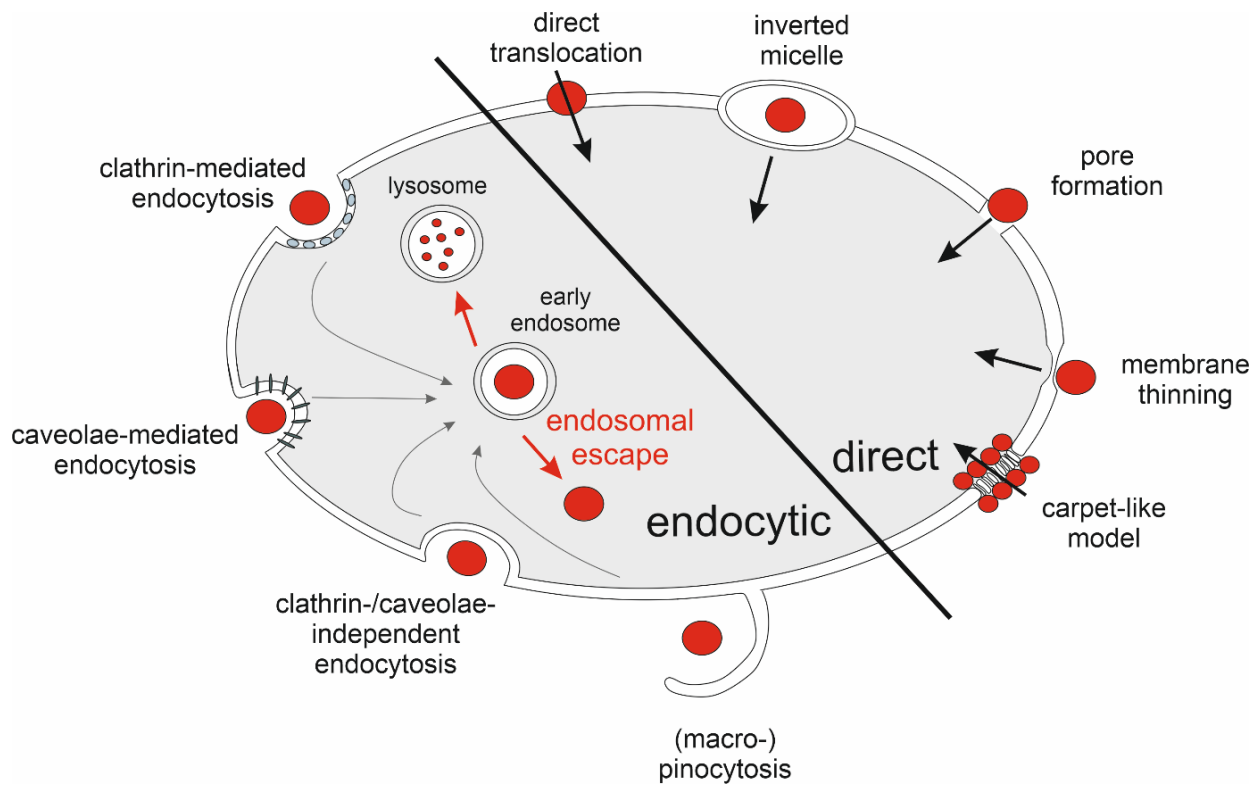


Figure 1. Overview of uptake mechanisms of cell-penetrating peptides. The uptake mechanisms can be categorized into endocytic (left) and direct (right) uptake ways. While the compound is instantly available in the cytoplasm after direct uptake, it initially ends up in early endosomes after endocytic uptake [12,13]. In this case, a further hurdle must be circumvented by means of endosomal escape in order to enter the cytoplasm. If this is not possible, the early endosomes undergo a maturing process, ending up in lysosomes, where acidic pH values and lysosomal enzymes lead to the degradation of the cargo [14].

Chapter 5

Although the mechanisms of CPP uptake have been studied intensively, they are not yet fully understood [15,16]. The process and extent of CPP-cargo-conjugate internalization and their endosomal escape depends on various factors like cargo size, hydrophobicity, CPP concentration, and surface density, or the resulting net charge [13,15,17,18]. There is also a great variability among CPPs, which can be categorized into different groups: cationic, amphiphatic, and hydrophobic CPPs. These groups have highly different properties, which in turn affect the CPP-cargo-conjugate characteristics [6,15,19]. Moreover, there is also a lack of comprehensive systematic studies regarding nanoparticle surface modifications with CPPs that would facilitate an assessment of resulting particle properties and cell uptake characteristics. Finally, CPPs are typically non-selective and enhance nanoparticle uptake in nearly all types of cells [20–22], which is detrimental to target cell selectivity. Therefore, in the case of active nanoparticle targeting, where selective ligands are attached to the nanoparticle surfaces to identify a certain cell type or tissue, their application as a tool to trigger cell uptake is hardly feasible [3,21].

In this work, we aimed to develop nanoparticles that rely on the cell uptake-enhancing properties of CPPs with utmost target cell selectivity. First, we systematically investigated nanoparticle modifications with various cell-penetrating peptides attached to the NP surface to identify the most suitable CPP candidate in terms of resulting particle size and stability. The nanoparticles had a core-shell structure, consisting of poly(D,L-lactide-co-glycolide) (PLGA) and a block copolymer of poly(lactic acid)-poly(ethylene glycole) (PLA_{10k}-PEG_{2k}). The CPPs were tethered to the PEG part, which built the nanoparticle shell, and were therefore localized directly visible on the particle surface (Fig. 2A, left). After selection of the most appropriate CPP, the CPP-modified polymer was combined with PLA_{10k}-PEG_{5k} polymer chains. On the one hand, the longer PEG chains hide the CPP inside the PEG shell and thus prevent unspecific cell internalization upon a first cell contact. On the other hand, PLA_{10k}-PEG_{5k} was equipped with MLN-4760 (MLN), a potent ACE2 inhibitor [23], that enables selective target cell recognition (Fig. 2A, right) via binding to ACE2 thus fixing the nanoparticle to the cell surface [24]. The newly achieved spatial proximity should ultimately lead to CPP exposure and induce uptake exclusively into target cells. In this way, we aim to provide a simple but effective strategy for the selective utilization of the unique properties of CPPs and thus establish a favorable, receptor-independent way of nanoparticle uptake into target cells, which is presumably associated with less side effects (Fig. 2B) [24]. While possible target tissues of the developed nanoparticles could be strongly ACE2-expressing compartments, including renal tubules,

Cell-Penetrating Peptides as Selective Nanoparticle Uptake Signal

gallbladder, cardiomyocytes, male reproductive cells, ductal cells, eye, and vasculature [25], the presented technology is a variable platform technology that can be adapted to various applications by changing the targeting ligand attached to longer polymer chains.

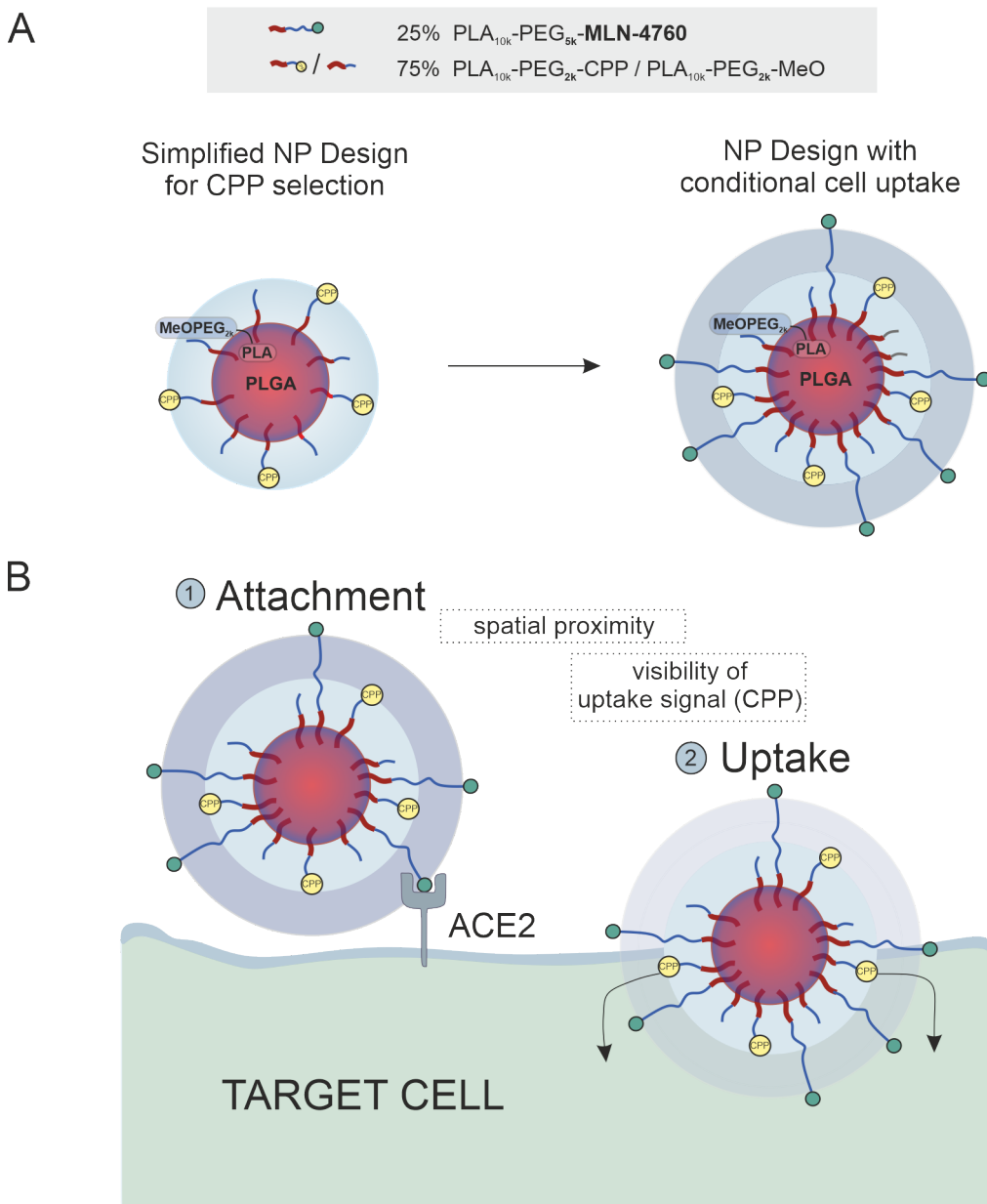


Figure 2. Nanoparticle structure and targeting approach. (A) Nanoparticle design. Different CPP modifications of polymeric nanoparticles with a core-shell structure were analyzed in a simplified particle design to select a suitable candidate for a conditional, sequential particle uptake (left). The nanoparticles consisted of PLGA and PLA_{10k}-PEG_{2k} block copolymers (PLA drawn in red, PEG in blue). Due to its higher hydrophilicity, PEG formed the NP shell (blue halo). Since PLGA and PLA are

Chapter 5

generally miscible [25], a PLGA-rich inner core layer (shown in orange/red) and a PLA-rich outer core layer (shown in red/blue) were obtained. The CPP was tethered to the PEG part and thus directly visible on the nanoparticle surface and able to mediate nanoparticle uptake. Methoxy-terminated polymers ($\text{PLA}_{10k}\text{-PEG}_{2k}\text{-MeO}$) served as space-filling polymers between the CPP-modified chains ($\text{PLA}_{10k}\text{-PEG}_{2k}\text{-CPP}$). The most promising candidate was established in a more complex particle design which promoted conditional, sequential nanoparticle uptake (right). Therefore, the CPP tethered to $\text{PLA}_{10k}\text{-PEG}_{2k}$ was combined with $\text{PLA}_{10k}\text{-PEG}_{5k}$ polymers, which had a longer PEG chain. The additional PEG length shielded the CPP during a first cell contact. Additionally, MLN-4760, a selective ACE2 inhibitor was attached to these longer polymer chains for selective target cell recognition ($\text{PLA}_{10k}\text{-PEG}_{5k}\text{-MLN}$). The proportion of long polymers was set to 25 % according to Walter et al. (2023) [24]. For control nanoparticles, the MLN-modified polymer was replaced by uncharged methoxy-terminated polymer ($\text{PLA}_{10k}\text{-PEG}_{5k}\text{-MeO}$). Different amounts of CPP modifications were evaluated (0 – 75 %) ($\text{PLA}_{10k}\text{-PEG}_{2k}\text{-CPP}$) and the proportion of short polymer, which should not be modified, was accordingly replaced by short methoxy-terminated polymers as placeholders ($\text{PLA}_{10k}\text{-PEG}_{2k}\text{-MeO}$). **(B)** Concept of a conditional, sequential nanoparticle uptake. Since the CPP is shielded by longer polymers during a first cell contact, the uptake-enhancing abilities of the ligand do not directly promote cell uptake. Only after a previous, selective binding of the nanoparticle to ACE2 via MLN-4760, the established spatial proximity exposes the uptake signal previously hidden inside the polymer shell. This leads to CPP-mediated uptake exclusively into ACE2-positive target cells.

2 Materials and Methods

2.1 Materials

Millipore water was generated by a Milli-Q water purification system (Millipore, Schwalbach, Germany). Unless otherwise stated, all chemicals and reagents were obtained from Sigma Aldrich (Taufkirchen, Germany) in analytical grade. Dulbecco's phosphate-buffered saline (PBS) was purchased from Sigma Aldrich (Taufkirchen, Germany). Poly(ethylene glycol)(PEG)-carboxylic acid with a molecular mass of 5,000 g mol⁻¹ (OH-PEG_{5k}-COOH) was sourced from Jenkem Technology USA Inc. (Allen, TX, USA). Poly(ethylene glycol)-methylether with a molecular mass of 5,000 g mol⁻¹ (OH-PEG_{5k}-MeO) as well as Resomer® RG 502, poly(D,L-lactide-co-glycolide) (lactide:glycolide 50:50; ester or acid terminated; M_w 7000–17,000 Da) (PLGA) were purchased from Sigma Aldrich (Taufkirchen, Germany). N,N'-Diisopropylcarbodiimide (DIC) and Oxyma were sourced from TCI (Eschborn, Germany). 1-[Bis(dimethylamino)methylene]-1*H*-1,2,3-triazolo[4,5-*b*]pyridinium 3-oxide hexafluorophosphate (HATU) and N,N-diisopropylethylamine (DIPEA) were obtained from ABCR (Karlsruhe, Germany). MLN-4760 was obtained from MedChemExpress (Monmouth Junction, NJ, USA). The fluorescent dyes were purchased from Lumiprobe (Hannover, Germany). Protected amino acids Fmoc-L-Arg(Pbf)-OH, Fmoc-L-Lys(Boc)-OH, Fmoc-L-Tyr(*t*Bu)-OH, Fmoc-L-Gln(Trt)-OH, and Fmoc-Gly-OH were purchased from Carbolution Chemicals (St. Ingbert, Germany). The cellulose dialysis membranes had a molecular weight cut-off of 6-8 kDa and were obtained from Spectrum Laboratories, Inc. (Rancho Domingues, CA, USA). The frits had a pore size of 35 µm and were sourced from Roland Vetter Laborbedarf (Ammerbuch, Germany). The centrifugal devices for nanoparticle concentration were purchased from Pall Life Sciences (Portsmouth, UK) and had a molecular weight cut-off of 30 kDa. The infrared lamp was obtained from Medisana (Neuss, Germany), with a thermostat from PEARL.GmbH (Buggingen, Germany). Syringes were purchased from Braun (Melsungen, Germany). NMR spectra were recorded on a Bruker Avance-400 NMR spectrometer (Bruker). High-resolution mass spectrometry (HRMS) was performed on a Q-TOF 6540 ultrahigh definition (UHD) LC/MS system (Agilent Technologies) using an electrospray ionization (ESI) source or on an AccuTOF GCX GC/MS system (Jeol) using an electron ionization (EI) source. Preparative HPLC was performed with a system from Thermo Fisher (Waltham, USA) with a binary pump HPG-3200BX and the detector VWD-3400RS.

Chapter 5

HEK293 cells were sourced from the German Collection of Microorganisms and Cell Cultures GmbH, DSMZ (Göttingen, Germany). Transfected, stably ACE2-expressing HEK293T cells were a kind gift from Prof. Dr. Ralf Wagner (Institute of Clinical Microbiology and Hygiene, University Hospital Regensburg). Fetal Bovine Serum (FBS) for the preparation of cell culture medium was purchased from Biowest (Nuaillé, France). For all microscopic experiments, the cells were seeded in 8-well microscope slides from Ibidi (Gräfelfing, Germany). Dako Faramount Mounting Medium was obtained from Agilent Technologies (Santa Clara, USA). Lysotracker™ Deep Red was purchased from Invitrogen, Life Technologies GmbH (Darmstadt, Germany).

2.2 Synthesis of Cell-Penetrating Peptides (CPPs)

To identify suitable CPPs for the sequential nanoparticle targeting concept in terms of particle stability, uptake improvement, and cytotoxicity, various potential CPP candidates were synthesized and characterized: oligoarginines [26] of different lengths (arginine-4 (R4), arginine-7 (R7), and arginine-10 (R10)), TAT47-57 (TAT) (one of the most characterized fragments of the human immunodeficiency virus (HIV) transactivator protein [27]), and the Bax-inhibiting peptide (Bip) VSALK (small hydrophobic CPP, described by Gomez et al. (2010) [28]) (Table 1).

Table 1. Peptide sequences and theoretical netto charges.

| Peptide | Sequence | Charge |
|-------------------|-------------|--------|
| Bip | VSALK | +1 |
| Arginine-4 (R4) | RRRR | +4 |
| Arginine-7 (R7) | RRRRRRR | +7 |
| TAT47-57 (TAT) | YGRKKRRQRRR | +8 |
| Arginine-10 (R10) | RRRRRRRRRR | +10 |

The corresponding results are provided in the supporting information (Fig. S1 – Fig. S20). The synthesis was performed using a standard Fmoc strategy following the procedure of Bresinsky et al. (2022) [29]. 2-Chlorotrityl-resin (300 mg, 1 eq) was weighted into a fritted 25 mL syringe. 15 mL of dichloromethane (DCM) was drawn up to swell the resin at room temperature for

30 min. Afterward, DCM was aspirated with a vacuum flask. The first amino acid (2.5 eq) was dissolved in the smallest possible volume of DCM (ca. 15 mL). If this was not possible, small amounts of dimethylformamide (DMF) were added until the amino acid was completely dissolved. 140 μ L (2.5 eq) of 2,4,6-collidine was added and the solution was drawn up into the syringe and shaken for 3 h at room temperature. After aspiration of the solvent, the resin with the bound amino acid was rinsed three times with 15 mL DCM. 15 mL of a mixture of piperidine 20 % (v/v) in DMF was drawn up and the syringe was shaken on an orbital shaker at 35 °C for 15 min to remove the N-terminal Fmoc-protecting group. During this, the shaker was covered with a box, insulated with aluminum foil, while the temperature was adjusted with an infrared lamp. The temperature was controlled by a thermostat. After deprotection, the liquid was removed using a vacuum flask, and the residual resin was washed three times with 15 mL DMF. For the following coupling steps, the corresponding amino acid (2.5 eq) and HATU (400 mg, 2.5 eq) were weighed into two separate Erlenmeyer flasks. Afterward, both were dissolved in 5 mL DMF, and collidine (140 μ L, 2.5 eq) was added to the solution of HATU. Then, both solutions were drawn up with the resin-loaded syringe and shaken at 35 °C for 60 min. The liquid was again removed using a vacuum flask followed by three washing steps with DMF. For the synthesis of the bax inhibiting peptide (Bip) VSALK different coupling reagents were used: HATU was replaced by Oxyma (2.5 eq) and *N,N*'-diisopropylcarbodiimide (2.5 eq) and no base additive was used for coupling. The coupling step was followed by the deprotection step with piperidine 20 % (V/V) in DMF. Both reactions were repeated until the desired CPP sequence was built up. The last step was the cleavage from the resin. After deprotection of the last amino acid, the syringe was successively rinsed with methanol (2 x 15 mL), DCM (2 x 15 mL), and diethyl ether (2 x 15 mL) and allowed to dry. The resin was poured into a round-bottom flask and a solution of hexafluoroisopropanol (HFIP) in DCM (20 %) was added dropwise. After stirring for 2 h the solution was filtrated and the filtrate was evaporated and analyzed via NMR, HPLC, and mass spectrometry. If necessary, the reaction products were purified by preparative HPLC (Scheme S1).

2.3 Polymer Synthesis and Ligand Coupling

The synthesis of the PLA-PEG block-copolymer was performed according to Qian et al. (2011) [30] with modifications as previously described by our group [31]. Directly prior to the polymerization reaction, 3,6-dimethyl-1,4-dioxane-2,5-dione was recrystallized from ethyl

Chapter 5

acetate at 85 °C and subsequently dried under vacuum at 38 °C overnight. The heterobifunctional PEG polymer OH-PEG_{2k}-COOH, OH-PEG_{5k}-COOH, or OH-PEG_{2k}-MeO respectively, served as macroinitiator for the reaction and was dissolved in 10 mL of anhydrous DCM in a round bottom flask (1 eq, 0.19 mmol). 1,8-Diazabicyclo[5.4.0] undec-7-ene (DBU) (3 eq, 0.57 mmol) was added, the round-bottom flask was fitted with a drying tube, and the reaction mixture was stirred for exactly one hour at RT. Subsequently, the polymerization reaction was quenched with benzoic acid (10 eq, 1.92 mmol). The reaction product was precipitated in 100 mL ice cold diethyl ether and dried under nitrogen flow overnight at RT. The resulting polymers were characterized via ¹H-NMR (Fig. S21-23). For the coupling of CPPs, PLA_{10k}-PEG_{2k}-COOH (4.165 μmol, 50 mg) was dissolved in anhydrous DMF. *N*-Hydroxysuccinimide (NHS) (25 eq) and *N*-(3-dimethylaminopropyl)-*N'*-ethylcarbodiimide hydrochloride (EDC) (25 eq) were added as powder and the polymer was activated for 1 h at room temperature (RT) under stirring. The excess of EDC was quenched by the addition of β-mercaptoethanol (14.3 M) (BME) (35 eq) for 15 min at RT. The protected CPP (3 eq) was solved in 1000 μL of DMF and added to the stirring polymer solution. Simultaneously *N,N*-diisopropylethylamine (DIPEA) (10 eq) was added and the reaction was stirred for 24 h at RT. Afterward, the reaction product was precipitated into 100 mL ice cold diethyl ether and dried under nitrogen flow. For the peptide synthesis and to enable the specific coupling to the polymer via the N-terminus afterward, all amino acids had to be used side chain-protected. Therefore, it was necessary to deprotect the peptide sequence after polymer modification. As the deprotection time in acidic environments should be kept as short as possible, due to hydrolysis instabilities of PLA-PEG polymers in acidic environments [32,33], the minimal reaction time for the cleavage of all protection groups was evaluated in advance (Supporting Information, Chapter 4). According to these results, the modified polymers were dissolved in a mixture of 10 mL dichloromethane (DCM) and 10 mL trifluoroacetic acid (TFA) and stirred at room temperature for 60 min (Scheme S2). The solvent was removed on a rotary evaporator and the polymer with the deprotected CPP was dried using a vacuum pump. The reaction product was dissolved in as less acetonitrile (ACN) as possible and added dropwise into a 10-fold excess of vigorously stirring millipore water to generate polymeric micelles. The solution was stirred for 3 h under a fume hood to evaporate the organic solvent. Unreacted CPP and reagents were removed by dialysis of the polymeric micelles in a dialysis tube with a molecular weight cut-off of 6-8 kDa against 4 L Millipore water with medium change after

Cell-Penetrating Peptides as Selective Nanoparticle Uptake Signal

30 min, 2 h, and 6 h. The coupling of MLN-4760 to PLA_{10k}-PEG_{5k}-COOH was performed according to Walter et al. (2023) [24].

2.4 Nanoparticle Preparation and Characterization

Ester-terminated 13.4 kDa PLGA as nanoparticle core-component and (modified) PLA-PEG block-copolymers constituting the nanoparticle shell were dissolved at a 30:70 mass ratio to a final concentration of 10 mg/mL in ACN. Various ratios of modified and unmodified shell polymers were investigated, which are precisely defined for the respective experiments and referred to as the degree of modification (DOM). The DOM corresponds to the mass fraction of PLA-PEG block copolymer with a CPP attached compared to the total shell polymer used for particle preparation; in other words, a DOM of 30 % implies 30 % CPP-modified PLA-PEG block copolymer and 70 % uncharged, methoxy-terminated PLA-PEG block copolymer. Nanoparticles were prepared via bulk nanoprecipitation. Therefore, the polymer mixtures were added dropwise into vigorously stirring 10 % PBS to a final polymer concentration of 1 mg/mL. The preparation was stirred for 3 h at room temperature and if necessary concentrated by centrifugal ultrafiltration in filters with a molecular weight cut-off of 30 kDa for 20 min at 3000 g. For the preparation of fluorescently labeled nanoparticles, the core component PLGA was functionalized according to Walter et al. (2023) [24]. For the preparation of shielded particles, TAT47-57 was attached to PLA_{10k}-PEG_{2k} block copolymer and covered by PLA_{10k}-PEG_{5k} polymers modified with the potent and selective ACE2 inhibitor MLN-4760 [24]. Nanoparticles with methoxy-terminated long polymer chains and consequently without a specific surface modification, served as negative control. Both nanoparticle types were prepared with varying amounts of TAT to identify the most suitable CPP surface density. The amount of longer polymer chains was set to 25 % since the particle design was based on a previous work of our group where nanoparticles with this surface density of MLN proved excellent particle avidities in the low nanomolar to picomolar range [24]. Zeta potential (ZP) and polydispersity index (PDI) were evaluated using a Malvern Zetasizer Nano ZS (Malvern, UK) by dynamic light scattering (DLS). The samples were analyzed with a 633 nm He-Ne laser at an angle of 137° at RT. Nanoparticle size and concentration were determined using nanoparticle tracking analysis (NTA) (NanoSight NS300, Malvern, UK). For NTA analysis particles were diluted with Millipore water to a particle concentration of 20 to 100 particles per frame.

Chapter 5

2.5 Cell Culture

HEK 293 cells were cultivated in Dulbecco's Modified Eagle Medium (DMEM) with 10 % FBS. For the cultivation of HEK293T cells, which were stably expressing ACE2, the same medium was used with blasticidin supplementation in a concentration of 10 μ g/mL. L929 cells were cultured in Eagle's minimum essential medium (EMEM) with 10 % FBS.

2.6 Cytotoxicity Assay

The cytotoxicity evaluation for CPP-modified nanoparticles was performed on L929 mouse fibroblasts because of their reproducible growth rates and biological responses [34]. 10,000 cells/well were seeded in a 96-well plate and incubated for 24 h at 37 °C. The nanoparticle solutions were diluted in serum-containing medium and 100 μ L per well were added. The cells were incubated for 24 h before the nanoparticle solution was aspirated. 200 μ L of 3-(4,5-dimethylthiazol-2-yl)-2,5-diphenyltetrazolium bromide (MTT) solution was added and incubated for 6 h. MTT solution was prepared by weighing the solid and solving it in PBS to a concentration of 2.5 mg/mL. The solution was sterile-filtered and afterward diluted to a concentration of 0.625 mg/mL with FBS-containing medium. After the incubation time, the supernatant was aspirated and 60 μ L of a solution of 10 % sodium dodecyl sulfate (SDS) in PBS was added. The 96-well plate was sealed with parafilm and stored overnight in the fridge. The next day the plate was shaken for 5 min on a plate shaker and absorption was measured at 570 and 690 nm with a Synergy Neo2 Multi-Mode Microplate Reader (Biotek Instrument Inc., Winooski, VT, USA). For the evaluation, the difference in absorbance at 570 and 690 nm was analyzed and the results were normalized to untreated cells.

2.7 Flow Cytometry

HEK293 cells, or HEK293T cells stably expressing ACE2 were seeded into 24-well plates at a concentration of 250,000 cells/well and incubated for 24 h at 37 °C. For co-culture experiments, HEK293T-ACE2 cells were previously stained with Cell Tracker Green (CTG). Therefore, the cells were incubated for 45 min at 37 °C in a 15 μ M solution of CTG in serum-free DMEM. Subsequently, 50,000 HEK293T-ACE2 cells and 50,000 HEK293 cells/well were seeded and incubated for 48 h at 37 °C. Both cell types were differentiated during measurements using the

Cell-Penetrating Peptides as Selective Nanoparticle Uptake Signal

fluorescein (FITC) channel. NPs were prepared using Cy5-labeled PLGA and adjusted to 100 pM by diluting the particles with Leibovitz medium (LM). The cell medium was aspirated and 300 μ L of particle solution was added to each well. After 60 min incubation at 37 °C, the particle solutions were aspirated, and the cells were detached using 300 μ L trypsin. All following work steps were carried out on ice. After all cells were detached, 700 μ L of DMEM supplemented with 10 % FBS was added to each well and the cells of each well were transferred to Eppendorf cups. These were centrifuged for 5 min at 200 g at 4 °C. The supernatant was aspirated, and the cell pellets were washed with 1 mL of PBS. The centrifugation and aspiration step were repeated, and the cell pellet was resuspended in 300 μ L PBS for flow cytometric measurement. The resuspended cells were stored on ice and protected from light until immediately before measurement. The samples were analyzed using a FACS Canto II (Becton Dickinson, Franklin Lakes, NJ, USA). NP fluorescence was excited at 633 nm and the emission was recorded using a 661/16 nm bandpass filter. The results were analyzed using Flowing software 2.5.1 (Turku Centre for Biotechnology, Finland).

2.8 Confocal Scanning Microscopy

For confocal scanning microscopy (CLSM) analysis of the interaction of CPP-modified nanoparticles with cells, 50,000 cells per well were seeded in an 8-well Ibidi slide and incubated for 24 h at 37 °C. The nanoparticle solutions were diluted to 100 pM in LM and 250 μ L/well were added. The nanoparticles were incubated for 1 h at 37 °C. Afterward the nanoparticle solution was aspirated, and the cells were washed twice with 200 μ L prewarmed PBS. The cells were fixed directly after the second washing step or medium was added and the cells were incubated overnight and fixed the following day. For cell fixation a 4 % paraformaldehyde (PFA) solution in PBS was used. PBS or cell medium was aspirated and 250 μ L of the PFA solution was added to each well. After incubation for 10 min at RT, the fixation solution was aspirated followed by two washing steps with PBS. Afterward, the cells were incubated with DAPI staining solution (1 μ g/mL in 0.1M PBS) for 10 min for cell nucleus labeling. After two more washing steps with 200 μ L PBS, the cells were mounted using Dako Faramount Mounting Medium and stored in the fridge (4 °C) until measurement. For the investigation of nanoparticle uptake ways and endosomal escape, experiments with a Lysotracker™ Deep Red staining were additionally performed. Therefore, 250 μ L of a nanoparticle solution of R7-modified NPs with a percentage of modified polymer of 50 % in a concentration of 100 pM in DMEM + 10 % FBS

Chapter 5

were added to the cells and incubated for 1 h at 37 °C. For this experiment, the nanoparticle core was labeled with 5-carboxytetramethylrhodamine (TAMRA) as already described by our group [24,31]. After expiry of the incubation period, the nanoparticles were aspirated and stained either directly or after a further incubation period of 24 h in fresh and particle-free medium. For staining, the cells were incubated with Lysotracker staining solution in a concentration of 50 nM for 1 h at 37 °C. Afterward, the staining solution was aspirated, and the cells were washed twice with 250 µL of fresh medium. Finally, 250 µL/well was added and the living cells were immediately analyzed by CLSM.

2.9 Data Analysis

2.9.1 Statistics

Statistical analysis was performed using GraphPad Prism Software 8.3.0. Ordinary one-way ANOVA with a Dunnett's (Fig. 5 and 7), or Tukey's (Fig. 9 monoculture) multiple comparisons test; and two-way ANOVA with a Sidak's multiple comparisons test (Fig. 9, co-culture) was performed for statistical evaluation of significance. The number of performed experiments (n) and the resulting significance levels are indicated in the figure legends.

2.9.2 Model for Data Fitting

The piecewise fitting model for zeta potential data is presented in Eq. 1.

$$f(\zeta) = \begin{cases} k, & \zeta < 0 \\ \frac{k_{max} \zeta}{\zeta_{1/2} + \zeta} + k, & \zeta \geq 0 \end{cases} \quad \text{Eq. 1}$$

It yields an uptake constant for negative potentials k as well as a maximum uptake ratio k_{max} and a half-maximum uptake zeta potential $\zeta_{1/2}$. The factors k_{max} and $\zeta_{1/2}$ describe (1) the potency of CPPs to increase cellular uptake and provide (2) an estimate of the threshold potential, above which further charges will not lead to a substantial improvement of uptake. Fitting of the piecewise model function was done using Origin (v. 10.1.0.178).

3 Results and Discussion

3.1 Systematic Evaluation of NP Surface Modifications with CPPs

3.1.1 Nanoparticle Preparation and Characterization

The effect of various CPP candidates with different amounts of positive charges as well as the influence of CPP surface density on nanoparticle characteristics were investigated in a simplified nanoparticle design using only polymers of uniform lengths (PLA_{10k}-PEG_{2k}). Control nanoparticles without CPPs attached to the NP surface had a size of 78 ± 1.8 nm. For CPP-modified particles, an increase in particle size was observed, that varied between different CPPs and DOMs resulting in sizes between 90 and 130 nm. The PDI values of all particles were in the range of 0.1-0.2, which proved a narrow size distribution (Fig. S28). Therefore, all modifications were shown to be suitable for NP surface modification regarding particle stability. The nanoparticle zeta potential served as a measure for the successful attachment of CPPs to particle surfaces (Fig. 3). As expected, increasing the ratio of polycationic CPP-modified polymer to uncharged methoxy-terminated spacer polymer resulted in a corresponding shift of the zeta potential to higher values. The net potential increase reached values of up to 59 mV, starting from a zeta potential of approximately -25 mV at a DOM of 0 % to +34 mV at a DOM of 75 % for R10-modified particles. Bip, which is a hydrophobic cell-penetrating peptide with only one basic amino acid and thus only one positive charge [35,36], showed accordingly only a minor increase of 3 mV. Based on our results, a good correlation between the number of positive charges per ligand and the absolute value of the zeta potential could be demonstrated for identical DOMFs.

Chapter 5

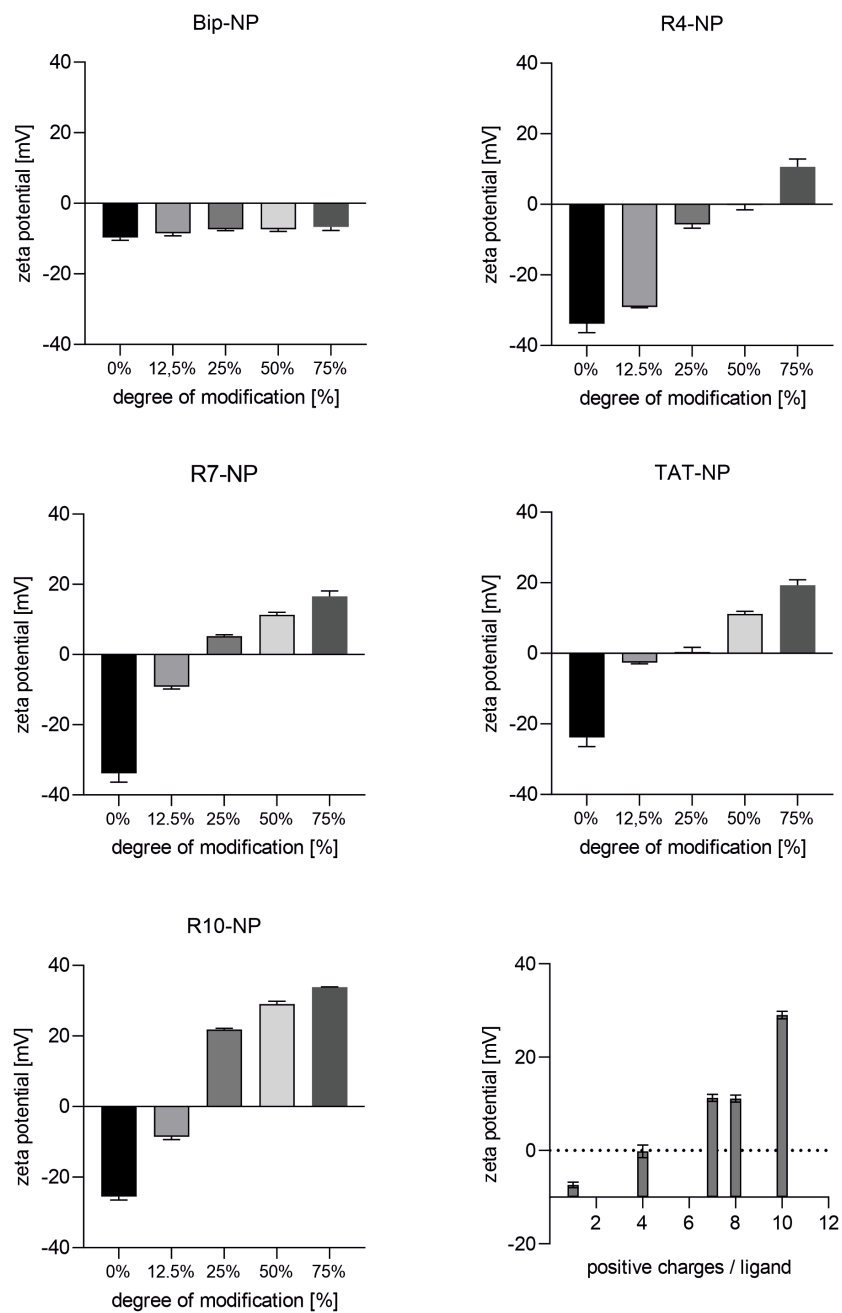


Figure 3. Characterization of the influence of nanoparticle modification with CPPs on their zeta potential. The zeta potential of nanoparticles modified with various CPPs (see diagram title) in different ratios of CPP-modified and unmodified methoxy-terminated polymer were analyzed. For all polycationic CPPs increasing proportions of CPP-modified polymer led to increasing zeta potentials. For the same DOM, a higher number of positive charges per ligand also led to higher absolute zeta potentials (shown in the lower right panel for a DOM of 50 %); (n = 3 technical replicates).

Cell-Penetrating Peptides as Selective Nanoparticle Uptake Signal

3.1.2 Qualitative Investigation of Nanoparticle Uptake

The qualitative investigation of particle uptake was performed for R7-modified particles as example to prove their ability to reach the cytosol and qualify for intracellular drug delivery (Fig. 4). For the advanced particle design with conditional CPP presentation and TAT as uptake signaling ligand, however, a corresponding internalization behavior was observed (Fig. 9D). The R7-modified nanoparticles initially accumulated at the cell membrane (Fig. 4). After 3 h, a faint fluorescence was visible in the cell interior, while there was almost no colocalization with endo- or lysosomes and most particles were localized outside the cell. After one day of incubation, the late endo- and lysosomes were occupied by nanoparticles to a high extent and the particles did no longer accumulate at the cell membrane. Additionally, the intracellular background fluorescence increased over time. These observations can be explained by uptake mechanisms of arginine-rich cell-penetrating peptides described in the literature: highly cationic structures strongly adsorb on membrane surfaces [37] due to the interaction with membrane-associated proteoglycans including heparan sulfate (HSPG), which was reported to play a crucial role for the subsequent endocytic uptake via micropinocytosis [37,38]. The observed fluorescence in the cytoplasm not colocalizing with endosomes indicates that a part of the nanoparticles was internalized via non-endocytic, direct uptake into the cytosol. This uptake mechanism was already postulated by different research groups for nanoparticles equipped with CPPs or high arginine surface densities [39–41]. As clear evidence for such direct penetration served an energy-independent cell uptake at 4 °C, as well as the diffuse cytosolic labeling after treatment with micropinocytosis inhibitors [42,43], which showed that endocytosis-independent uptake pathways must be involved [37,44]. However, the high colocalization of the nanoparticles and the lysotracker after 24 h (Fig. 4) proved that endocytic uptake mechanisms played a major role in nanoparticle internalization. This is in line with the often-described simultaneous prevalence of multiple internalization pathways [37,45,46]. As a result, a certain number of NPs may suffer from endosomal entrapment and lysosomal degradation processes [47–49]. Nevertheless, as the fluorescence in the cytosol increased considerably (Fig. 4), it can be concluded that a decent share of nanoparticles can reach their destination and is, therefore, suitable for intracellular drug delivery.

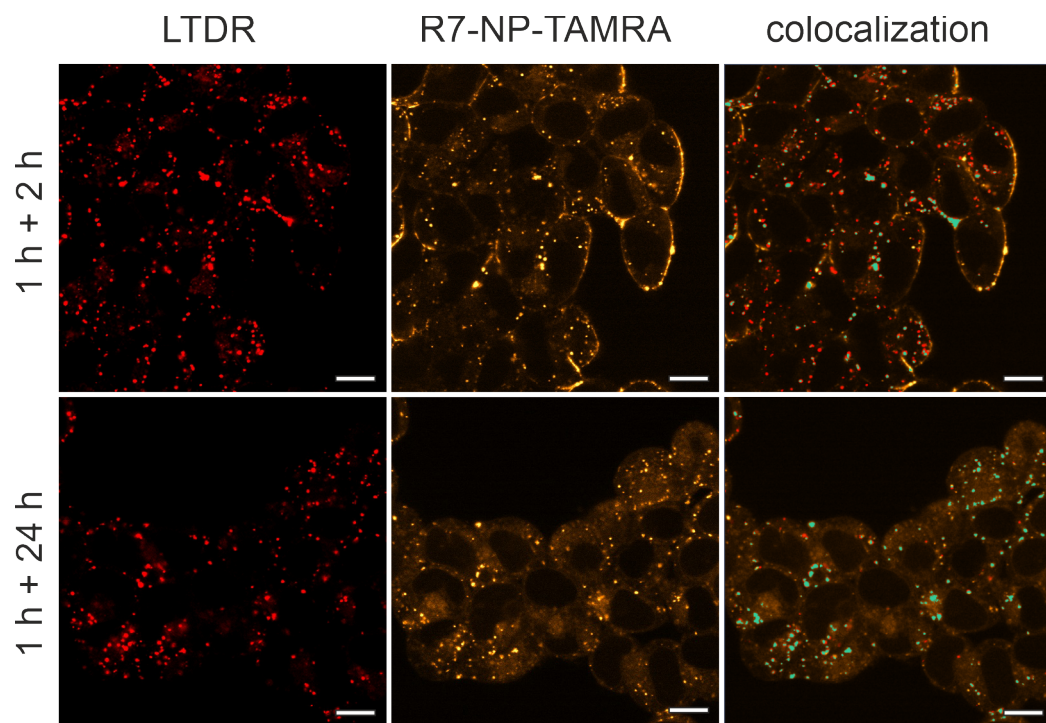


Figure 4. CLSM image of the qualitative evaluation of nanoparticle uptake. R7-modified nanoparticle binding and uptake were tracked after two different time points: the cells were incubated with NPs for 1 h. Afterward, the particles were removed, followed by further incubation for 2 h (1 h + 2 h) or 24 h (1 h + 24 h) respectively. Colocalization of lysotracker deep red (LTDR), staining late endosomes and lysosomes (red), and R7-modified nanoparticles with a DOM of 50 % labeled with TAMRA (R7-NP-TAMRA) (yellow) is shown in turquoise. The simultaneous employment of direct and endosomal uptake ways is presumed since after 3 h most particles still accumulated at the cell surface, but there was already background fluorescence visible inside the cell showing nanoparticle distribution in the cytoplasm. At this time point, almost no colocalization between particles and LTDR was visible, which indicates direct nanoparticle uptake. After 25 h high endosomal entrapment was shown, which proves additional endosomal uptake. The increasing background fluorescence demonstrated that the CPP-modified particles reached the cytosol and therefore their destination inside the cell. Scale bar: 10 μ m.

Cell-Penetrating Peptides as Selective Nanoparticle Uptake Signal

3.1.3 Quantitative Evaluation of Nanoparticle Uptake

The uptake-enhancing properties of the various CPP candidates were systematically analyzed (Fig. 5). For R4-modified nanoparticles the trend became apparent, that higher surface densities were initially accompanied by a decrease in binding and uptake. This tendency reversed as soon as a certain minimum surface density was reached and the particles with a high DOM of 75 % were taken up to a significantly higher amount than unmodified particles. Remarkably, this value correlated with the DOM, above which the R4-modified particles also showed a positive zeta potential. This observation revealed the fact that a significant uptake improvement can be achieved with a relatively low number of positive charges per peptide if the peptides are attached to the nanoparticle surface with a sufficiently high surface density, which compensates the missing peptide length. The CPPs with a higher number of positive charges per peptide, R7, TAT47-57, and R10 achieved uptake improvement even with a lower surface modification of at least 25 %, and increasing amounts of CPP surface density resulted in increasing nanoparticle binding and uptake, as expected. Increasing the amount of Bip was demonstrated to constantly decrease nanoparticle binding and uptake. In the literature, the uptake characteristics of small hydrophobic CPPs, which include various Bax-inhibiting peptides such as the Bip VSALK, are controversially discussed and poorly understood [35,50]. There are different reports on their ability to transport cargos into the cell interior [28,35,51]. However, since we did not observe any beneficial effects regarding nanoparticle uptake and it has already been shown that also scrambling of the peptide sequence does not significantly affect cellular uptake, we assume that other similar structures do not provide any advantages either [19,51]. For this reason, this category of CPPs was not further considered for the establishment of nanoparticles with conditional CPP-mediated cell uptake.

The flow cytometric analysis findings were confirmed by CLSM for R7-modified particles as an example (Fig. 6). The microscopic evaluation also verified the behavior of CPP-modified particles described in chapter 3.1.2, i.e. that the surface modification with polycationic CPPs initially led to an increased accumulation at the cell membrane after 1 h of incubation. Therefore, the uptake properties were again investigated 16 h after particle incubation. At this time point, no more membrane accumulation was visible and most of the nanoparticles were taken up into the cells (Fig. S29).

Chapter 5

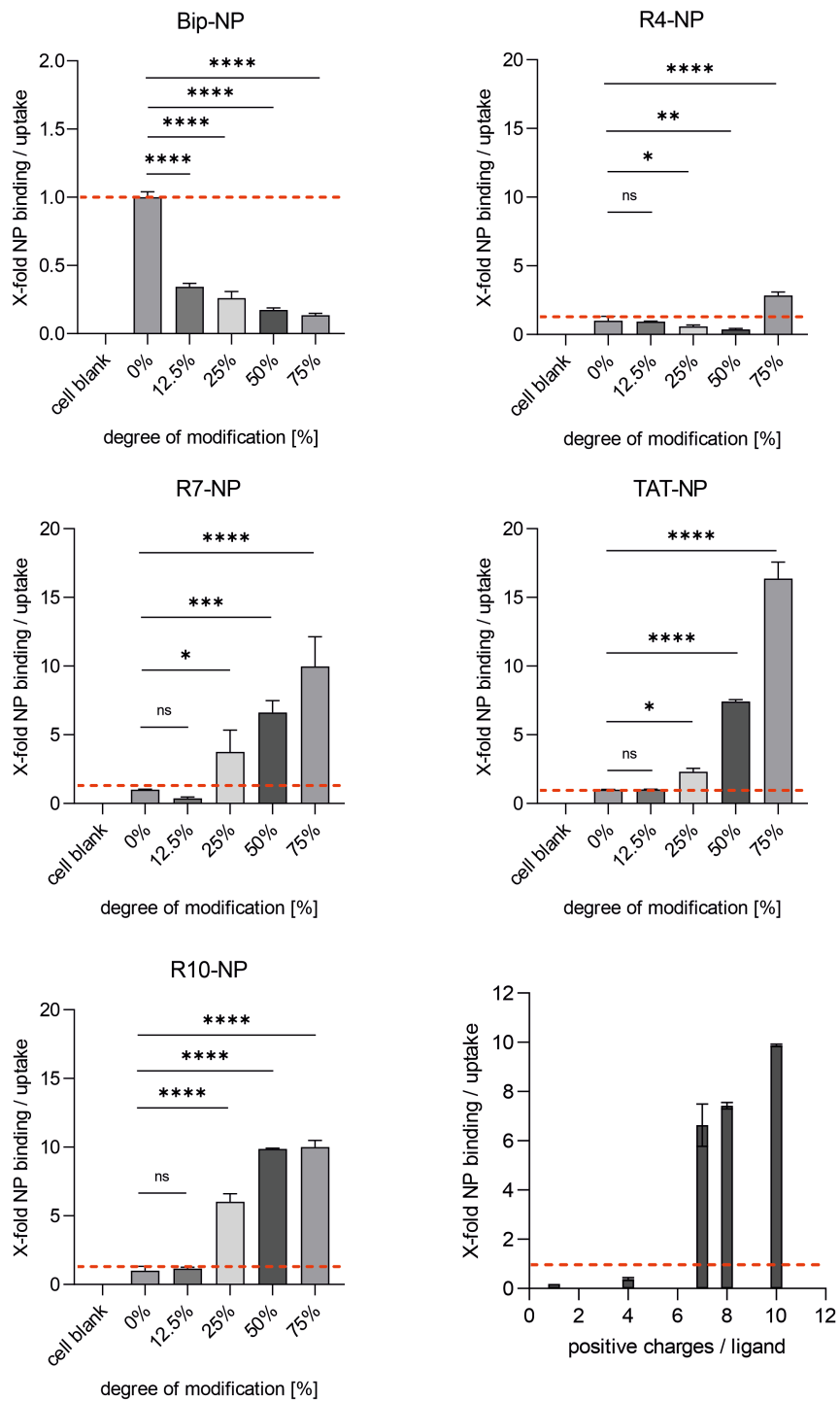


Figure 5. Comparison of nanoparticle binding/uptake improvement for different CPP-modifications and different ratios of modified to unmodified polymer. The respective CPPs are indicated in the diagram headings. The panel at the bottom right shows the correlation between particle binding and uptake and the number of positive charges per ligand (DOM = 50 %). Results represent mean \pm SD ($n = 3$, levels of statistical significance are indicated as * $p \leq 0.05$, ** $p \leq 0.01$, *** $p \leq 0.001$, **** $p \leq 0.0001$).

Cell-Penetrating Peptides as Selective Nanoparticle Uptake Signal

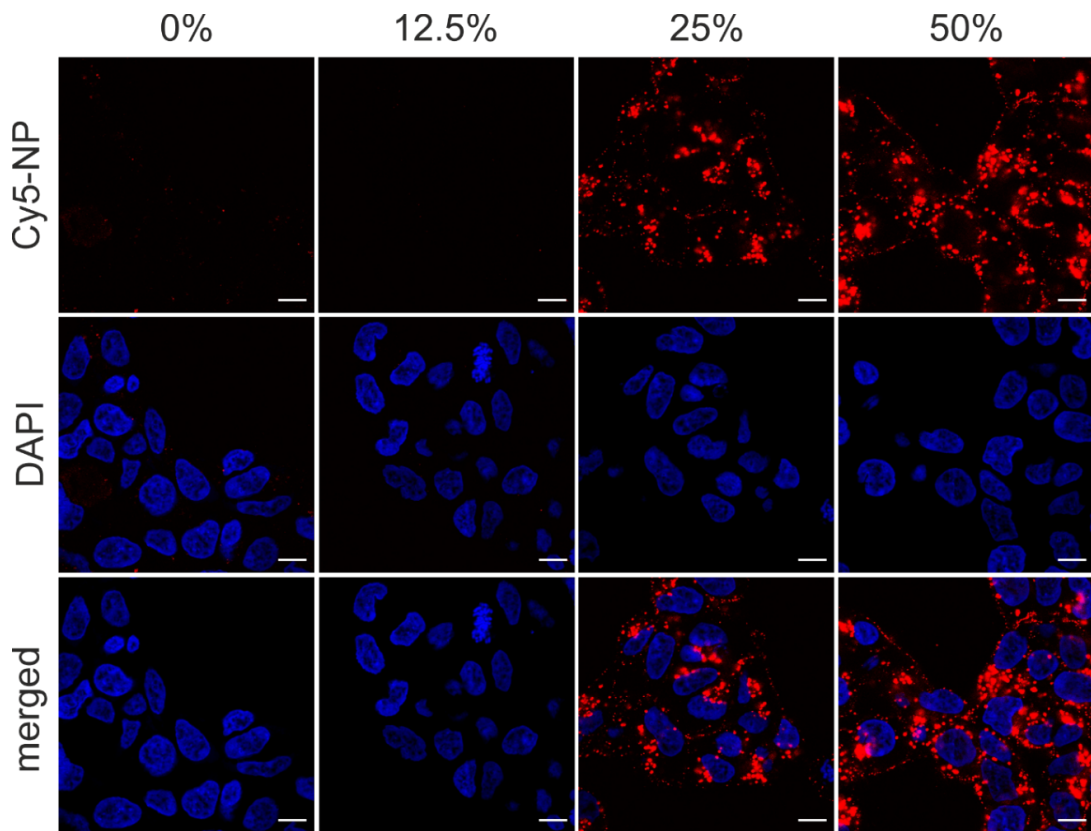


Figure 6. CLSM images of the uptake of Cy5-labeled R7-modified NPs with different DOMs in HEK293 cells. Cell nucleus labeling with DAPI (blue) served for cell localization. Increasing ratios of CPP-modified polymer mediated enhanced the uptake of the Cy5-labeled nanoparticles (Cy5-NP) (red) into HEK293 cells. Scale bar: 10 μ m.

A higher theoretical net charge of the attached ligand was accompanied by a stronger influence on particle uptake, which was shown as an example for a constant DOM of 50 %. (Lower right panel, Fig. 5) This is consistent with the literature, which describes an increase in cell penetration properties for longer arginine chains [52]. However, this has not yet been quantitatively investigated for the modification of nanoparticle surfaces and the resulting changes in particle uptake. Additionally, this aspect suggests that there is not only a correlation between the theoretical net charge of the ligand but also between the total nanoparticle zeta potential influenced by the CPP modification and its uptake. The preparation of nanoparticles with an equivalent surface density of R7 ligands, but negatively charged spacer polymers replacing the uncharged methoxy-terminated polymers, resulted in a shift to lower zeta potentials. Therefore, higher CPP-surface densities were necessary to reach a positive zeta potential (Fig. 7A). As expected, there was also a shift to higher DOMs for the significant

Chapter 5

uptake enhancement in HEK cells (Fig. 7B). Only with 75 % CPP modification, where a positive zeta potential was detected, the particles showed a significantly increased uptake. Based on the zeta potentials and corresponding uptake values of the different CPP modifications (Fig. 3, 5) we developed a model to quantitatively describe the relationship between surface charge and increased cellular uptake (Fig. 7C). This allowed the assessment of a maximum improvement of cellular uptake of the described particle system (k_{max}) achievable by CPP functionalization and the zeta potential required to obtain half-maximum uptake improvement $\zeta_{1/2}$. We found that the CPP functionalization was capable to induce an up to 15.8-fold increase in cellular uptake. Above a threshold potential of 17.4 mV, increasing charges will not lead to a substantial improvement in particle uptake. However, this correlation holds only as long as the CPP is directly visible on the particle surface. For more complex systems, where the CPP is shielded by longer polymers, it is no longer maintained (Fig. S30). Nevertheless, the results are highly valuable for the development of CPP-modified nanoparticle design strategies since they allow for an initial assessment of whether a modification can ensure the desired cellular uptake by determining the nanoparticle zeta potential.

Since high amounts of positive charges are also associated with cytotoxicity [52,53], a compromise must be found between uptake enhancement and cytotoxic effects. Our $\zeta_{1/2}$ value could serve as an orientation benchmark for this. R10-modified particles showed high cytotoxicity (Fig. S31), which could be diminished, but not to a sufficient extent, via steric shielding (Fig. S32). Therefore, TAT47-57 modification, which was associated with less cytotoxicity (Fig. S33), was used for the following CPP-shielding experiments.

Cell-Penetrating Peptides as Selective Nanoparticle Uptake Signal

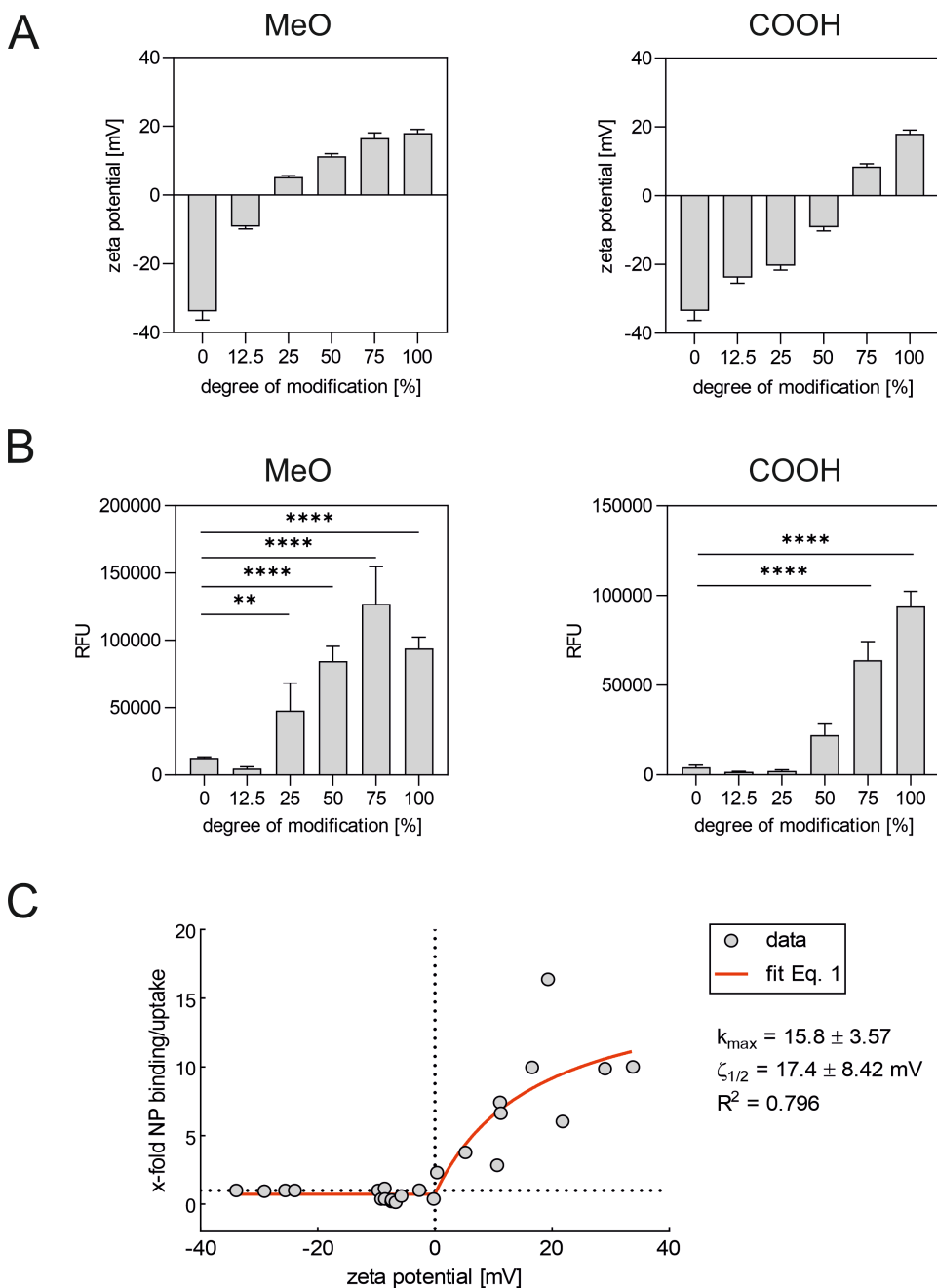


Figure 7. Correlation zeta potential and uptake improvement of CPP-modified nanoparticles in HEK293 cells. The relationship between zeta potential and uptake enhancement was verified using both an experimental (A+B) and a theoretical (C) approach. **(A+B)** NPs with identical CPP modifications (R7) and differently charged space-filling polymers (uncharged methoxy-terminated block copolymer (MeO) (left) and negatively charged carboxy-terminated block copolymer (COOH) (right)) were prepared. Zeta potential measurements **(A)** and flow cytometric experiments **(B)** demonstrated that a positive zeta potential was directly associated with a significant enhancement of particle uptake. **(C)** To quantitatively describe the relationship between surface charge and increased cellular uptake, a model

Chapter 5

was developed to deduct the maximum improvement of cellular uptake achievable (k_{max}) by CPP functionalization and the zeta-potential required to obtain half-maximum uptake improvement $\zeta_{1/2}$. Results represent mean \pm SD (n = 3, levels of statistical significance are indicated as *p \leq 0.05, **p \leq 0.01, ***p \leq 0.001, ****p \leq 0.0001) (RFU = relative fluorescence units).

3.2 Conditional CPP-Mediated Nanoparticle Uptake in Target Cells

3.2.1 Nanoparticle Characterization

To enable a selective uptake improvement by CPPs attached to the nanoparticle surface, the polycationic uptake signal was sterically shielded by longer PEG chains. Control particles without TAT modification had a size of 77.6 ± 1.0 nm, which increased to values of 89.9 ± 0.3 nm to 106.4 ± 1.3 nm depending on the DOM. NPs with additional MLN-modification were slightly larger and had a size of 85.4 nm \pm 1.3 nm without TAT modification and varying particle sizes of 97.4 nm \pm 1.5 nm to 108.8 nm \pm 1.5 nm for different DOMs (Fig. 8). However, due to the small differences in size, it can be assumed that there are no size-dependent differences in cellular uptake. The nanoparticles with shielded CPPs showed similar PDI values to the unshielded particles between 0.1 and 0.2 and thus a narrow size distribution. Compared to the nanoparticles with CPPs directly visible on the NP surface, it was noticeable that the zeta potential was hardly influenced by the positive charge of the polycationic ligands, since they were hidden inside the NP shell. Although the zeta potential increased with rising TAT modification, positive zeta potentials were only achieved at higher DOMs and the values were also significantly lower in absolute terms. For example, a DOM of 75 % resulted in a zeta potential of 4.84 ± 0.36 mV for the shielded particles, while without shielding polymers the zeta potential was markedly higher at 19.33 ± 1.21 mV. All MLN-modified particles had a slightly more negative zeta potential than the unmodified control particles. This was caused by the negatively charged carboxy groups of MLN.

Cell-Penetrating Peptides as Selective Nanoparticle Uptake Signal

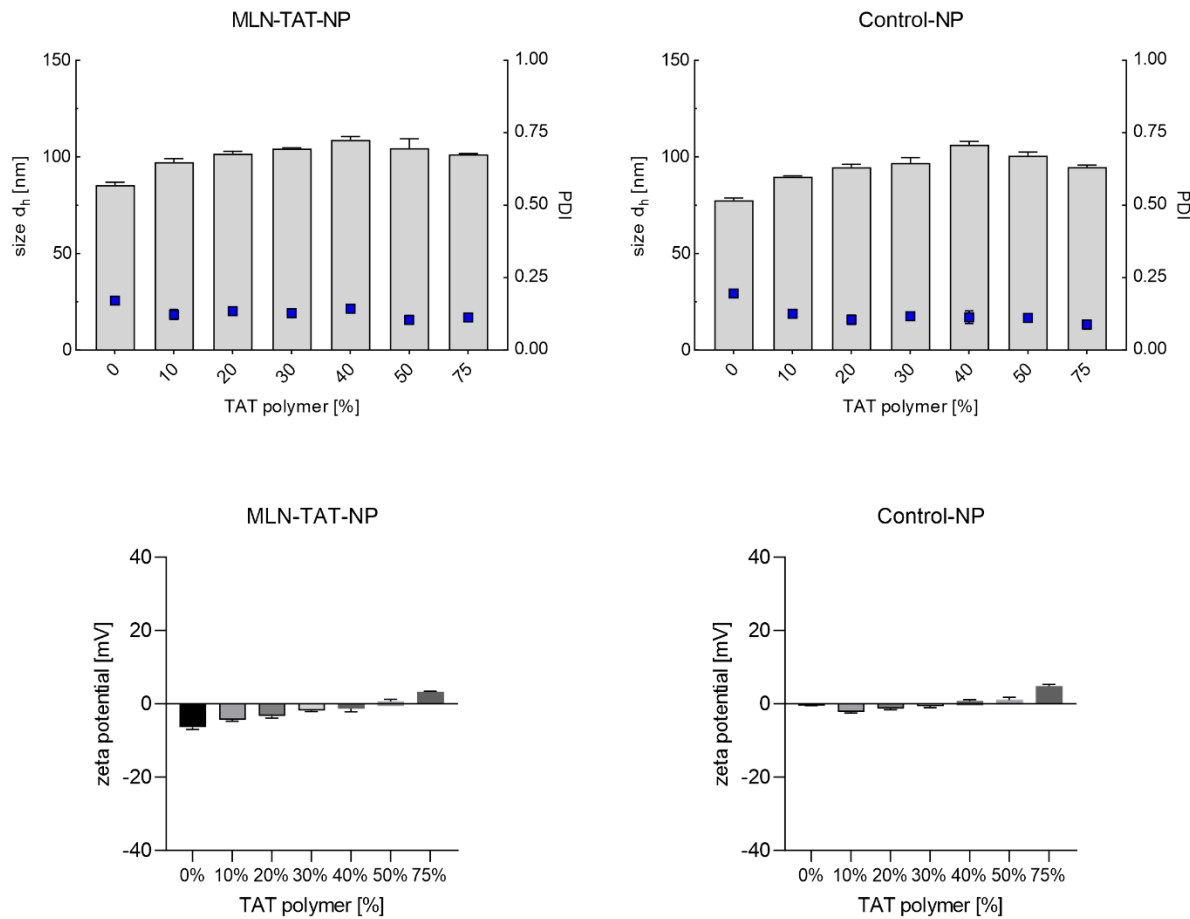


Figure 8. Characterization of nanoparticles with shielded CPP modification. The nanoparticles with TAT modification on short polymer chains (PEG_{2k}) and MLN-4760 attached to long polymer chains (PEG_{5k}) were characterized via DLS and NTA. Control-NP contained methoxy-terminated longer polymers instead of the MLN-4760-modified polymers. The proportion of long polymers was set to 25 %. The proportion of TAT-modified polymer varies and is indicated for every bar in the diagram (n = 3 technical replicates).

Chapter 5

3.2.2 Nanoparticle Binding and Uptake

Different amounts of TAT were examined to find a combination of the two ligands that ensures both, high uptake, and high selectivity. The MLN-modified particles bound reliably to a higher degree to the target cells than unmodified control particles up to a modification level of 50 %. With a DOM of 75 %, there was no significant difference between MLN-modified and control particles (Fig. 9A). This was in line with our expectations, as the specific interaction itself led to increased binding, as demonstrated by the particles with MLN but without TAT modification (DOM 0 %), and the spatial proximity increases TAT visibility. If the number of TAT ligands on the surface is too high, they led to a strong effect even without additional MLN surface modification. Therefore, a compromise must be found between the highest possible selectivity and the highest possible uptake in target cells. Based on our described preliminary experiments (Fig. 9A), a combination of 25 % MLN-modified polymer and a DOM of TAT of 30 % was considered for further investigations. To ensure that the effect of enhanced binding with MLN attached to the NP surface results from specific binding to ACE2, the particle binding was additionally evaluated with untransfected HEK cells as off-target cells. In this case neither the modification with MLN nor the dual modification led to improved particle uptake, which confirmed the target cell selectivity of the established concept (Fig. 9B). The results found in flow cytometry were additionally investigated by CLSM measurements (Fig. 9C). The microscopic evaluation supported the results and showed that although the modification with solely TAT or MLN also led to an improvement in particle binding to the target cells, this effect could be significantly increased by combining the ligands in the sequential targeting system. The fact that NP binding ultimately results in particle uptake into target cells was explicitly demonstrated for this case by further incubation of the cells after particle removal for 24 h (Fig. 9D). To investigate target cell selectivity even in the presence of off-target cells, co-culture experiments were performed. It could be demonstrated that the dual-modified particles are considerably superior in their ability to distinguish between target and off-target cells compared to control NP and thus bind to a higher extent to the surface of target cells (Fig. 9E).

Cell-Penetrating Peptides as Selective Nanoparticle Uptake Signal

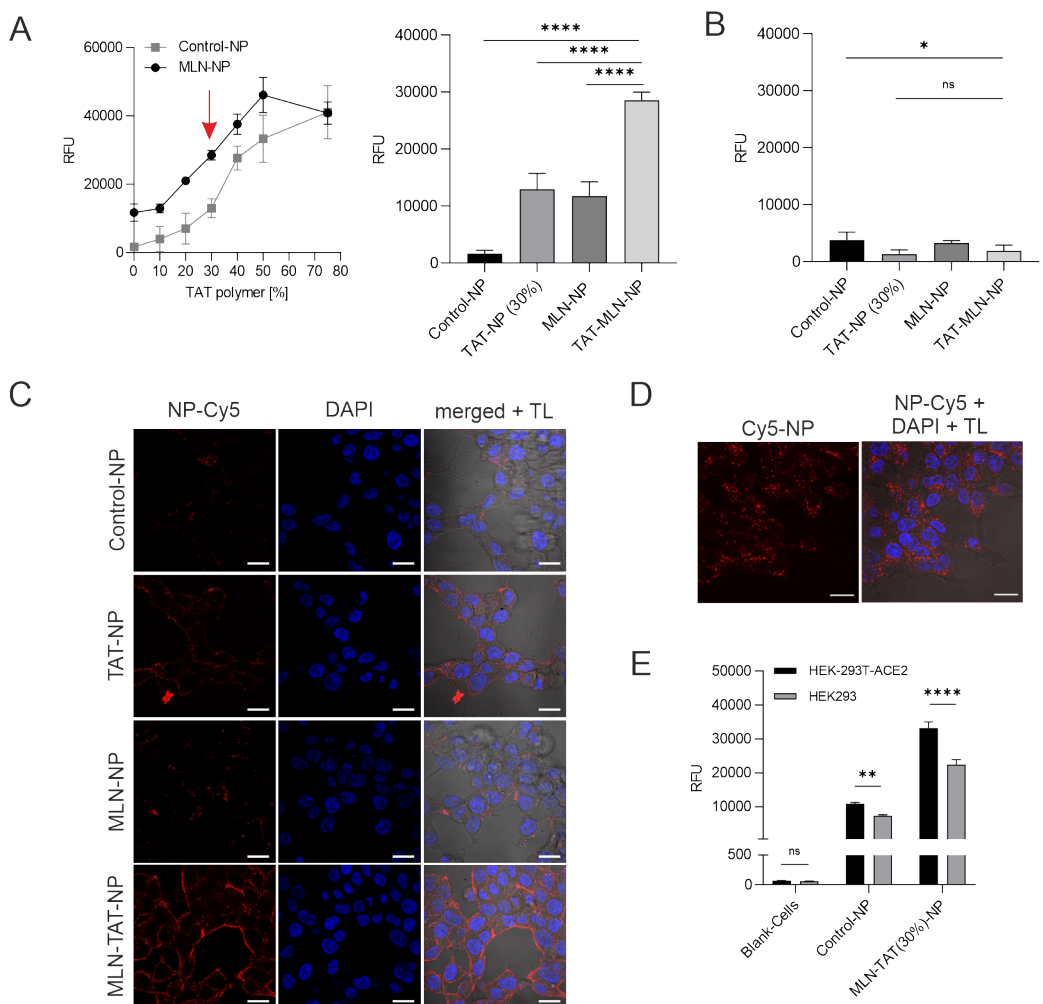


Figure 9. Flow cytometric and CLSM analysis of steric shielded NP binding and uptake. (A) Flow cytometric measurements of NP binding/uptake to ACE2-positive stable transfected HEK293T target cells. Different degrees of TAT47-57 functionalization (percentage of the shell polymer) were investigated and are stated on the x-axis to find a suitable CPP amount for the sequential targeting concept. A DOM of 30 % was considered for further experiments (red arrow). (B) Negative control with ACE2-negative HEK293 cells. (C) Confirmation of the results of (A) via CLSM analysis for a DOM of 30 %. NPs were labeled with Cy5, cell nuclei were stained with DAPI. In the right row, the Cy5 and DAPI channels were merged and supplemented by transmitted light (TL) for cell localization. (D) CLSM evaluation of MLN-TAT-NP from (C) with further 24 h of incubation. (E) Co-culture experiments with HEK293T-ACE2 stable cells and untransfected HEK293 cells. Scale bar: 20 μ m. Results represent mean \pm SD ($n \geq 3$, levels of statistical significance are indicated as * $p \leq 0.05$, ** $p \leq 0.01$, *** $p \leq 0.001$, **** $p \leq 0.0001$) (RFU, relative fluorescence units).

4 Conclusion

In this study, we systematically evaluated the effect of nanoparticle surface modifications with various cell-penetrating peptides. We identified correlations between the number of positive charges per peptide, surface density, zeta potential, and the corresponding uptake enhancement in cell experiments, which is highly valuable for the implementation of nanoparticle design strategies containing cell-penetrating peptides. Based on these data, we established a targeting strategy, that allows to utilize the unique uptake-enhancing properties of cell-penetrating peptides selectively by promoting a conditional cell internalization only after a prior selective cell binding has revealed the uptake signal. In conclusion, we have achieved a selective, completely receptor-independent nanoparticle uptake into target cells, which is expected to be beneficial with respect to targeting-related side effects and enables an exclusively cargo-dependent pharmacological effect.

References

- [1] S. Silva, A.J. Almeida, N. Vale, Combination of Cell-Penetrating Peptides with Nanoparticles for Therapeutic Application: A Review, *Biomolecules* 9 (2019). <https://doi.org/10.3390/biom9010022>.
- [2] M. Zorko, Ü. Langel, Studies of cell-penetrating peptides by biophysical methods, *Quarterly Reviews of Biophysics* 55 (2022) 1–55. <https://doi.org/10.1017/S0033583522000026>.
- [3] I. Gessner, I. Neundorf, Nanoparticles Modified with Cell-Penetrating Peptides: Conjugation Mechanisms, Physicochemical Properties, and Application in Cancer Diagnosis and Therapy, *Int. J. Mol. Sci.* 21 (2020). <https://doi.org/10.3390/ijms21072536>.
- [4] H.M. Kondow-McConaghy, N. Muthukrishnan, A. Erazo-Oliveras, K. Najjar, R.L. Juliano, J.-P. Pellois, Impact of the Endosomal Escape Activity of Cell-Penetrating Peptides on the Endocytic Pathway, *ACS Chem. Biol.* 15 (2020) 2355–2363. <https://doi.org/10.1021/acschembio.0c00319>.
- [5] M. Gestin, M. Dowaidar, Ü. Langel, Uptake Mechanism of Cell-Penetrating Peptides, *Adv. Exp. Med. Biol.* 1030 (2017) 255–264. https://doi.org/10.1007/978-3-319-66095-0_11.
- [6] D. Kalafatovic, E. Giralt, Cell-Penetrating Peptides: Design Strategies beyond Primary Structure and Amphipathicity, *Molecules* 22 (2017). <https://doi.org/10.3390/molecules22111929>.
- [7] K. Abstiens, S. Maslanka Figueroa, M. Gregoritza, A.M. Goepferich, Interaction of functionalized nanoparticles with serum proteins and its impact on colloidal stability and cargo leaching, *Soft Matter* 15 (2019) 709–720. <https://doi.org/10.1039/C8SM02189A>.
- [8] A. Erazo-Oliveras, N. Muthukrishnan, R. Baker, T.-Y. Wang, J.-P. Pellois, Improving the endosomal escape of cell-penetrating peptides and their cargos: strategies and challenges, *Pharmaceuticals* 5 (2012) 1177–1209. <https://doi.org/10.3390/ph5111177>.
- [9] J.M. Steinbach, Y.-E. Seo, W.M. Saltzman, Cell penetrating peptide-modified poly(lactic-co-glycolic acid) nanoparticles with enhanced cell internalization, *Acta Biomaterialia* 30 (2016) 49–61. <https://doi.org/10.1016/j.actbio.2015.11.029>.
- [10] S. Streck, S.S.-R. Bohr, D. Birch, T. Rades, N.S. Hatzakis, A. McDowell, H. Mørck Nielsen, Interactions of Cell-Penetrating Peptide-Modified Nanoparticles with Cells

Chapter 5

Evaluated Using Single Particle Tracking, *ACS Applied Bio Materials* 4 (2021) 3155–3165. <https://doi.org/10.1021/acsabm.0c01563>.

[11] N. Feiner-Gracia, A. Dols-Perez, M. Royo, C. Solans, M.J. Garcia-Celma, C. Fornaguera, Cell penetrating peptide grafting of PLGA nanoparticles to enhance cell uptake, *European Polymer Journal* 108 (2018) 429–438. <https://doi.org/10.1016/j.eurpolymj.2018.09.026>.

[12] S. Trabulo, A.L. Cardoso, M. Mano, M.C.P. de Lima, Cell-Penetrating Peptides—Mechanisms of Cellular Uptake and Generation of Delivery Systems, *Pharmaceuticals* 3 (2010) 961–993. <https://doi.org/10.3390/ph3040961>.

[13] H. de Jong, K.M. Bonger, D.W.P.M. Löwik, Activatable cell-penetrating peptides: 15 years of research, *RSC Chem. Biol.* 1 (2020) 192–203. <https://doi.org/10.1039/d0cb00114g>.

[14] D. Pei, M. Buyanova, Overcoming Endosomal Entrapment in Drug Delivery, *Bioconjug. Chem.* 30 (2019) 273–283. <https://doi.org/10.1021/acs.bioconjchem.8b00778>.

[15] A. Gori, G. Lodigiani, S.G. Colombarolli, G. Bergamaschi, A. Vitali, Cell Penetrating Peptides: Classification, Mechanisms, Methods of Study, and Applications, *ChemMedChem* 18 (2023) e202300236. <https://doi.org/10.1002/cmdc.202300236>.

[16] A. Komin, L.M. Russell, K.A. Hristova, P.C. Searson, Peptide-based strategies for enhanced cell uptake, transcellular transport, and circulation: Mechanisms and challenges, *Adv. Drug Deliv. Rev.* 110-111 (2017) 52–64. <https://doi.org/10.1016/j.addr.2016.06.002>.

[17] J. Allen, J.-P. Pellois, Hydrophobicity is a key determinant in the activity of arginine-rich cell penetrating peptides, *Sci Rep* 12 (2022) 15981. <https://doi.org/10.1038/s41598-022-20425-y>.

[18] J.R. Maiolo, M. Ferrer, E.A. Ottinger, Effects of cargo molecules on the cellular uptake of arginine-rich cell-penetrating peptides, *Biochim. Biophys. Acta* 1712 (2005) 161–172. <https://doi.org/10.1016/j.bbamem.2005.04.010>.

[19] F. Milletti, Cell-penetrating peptides: classes, origin, and current landscape, *Drug Discovery Today* 17 (2012) 850–860. <https://doi.org/10.1016/j.drudis.2012.03.002>.

[20] S. Aroui, S. Brahim, M. de Waard, A. Kenani, Cytotoxicity, intracellular distribution and uptake of doxorubicin and doxorubicin coupled to cell-penetrating peptides in different cell lines: a comparative study, *Biochemical and Biophysical Research Communications* 391 (2010) 419–425. <https://doi.org/10.1016/j.bbrc.2009.11.073>.

Cell-Penetrating Peptides as Selective Nanoparticle Uptake Signal

[21] J. Feng, L. Tang, The cell-type specificity and endosomal escape of cell-penetrating peptides, *Current Pharmaceutical Design* 21 (2015) 1351–1356. <https://doi.org/10.2174/1381612820666141023155017>.

[22] M. Sun, Y. Gao, Z. Zhu, H. Wang, C. Han, X. Yang, W. Pan, A systematic in vitro investigation on poly-arginine modified nanostructured lipid carrier: Pharmaceutical characteristics, cellular uptake, mechanisms and cytotoxicity, *Asian Journal of Pharmaceutical Sciences* 12 (2017) 51–58. <https://doi.org/10.1016/j.ajps.2016.07.007>.

[23] J.J. Byrnes, S. Gross, C. Ellard, K. Connolly, S. Donahue, D. Picarella, Effects of the ACE2 inhibitor GL1001 on acute dextran sodium sulfate-induced colitis in mice, *Inflamm. Res.* 58 (2009) 819–827. <https://doi.org/10.1007/s00011-009-0053-3>.

[24] M. Walter, F. Baumann, K. Schorr, A. Goepferich, Ectoenzymes as Promising Cell Identification Structures for the High Avidity Targeting of Polymeric Nanoparticles, *International Journal of Pharmaceutics* (2023) 123453. <https://doi.org/10.1016/j.ijpharm.2023.123453>.

[25] A.K. Parthipan, N. Gupta, K. Pandey, B. Sharma, J. Jacob, S. Saha, One-step fabrication of bicompartimental microparticles as a dual drug delivery system for Parkinson's disease management, *J Mater Sci* 54 (2019) 730–744. <https://doi.org/10.1007/s10853-018-2819-x>.

[26] I. Szabó, F. Illien, L.E. Dókus, M. Yousef, Z. Baranyai, S. Bősze, S. Ise, K. Kawano, S. Sagan, S. Futaki, F. Hudecz, Z. Bánóczi, Influence of the Dabcyl group on the cellular uptake of cationic peptides: short oligoarginines as efficient cell-penetrating peptides, *Amino Acids* 53 (2021) 1033–1049. <https://doi.org/10.1007/s00726-021-03003-w>.

[27] C. Neale, K. Huang, A.E. García, S. Tristram-Nagle, Penetration of HIV-1 Tat47-57 into PC/PE Bilayers Assessed by MD Simulation and X-ray Scattering, *Membranes* (Basel) 5 (2015) 473–494. <https://doi.org/10.3390/membranes5030473>.

[28] J.A. Gomez, J. Chen, J. Ngo, D. Hajkova, I.-J. Yeh, V. Gama, M. Miyagi, S. Matsuyama, Cell-Penetrating Penta-Peptides (CPP5s): Measurement of Cell Entry and Protein-Transduction Activity, *Pharmaceutics* (Basel) 3 (2010) 3594–3613. <https://doi.org/10.3390/ph3123594>.

[29] M. Bresinsky, J.M. Strasser, A. Hubmann, B. Vallaster, W.M. McCue, J. Fuller, G. Singh, K.M. Nelson, M.E. Cuellar, B.C. Finzel, K.H. Ashe, M.A. Walters, S. Pocke, Characterization of caspase-2 inhibitors based on specific sites of caspase-2-mediated

Chapter 5

proteolysis, Archiv der Pharmazie 355 (2022) 355–356. e2200095. <https://doi.org/10.1002/ardp.202200095>.

[30] H. Qian, A.R. Wohl, J.T. Crow, C.W. Macosko, T.R. Hoyer, A Strategy for Control of "Random" Copolymerization of Lactide and Glycolide: Application to Synthesis of PEG-b-PLGA Block Polymers Having Narrow Dispersity, *Macromolecules* 44 (2011) 7132–7140. <https://doi.org/10.1021/ma201169z>.

[31] K. Abstiens, M. Gregoritza, A.M. Goepferich, Ligand Density and Linker Length are Critical Factors for Multivalent Nanoparticle-Receptor Interactions, *ACS Appl. Mater. Interfaces* 11 (2019) 1311–1320. <https://doi.org/10.1021/acsami.8b18843>.

[32] G.L. Siparsky, K.J. Voorhees, F. Miao, Hydrolysis of Polylactic Acid (PLA) and Polycaprolactone (PCL) in Aqueous Acetonitrile Solutions: Autocatalysis, *Journal of Polymers and the Environment* 6 (1998) 31–41. <https://doi.org/10.1023/A:1022826528673>.

[33] A. Göpferich, Mechanisms of polymer degradation and erosion, *Biomaterials* 17 (1996) 103–114. [https://doi.org/10.1016/0142-9612\(96\)85755-3](https://doi.org/10.1016/0142-9612(96)85755-3).

[34] K.G. Ozdemir, H. Yilmaz, S. Yilmaz, In vitro evaluation of cytotoxicity of soft lining materials on L929 cells by MTT assay, *J. Biomed. Mater. Res. B Appl. Biomater.* 90 (2009) 82–86. <https://doi.org/10.1002/jbm.b.31256>.

[35] J. Xie, Y. Bi, H. Zhang, S. Dong, L. Teng, R.J. Lee, Z. Yang, Cell-Penetrating Peptides in Diagnosis and Treatment of Human Diseases: From Preclinical Research to Clinical Application, *Front. Pharmacol.* 11 (2020) 697. <https://doi.org/10.3389/fphar.2020.00697>.

[36] J.M. Wolfe, C.M. Fadzen, Z.-N. Choo, R.L. Holden, M. Yao, G.J. Hanson, B.L. Pentelute, Machine Learning To Predict Cell-Penetrating Peptides for Antisense Delivery, *ACS Central Science* 4 (2018) 512–520. <https://doi.org/10.1021/acscentsci.8b00098>.

[37] I. Nakase, T. Takeuchi, G. Tanaka, S. Futaki, Methodological and cellular aspects that govern the internalization mechanisms of arginine-rich cell-penetrating peptides, *Adv. Drug Deliv. Rev.* 60 (2008) 598–607. <https://doi.org/10.1016/j.addr.2007.10.006>.

[38] S.M. Fuchs, R.T. Raines, Pathway for polyarginine entry into mammalian cells, *Biochemistry* 43 (2004) 2438–2444. <https://doi.org/10.1021/bi035933x>.

[39] R. Ray, S. Ghosh, A. Maity, N.R. Jana, Arginine Surface Density of Nanoparticles Controls Nonendocytic Cell Uptake and Autophagy Induction, *ACS Appl. Mater. Interfaces* 16 (2024) 5451–5461. <https://doi.org/10.1021/acsami.3c14472>.

Cell-Penetrating Peptides as Selective Nanoparticle Uptake Signal

[40] P. Panja, N.R. Jana, Arginine-Terminated Nanoparticles of <10 nm Size for Direct Membrane Penetration and Protein Delivery for Straight Access to Cytosol and Nucleus, *The Journal of Physical Chemistry Letters* 11 (2020) 2363–2368. <https://doi.org/10.1021/acs.jpclett.0c00176>.

[41] J. Váňová, A. Hejtmánková, M.H. Kalbáčová, H. Španielová, The Utilization of Cell-Penetrating Peptides in the Intracellular Delivery of Viral Nanoparticles, *Materials* 12 (2019) 2671. <https://doi.org/10.3390/ma12172671>.

[42] M. Fretz, J. Jin, R. Conibere, N.A. Penning, S. Al-Taei, G. Storm, S. Futaki, T. Takeuchi, I. Nakase, A.T. Jones, Effects of Na⁺/H⁺ exchanger inhibitors on subcellular localisation of endocytic organelles and intracellular dynamics of protein transduction domains HIV-TAT peptide and octaarginine, *Journal of Controlled Release* 116 (2006) 247–254. <https://doi.org/10.1016/j.jconrel.2006.07.009>.

[43] F. Duchardt, M. Fotin-Mleczek, H. Schwarz, R. Fischer, R. Brock, A comprehensive model for the cellular uptake of cationic cell-penetrating peptides, *Traffic* 8 (2007) 848–866. <https://doi.org/10.1111/j.1600-0854.2007.00572.x>.

[44] I. Nakase, M. Niwa, T. Takeuchi, K. Sonomura, N. Kawabata, Y. Koike, M. Takehashi, S. Tanaka, K. Ueda, J.C. Simpson, A.T. Jones, Y. Sugiura, S. Futaki, Cellular uptake of arginine-rich peptides: roles for macropinocytosis and actin rearrangement, *Mol. Ther.* 10 (2004) 1011–1022. <https://doi.org/10.1016/j.ymthe.2004.08.010>.

[45] F. Madani, S. Lindberg, U. Langel, S. Futaki, A. Gräslund, Mechanisms of cellular uptake of cell-penetrating peptides, *J. Biophys.* 2011 (2011) 414729. <https://doi.org/10.1155/2011/414729>.

[46] S.M. Farkhani, A. Valizadeh, H. Karami, S. Mohammadi, N. Sohrabi, F. Badrzadeh, Cell penetrating peptides: efficient vectors for delivery of nanoparticles, nanocarriers, therapeutic and diagnostic molecules, *Peptides* 57 (2014) 78–94. <https://doi.org/10.1016/j.peptides.2014.04.015>.

[47] A. Ahmad, J.M. Khan, S. Haque, Strategies in the design of endosomolytic agents for facilitating endosomal escape in nanoparticles, *Biochimie* 160 (2019) 61–75. <https://doi.org/10.1016/j.biochi.2019.02.012>.

[48] R.N. Majzoub, C.-L. Chan, K.K. Ewert, B.F.B. Silva, K.S. Liang, C.R. Safinya, Fluorescence microscopy colocalization of lipid-nucleic acid nanoparticles with wildtype and mutant Rab5-GFP: A platform for investigating early endosomal events, *Biochim. Biophys. Acta* 1848 (2015) 1308–1318. <https://doi.org/10.1016/j.bbamem.2015.03.001>.

Chapter 5

[49] S. Ahmed, S. Fujita, K. Matsumura, Enhanced protein internalization and efficient endosomal escape using polyampholyte-modified liposomes and freeze concentration, *Nanoscale* 8 (2016) 15888–15901. <https://doi.org/10.1039/c6nr03940e>.

[50] J.A. Gomez, V. Gama, T. Yoshida, W. Sun, P. Hayes, K. Leskov, D. Boothman, S. Matsuyama, Bax-inhibiting peptides derived from Ku70 and cell-penetrating pentapeptides, *Biochem Soc Trans* 35 (2007) 797–801. <https://doi.org/10.1042/BST0350797>.

[51] K. Kardani, A. Milani, S. H Shabani, A. Bolhassani, Cell penetrating peptides: the potent multi-cargo intracellular carriers, *Expert Opin. Drug Deliv.* 16 (2019) 1227–1258. <https://doi.org/10.1080/17425247.2019.1676720>.

[52] B. Ghaemi, S. Tanwar, A. Singh, D.R. Arifin, M.T. McMahon, I. Barman, J.W.M. Bulte, Cell-Penetrating and Enzyme-Responsive Peptides for Targeted Cancer Therapy: Role of Arginine Residue Length on Cell Penetration and In Vivo Systemic Toxicity, *ACS Appl. Mater. Interfaces* 16 (2024) 11159–11171. <https://doi.org/10.1021/acsami.3c14908>.

[53] X.-R. Shao, X.-Q. Wei, X. Song, L.-Y. Hao, X.-X. Cai, Z.-R. Zhang, Q. Peng, Y.-F. Lin, Independent effect of polymeric nanoparticle zeta potential/surface charge, on their cytotoxicity and affinity to cells, *Cell Prolif.* 48 (2015) 465–474. <https://doi.org/10.1111/cpr.12192>.

Cell-Penetrating Peptides as Selective Nanoparticle Uptake Signal

Chapter 5

Chapter 5

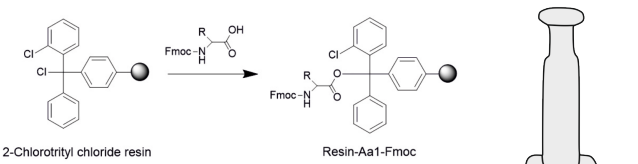
Supporting Information

Chapter 5 – Supporting Information

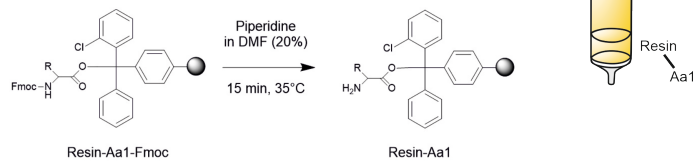
1 Synthesis of Side Chain-Protected Cell-Penetrating Peptides

1.1 Detailed Synthesis Scheme of Side Chain-protected CPPs

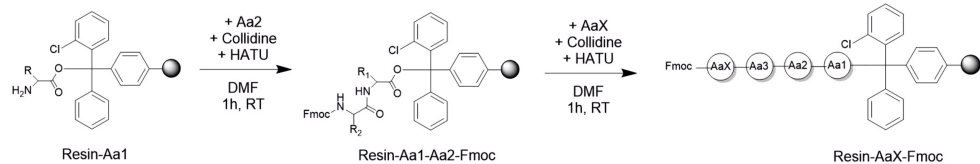
1) Loading of the resin with the first amino acid (Aa1)



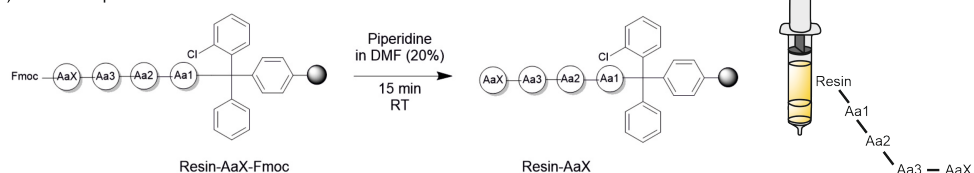
2) Fmoc deprotection



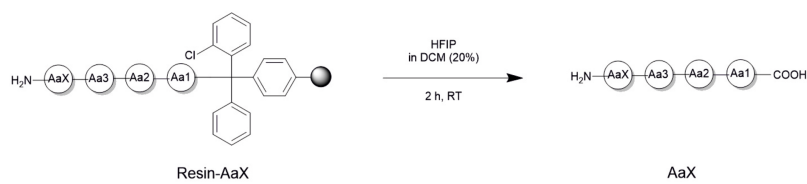
3) Coupling of further amino acids (AaX)



4) Fmoc deprotection



5) Cleavage from solid phase



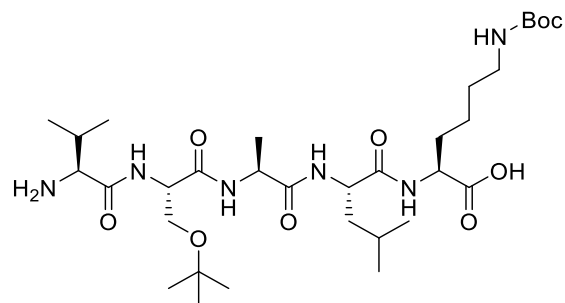
Scheme S1. Detailed synthesis scheme.

Chapter 5 – Supporting Information

2 Analytics of Cell-Penetrating Peptides

2.1 Bip_{prot}.

2.1.1 Structure



Chemical Formula: C₃₂H₆₀N₆O₉

Exact Mass: 672,44

Molecular Weight: 672,87

Figure S1. Structure of Bip_{prot}.

2.1.2 NMR

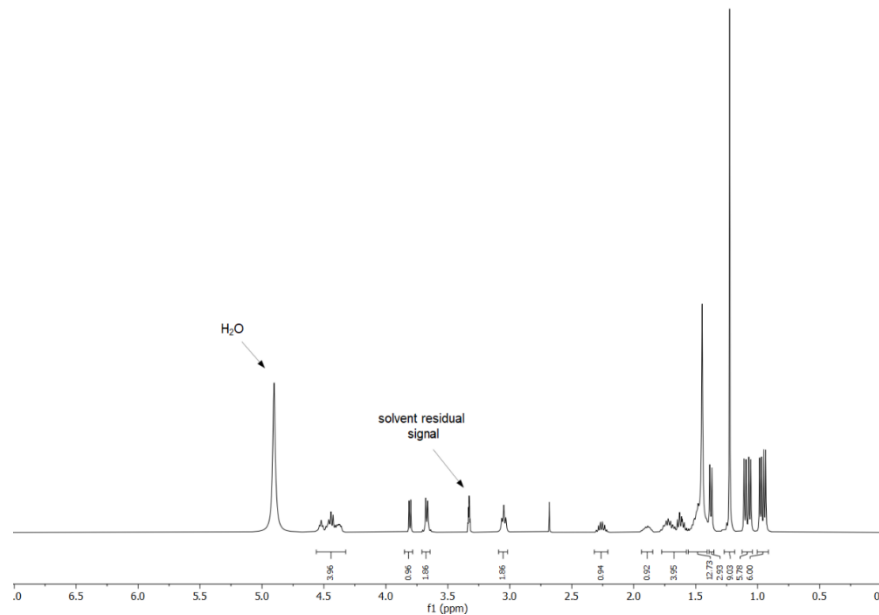


Figure S2. ¹H-NMR of Bip_{prot}. ¹H-NMR (400 MHz, CD₃OD) δ 4.58 – 4.31 (m, 4H), 3.81 (d, *J* = 5.7 Hz, 1H), 3.67 (d, *J* = 5.9, 1.3 Hz, 2H), 3.05 (t, *J* = 6.7 Hz, 2H), 2.32 – 2.20 (m, 1H), 1.94 – 1.82 (m, 1H), 1.79 – 1.57 (m, 4H), 1.56 – 1.40 (m, 13H), 1.38 (d, *J* = 7.0 Hz, 3H), 1.23 (s, 9H), 1.08 (dd, *J* = 15.2, 6.9 Hz, 6H), 0.96 (dd, *J* = 13.3, 6.4 Hz, 6H).

Supporting Information – CPPs as Selective Nanoparticle Uptake Signal

2.1.3 Mass spectrometry

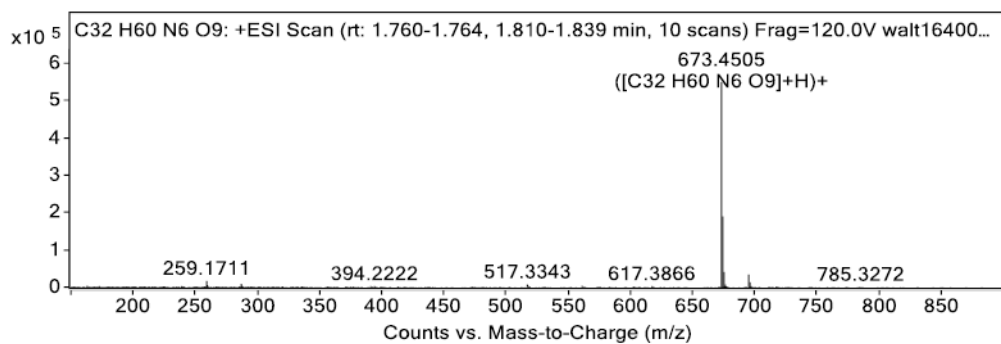


Figure S3. Mass spectrum of $\text{Bip}_{\text{prot.}}$. HRMS: $(\text{M}+\text{H})^+$ m/z calculated for $\text{C}_{32}\text{H}_{61}\text{N}_6\text{O}_9^+$: 673.4495, found: 673.4505.

2.1.4 HPLC

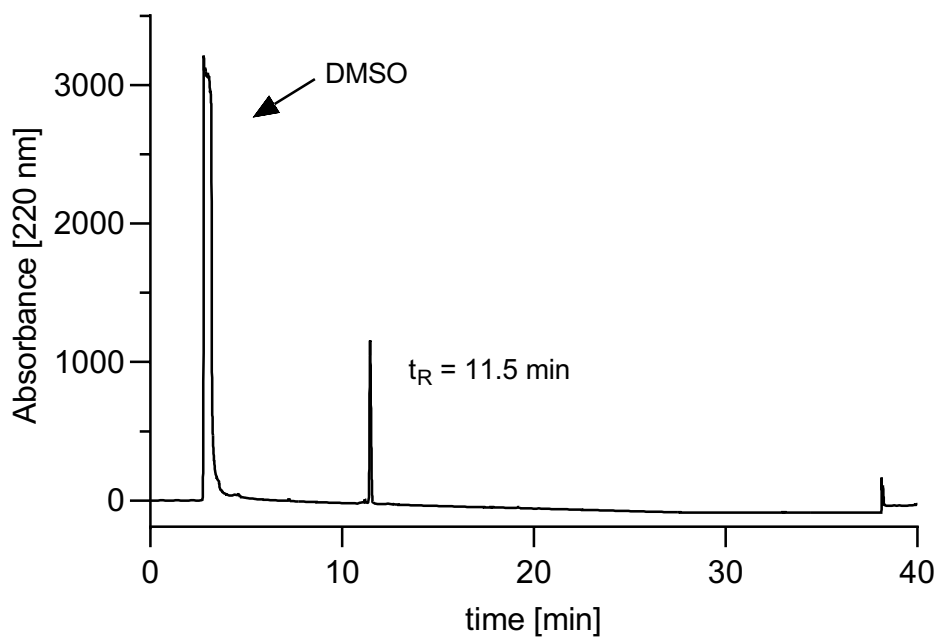
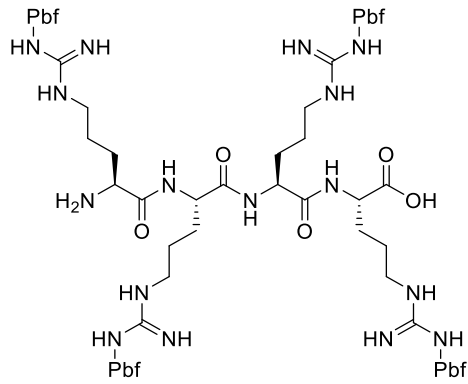


Figure S4. RP-HPLC analysis of $\text{Bip}_{\text{prot.}}$. Retention time t_R of $\text{Bip}_{\text{prot.}}$: 11.5 min.

Chapter 5 – Supporting Information

2.2 R4_{prot.}

2.2.1 Structure



Chemical Formula: C₇₆H₁₁₄N₁₆O₁₇S₄

Exact Mass: 1650,74

Molecular Weight: 1652,08

Figure S5. Structure of R4_{prot.}.

2.2.2 NMR

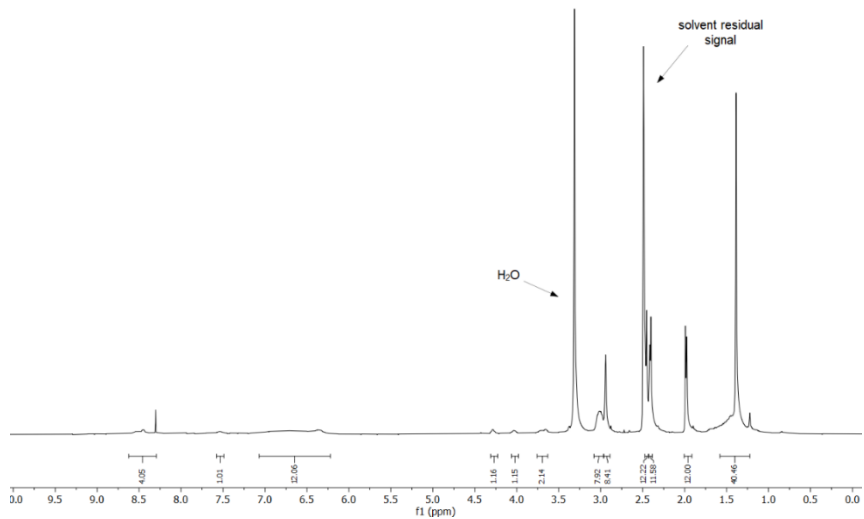


Figure S6. ¹H-NMR spectrum of R4_{prot.} ¹H-NMR (400 MHz, DMSO-d6) δ 8.61 – 8.29 (m, 4H), 7.54 (s, 1H), 7.07 – 6.20 (m, 12H), 4.28 (s, 1H), 4.03 (s, 1H), 3.69 (d, *J* = 26.2 Hz, 2H), 3.08 – 2.96 (m, 8H), 2.94 (s, 8H), 2.47 – 2.43 (m, 12H), 2.42 – 2.39 (m, 12H), 1.98 (d, *J* = 6.2 Hz, 12H), 1.60 – 1.20 (m, 40H).

Supporting Information – CPPs as Selective Nanoparticle Uptake Signal

2.2.3 Mass spectrometry

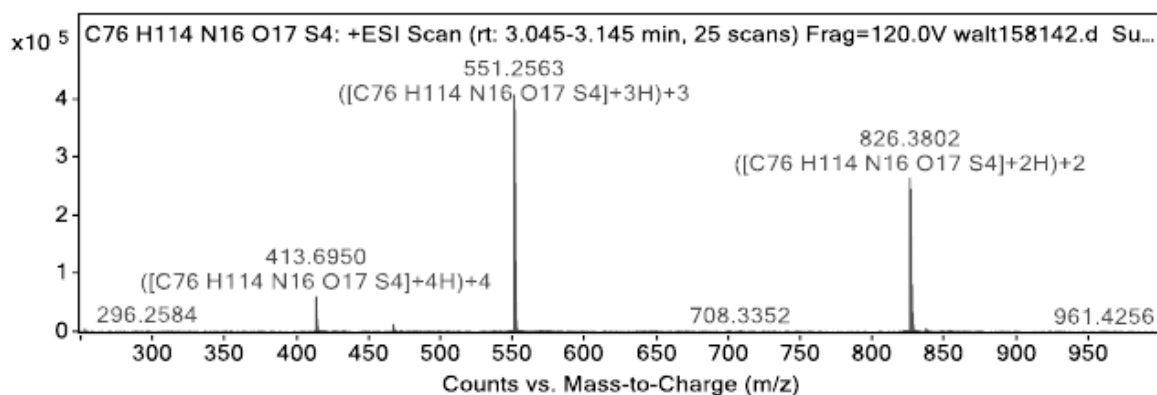


Figure S7. Mass spectrum of R4_{prot}. HRMS: $(M+2H)^{+2}$ m/z calculated for $C_{76}H_{116}N_{16}O_{17}S_4^{2+}$: 826.3788, found: 826.3802.

2.2.4 HPLC

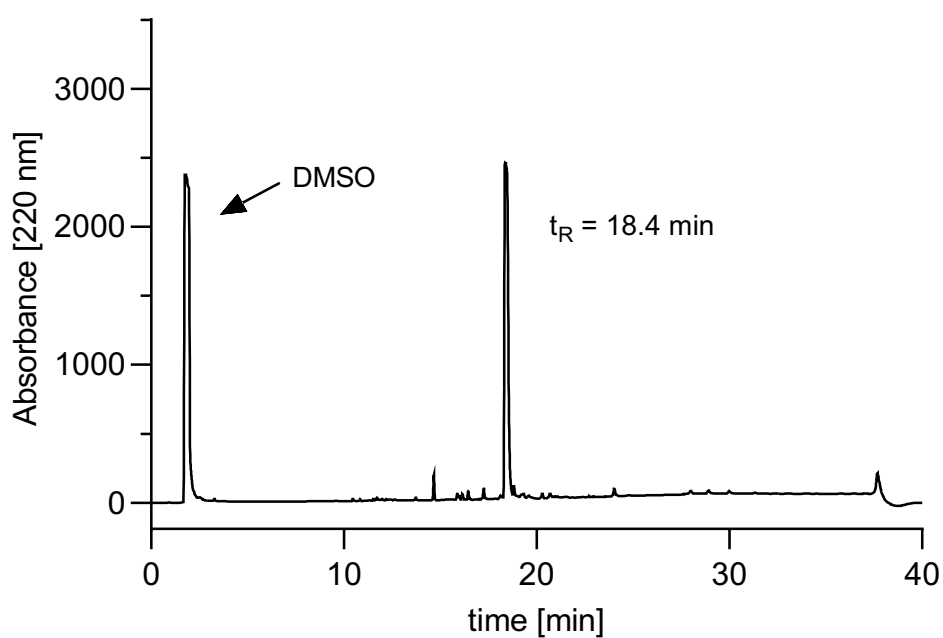
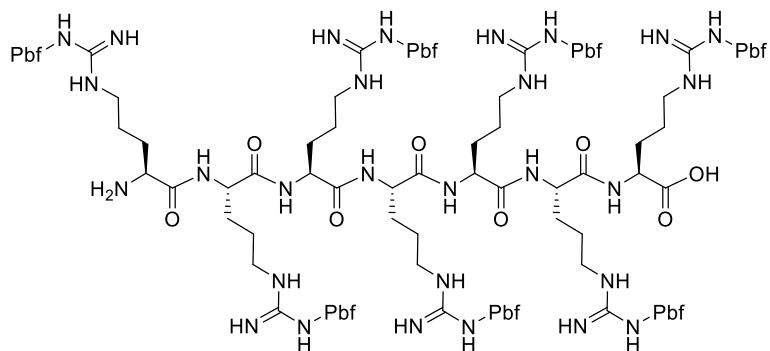


Figure S8. RP-HPLC analysis of R4_{prot}. Retention time t_R of R4_{prot}: 18.4 min.

Chapter 5 – Supporting Information

2.3 R7_{prot.}

2.3.1 Structure



Chemical Formula: C₁₃₃H₁₉₈N₂₈O₂₉S₇

Exact Mass: 2875,29

Molecular Weight: 2877,63

Figure S9. Structure of R7_{prot}.

2.3.2 NMR

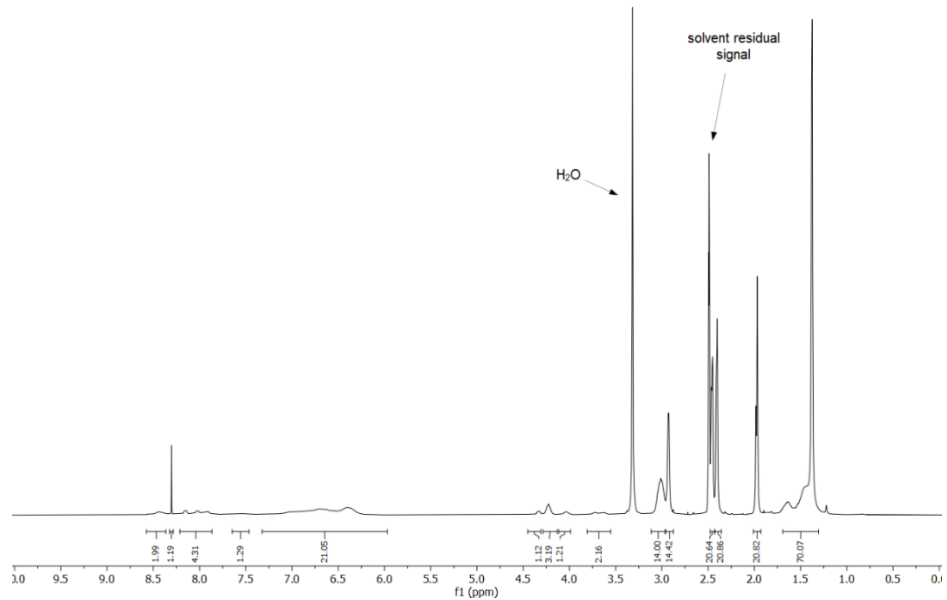


Figure S10. ^1H -NMR spectrum of R7_{prot}. ^1H -NMR (400 MHz, DMSO-d6) δ 8.43 (s, 2H), 8.30 (s, 1H), 8.21 – 7.83 (m, 4H), 7.50 (s, 1H), 7.31 – 6.06 (m, 21H), 4.44 – 4.30 (m, 1H), 4.27 – 4.14 (m, 3H), 4.03 (s, 1H), 3.67 (d, J = 37.5 Hz, 2H), 3.10 – 2.96 (m, 14H), 2.93 (s, 14H), 2.48 – 2.43 (m, 21H), 2.42 – 2.36 (m, 21H), 2.01 – 1.93 (m, 21H), 1.71 – 1.25 (m, 70H).

Supporting Information – CPPs as Selective Nanoparticle Uptake Signal

2.3.3 Mass spectrometry

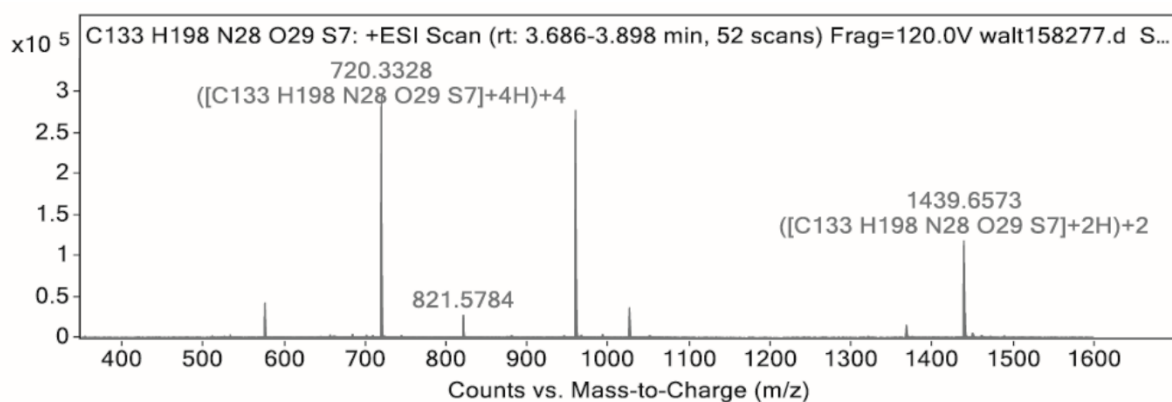


Figure S11. Mass spectrum of $R7_{\text{prot.}}$. HRMS: $(M+2H)^{+2}$ m/z calculated for $C_{133}H_{200}N_{28}O_{29}S_7^{2+}$: 1439.6554, found: 1439.6573.

2.3.4 HPLC

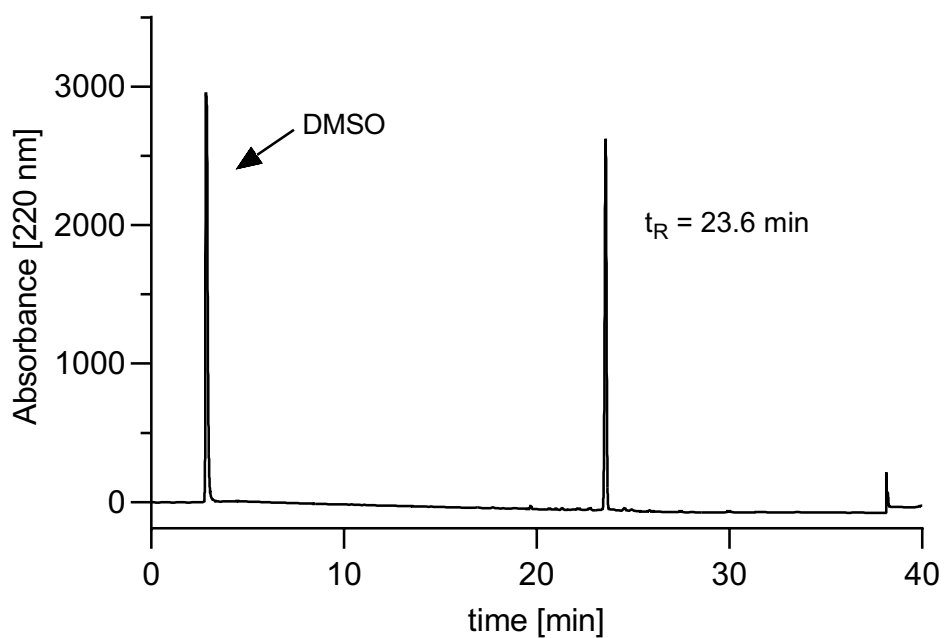
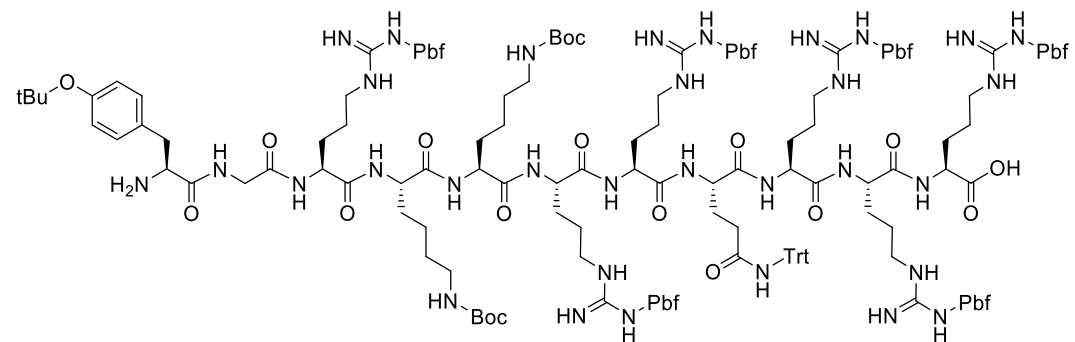


Figure S12. RP-HPLC analysis of $R7_{\text{prot.}}$. Retention time t_R of $R7_{\text{prot.}}$: 23.6 min.

Chapter 5 – Supporting Information

2.4 TAT(47-57)_{prot}.

2.4.1 Structure



Chemical Formula: C₁₇₅H₂₅₂N₃₂O₃₆S₆

Exact Mass: 3569,72

Molecular Weight: 3572,49

Figure S13. Structure of TAT(47-57)_{prot}.

2.4.2 NMR

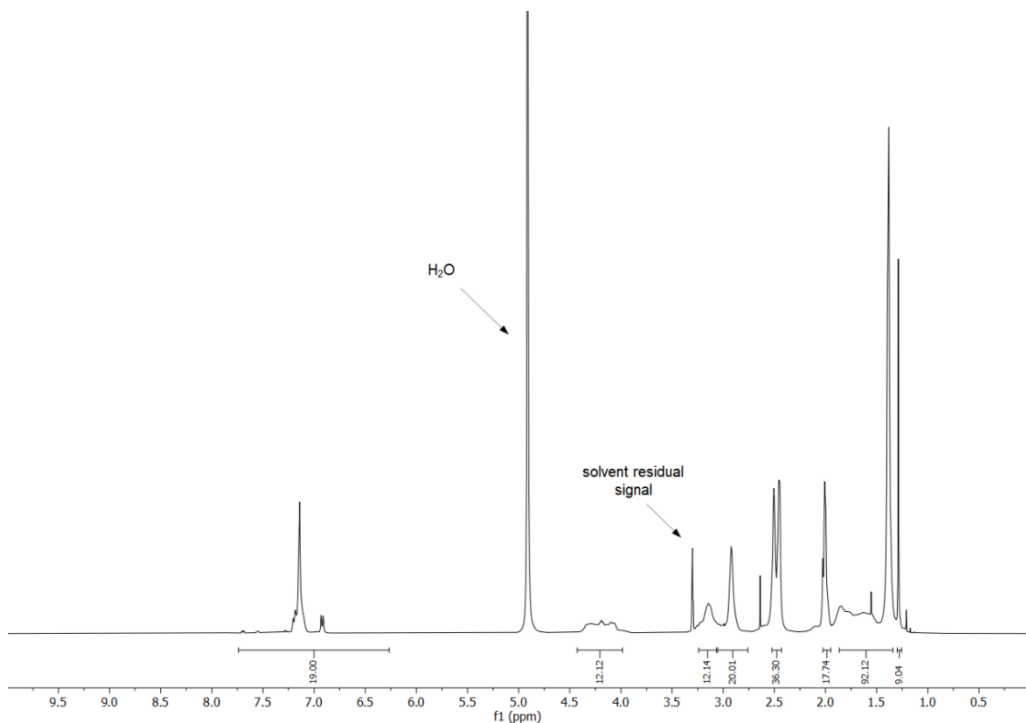


Figure S14. ¹H-NMR spectrum of TAT(47-57)_{prot}. ¹H-NMR (400 MHz, CD₃OD) δ 7.72 – 6.26 (m, 19H), 4.41 – 3.92 (m, 12H), 3.23 – 3.07 (m, 12H), 3.03 – 2.80 (m, 20H), 2.52 – 2.41 (m, 36H), 2.05 – 1.94 (m, 18H), 1.88 – 1.34 (m, 92H), 1.29 (s, 9H).

Supporting Information – CPPs as Selective Nanoparticle Uptake Signal

2.4.3 Mass spectrometry

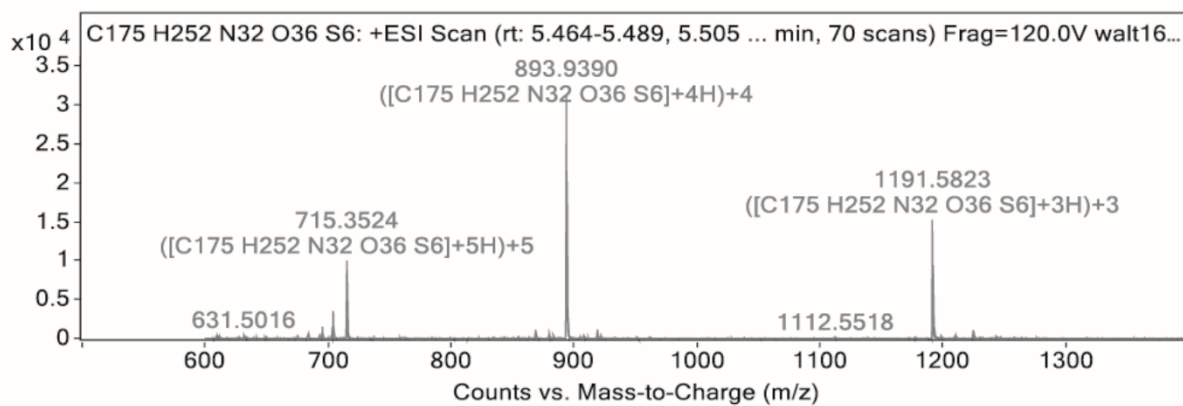


Figure S15. Mass spectrum of $\text{TAT}(47-57)_{\text{prot.}}$. HRMS: $(\text{M}+3\text{H})^{+3}$ m/z calculated for $\text{C}_{175}\text{H}_{255}\text{N}_{32}\text{O}_{36}\text{S}_6^{3+}$: 1181.5823, found: 1191.5821.

2.4.4 HPLC

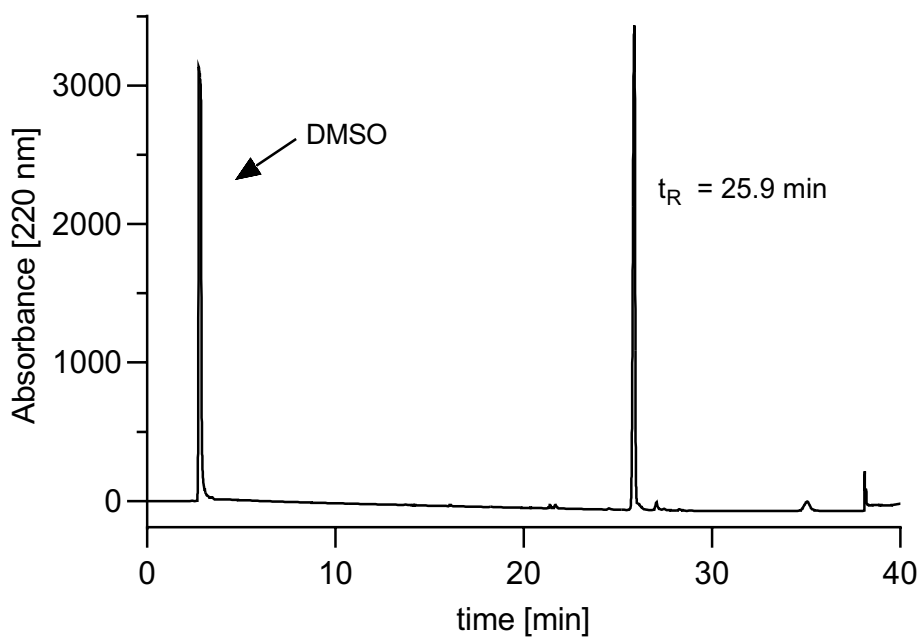


Figure S16. RP-HPLC analysis of $\text{TAT}(47-57)_{\text{prot.}}$. Retention time t_R of $\text{TAT}(47-57)_{\text{prot.}}$: 25.9 min.

Chapter 5 – Supporting Information

2.5 R10_{prot.}

2.5.1 Structure

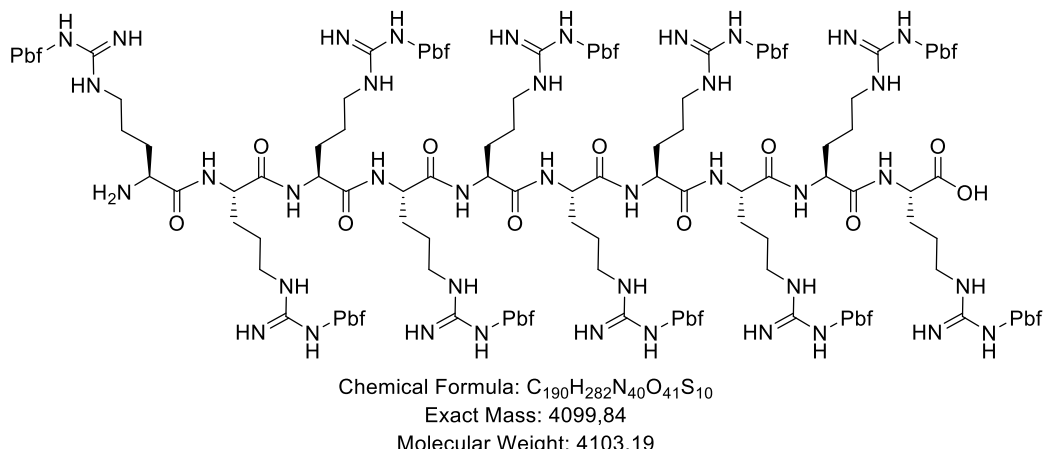


Figure S17. Structure of R10_{prot.}.

2.5.2 *NMR*

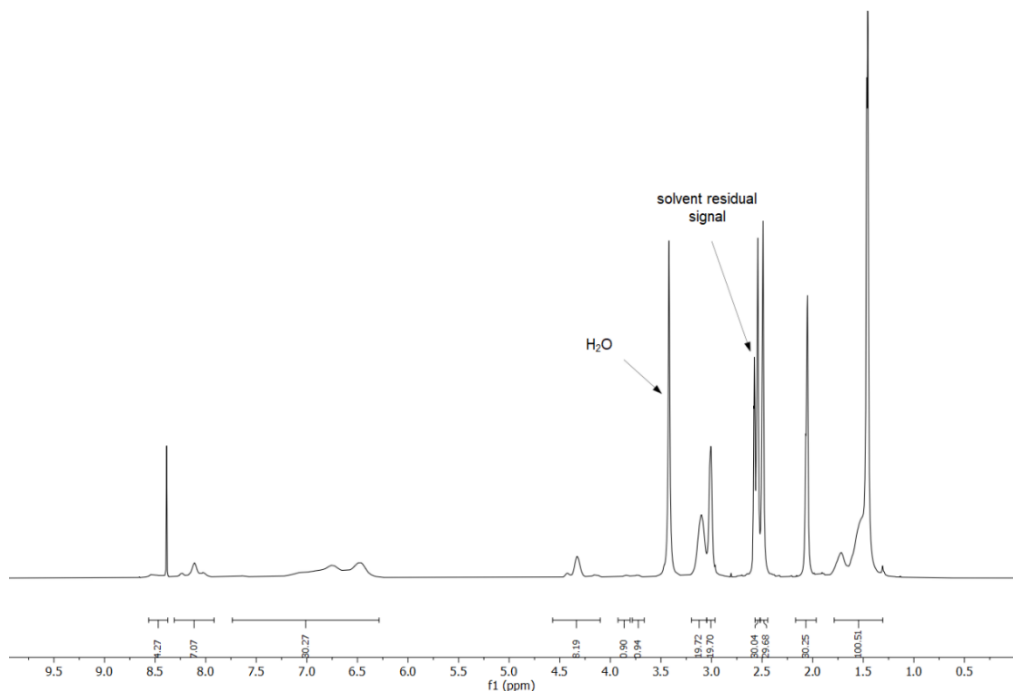


Figure S18. $^1\text{H-NMR}$ spectrum of R10_{prot}. $^1\text{H-NMR}$ (400 MHz, DMSO-d6) δ 8.61 – 8.36 (m, 4H), 8.32 – 7.91 (m, 7H), 7.75 – 6.25 (m, 30H), 4.57 – 4.08 (m, 8H), 3.84 (s, 1H), 3.73 (s, 1H), 3.17 – 3.05 (m, 20H), 3.05 – 2.96 (m, 20H), 2.55 (s, 30H), 2.49 (s, 30H), 2.14 – 1.95 (m, 30H), 1.81 – 1.29 (m, 100H).

Supporting Information – CPPs as Selective Nanoparticle Uptake Signal

2.5.3 Mass spectrometry

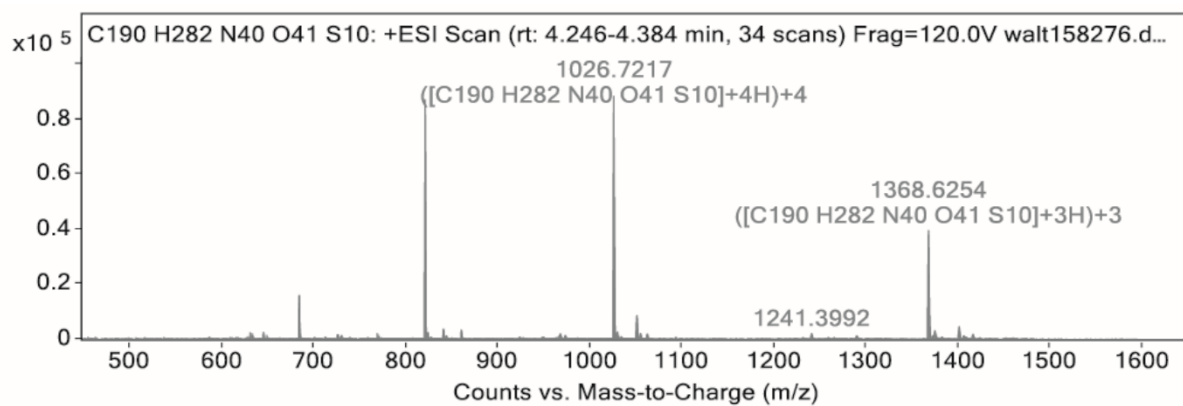


Figure S19. Mass spectrum of R10_{prot}. HRMS: (M+3H)⁺³ *m/z* calculated for C₁₉₀H₂₈₅N₄₀O₄₁S₁₀³⁺: 1368.6237, found: 1369.6257.

2.5.4 HPLC

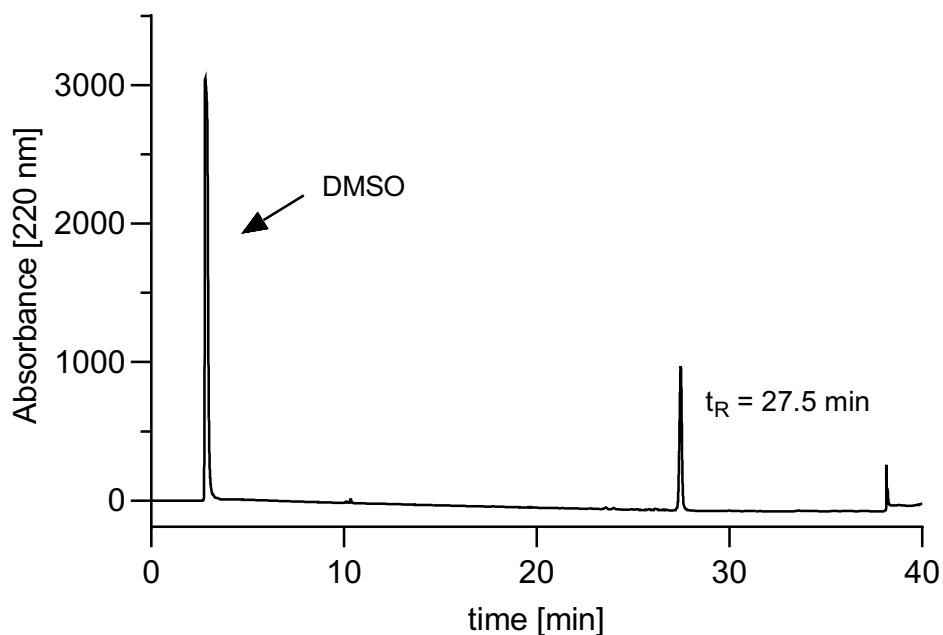


Figure S20. RP-HPLC analysis of R10_{prot}. Retention time t_R of R10_{prot}: 27.5 min.

3 Characterization of PLA-PEG Block Copolymers

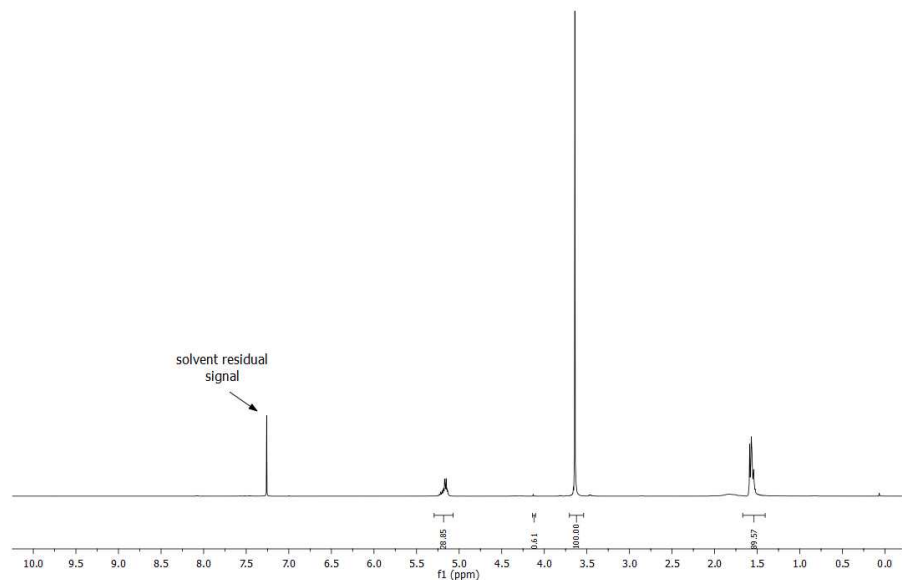


Figure S21. ¹H-NMR spectrum of COOH-PEG_{5k}PLA_{10k}. ¹H-NMR (400 MHz, CDCl₃) δ (ppm) 5.30 – 5.06 (m, 29H) (-CH₃H-); 4.13 (s, 1H) (-OCH₂CH₂-O(CO)-); 3.64 (s, 100H) (-OCH₂CH₂-); 1.60 – 1.37 (m, 90H) (-C(CH₃)H-). PEG (5000 Da) signal normalized to an integral area of 100. Integrating the PLA peaks resulted in a total molecular weight of the polymer of 14989 Da.

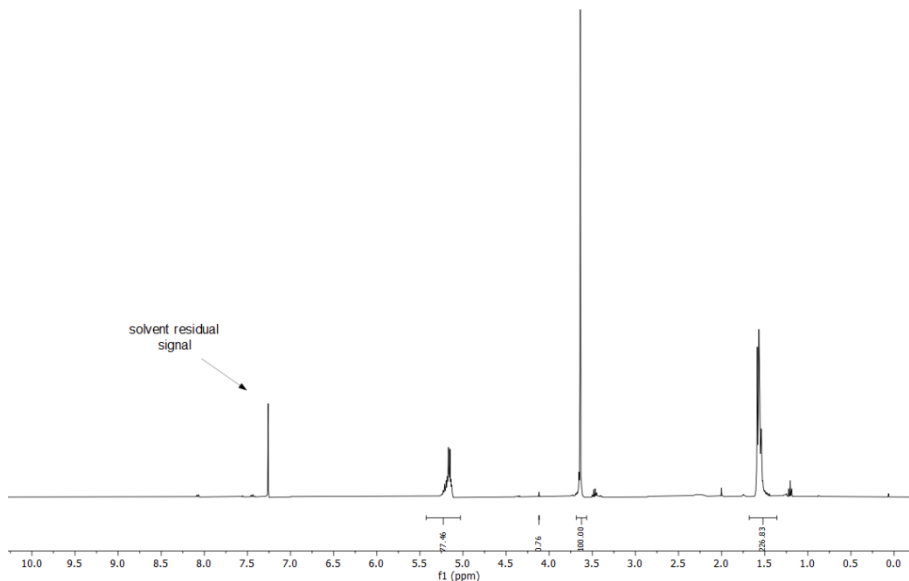


Figure S22. ¹H-NMR spectrum of COOH-PEG_{2k}PLA_{10k}. ¹H-NMR (400 MHz, CDCl₃) δ 5.40 – 5.02 (m, 77H) (-CH₃H-); 4.12 (s, 1H) (-OCH₂CH₂-O(CO)-); 3.64 (s, 100H) (-OCH₂CH₂-); 1.67 – 1.35 (m, 227H) (-C(CH₃)H-). PEG (2000 Da) signal normalized to an integral area of 100. Integrating the PLA peaks resulted in a total molecular weight of the polymer of 11983 Da.

Supporting Information – CPPs as Selective Nanoparticle Uptake Signal

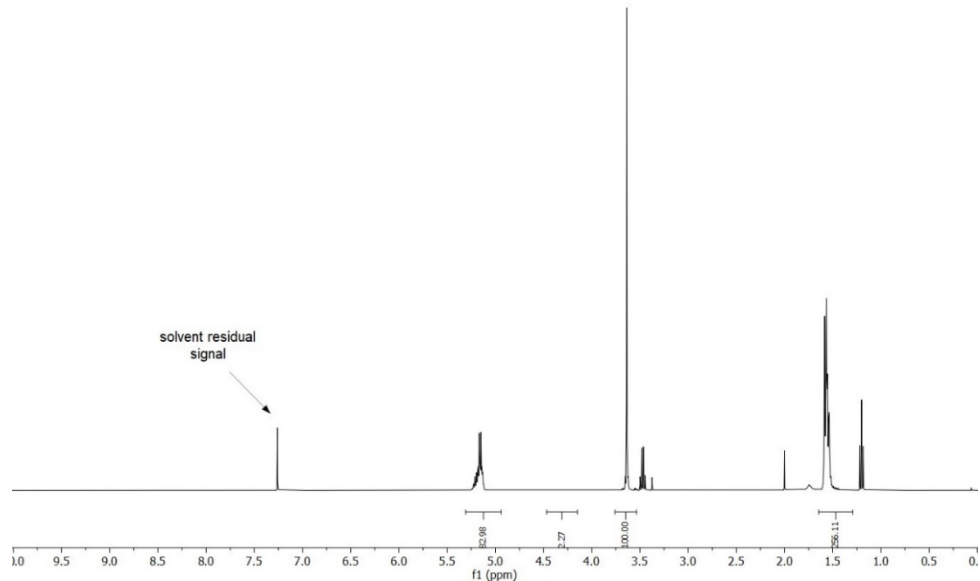


Figure S23. ¹H-NMR spectrum of PLA-PEG_{2k}-MeO. ¹H-NMR (400 MHz, CDCl₃) δ 5.31 – 4.93 (m, 33H) (-(CH₃)H-); 4.40 – 4.21 (m, 2H) (-OCH₂CH₂-O(CO)-); 3.64 (s, 100H) (-OCH₂CH₂-); 1.65 – 1.45 (m, 256H) (-C(CH₃)H-). PEG (2000 Da) signal normalized to an integral area of 100. Integrating the PLA peaks resulted in a total molecular weight of the polymer of 11524 Da.

4 Polymer Modification and Deprotection of Side Chain-protected Amino Acids

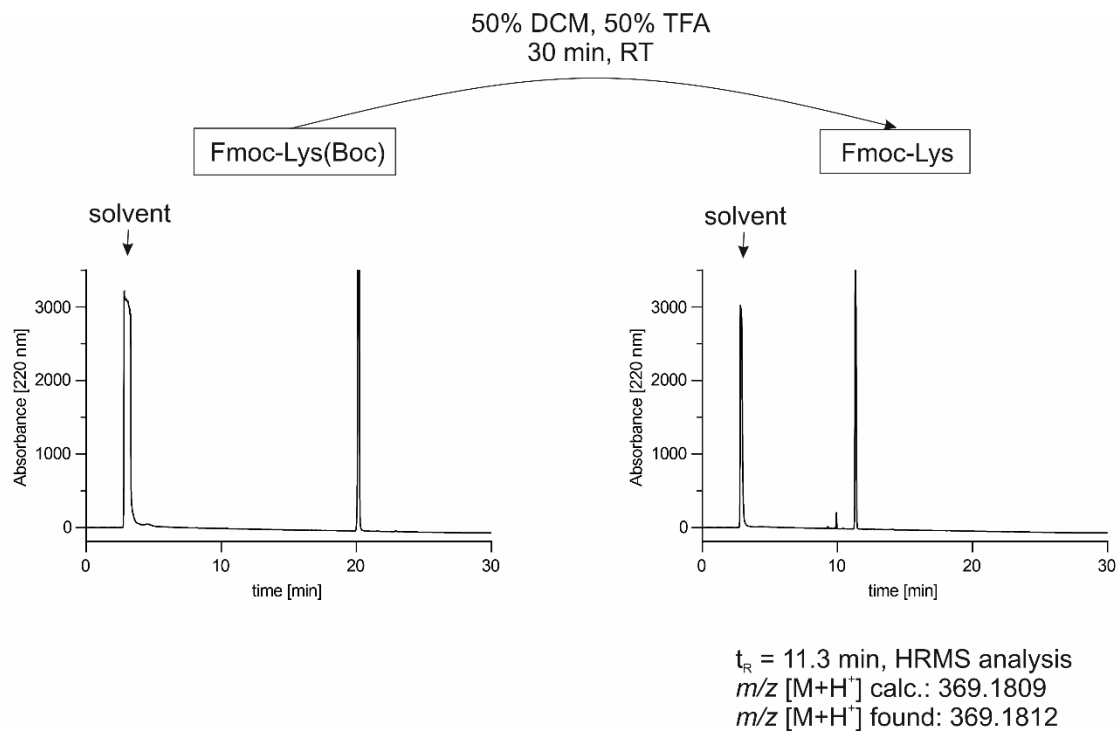


Figure S24. Test deprotection of Boc.

Supporting Information – CPPs as Selective Nanoparticle Uptake Signal

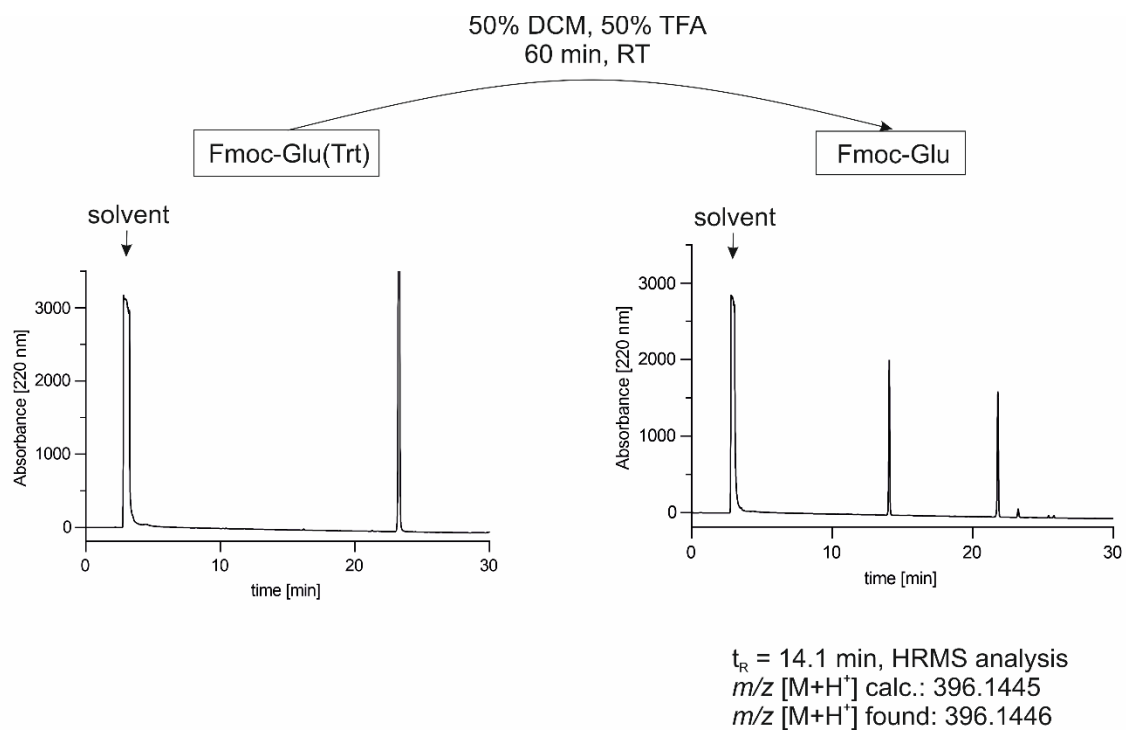


Figure S25. Test deprotection of Trt.

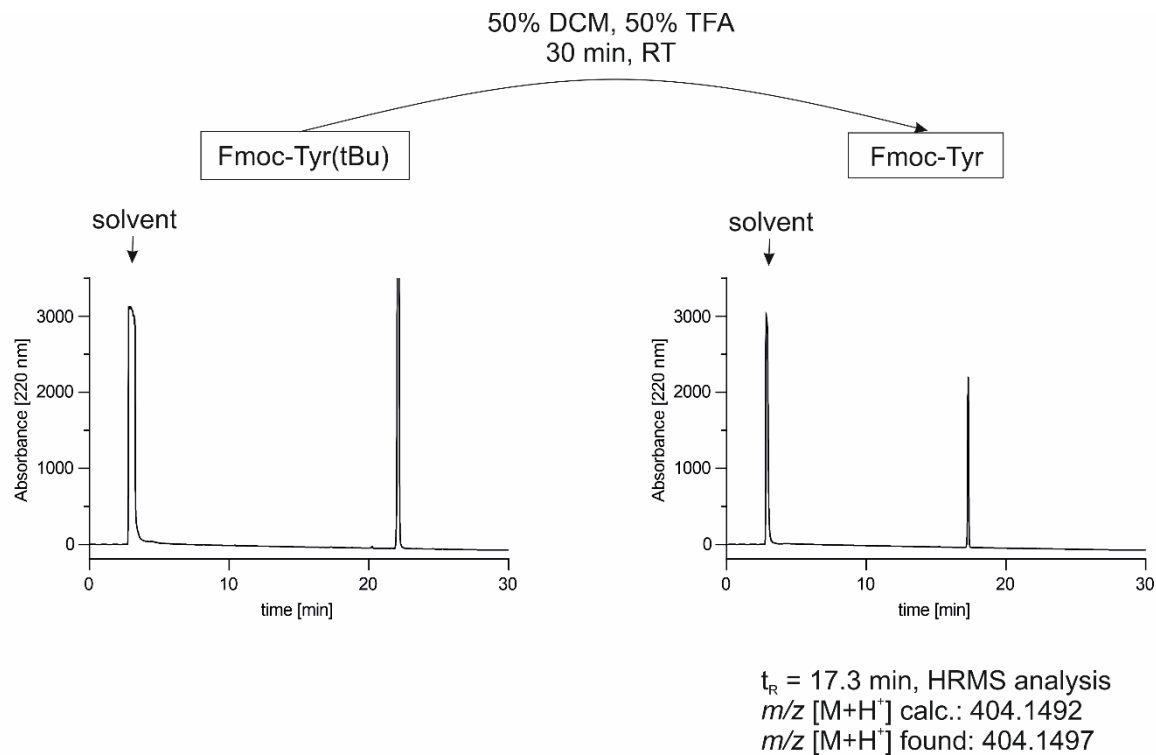


Figure S26. Test deprotection of tBu.

Chapter 5 – Supporting Information

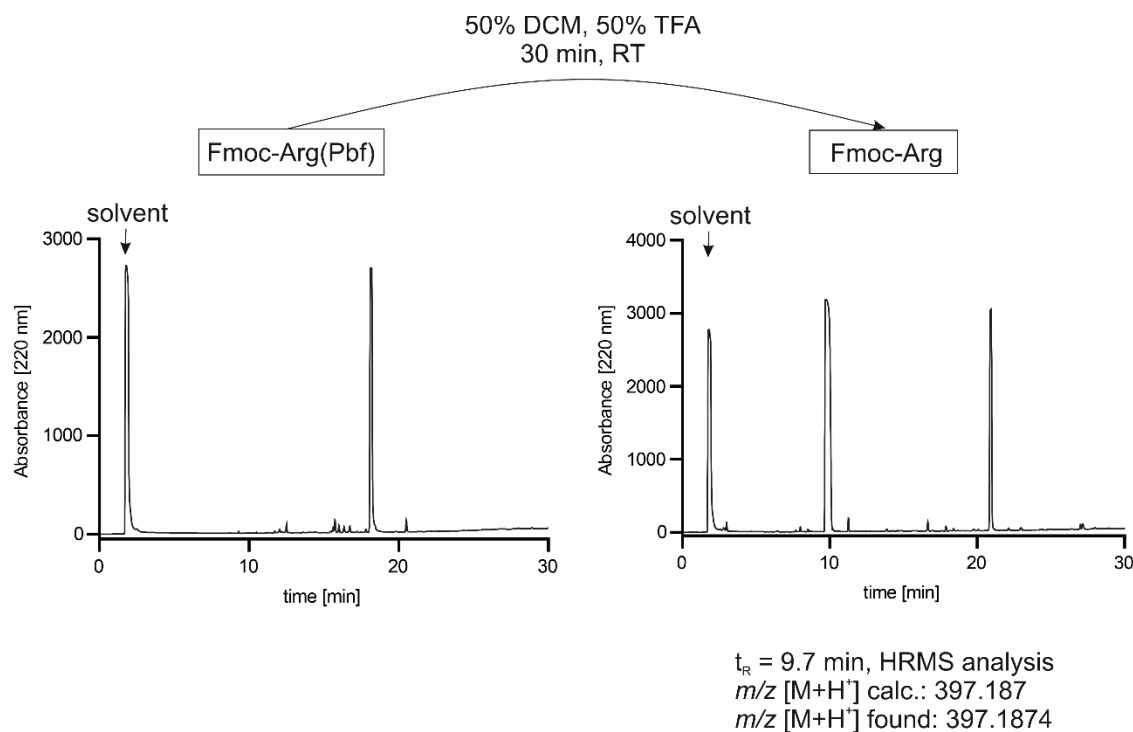
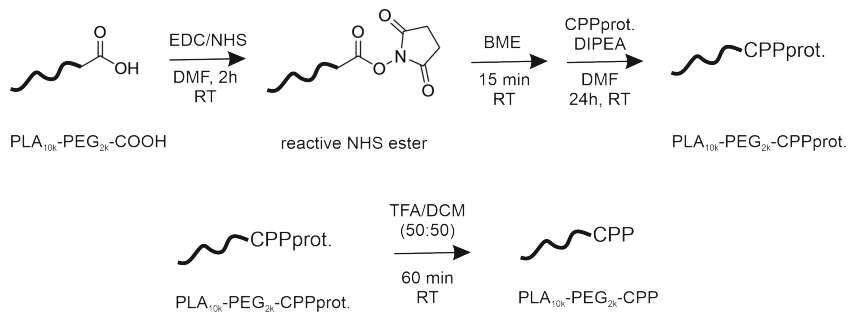


Figure S27. Test deprotection Pbf.



Scheme S2. Modification of the PLA_{10k}-PEG_{2k}-block copolymer used as shell component for particle preparation with different CPPs. Side chain-protected amino acids were used within the CPP synthesis to allow subsequent specific coupling via the N-terminus (PLA_{10k}-PEG_{2k}-CPPprot.). Afterward, the coupled CPP was deprotected in a mixture of DCM and TFA (50/50), resulting in the free CPP attached to the polymer as reaction product (PLA_{10k}-PEG_{2k}-CPP).

5 Characterization of CPP-modified NPs

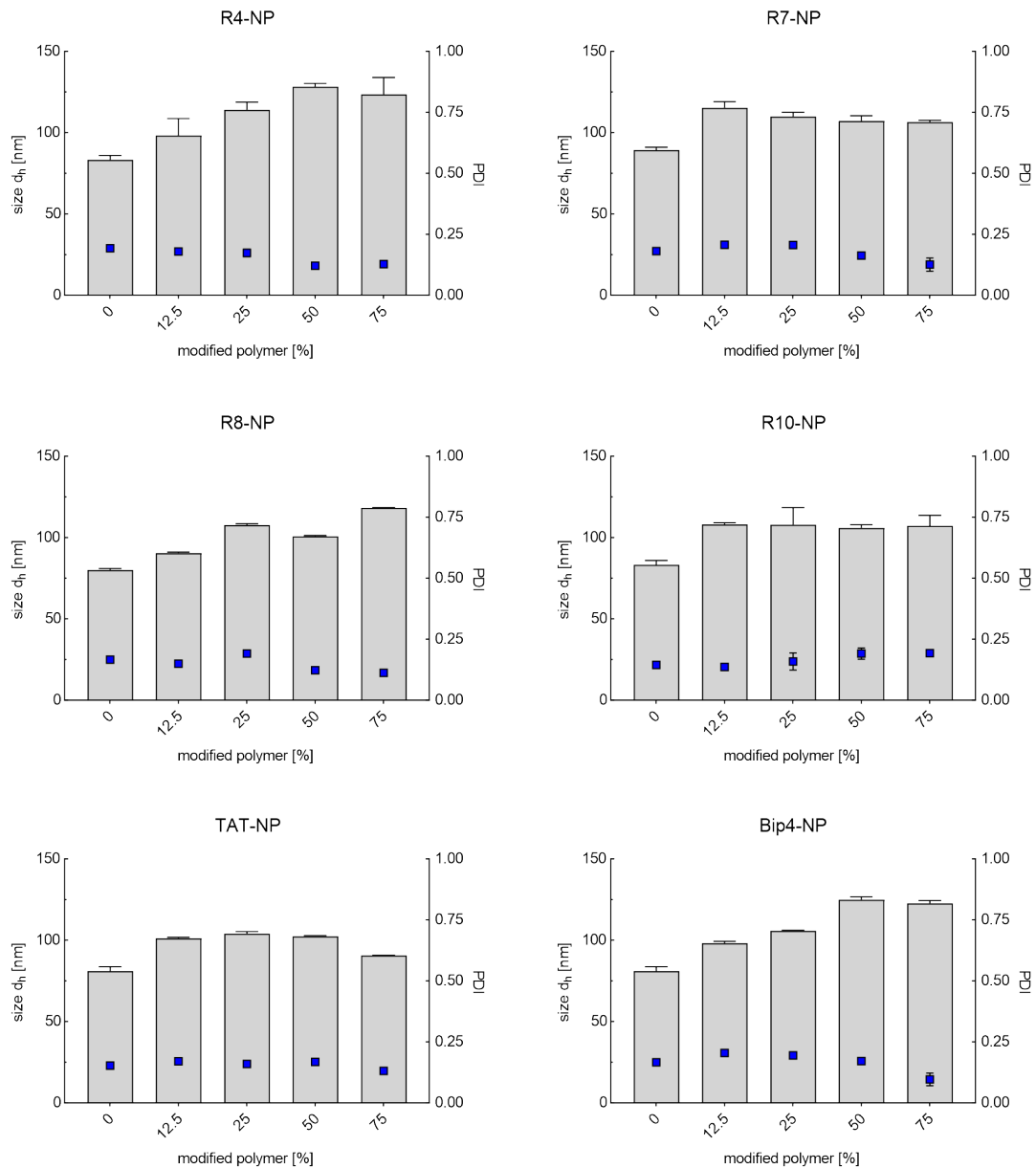


Figure S28. Characterization of size and PDI value of CPP-modified nanoparticles. The nanoparticle size was determined by nanoparticle tracking analysis (NTA) and shown as gray bar; the PDI value was analyzed via dynamic light scattering (DLS) and indicated as blue square. The particles consisted of core-polymer (PLGA) and shell-polymer chains of uniform length (PLA_{10k}-PEG_{2k}). Therefore, the coupled cell-penetrating peptide (CPP) was localized on the nanoparticle surface. Different mass-ratios of CPP-modified polymer and unfunctionalized, uncharged methoxy polymer were evaluated as indicated in the diagrams. By modifying the particles with CPPs, the size increased for all ligands compared to unmodified control nanoparticles (n=3 technical replicates).

6 Uptake Behavior of CPP-modified Nanoparticles

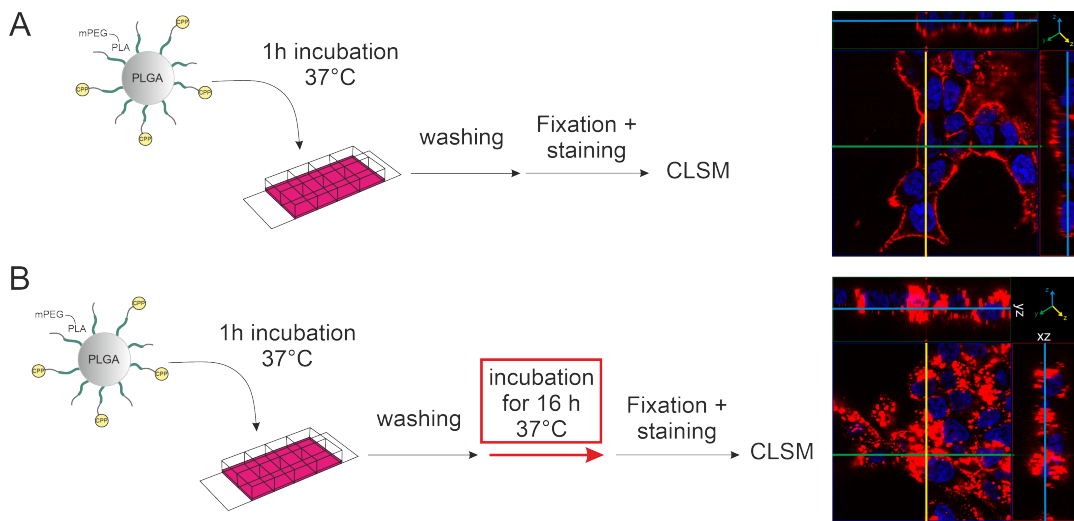


Figure S29. CLSM images of time dependence of R7-modified NP uptake into HEK293 cells. **(A)** Procedure Ibidi-slide preparation and Z-stack of nanoparticle binding/uptake after 1 h of incubation time. **(B)** Procedure Ibidi-slide preparation and Z-stack of nanoparticle binding/uptake after 1 h of incubation and additional 16 h of incubation after nanoparticle expiration and washing. Nanoparticles were covalently core-labeled with Cy5 (red). Cell nuclei were stained with DAPI (blue). After 1 h of incubation, the majority of the nanoparticles were bound to the nanoparticle surface. After an additional incubation period of 16 h, the nanoparticles were taken up into the cells.

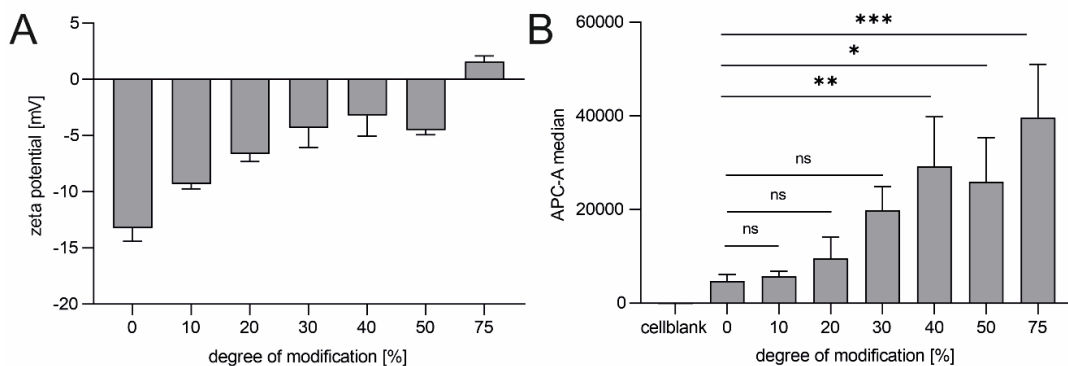


Figure S30. Shielding of R7 by PLA_{10k}-PEG_{5k}-COOH polymer led to the loss of zeta-potential and significant uptake improvement-correlation in HEK293 cells. The cells were incubated with Cy5-labeled nanoparticles for 1 h at 37 °C and afterward analyzed via flow cytometry. **(A)** Zeta potential measurements of the particles. **(B)** Flow cytometric evaluation. Results represent mean \pm SD (n = 3, levels of statistical significance are indicated as *p \leq 0.05, **p \leq 0.01, ***p \leq 0.001, ****p \leq 0.0001).

7 Cytotoxicity of Modified Nanoparticles

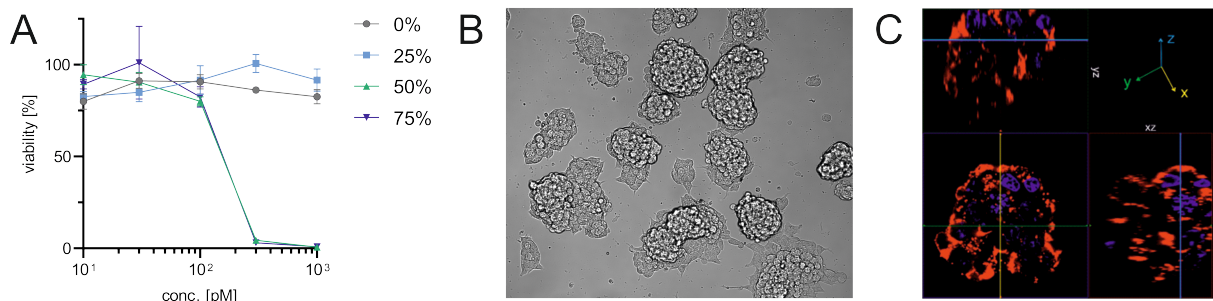


Figure S31. Evaluation of the cytotoxicity of R10-modified nanoparticles. (A) MTT assay performed with L929-cells. The different DOMs investigated are indicated in the figure legend. (B) TL-image showing the aggregation of HEK293 cells after treatment with R10-modified NPs DOM 50 % in a concentration of 100 pM after 1 h of incubation with particles and further 15 h of incubation after particle removement. (C) CLSM image: z-stack orthogonal view showing the aggregation of HEK293 cells.

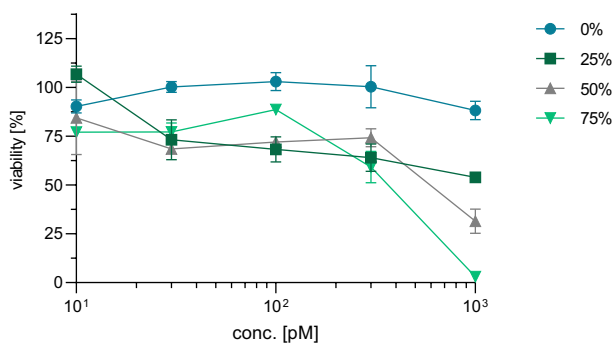


Figure S32. Effect of CPP shielding on R10-NP-cytotoxicity. The CPPs were sterically shielded by the usage of 25 % longer polymers (PLA_{10k}-PEG_{5k}-COOH) and the cytotoxicity was evaluated via an MTT assay performed with L929-cells. The different DOMs investigated are indicated in the figure legend. Compared to particles with unshielded R10 a shift of cytotoxicity to higher nanoparticle concentrations could be detected.

Chapter 5 – Supporting Information

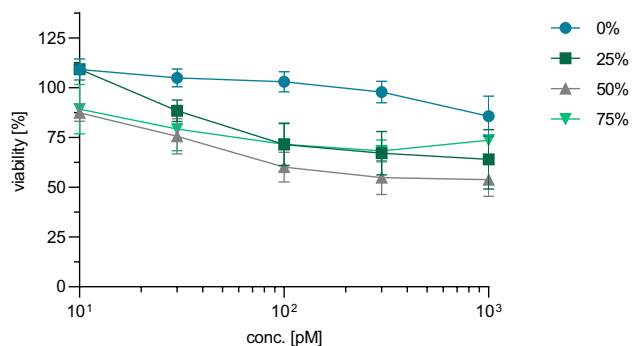


Figure S33. Evaluation of the cytotoxicity of NPs surface-modified with TAT(47-57). The MTT assay was performed with L929 cells. The different DOMs investigated are indicated in the figure legend.

The cytotoxicity of MLN-TAT NPs and control NPs was additionally investigated with HEK293T-ACE2 cells under the conditions of the flow cytometry experiments. Since HEK293 cells show only weak adherence, the utilized 96-well plates were initially coated using Collagen A (Biochrom GmbH, Berlin, Germany). Therefore, 1.25 mL collagen A 1 mg/mL was mixed with 11.25 mL PBS pH 2.4 (pH adjusted with 37 % hydrochloric acid), and 250 μ L/well was added. The solution was incubated for 1 h at 37 °C. Afterward, the collagen was removed carefully. The wells were washed using 250 μ L DMEM + 10 % FBS. Directly after the coating step, 75,000 cells/well were seeded into the coated plate and incubated for 24 h at 37 °C. Unlabeled MLN-TAT NPs and control NPs were prepared according to chapter 2.4 and the particle concentration was adjusted to 100 pM with Leibovitz medium. The cell medium was aspirated and the particles were added and incubated for 1 hour. Subsequently, the particle solution was aspirated and the cells were incubated with 200 μ L MTT working reagent, prepared as described in chapter 2.6, for 3 h at 37 °C. All the following steps were performed according to chapter 2.6. A cell viability of 99.86 ± 5.48 % was demonstrated after treatment with MLN-TAT-NPs and 92.97 ± 6.51 % after treatment with control-NPs.

Supporting Information – CPPs as Selective Nanoparticle Uptake Signal

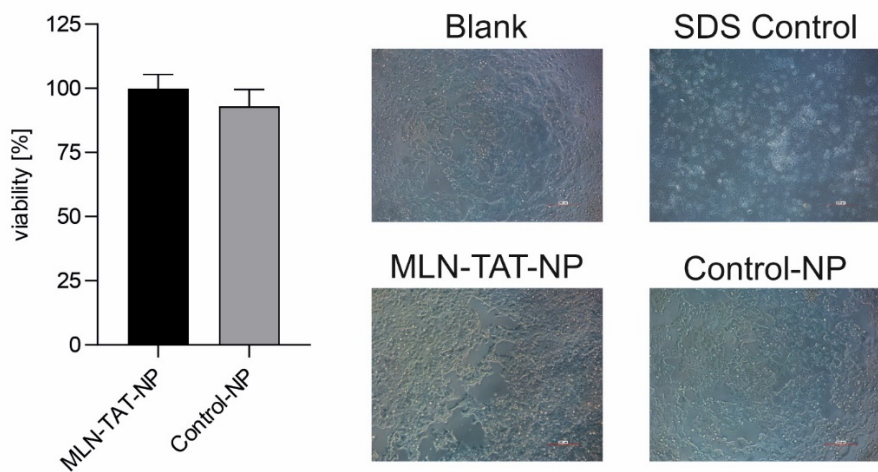


Figure S34. Evaluation of the cell viability of HEK293T-ACE2 cells under flow cytometry experimental conditions (n=6).

Chapter 5 – Supporting Information

Chapter 6

Nanoparticles Mimicking the Viral Infection Pathway for Targeting SARS-CoV-2 Host Cells

Chapter 6

Abstract

The COVID-19 virus, which first emerged in 2019, has caused more than 700 million infections and at least 7 million deaths worldwide. Although the pandemic has been contained with the development of vaccines, new outbreaks continue to occur. Furthermore, due to ongoing mutations and the post-COVID syndrome, a potential following disease, COVID-19 still has a major impact today. In recent years, numerous therapeutic approaches have been developed that target different stages of the viral replication cycle. However, a resounding success in containing the spread of SARS-CoV-2 could not be achieved. One possibility to increase the therapeutic efficacy of the developed drugs could be the direct transfer to the viral host target cells. Therefore, polymeric nanoparticles are supposed to imitate the internalization pathway of SARS-CoV-2 to mimic the infection and track the virus through the organism. In the first step, the virus attaches to the angiotensin-converting enzyme 2 (ACE2) via its spike protein. Subsequently, there are two possibilities for viral entry: an endosomal, transmembrane protease serine subtype 2 (TMPRSS2)-independent, pathway, and a TMPRSS2-dependent pathway via membrane fusion. This chapter discusses the translation of these two mechanisms into targeting strategies and provides an outlook on the next steps toward the establishment of antiviral nanoparticle therapy.

Chapter 6

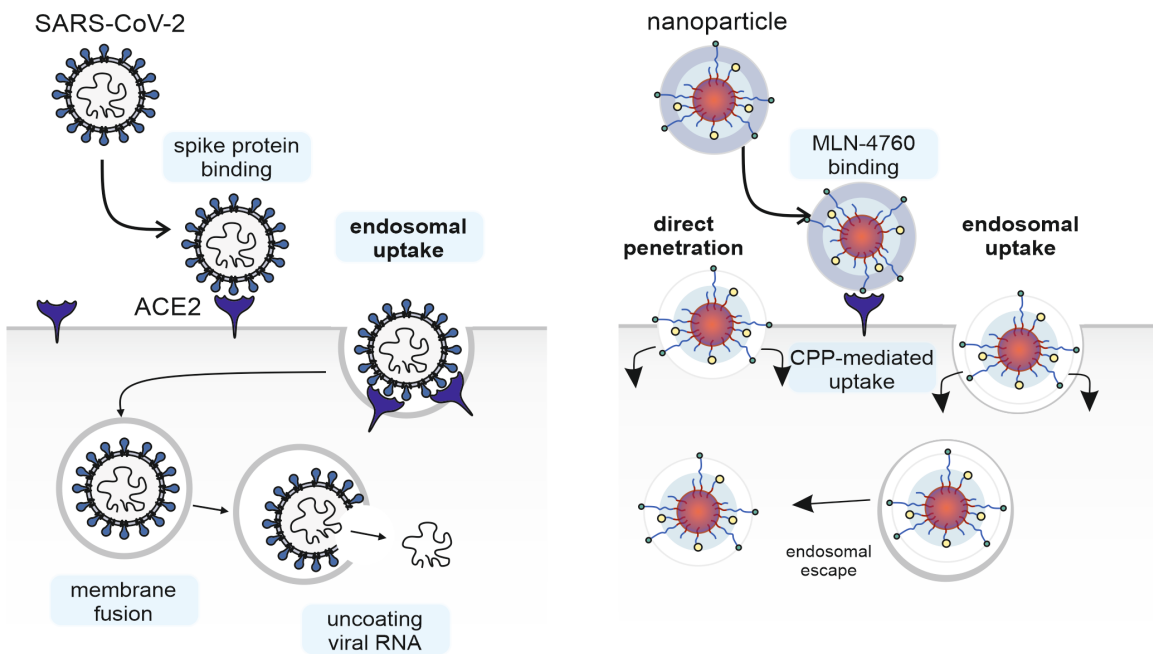
1 Introduction

The first reports of a rapidly increasing number of a severe acute respiratory syndrome (SARS) in Wuhan, China emerged in December 2019. The genomic sequence of the virus SARS-CoV-2 was rapidly identified and published in January 2020 [1], followed by the designation of the triggered disease as coronavirus disease 2019 (COVID-19) [2]. Nevertheless, it was not possible to prevent viral spread, which led to the declaration of a global pandemic by the World Health Organization (WHO) in March 2020, with more than 700 million cases and at least 7 million deaths worldwide to date [3]. Even though the end of the pandemic was declared in 2023, the disease regularly relapses, and even after recovery, there may be lasting symptoms, known as post-COVID syndrome, which can affect anyone exposed to SARS-CoV-2, regardless of age, severity, or original symptoms [4]. Although the development of vaccines made major contributions to the end of the pandemic, the analysis of breakthrough SARS-CoV-2 infections (BTI) in vaccinated people has shown that vaccination before infection confers only particle protection of the post-acute phase of the disease and may not sufficiently protect long-term consequences of an infection [5]. In addition, ongoing virus mutations lead to concerns about SARS-CoV-2 variants that could worsen the severity of the disease or reduce the efficacy of vaccination [6,7]. These findings emphasize the need for novel therapies for fast and consequent interruption of viral spread and virus elimination. Therefore, in recent years, many studies have been performed, focussing on the development of antiviral therapies to combat the spread of SARS-CoV-2. The majority of the described potential drug candidates are intended to intervene in intracellular processes of the SARS-CoV-2 host target cells [8–10]. Thus, a drug delivery system, enabling the selective transfer of active substances into the concerned cells, could considerably improve therapy efficacy by increasing the drug amount at the site of action and minimizing unintended adverse drug effects.

Therefore, the aim of this study was the development of a nanoparticle targeting strategy that mimics the uptake mechanisms of SARS-CoV-2. In this way, the nanoparticles are supposed to track the viral infection inside the organism and accumulate at the site of viral replication. The encapsulation of an antiviral substance into the particle system thus enables active substances to precisely attack the virus and efficiently prevent viral spread.

Chapter 6

TMPRSS2-independent uptake pathway



TMPRSS2-dependent uptake pathway

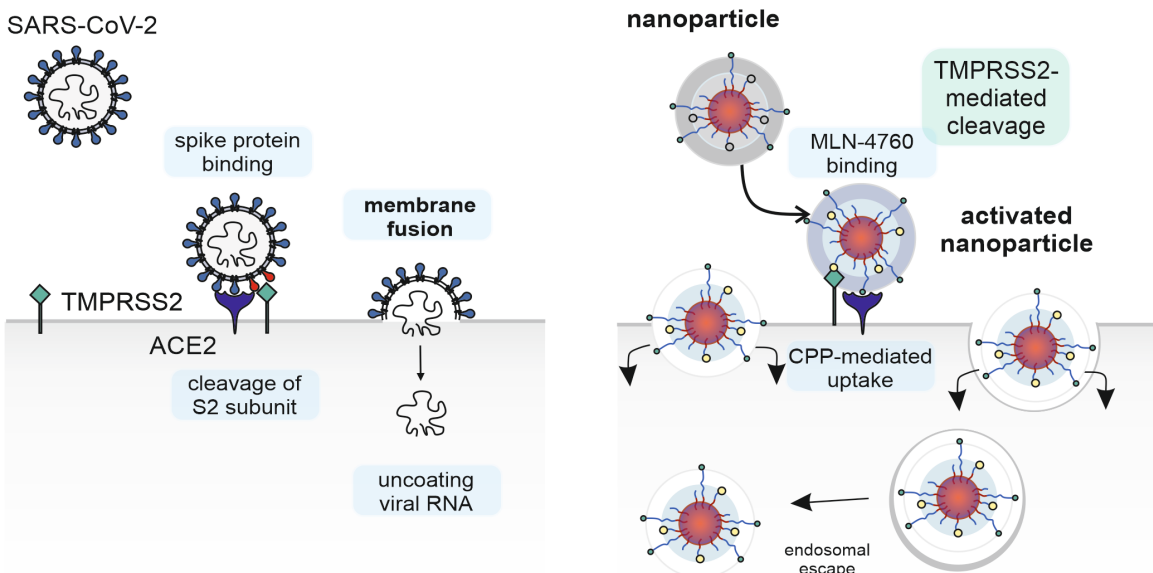


Figure 1. Uptake of SARS-CoV-2 into host target cells and strategies for viral mimicry. Virus binding to ACE2 induces conformational changes in the S1 subunit of the viral spike protein and exposes the S2'-cleavage site of the S2 subunit. If the target cell does not express TMPRSS2 or the ACE2-virus-complex does not encounter the transmembrane protease on the cell surface, the virus internalizes via the endosomal pathway. Due to the cleavage of the S2'-site by cathepsin in the acidic environment of

late endosomes or lysosomes, the fusion peptide (FP) is exposed. The dissociation of S1 from S2 results in dramatic conformational changes, initiating membrane fusion. The viral RNA is thus released into the host cell cytoplasm via a fusion pore. If the host target cell expresses TMPRSS2, S2'-cleavage already occurs at the cell surface, initiating viral fusion with the cell membrane. For the mimicry of the TMPRSS2-independent pathway, the selective ACE2 inhibitor MLN-4760 is tethered to the NP surface and promotes binding and thus NP fixation via ACE2. Due to the newly achieved spatial proximity of the NP to the cell surface, a previously sterically shielded cell-penetrating peptide is revealed and initiates particle uptake. For TMPRSS2-dependent uptake, the CPP is not simply covered by steric hindrance, but by a shielding element, which is conjugated to the CPP via a TMPRSS2 cleavage sequence (inactivated nanoparticle). Therefore, the uptake signal is only exposed by enzymatic activity (activated nanoparticle), resulting in particle internalization.

Simplified, SARS-CoV-2 uptake consists of two essential factors. The primary step is the binding to angiotensin-converting enzyme 2 (ACE2) on the membrane surface via the S1 domain of its spike protein [11,12]. For the second step, there are two different possibilities: the endosomal entry via clathrin-coated pits (CCPs) [13] and lipid rafts [14], or the cell surface entry, which is promoted by the cleavage of the spike protein at its S2' site by transmembrane protease serine subfamily (TMPRSS) proteases, mainly the TMPRSS subtype 2 (TMPRSS2) that enables membrane fusion [15–17] (Fig. 1).

A strategy for the mimicry of the TMPRSS2-independent nanoparticle uptake is demonstrated in **Chapter 5**, using the conditional uptake of cell-penetrating peptides after an initial attachment to ACE2 via the selective and potent inhibitor MLN-4760 [18]. However, since the endosomal uptake relies on a slow acid-activated late endosomal pathway for infection, the fast pH-independent TMPRSS2-dependent cell surface entry is preferred to infect cells [19].

For this reason, this chapter provides initial contributions to the extension of the already established SARS-CoV-2 mimetic targeting concept for an additional, TMPRSS2-mediated nanoparticle activation step. The aim is to increase the selectivity for ACE2/TMPRSS2 dual-positive cells, thereby targeting the most severely affected cells in particular.

Chapter 6

2 Materials and Methods

2.1 Materials

If not otherwise declared, all chemicals and reagents were obtained from Sigma-Aldrich (Taufkirchen, Germany) in analytical grade. The millipore water used was generated by a Milli-Q water purification system (Millipore, Schwalbach, Germany). Dulbecco's phosphate-buffered saline was obtained from Sigma-Aldrich (Taufkirchen, Germany). HEK293 cells were obtained from the German Collection of Microorganisms and Cell Cultures GmbH, DSMZ (Göttingen, Germany) and HEK293T cells which are stably expressing ACE2 were kindly provided by Prof. Dr. Ralf Wagner (Institute of Clinical Microbiology and Hygiene, University Hospital Regensburg, Germany). Fetal bovine serum (FBS) was obtained from Biowest (Nuaillé, France). The lentiviral preps used for transduction were purchased from Addgene (Addgene viral prep # 154985-LV; # 154982-LV). Blasticidin was purchased from Invivogen (Toulouse, France). Puromycin was sourced from Enzo Life Sciences (Farmingdale, NY, USA). For flow cytometry analysis, the flow cytometry staining buffer, the labeled antibodies anti-human ACE2 (hACE2)-AlexaFluor®647-conjugated Mouse IgG, and Mouse IgG2A control AlexaFluor®647-conjugated were purchased from R&D Systems (Minneapolis, MA, USA). The ACE2 activity assay kit (fluorometric) was obtained from Abcam (Cambridge, UK). The fluorescence was measured at a Synergy Neo2 Multi-Mode Microplate Reader (Biotek Instrument Inc., Winooski, VT, USA). PeqGOLD TriFastreagent was purchased from VWR International (Radnor, PA, USA), the qScript cDNA Synthesis Kit was sourced from Quantabio (Beverly, MA, USA), and Takyon ROX SYBR 2x MasterMix dTTP blue from Eurogentec (Seraing, Belgium). The fluorogenic substrate Boc-QAR-AMC of TMPRSS2 was obtained from R&D Systems, Inc. (Minneapolis, MA, USA). Camostate mesylate was sourced from MedchemExpress (Monmouth Junction, NJ, USA). *N,N*'-Diisopropylcarbodiimide (DIC) was purchased from TCI (Eschborn, Germany). 1-[Bis(dimethylamino)methylene]-1*H*-1,2,3-triazolo[4,5-*b*]pyridinium 3-oxide hexafluorophosphate (HATU) and *N,N*-diisopropylethylamine (DIPEA) were obtained from ABCR (Karlsruhe, Germany). The protected amino acids Fmoc-L-Lys(Boc)-OH, Fmoc-L-Ala-(OH), Fmoc-L-Arg(Pbf)-OH, Fmoc-L-Ser(tBu)-OH, Fmoc-L-Phe-OH, and Boc-L-Lys(Fmoc)-OH were purchased from Carbolution Chemicals (St. Ingbert, Germany). Frits with a pore size of 35 µm were sourced from Roland Vetter Laborbedarf (Ammerbuch, Germany). The infrared lamp was obtained from Medisana

(Neuss, Germany) and the thermostat was sourced from PEARL GmbH (Buggingen, Germany). Syringes were purchased from Braun (Melsungen, Germany). High-resolution mass spectrometry (HRMS) was performed using a Q-TOF 6450 ultrahigh definition (UHD) LC/MS system from Agilent Technologies (Santa Clara, CA, USA), using an electrospray ionization (ESI) source. NMR spectra were recorded on a Bruker Advance-400 NMR spectrometer (Bruker, Billerica, MA, USA).

2.2 Evaluation of Antibiotic Resistance

To enable the antibiotic selection of transduced and untransduced cells, the antibiotic resistance of HEK293 cells for blasticidin and puromycin were evaluated. Therefore, 3000 cells/well were seeded into a 96-well plate and incubated for 24 h at 37 °C in Dulbecco's modified eagle medium (DMEM), supplemented with 10 % fetal bovine serum (FBS). A concentration series of blasticidin or puromycin in cell culture medium was prepared. After aspiration of the cell culture medium, the dilutions were added, and the cells were incubated until the blank, which were cells without the addition of antibiotics, had grown confluent. MTT working reagent was prepared by diluting 3-(4,5-dimethylthiazol-2-yl)-2,5-diphenyltetrazolium bromide in DMEM supplemented with 10 % FBS in a concentration of 1 mg/mL. The antibiotic dilutions were aspirated and 100 µL working reagent per well was added. After 3 h the supernatant was aspirated and 100 µL isopropanol was added to solve the formed violet crystals. The plate was shaken protected from light until all crystals were dissolved for at least 30 min. The absorption was measured at 570 and 690 nm with a Synergy Neo2 Multi-Mode Microplate Reader (Biotek Instrument Inc., Winooski, VT, USA). The difference in absorbance was analyzed and the results were normalized to untreated cells.

2.3 Cell Culture

HEK293 cells were cultivated in DMEM, supplemented with 10 % FBS. For the cultivation of HEK293-TMPRSS2 10 µg/mL blasticidin were added to the medium. For the cultivation of HEK293-TMPRSS2-ACE2 dual-transfected cells puromycin was supplemented additionally in a concentration of 0.5 µg/mL. Calu-3 cells were cultivated in DMEM/F12/GlutaMax medium supplemented with 10 % FBS, 1 % HEPES, and 1 % L-glutamin.

Chapter 6

2.4 Lentiviral Transduction

For lentiviral transduction, 300,000 HEK293 cells/well were seeded in a 6-well plate and incubated for 24 h at 37 °C. The cell transduction medium, DMEM supplemented with 10 % FBS and 10 µg/mL polybrene, was prepared immediately before the transduction. The lentiviral prep aliquot was thawed at room temperature and a range of dilutions of the lentivirus (1:5, 1:10, 1:50, 1:100, 1:500 of the titer stock solution 1 mL $\geq 1 \times 10^6$ transduction units (TU)/mL) in the transduction medium were prepared. The medium in each well was aspirated and 500 µL of the corresponding single viral dilution was added. The cells were incubated with the virus for 24 h. Afterward, the medium was aspirated gently, and the cells were incubated for 24 h with DMEM + 10 % FBS. 48 h after transduction the medium was aspirated and replaced by the antibiotic-containing medium to perform the antibiotic selection. The selection concentrations of blasticidin and puromycin were evaluated in a preliminary MTT experiment and set at 10 µg/mL for blasticidin and 0.5 µg/mL for puromycin, as untreated HEK293 cells reliably died at this concentration. (Supporting Information, Chapter 1.1) The cells were observed under daily medium changes until all cells in an untransduced control well died.

2.5 TMPRSS2 Activity Screening

Preliminary experiments with soluble TMPRSS2 were carried out to determine the assay conditions. The results of these preliminary tests can be found in the supporting information (Chapter 1.2). The test procedure and the composition of the utilized assay buffer were based on Fraser et al. (2022) [20]. TMPRSS2 was solved in a mixture of millipore water and glycerol (1:1) to a concentration of 10 µM. The stock solution was diluted with PBS to a concentration of 50 nM. The fluorogenic assay was performed in a black 96-well plate. 98.5 µL assay buffer (25 mM Tris pH 8.0, 75 mM NaCl, 2 mM CaCl₂) or PBS, respectively, were mixed with 0.5 µL of the TMPRSS2 solution. Immediately before the measurement, 1 µL of a 100 µM solution of the fluorogenic substrate Boc-GlnAlaArg-AMC (Boc-QAR-AMC) was added. For this purpose, the fluorogenic substrate was dissolved in dimethylsulfoxide (DMSO) to a concentration of 10 mM and afterward diluted with PBS. The plate was shaken gently, and the fluorescence was measured for 90 min at 37 °C (excitation/emission: 341/441 nm). Due to occurring cell lysis in the assay buffer, all cell-based experiments had to be performed in PBS.

After the transduced cells, prepared with different viral dilutions, had grown confluent, they were transferred to a T75 culture flask. Once all the cells had reached a density of at least 70 %, they were subjected to an initial screening activity assay. Therefore, 100,000 cells/well from each transduced cell line and wild-type HEK293 control cells were seeded in a black 96-well plate and incubated for 24 h (n=10). A 10 mM stock solution of the fluorogenic substrate Boc-QAR-AMC was prepared in DMSO and subsequently diluted to a final concentration of 200 μ M in PBS. The medium was aspirated and 100 μ L PBS was added to each well. Directly before measurement 50 μ L of the fluorogenic substrate solution was added and the fluorescence was measured kinetically every 2 min (excitation/emission: 341/441 nm). The experimental data of the initial screening are shown in chapter 1.3 of the supporting information. The cell line which showed the highest activity in the preliminary screening was retested with and without enzyme inhibition of TMPRSS2 to ensure specific substrate cleavage. Therefore 90,000 cells/well were seeded in a black 96-well plate and incubated for 24 h. Camostat mesylate was dissolved in DMSO to a concentration of 200 mM and diluted with PBS to a concentration of 1 mM. The cell medium was aspirated and 50 μ L of the camostat solution or PBS without inhibitor, respectively, was added and the cells were incubated for 15 min at RT. Immediately before measurement, 50 μ L of the 200 μ M fluorogenic substrate solution was added and the fluorescence was detected for 90 min.

2.6 qPCR Analysis of TMPRSS2 Expression

For quantitative polymerase chain reaction (qPCR) analysis, 400,000 HEK293 cells/well, 400,000 HEK293-TMPRSS2 cells/well, and 300,000 Calu-3 cells/well, acting as a positive control [21], were seeded in a 12-well plate and incubated for 24 h at 37 °C. Afterward, the cells were washed twice with PBS and stored on ice. The cells were lysed with peqGOLD TriFast reagent by adding 500 μ L to each well, incubating for 5 min, and transferring the cell lysate into Eppendorf cups. 100 μ L chloroform were added and the Eppendorf cups were stored on ice for 10 min. The solutions were centrifuged at 12,000 g at 4 °C for 20 min. The aqueous phase was transferred to a new Eppendorf cup and diluted with cooled isopropanol in a ratio of 1:1. The solution was stored in the freezer at -20 °C overnight to precipitate the isolated RNA. The next day, the supernatant was removed, and the pellet was washed twice with 1 mL of 75 % ethanol per analysis (p.a.) by adding the solvent, incubating the pellet on ice for 20 min, centrifugation at 12,000 g at 4 °C for 5 min, and removing the supernatant. The isolated RNA

Chapter 6

was stored on ice for one hour. Subsequently, the concentration was measured via nanodrop analysis. 500 ng of the isolated RNA were transcribed to the corresponding cDNA using a qScript cDNA Synthesis Kit. Negative controls without reverse transcriptase were performed to detect impurities of genomic DNA. The Real-Time (RT)-PCR was implemented on a CFX Connect Real-Time PCR Detection System (Biorad, Hercules, CA, USA) with 50 cycles of 10 s melting at 95 °C, a following step of annealing at 60 °C for 20 s and elongation for 30 s at 72°C. In order to identify a suitable primer for analyzing the manipulated cell line, various primers were initially evaluated. The corresponding data can be found in the supporting information (Chapter 1.4). A genstudy was performed to identify a reliable housekeeping gene (Supporting Information, Chapter 1.5). Data analysis was performed using Bio-Rad CFX Manager 3.0 (Hercules, CA, USA).

2.7 Antibody Staining

Flow cytometry experiments were performed to verify the expression of ACE2 on the cell surface via the binding of fluorogenically labeled antibodies. For that purpose, the cells in the culture flask were gently washed with PBS. Subsequently, 10 mL of PBS was added, and the cells were detached by pipetting the solution up and down. The cells were aliquoted to 1×10^6 cells and transferred into protein low bind Eppendorf cups. 5 μ L of the anti-hACE2 AlexaFluor 647-labeled antibody or its isotype control, respectively, were added and the mixture was incubated for 30 min at room temperature in the dark. Afterward, the cells were centrifuged for 5 min at 300 g and the supernatant was removed to separate the unbound antibody. The cells were resuspended in 2 mL flow cytometry staining buffer and the purification step was repeated twice. The resulting cell pellet was resuspended in 500 μ L of flow cytometry staining buffer and analyzed immediately. The flow cytometric analysis was performed on a FACS Canto II (Becton Dickinson, Franklin Lakes, NJ, USA). The labeled antibodies were detected by excitation at 633 nm and analysis of the emission using a 661/16 nm bandpass filter.

2.8 ACE2 Activity Assay

To evaluate the cleavage activity of ACE2 of the transduced cells, a fluorometric ACE2 activity assay kit was used. The cells were washed with serum-free DMEM and aliquoted to 250,000 cells in Eppendorf cups. After centrifugation for 5 min at 300 g the supernatant was aspirated gently. The cells were resuspended in lysis buffer, stored on ice, and digested with a Dounce homogenizer. After 10 min incubation on ice, the cells were vortexed and incubated for a further 10 min. Subsequently, the samples were centrifuged (16,000 g, 10 min, 4 °C), transferred to a black 96-well plate, and incubated for 15 min at room temperature. For each sample, 2 µL of the 7-methoxycoumarin-4-acetic acid (MCA)-based fluorogenic substrate was diluted with 48 µL ACE2 assay buffer and the solution was added to the well plate. The samples were mixed by shaking the plate gently. Subsequently, the fluorescence was measured with an excitation wavelength of 320 nm and an emission wavelength of 420 nm at room temperature in the kinetic mode for 90 min with measurement steps of 2 min.

2.9 Solid Phase Synthesis of the Cleavage Sequence

The TMPRSS2 cleavage sequence was synthesized according to Walter et al. (2024) [18] using a standard Fmoc strategy. All amino acids used were side chain-protected. 2-Chlorotrityl-resin (300 mg, 1 eq) was weighted into a fritted 25 mL syringe and 15 mL of dichloromethane (DCM) was drawn up to swell the resin at room temperature (RT) for 30 min. The first amino acid starting from the C-terminus (Fmoc-alanine) (2.5 eq) was dissolved in 15 mL DCM and 140 µL (2.5 eq) of 2,4,6-collidine was added. The DCM in the syringe was aspirated with a vacuum flask and the solution containing the amino acid and collidine was drawn up into the syringe and shaken for 3 h at room temperature. Subsequently, the solution was aspirated, and the bound amino acid was rinsed three times with 15 mL DCM. A mixture of piperidine 20 % (v/v) in dimethylformamide (DMF) was prepared and 15 mL was drawn up into the syringe, which was subsequently shaken on an orbital shaker at 35 °C for 15 min to remove the N-terminal Fmoc-protecting group. After aspirating the solution with a vacuum flask, the modified resin was washed three times with 15 mL DMF. For all following coupling steps, the amino acid (2.5 eq) and 1-[bis(dimethylamino)methylene]-1*H*-1,2,3-triazolo-[4,5-*b*]pyridinium 3-oxide hexa-fluorophosphate (HATU) (2.5 eq) were weighed into two separate Erlenmeyer flasks, dissolved in 5 mL DCM, and collidine (2.5 eq) was added to the solution containing HATU. Afterward,

Chapter 6

both solutions were drawn up into the syringe and the syringe was shaken at 35 °C for 60 min. After removing the solution with a vacuum flask and three washing steps with DMF, the next amino acid was coupled under the same conditions until the entire peptide was built up on the solid phase. To cleave the peptide from the resin, after the last Fmoc deprotection step, the syringe was rinsed with methanol, DCM, and diethyl ether (2 x 15 mL) and allowed to dry. The dried resin was transferred to a round-bottom flask and a solution of hexafluoroisopropanol (HFIP) in DCM (20 %) was added dropwise. The mixture was stirred for 2 h. After filtration, the filtrate was evaporated on a rotary evaporator and the side chain-protected reaction product was analyzed via HPLC, and mass spectrometry (Supporting Information, Chapter 2.1). The synthesis of the cleavage sequence with the fluorophore-quencher pair (dansyl/dabsyl) proceeded equivalently under light protection. The reaction product was analyzed via HRMS (Supporting Information, Chapter 2.4).

2.10 Synthesis of Fmoc-Lys(dansyl) and Fmoc-Lys(dabsyl)

2-Chlorotriyl-resin (10 g, 1 eq) was weighed into a round bottom flask. 40 mL of DCM was added and the resin was swollen for 30 min at RT. Boc-Lys(Fmoc)-OH (11.2 g, 2 eq) was solved in DCM, and DIPEA (4.19 mL, 2 eq) was added. The solution was transferred into the round bottom flask containing the resin and the mixture was stirred for 3 h to couple the amino acid to the solid phase via its C-terminus. The mixture was filtered through a frit and washed with DCM, followed by an end-capping step of the resin with DCM (20 mL), methanol (MeOH) (5 mL), and 4.2 mL DIPEA (1 eq). The reaction was stirred for 15 min at RT and subsequently filtered through a frit. Afterward, the resin was washed with DCM, MeOH, and diethyl ether and allowed to dry. To cleave the Fmoc protection group from the side chain, 40 mL of a solution of piperidine in DMF (20 %) was mixed with the solid phase in a round bottom flask and stirred for 15 min, followed by washing steps with DCM, MeOH, and diethyl ether through a frit.

2 g (1 eq) of the Boc-protected, lysine-modified resin was weighed into a syringe. To couple dansyl to the primary amine of the lysine side chain, dansylchloride (0.67 g, 1.3 eq) was solved in 5 mL DMF. In a separate snap cap tube, DIPEA (435 μ L, 1.3 eq) was added to 2 mL DMF and subsequently, both solutions were drawn up into the syringe containing the lysine-modified resin. The syringe was shaken overnight at RT in the dark. After a washing step with DCM,

MeOH, and diethylether (15 mL), the resin was transferred to a round bottom flask. A solution of 20 % trifluoroacetic acid (TFA) in DCM was added and the reaction was stirred for 60 min to cleave the dansyl-modified lysine from the resin. Subsequently, the mixture was filtrated, and the resin was washed until the resulting filtrate was clear. The filtrate was evaporated on a rotary evaporator and left to dry on a vacuum pump overnight. The Fmoc protection was performed according to Singh et al. (2022) [22]. The reaction product (1.24 g, 1 eq) was dissolved in 10 % aqueous (aq.) Na_2CO_3 (50 mL). Fmoc-OSu (1.10 g, 1 eq) in THF (50 mL) was added to the mixture dropwise. After completion 100 mL millipore water was added to the solution and stirring was continued overnight at room temperature. The reaction progress was monitored by thin layer chromatography (TLC). The mixture was acidified to pH 3 by addition of aq. HCl (1 N) and the reaction product was extracted with ethyl acetate and DCM. The combined organic layers were dried over Na_2SO_4 and evaporated, yielding a yellow solid. The reaction product was analyzed by HRMS (Supporting Information; Chapter 2.2).

For the synthesis of Fmoc-Lys(dabsyl)-OH, Boc-Lys(Fmoc)-OH was coupled to the 2-chlorotrityl-resin according to the synthesis of Fmoc-Lys(dansyl)-OH. 1 g of the Boc-protected, lysine-modified resin was weighed in a syringe. Dabsylchloride (0.41 g, 1.3 eq) was weighed in a snap cap tube and dissolved in 5 mL DMF. In a separate snap cap tube, 2 mL DMF was mixed with DIPEA (218 μL , 1.3 eq) and both solutions were drawn up in the syringe containing the modified resin. All further steps were carried out analogous to the synthesis of Fmoc-Lys-dansyl-OH. The reaction product, which was a red solid, was analyzed via HRMS (Supporting Information; Chapter 2.3).

2.11 Statistics

Statistical analysis was performed using GraphPad Prism Sofware 8.3.0. Ordinary one-way ANOVA with a Tukey's multiple comparisons test was performed for statistical evaluation of significance (Fig. 3B). The resulting significance levels are indicated in the figure legend.

Chapter 6

3 Results and Discussion

3.1 Lentiviral Transduction of HEK293 cells for TMPRSS2 Expression

In order to investigate the dependence of nanoparticle binding and uptake on the interaction with ACE2 and/or TMPRSS2, it was necessary to generate cell lines expressing either one or both enzymes in combination, but which are otherwise indistinguishable. Therefore, HEK293 cells were initially transduced with lentiviral vectors for the stable expression of TMPRSS2, followed by antibiotic selection with blasticidin (Supporting Information; Chapter 1). The transduction success and the activity of the expressed transmembrane protease TMPRSS2 were then analyzed by quantitative PCR (qPCR) (Fig. 2) and a fluorogenic activity assay (Fig. 3).

The qPCR analysis demonstrated that no expression of TMPRSS2 could be detected in wild-type HEK293 cells (quantification cycle (C_q): 39.87 ± 0.96 ; negative controls: no reverse transcriptase (noRT): 40.43 ± 1.21 ; no template control (NTC): 41.20 ± 0.66), which is consistent with data from the human protein atlas [21] and from literature [23,24]. After lentiviral transduction, the cell line (HEK293-TMPRSS2) showed a pronounced expression of TMPRSS2, with a C_q value of 20.68 with equivalent expression of the housekeeper gene hRPL32 (C_q (HEK293) = 15.54 ± 0.19 ; C_q (HEK-TMPRSS2) = 15.51 ± 0.09).

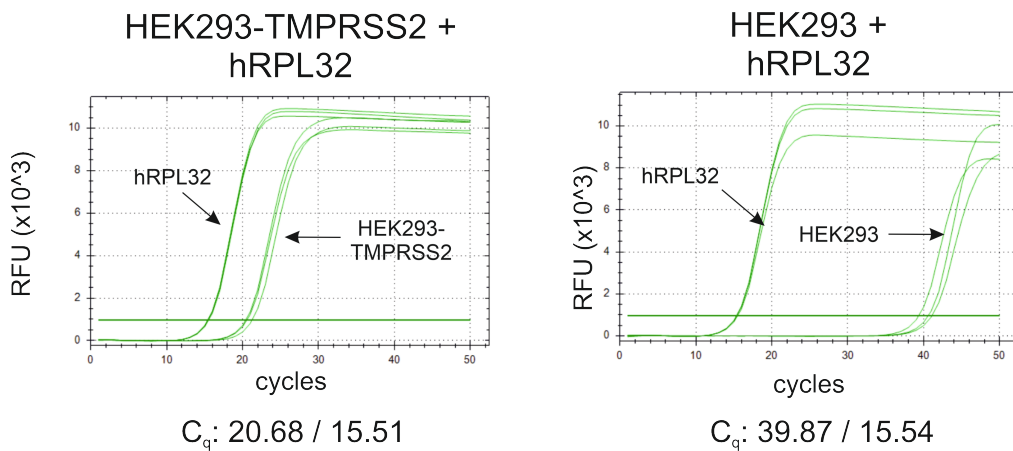


Figure 2. qPCR Analysis of the transduced cells (HEK293-TMPRSS2) compared to wild-type HEK293. With equal expression of the housekeeper gene hRPL32, the transduced cells showed significant expression of TMPRSS2, whereas no expression was detected in wild-type cells (RFU = relative fluorescence units).

When the initially quenched fluorogenic substrate Boc-QAR-AMC was incubated with the transduced cells, the fluorescence intensity increased over time due to cleavage by TMPRSS2, expressed on the cell surface (Fig. 3). The observed cleavage activity could be blocked by the addition of the TMPRSS2 inhibitor camostate mesylate, indicating a specific reaction. In contrast, non-transfected HEK293 cells showed little or no substrate conversion. Slight increases in fluorescence may be caused by non-specific cleavage by other proteases on the cell surface. In conclusion, the expression and activity of the transmembrane protease TMPRSS2 in HEK293 cells have been verified.

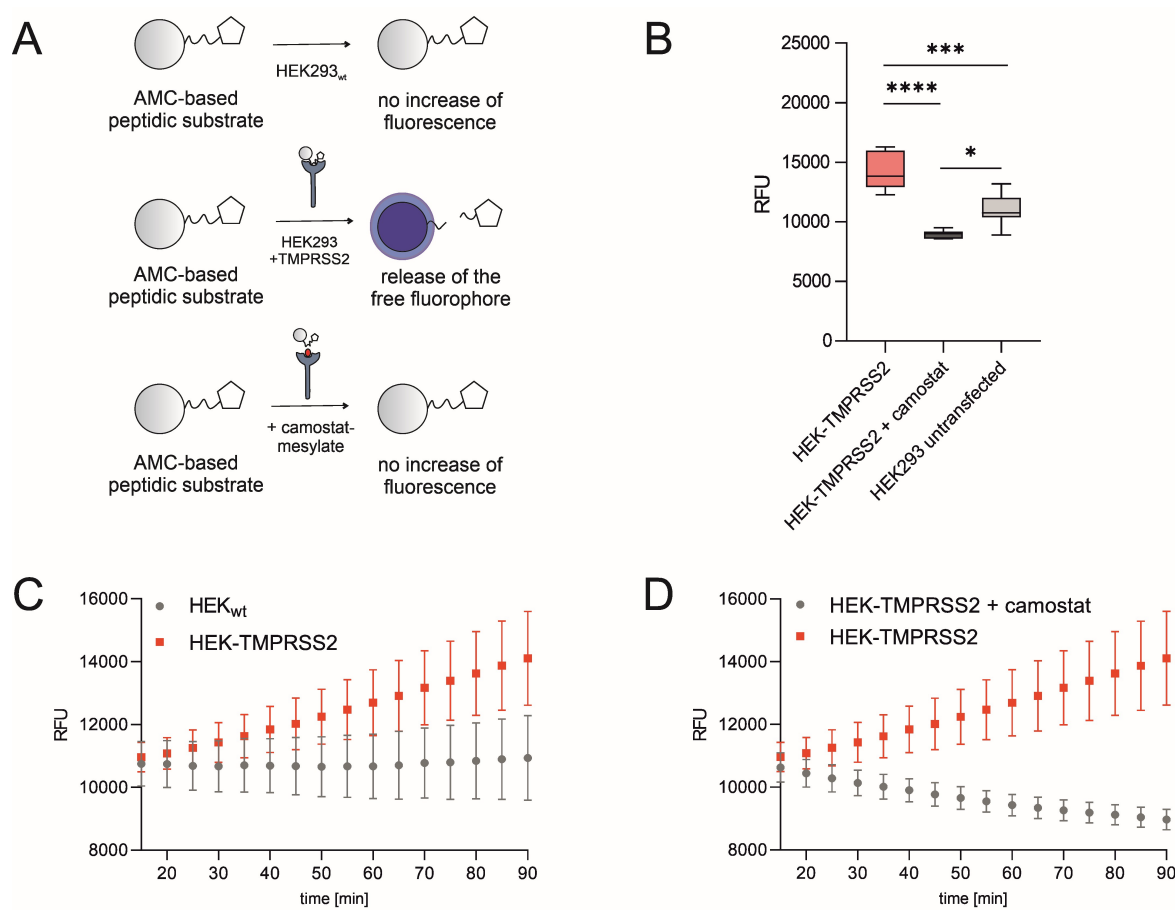


Figure 3. Fluorogenic TMPRSS2 activity assay analyzing the transduced cell line HEK293-TMPRSS2. (A) Schematic representation of the activity assay. An initially quenched fluorophore is released by the protease activity of TMPRSS2 in transduced HEK293 cells (HEK293-TMPRSS2), resulting in an increase in fluorescence intensity. Non-transduced cells that do not express TMPRSS2 (HEK293) are supposed to show no or only a slight increase in fluorescence intensity due to non-specific protease activity. Proteolytic cleavage is supposed to be prevented by the addition of the TMPRSS2 inhibitor camostat mesylate. **(B)** Comparison of fluorescence intensity after incubation for 90 min.

Chapter 6

Incubation of the AMC-based substrate with the transduced cells (HEK293-TMPRSS2) resulted in a significantly higher fluorescence intensity than incubation with non-transfected cells. The proteolytic cleavage could be inhibited by the addition of the inhibitor camostate mesylate (RFU = relative fluorescence units). **(C)** Comparison of substrate cleavage by HEK293 wild-type (wt) cells (HEK293_{wt}) and transduced cells (HEK-TMPRSS2). **(D)** Comparison of substrate cleavage with and without TMPRSS2 inhibitor over time. Results represent mean \pm standard deviation (SD) (n=7, levels of statistical significance are indicated as *p \leq 0.05, **p \leq 0.01, ***p \leq 0.001, ****p \leq 0.0001).

3.2 Lentiviral Transduction for Additional ACE2 Expression

After the additional transduction for ACE2 expression, the TMPRSS2/ACE2 double positive cell line was analyzed using antibody staining, with fluorogenic detection by flow cytometry (Fig. 4A). As expected, HEK293 wild-type cells did not bind the labeled anti-hACE2 antibody and served as an additional negative control to staining with isotype control antibodies. HEK293T-ACE2 cells, which have previously been shown to express ACE2 [25], provided a positive control and showed an increase in fluorescence due to the binding of the labeled antibody. All transduced cell lines prepared with different virus dilutions (1:5, 1:50, 1:500) bound the labeled anti-hACE2 antibody on their surface and thus expressed ACE2. The higher the concentration of the virus used for transduction, the lower was the resulting antibody binding. The reason for this is that cytotoxic effects of high virus concentrations may lead to cellular stress, resulting in reduced protein expression. Therefore, a balance must be found between maximum gene transfer and cell viability [26,27]. In addition to the expression of the enzyme, the cleavage activity had to be evaluated (Fig. 4B). Incubation of the transduced cells with a previously quenched MCA-based fluorogenic substrate for 90 min resulted in an increase in fluorescence intensity due to the release of free fluorophore. As the cell line resulting from transduction with the 1:50 viral dilution showed the highest activity in the fluorogenic assay, this cell line is supposed to be used for further experiments. The discrepancy between protein expression and activity could be caused by an unfavorable folding or orientation of ACE2 on the cell surface, allowing binding of the antibody, but not cleavage of its substrate [28].

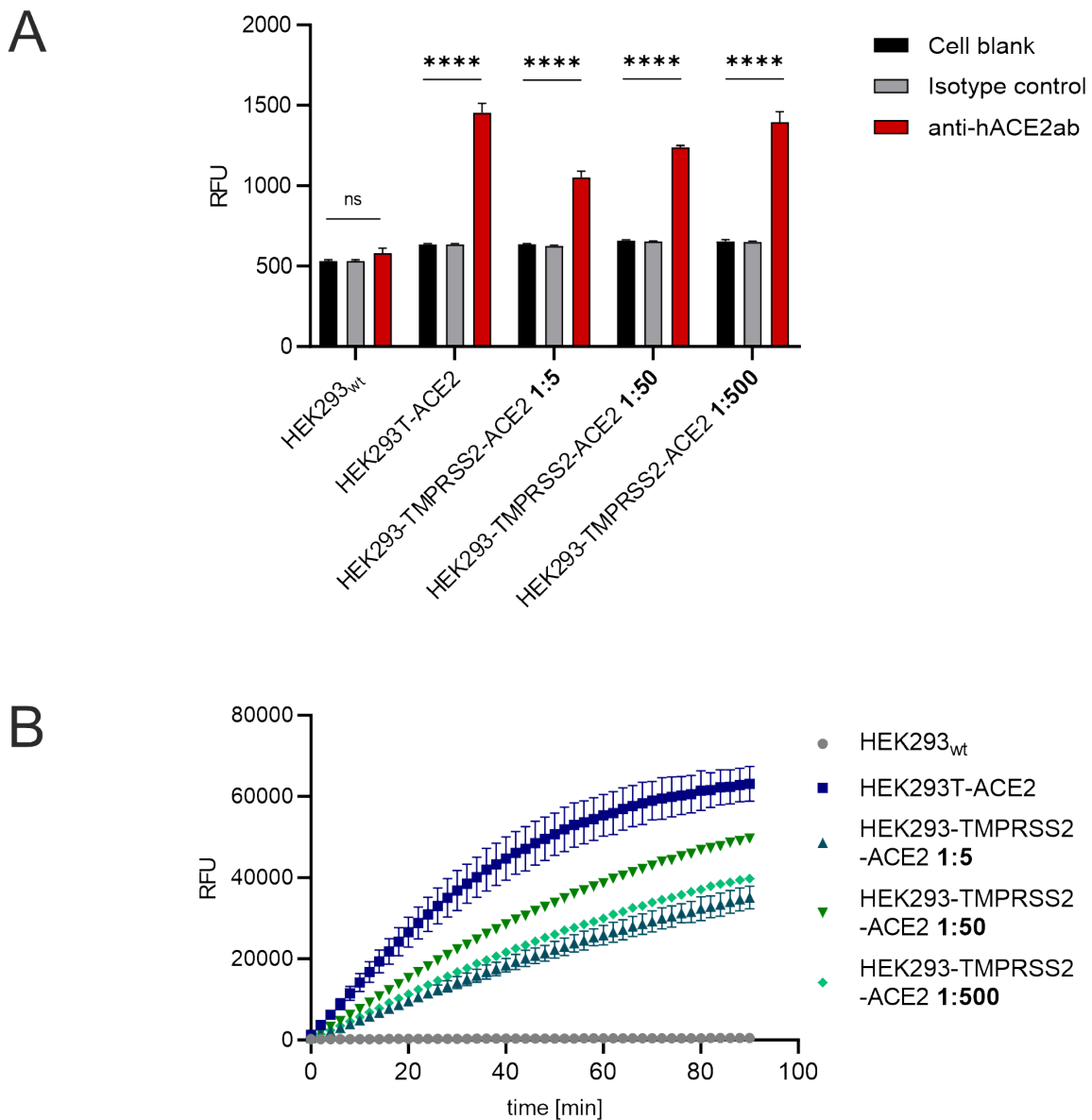


Figure 4. Analysis of the produced cell line HEK293-TPRSS2-ACE2 for expression and activity of ACE2. (A) Antibody staining using AlexaFluor647-labeled antibodies for hACE2 with analysis via flow cytometry. **(B)** Measurement of ACE2 cleavage activity by a fluorogenic assay (RFU = relative fluorescence units).

Chapter 6

3.3 Development of a TMPRSS2-responsive Nanoparticle Targeting Concept

The TMPRSS2-independent targeting concept presented in **Chapter 5** [18] was modified to achieve higher selectivity for ACE2/TMPRSS2 double-positive target cells, which are particularly susceptible to SARS-CoV-2 infection. TAT47-57 is to be covered by a shielding unit coupled via a cleavage sequence of TMPRSS2 (Fig. 5). Particle internalization thus only occurs if cells express both ACE2 and TMPRSS2 on the cell surface, and proteolytic cleavage reveals the uptake signal.

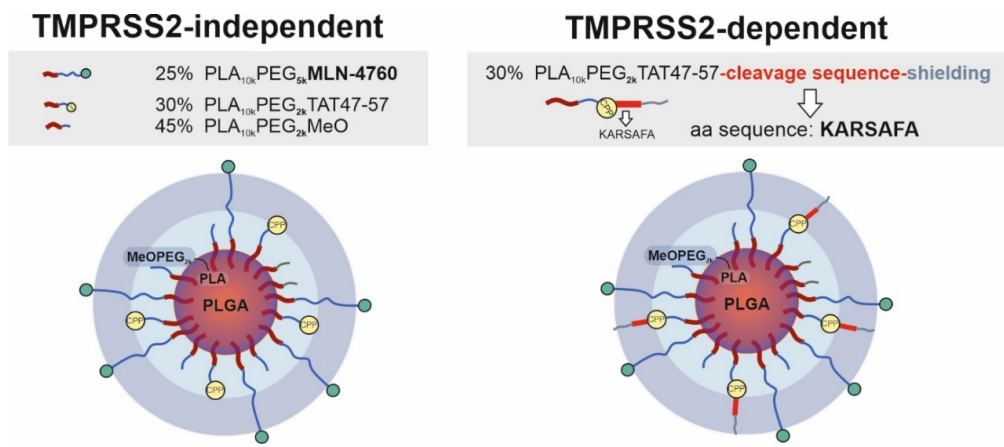


Figure 5. Proposed modification of the nanoparticle structure to achieve dual responsibility for ACE2 and TMPRSS2. A shielding unit is supposed to be attached to TAT47-57, coupled via a TMPRSS2 cleavage sequence. The proteolytic activity of the enzyme should thus reveal the uptake signal and mediate nanoparticle uptake.

The peptidic substrate KARSAFA, which has been identified as a promising cleavage sequence of TMPRSS2 by Mahoney et al. (2021) [29], was synthesized with side chain-protected amino acids, and analyzed via HRMS and HPLC. The corresponding analysis data can be found in the supporting information (Chapter 2.1). Since it is not clear whether the cleavage sequence is accessible on the nanoparticle surface, a test system must be established to detect peptide cleavage. Therefore, the proteolytic activity should be evaluated fluorogenically by a Förster resonance energy transfer (FRET) assay [30,31] (Fig. 6).

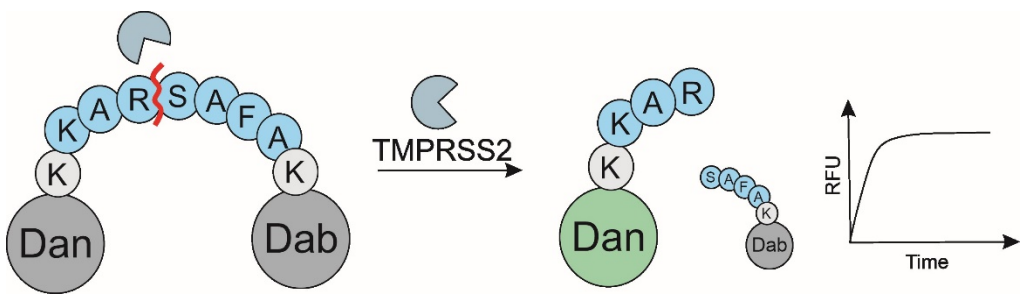
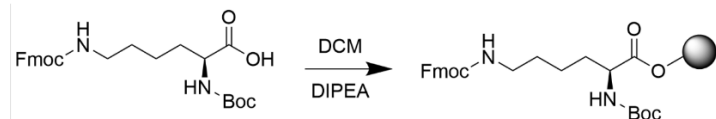


Figure 6. Approach for the development of a detection system for peptide cleavage on the NP surface and thus nanoparticle activation. Binding of the Förster resonance energy transfer (FRET) partners dansyl and dabsyl on opposite sides of the TMPRSS2 cleavage sequence. Cleavage at the R↑S interface should promote spatial separation of the quencher dabsyl from the corresponding fluorophor dansyl, resulting in an increase in fluorescence intensity (RFU = relative fluorescence units).

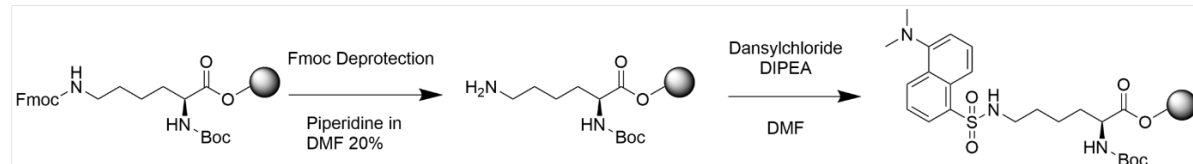
Therefore, as a first step, the fluorophor dansyl and its FRET partner dabsyl had to be coupled to an amino acid to enable the incorporation into the peptide chain (Supporting Information, Chapter 2.3, Scheme 1). Due to the favorable reactivity of its primary amine, lysine was selected for this purpose. The analytics of the successfully synthesized lysine-dansyl and lysine-dabsyl conjugates can be found in supporting information (Chapter 2.2-2.3). Subsequently, the protected cleavage sequence with flanking FRET partners (Lys(Dan)-KARSAFA-Lys(Dab))_{prot} was synthesized via solid phase synthesis. The corresponding molecule structure and analysis data can be found in the supporting information (Chapter 2.4).

Chapter 6

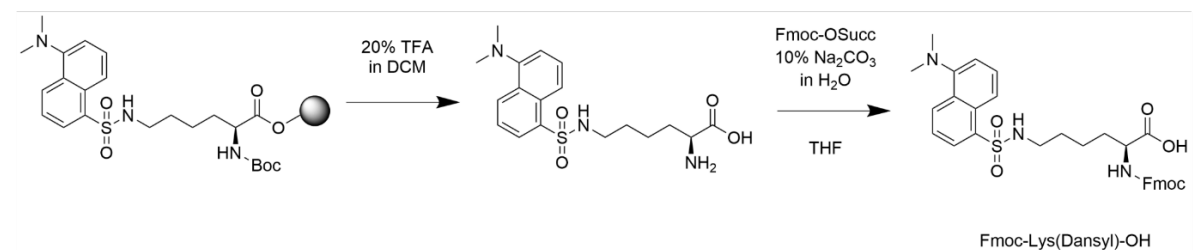
1) Protection of all reactive groups (coupling C-terminus to chlorotriyl-resin)



2) Coupling of dansyl to the primary amine of the amino acid (lysine) side chain



3) Cleavage from the resin, Boc deprotection, Fmoc protection



Scheme 1. Synthesis Scheme of Fmoc-Lys(dansyl)-OH. As a first step, lysine with a Boc-protected N-terminus and an Fmoc-protected side chain was immobilized on a solid phase via its C-terminus to prevent unspecific coupling reactions. Subsequently, the Fmoc-protection group was cleaved selectively using piperidine in dimethylformamide (DMF), followed by coupling of dansyl to the released primary amine of the lysine side chain utilizing *N,N*-diisopropylethylamine (DIPEA) as base. After cleavage from the resin and Boc-deprotection with trifluoroacetic acid (TFA) in dichloromethane (DCM), the N-terminus was protected with an Fmoc-protecting group using Fmoc-succinimide (Fmoc-Osuc) to enable the coupling via the classical Fmoc-strategy.

4 Conclusion and Outlook

This work lays the basis for the development of an ACE2/TMPRSS2 dual-responsive targeting concept that can direct nanoparticles to the host target cells of the SARS-CoV-2 virus solely through interaction with ectoenzymes. HEK293 cells were successfully transduced using lentiviral vectors and subsequently characterized to serve as target cells for the developed SARS-CoV-2-mimetic concept. Subsequently, a nanoparticle design strategy was presented that allows selective internalization exclusively after proteolytic cleavage by TMPRSS2. A method for detecting proteolytic cleavage at the particle surface and thus nanoparticle activation using a FRET assay was also proposed. The corresponding cleavage sequence, combined with fluorophore and quencher, was synthesized as a first starting point.

After the successful preparation of the two SARS-CoV-2-mimetic nanoparticle types, the encapsulation of an antiviral drug with an intracellular target in SARS-CoV-2 host cells should follow. A viral challenging model could then be used to assess whether targeted drug delivery can enhance the efficacy of recently developed antiviral compounds. It is essential that *in vivo* experiments are carried out in the following, as the transferability of successful *in vitro* results needs to be assessed in individual cases.

Chapter 6

References

- [1] R. Lu, X. Zhao, J. Li, P. Niu, B. Yang, H. Wu, W. Wang, H. Song, B. Huang, N. Zhu, Y. Bi, X. Ma, F. Zhan, L. Wang, T. Hu, H. Zhou, Z. Hu, W. Zhou, L. Zhao, J. Chen, Y. Meng, J. Wang, Y. Lin, J. Yuan, Z. Xie, J. Ma, W.J. Liu, D. Wang, W. Xu, E.C. Holmes, G.F. Gao, G. Wu, W. Chen, W. Shi, W. Tan, Genomic characterisation and epidemiology of 2019 novel coronavirus: implications for virus origins and receptor binding, *The Lancet* 395 (2020) 565–574. [https://doi.org/10.1016/S0140-6736\(20\)30251-8](https://doi.org/10.1016/S0140-6736(20)30251-8).
- [2] D. Zhou, W. Dejnirattisai, P. Supasa, C. Liu, A.J. Mentzer, H.M. Ginn, Y. Zhao, H.M.E. Duyvesteyn, A. Tuekprakhon, R. Nutalai, B. Wang, G.C. Paesen, C. Lopez-Camacho, J. Slon-Campos, B. Hallis, N. Coombes, K. Bewley, S. Charlton, T.S. Walter, D. Skelly, S.F. Lumley, C. Dold, R. Levin, T. Dong, A.J. Pollard, J.C. Knight, D. Crook, T. Lambe, E. Clutterbuck, S. Bibi, A. Flaxman, M. Bittaye, S. Belij-Rammerstorfer, S. Gilbert, W. James, M.W. Carroll, P. Klenerman, E. Barnes, S.J. Dunachie, E.E. Fry, J. Mongkolsapaya, J. Ren, D.I. Stuart, G.R. Screamton, Evidence of escape of SARS-CoV-2 variant B.1.351 from natural and vaccine-induced sera, *Cell* 184 (2021) 2348-2361.e6. <https://doi.org/10.1016/j.cell.2021.02.037>.
- [3] COVID - Coronavirus Statistics - Worldometer, 2024. <https://www.worldometers.info/coronavirus/> (accessed 22 August 2024).
- [4] Post COVID-19 condition (Long COVID), 2024. <https://www.who.int/europe/news-room/fact-sheets/item/post-covid-19-condition> (accessed 22 August 2024).
- [5] Z. Al-Aly, B. Bowe, Y. Xie, Long COVID after breakthrough SARS-CoV-2 infection, *Nat Med* 28 (2022) 1461–1467. <https://doi.org/10.1038/s41591-022-01840-0>.
- [6] L. Alquraan, K.H. Alzoubi, S.Y. Rababa'h, Mutations of SARS-CoV-2 and their impact on disease diagnosis and severity, *Informatics in Medicine Unlocked* 39 (2023) 101256. <https://doi.org/10.1016/j.imu.2023.101256>.
- [7] B. Bakhshandeh, Z. Jahanafrooz, A. Abbasi, M.B. Goli, M. Sadeghi, M.S. Mottaqi, M. Zamani, Mutations in SARS-CoV-2; Consequences in structure, function, and pathogenicity of the virus, *Microbial Pathogenesis* 154 (2021) 104831. <https://doi.org/10.1016/j.micpath.2021.104831>.
- [8] M. Zmudzinski, W. Rut, K. Olech, J. Granda, M. Giurg, M. Burda-Grabowska, R. Kaleta, M. Zgarbova, R. Kasprzyk, L. Zhang, X. Sun, Z. Lv, D. Nayak, M. Kesik-Brodacka, S.K. Olsen, J. Weber, R. Hilgenfeld, J. Jemielity, M. Drag, Ebselein derivatives inhibit SARS-

CoV-2 replication by inhibition of its essential proteins: PLpro and Mpro proteases, and nsp14 guanine N7-methyltransferase, Sci Rep 13 (2023) 9161. <https://doi.org/10.1038/s41598-023-35907-w>.

[9] A. Saxena, Drug targets for COVID-19 therapeutics: Ongoing global efforts, J Biosci 45 (2020) 1–24. <https://doi.org/10.1007/s12038-020-00067-w>.

[10] R.P. Joyce, V.W. Hu, J. Wang, The history, mechanism, and perspectives of nirmatrelvir (PF-07321332): an orally bioavailable main protease inhibitor used in combination with ritonavir to reduce COVID-19-related hospitalizations, Med Chem Res 31 (2022) 1637–1646. <https://doi.org/10.1007/s00044-022-02951-6>.

[11] R. Yan, Y. Zhang, Y. Li, L. Xia, Y. Guo, Q. Zhou, Structural basis for the recognition of SARS-CoV-2 by full-length human ACE2, Science 367 (2020) 1444–1448. <https://doi.org/10.1126/science.abb2762>.

[12] S. Borkotoky, D. Dey, Z. Hazarika, Interactions of angiotensin-converting enzyme-2 (ACE2) and SARS-CoV-2 spike receptor-binding domain (RBD): a structural perspective, Mol Biol Rep 50 (2023) 2713–2721. <https://doi.org/10.1007/s11033-022-08193-4>.

[13] A. Bayati, R. Kumar, V. Francis, P.S. McPherson, SARS-CoV-2 infects cells after viral entry via clathrin-mediated endocytosis, Journal of Biological Chemistry 296 (2021) 100306. <https://doi.org/10.1016/j.jbc.2021.100306>.

[14] H. D'Avila, C.N.R. Lima, P.G. Rampinelli, L.C.O. Mateus, R.V. de Sousa Silva, J.R. Correa, P.E. de Almeida, Lipid Metabolism Modulation during SARS-CoV-2 Infection: A Spotlight on Extracellular Vesicles and Therapeutic Prospects, Int. J. Mol. Sci. 25 (2024) 640. <https://doi.org/10.3390/ijms25010640>.

[15] G. Li, R. Hilgenfeld, R. Whitley, E. de Clercq, Therapeutic strategies for COVID-19: progress and lessons learned, Nat Rev Drug Discov 22 (2023) 449–475. <https://doi.org/10.1038/s41573-023-00672-y>.

[16] P. Chen, M. Wu, Y. He, B. Jiang, M.-L. He, Metabolic alterations upon SARS-CoV-2 infection and potential therapeutic targets against coronavirus infection, Sig Transduct Target Ther 8 (2023) 237. <https://doi.org/10.1038/s41392-023-01510-8>.

[17] L. Wettstein, F. Kirchhoff, J. Münch, The Transmembrane Protease TMPRSS2 as a Therapeutic Target for COVID-19 Treatment, Int. J. Mol. Sci. 23 (2022) 1351. <https://doi.org/10.3390/ijms23031351>.

Chapter 6

[18] M. Walter, M. Bresinsky, O. Zimmer, S. Pockes, A. Goepferich, Conditional Cell-Penetrating Peptide Exposure as Selective Nanoparticle Uptake Signal, *ACS Appl. Mater. Interfaces* 16 (2024) 37734–37747. <https://doi.org/10.1021/acsami.4c07821>.

[19] J. Koch, Z.M. Uckley, P. Doldan, M. Stanifer, S. Boulant, P.-Y. Lozach, TMPRSS2 expression dictates the entry route used by SARS-CoV-2 to infect host cells, *EMBO J.* 40 (2021) e107821. <https://doi.org/10.15252/embj.2021107821>.

[20] B.J. Fraser, S. Beldar, A. Seitova, A. Hutchinson, D. Mannar, Y. Li, D. Kwon, R. Tan, R.P. Wilson, K. Leopold, S. Subramaniam, L. Halabelian, C.H. Arrowsmith, F. Bénard, Structure and activity of human TMPRSS2 protease implicated in SARS-CoV-2 activation, *Nat Chem Biol* 18 (2022) 963–971. <https://doi.org/10.1038/s41589-022-01059-7>.

[21] Cell line - TMPRSS2 - The Human Protein Atlas, 2024. <https://www.proteinatlas.org/ENSG00000184012-TMPRSS2/cell+line> (accessed 26 August 2024).

[22] G. Singh, P. Liu, K.R. Yao, J.M. Strasser, C. Hlynialuk, K. Leinonen-Wright, P.J. Teravskis, J.M. Choquette, J. Ikramuddin, M. Bresinsky, K.M. Nelson, D. Liao, K.H. Ashe, M.A. Walters, S. Pockes, Caspase-2 Inhibitor Blocks Tau Truncation and Restores Excitatory Neurotransmission in Neurons Modeling FTDP-17 Tauopathy, *ACS Chem. Neurosci.* 13 (2022) 1549–1557. <https://doi.org/10.1021/acschemneuro.2c00100>.

[23] R. Strobel, J. Adler, N. Paran, Y. Yahalom-Ronen, S. Melamed, B. Politi, Z. Shulman, D. Schmiedel, Y. Shaul, Imatinib inhibits SARS-CoV-2 infection by an off-target-mechanism, *Sci Rep* 12 (2022) 5758. <https://doi.org/10.1038/s41598-022-09664-1>.

[24] R. Zang, Maria Florencia Gomez Castro, B.T. Mccune, Q. Zeng, P.W. Rothlauf, N.M. Sonnek, Z. Liu, K.F. Brulois, X. Wang, H.B. Greenberg, M.S. Diamond, M.A. Ciorba, Sean P. J. Whelan, S. Ding, American Association for the Advancement of Science (13 May 2020).

[25] M. Walter, F. Baumann, K. Schorr, A. Goepferich, Ectoenzymes as Promising Cell Identification Structures for the High Avidity Targeting of Polymeric Nanoparticles, *International Journal of Pharmaceutics* (2023) 123453. <https://doi.org/10.1016/j.ijpharm.2023.123453>.

[26] Addgene: Virus Protocol - Generating Stable Cell Lines, 2024 (accessed 27 August 2024).

[27] T. Sakuma, M.A. Barry, Y. Ikeda, Lentiviral vectors: basic to translational, *Biochem. J.* 443 (2012) 603–618. <https://doi.org/10.1042/BJ20120146>.

[28] Bruce Alberts, Alexander Johnson, Julian Lewis, Martin Raff, Keith Roberts, Peter Walter, The Shape and Structure of Proteins, in: B. Alberts, A. Johnson, J. Lewis, M. Raff, K. Roberts, P. Walter (Eds.), *Molecular Biology of the Cell*. 4th edition, Garland Science, 2002.

[29] M. Mahoney, V.C. Damalanka, M.A. Tartell, D.h. Chung, A.L. Lourenço, D. Pwee, A.E. Mayer Bridwell, M. Hoffmann, J. Voss, P. Karmakar, N.P. Azouz, A.M. Klingler, P.W. Rothlauf, C.E. Thompson, M. Lee, L. Klampfer, C.L. Stallings, M.E. Rothenberg, S. Pöhlmann, S.P.J. Whelan, A.J. O'Donoghue, C.S. Craik, J.W. Janetka, A novel class of TMPRSS2 inhibitors potently block SARS-CoV-2 and MERS-CoV viral entry and protect human epithelial lung cells, *Proc. Natl. Acad. Sci. U. S. A.* 118 (2021) e2108728118. <https://doi.org/10.1073/pnas.2108728118>.

[30] M.S. Piel, G.H.J. Peters, J. Brask, Chemoenzymatic synthesis of fluorogenic phospholipids and evaluation in assays of phospholipases A, C and D, *Chemistry and Physics of Lipids* 202 (2017) 49–54. <https://doi.org/10.1016/j.chemphyslip.2016.12.002>.

[31] A.S. Khadria, A. Senes, Fluorophores, environments, and quantification techniques in the analysis of transmembrane helix interaction using FRET, *Biopolymers* 104 (2015) 247–264. <https://doi.org/10.1002/bip.22667>.

Chapter 6 – Supporting Information

Chapter 6

Supporting Information

Chapter 6 – Supporting Information

1 Lentiviral Transduction

1.1 Antibiotic Selection

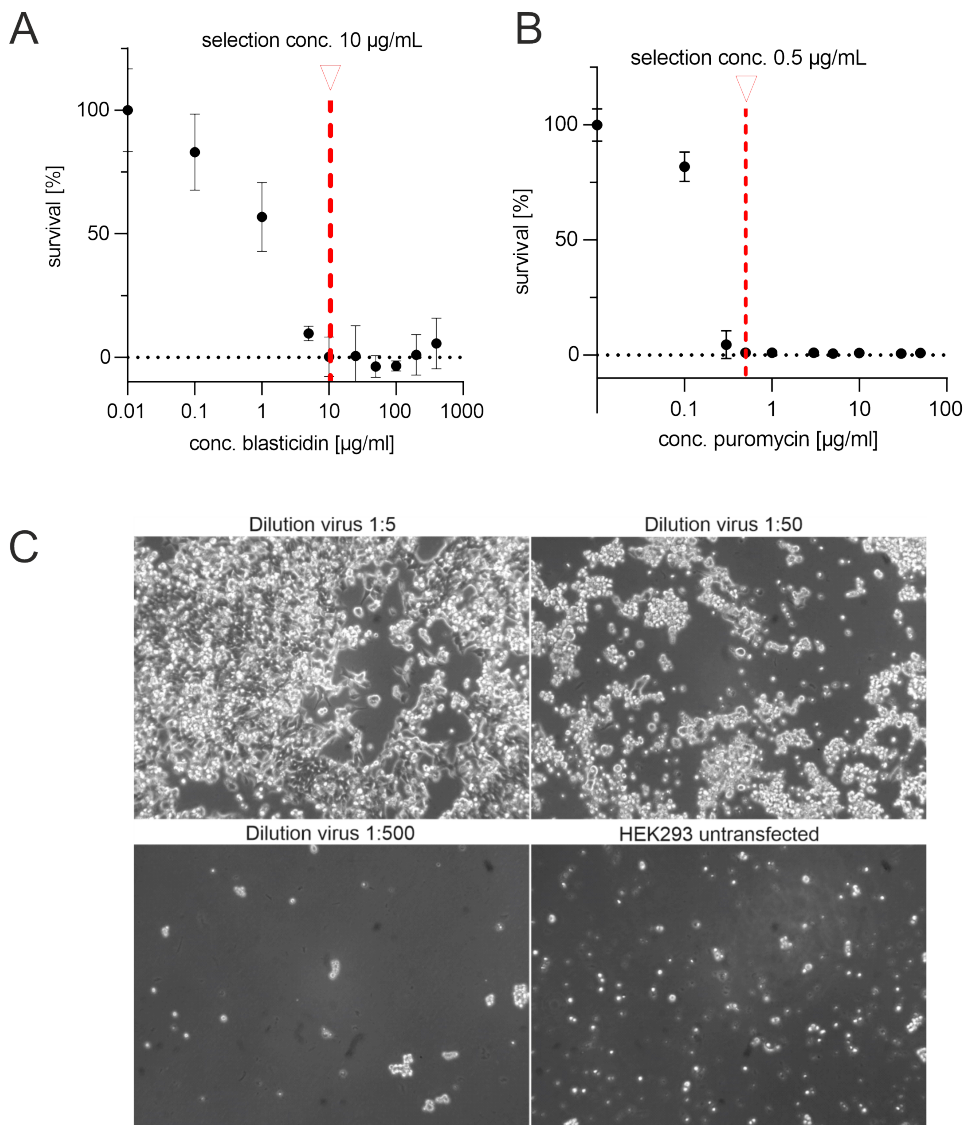


Figure S1. Evaluation of antibiotic resistance of HEK293 cells for the antibiotic selection after lentiviral transduction via an MTT-Assay. (A) Determination of the selection concentration for blasticidin (TMPRSS2 transduction). **(B)** Determination of the selection concentration for puromycin (ACE2 transduction). **(C)** Tracking of the antibiotic selection after lentiviral transduction of cells treated with different virus dilutions (dilution of the virus stock solution with a titer $\geq 1 \times 10^6$ transducing units (TU)/mL. The higher the concentration of the viral vector, the higher the proportion of transduced cells that survive antibiotic selection. All untransduced cells died, as confirmed by the negative control.

Chapter 6 – Supporting Information

1.2 TMPRSS2 Activity Assay – Preliminary Tests Using Soluble TMPRSS2

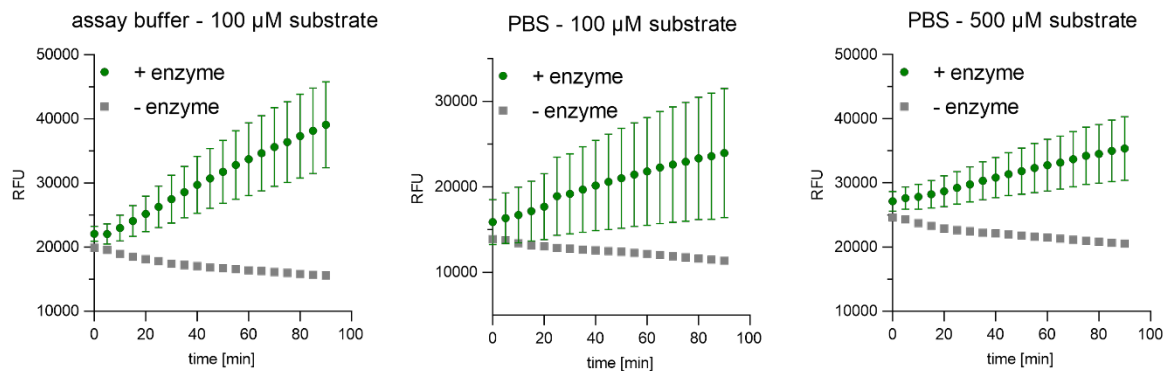


Figure S2. Pretest TMPRSS2 activity assay with soluble TMPRSS2. Evaluation of different buffers and substrate concentrations (RFU = relative fluorescence units).

1.3 Prescreening HEK293-TMPRSS2 Cells Transduced with Different Viral Dilutions – TMPRSS2 Activity Assay

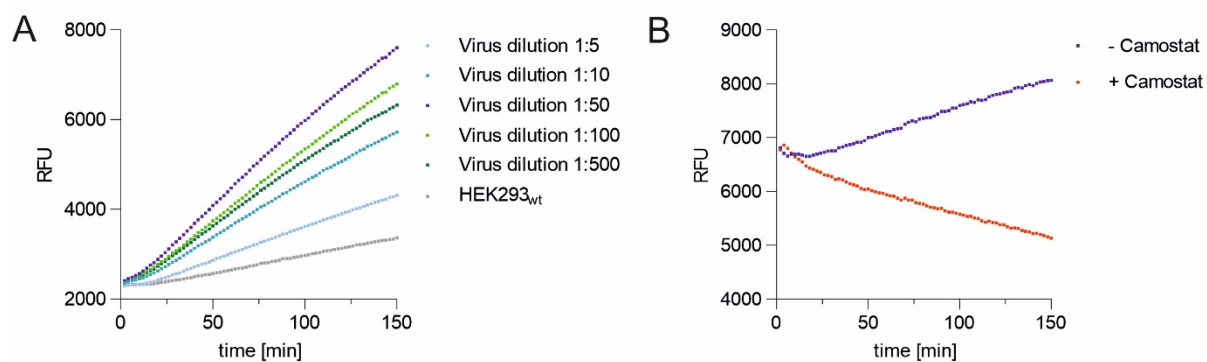


Figure S3. Prescreening activity of HEK293-TMPRSS2 cells. (A) Comparison of cell lines transduced with different viral dilutions. (B) Investigation of the cleavage selectivity of HEK293-TMPRSS2 transduced with 1:50 viral dilution by inhibition with the TMPRSS2 inhibitor camostat mesylate (RFU = relative fluorescence units).

Supporting Information - SARS-CoV2 host cell targeting

1.4 Primer Testing for qPCR Analysis of HEK293-TMPRSS2

To evaluate the expression of TMPRSS2 after lentiviral transduction, different primer pairs were analyzed for their suitability. They were purchased from Sigma Aldrich GmbH (Taufkirchen, Germany). The sequence of PP1 was adapted from OriGene Technologies, Inc. (Rockville, USA) (CAT#: HP208758).

Table S1. Primer sequences.

| Primer | Oligo sequence (5' to 3') |
|-------------------|---------------------------|
| huTMPRSS2_fwd_PP1 | CCTCTAACTGGTGTGATGGCGT |
| huTMPRSS2_rvs_PP1 | TGCCAGGACTTCCTCTGAGATG |
| huTMPRSS2_fwd_PP2 | CAGACCAGGAGTGTACGGGA |
| huTMPRSS2_rvs_PP2 | TGGATTAGCCGTCTGCCCTC |
| huTMPRSS2_fwd_PP3 | CCAGGAGTGTACGGGAATGTG |
| huTMPRSS2_rvs_PP3 | GGATTAGCCGTCTGCCCTCATTT |
| huTMPRSS2_fwd_PP4 | AGACCAGGAGTGTACGGGAA |
| huTMPRSS2_rvs_PP4 | TTAGCCGTCTGCCCTCATTT |

Table S2. Evaluation of qPCR analysis using different primers.

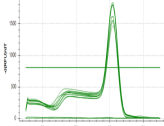
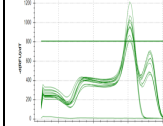
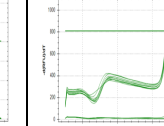
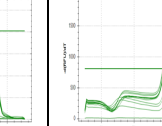
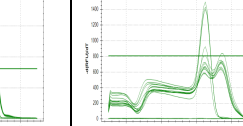
| Primer pair (PP) | C _q (HEK-TMPRSS2) | C _q (Calu3) | C _q (no reverse transcriptase, noRT) | No template control (NTC) |
|------------------|------------------------------|------------------------|---|---------------------------|
| 1 | 18.99 ± 0.35 | 28.77 ± 0.27 | 42.69 ± 1.48 | N/A |
| 2 | 18.86 ± 0.31 | 27.83 ± 0.47 | 33.31 ± 0.20 | 40.58 |
| 3 | 18.88 ± 0.30 | 28.78 ± 0.32 | 32.75 ± 0.52 | 46.54 |
| 4 | 18.83 ± 0.31 | 28.50 ± 0.19 | 32.64 ± 0.87 | 48.33 |

→ Primer pair 1 was used for all further experiments.

Chapter 6 – Supporting Information

1.5 Genstudy – Selection of the Housekeeping Gene for qPCR HEK293-TMPRSS2 Analysis

Table S3. Selection of a housekeeping gene as reference for the expression of TMPRSS2

| Housekeeper gene | hRPL32 | hGNb2L | hLaminA/C | hGAPDH | 18CS |
|---|---|---|---|--|---|
| C_q | 15.69 | 18.61 | 30.01 | 18.38 | 7.22 |
| Melting curve |  |  |  |  |  |
| Gene expression stability (recommended: $CV < 0.5$; $M < 1$) | CV: 0.0690 M: 0.1245 | CV: 0.0092 M: 0.0673 | CV: 0.0943 M: 0.1703 | CV: 0.0197 M: 0.0711 | CV: 0.0711 M: 0.0719 |

→ hRPL32 was selected as housekeeping gene.

2 Development of Enzyme-Responsive Nanoparticles

2.1 Analysis Data of KARSAFA_{prot}.

2.1.1. Structure

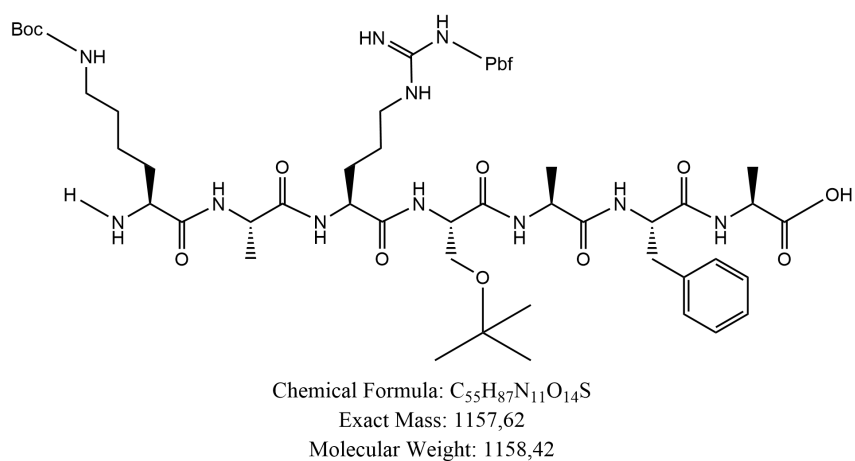


Figure S4. Structure of KARSAFA side chain-protected (KARSAFA_{prot}).

2.1.2 HRMS

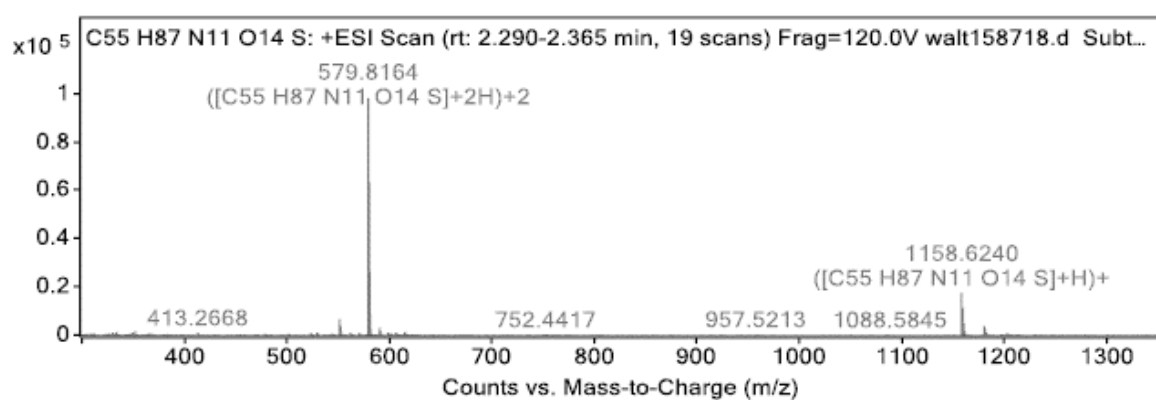


Figure S5. HRMS analysis of KARSAFA_{prot}. HRMS: (M+2H)⁺² *m/z* calculated for C₅₅H₈₇N₁₁O₁₄S: 579.8150, found: 579.8164.

Chapter 6 – Supporting Information

2.1.3 HPLC

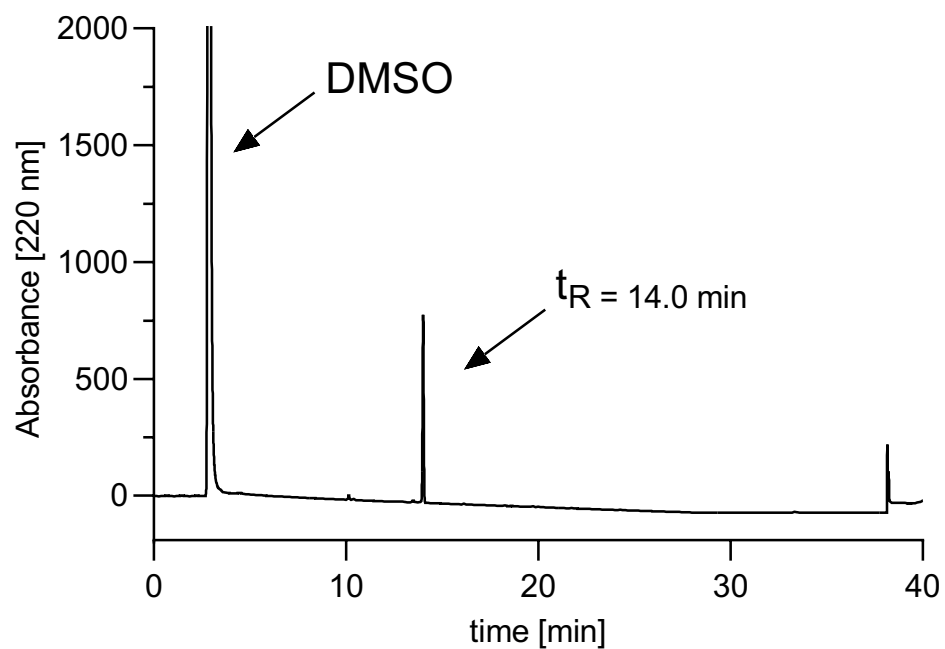


Figure S6. Reversed Phase (RP)-HPLC analysis of KARSAFA_{prot}. Retention time t_R of KARSAFA_{prot}: 14.0 min.

2.2 Analytics of Fmoc-Lys(dansyl)-OH

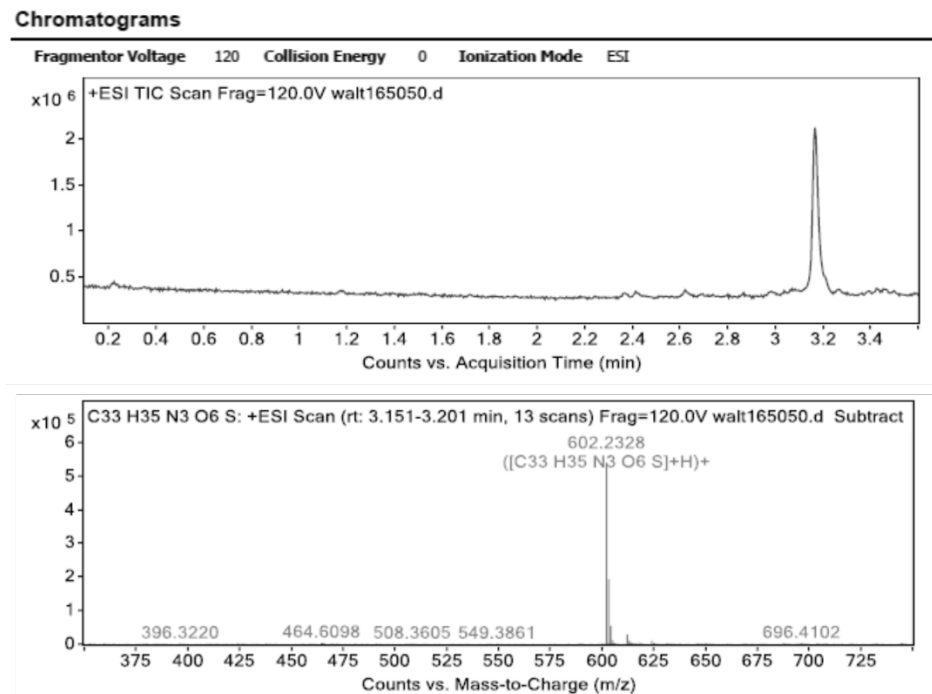
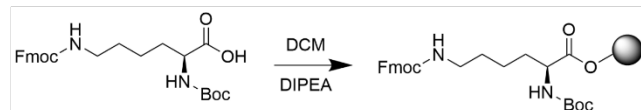


Figure S7. HRMS analysis of Fmoc-Lys(dansyl)-OH. HRMS: m/z $(M+H)^+$ calculated: 602.2319, found: 602.2328.

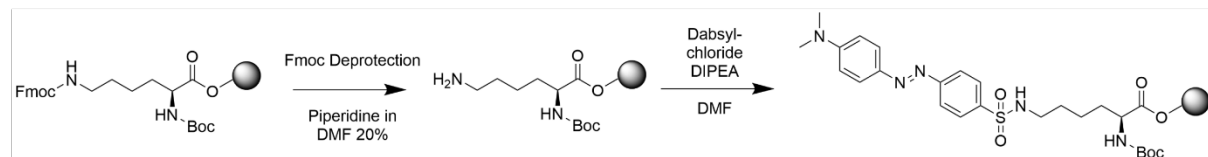
Chapter 6 – Supporting Information

2.3 Synthesis and Analytics of Fmoc-Lys(dabsyl)-OH

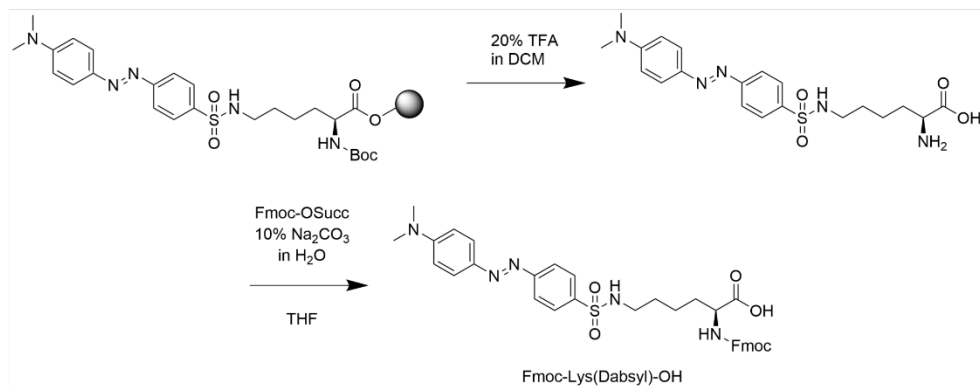
1) Protection of all reactive groups (coupling C-terminus to chlorotriyl-resin)



2) Coupling of dabsyl to the primary amine of the amino acid (lysine) side chain



3) Cleavage from the resin, Boc deprotection, Fmoc protection



Scheme S1. Synthesis of Fmoc-Lys(dabsyl)-OH

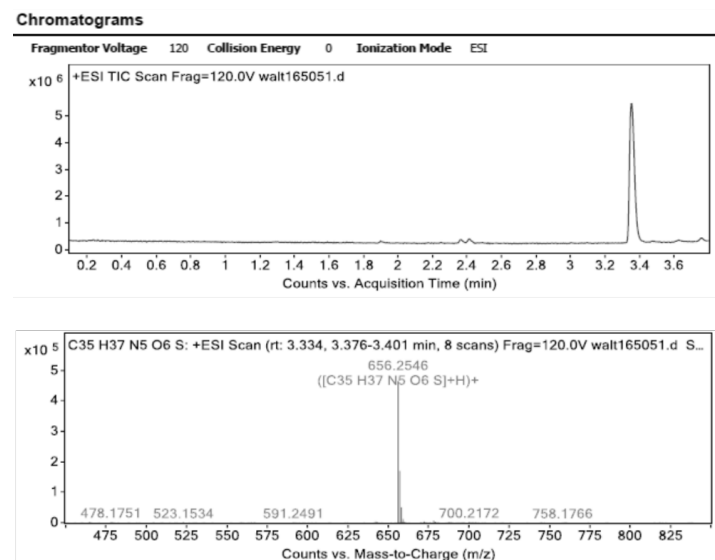


Figure S8. HRMS analysis of Fmoc-Lys(dabsyl)-OH. HRMS: m/z ($M+H$)⁺ calculated: 656.2537, found: 656.2546

2.4 Synthesis of Lys(Dan)-KARSAFA-Lys(Dab)_{prot}.

2.4.1 Structure

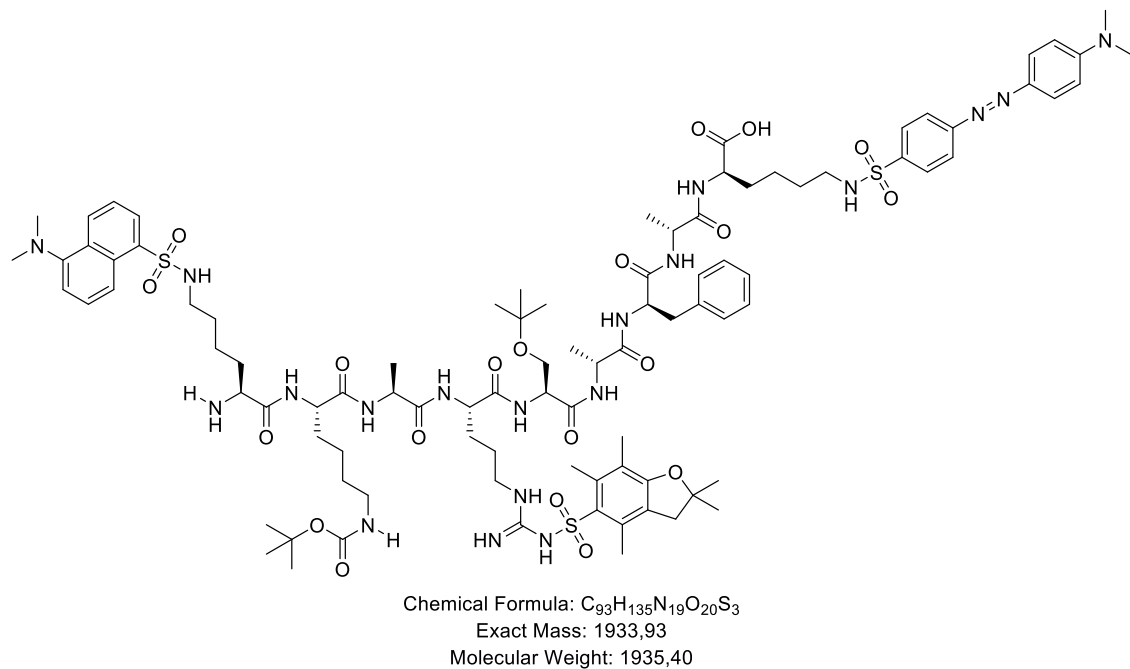


Figure S9. Structure of Lys(Dan)-KARSAFA-Lys(Dab)_{prot}.

2.4.2 HRMS Analysis

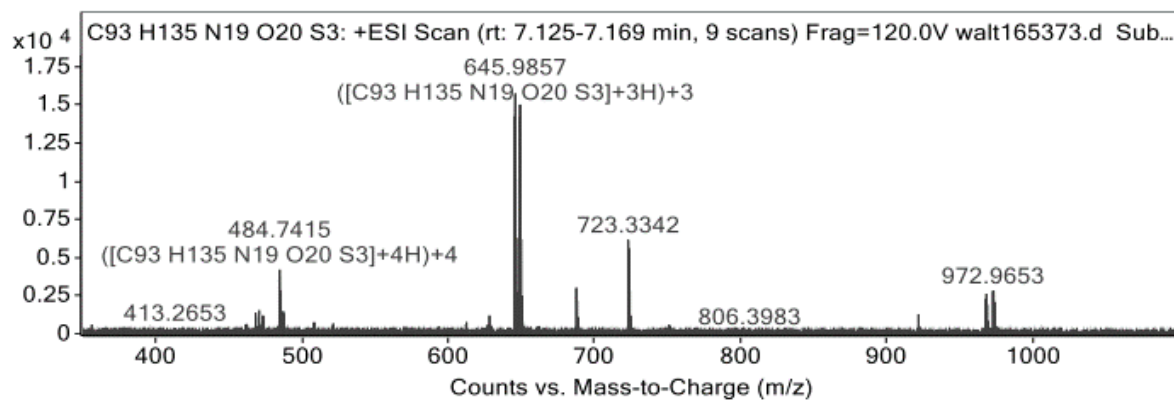


Figure S10. HRMS analysis of K(Dan)KARSAFAK(Dab)_{prot}. HRMS: *m/z* (M+3H)⁺³ calculated: 645.6504, found: 645.6513.

Chapter 6 – Supporting Information

Chapter 7

Summary and Conclusion

Chapter 7

Summary

A common reason for treatment failure in conventional drug therapy is that only insufficient amounts of the active substance reach the target site. More so, dose escalation is frequently not possible due to intolerable adverse drug effects. Targeted drug delivery using nanoparticles could provide a solution to this shortcoming [1]. However, nanoparticles face numerous obstacles such as premature elimination by the MPS, considerable off-target accumulation, or uncontrolled drug release, leading to disappointing therapy outcomes [2,3]. To overcome these drawbacks, increasingly complex strategies have been developed, such as the design of nanoparticles with multiple switchable properties activatable by intrinsic or extrinsic stimuli [4]. Although these concepts often show promising results *in vitro*, the question arises as to whether their performance can be transferred to *in vivo* conditions. Therefore, it is questionable whether highly complex strategies offer significant advantages and whether the challenging particle production and characterization can be justified (**Chapter 1**). To strike a balance between effective targeted drug delivery and rational particle preparation, nanoparticles were designed based on a blueprint from nature: viruses possess several characteristics from which a nanoparticle-based therapy may benefit tremendously. For example, they can overcome complex biological barriers, evade clearance by the immune system, selectively identify and infect their host target cells, and are able to escape the endosomal pathway effectively [5]. By developing virus-mimetic nanoparticles, these capabilities should also be transferred to the synthetic drug carriers.

The first part of the project involved the development of an adenovirus-mimetic nanoparticulate drug delivery system for the treatment of mesangial cell-associated diseases such as IgA nephropathy, diabetic nephropathy, or lupus nephritis (**Chapter 3**). The nanoparticles were anchored to their target cells by the interaction of the inhibitory ligand EXP-3174 with the AT1R on the mesangial cell surface, revealing the previously hidden receptor agonist cRGD. The nanoparticle binding subsequently promoted receptor-mediated uptake via the $\alpha_v\beta_3$ -integrin receptor and the nanoparticles selectively accumulated in the mesangial cells of the renal glomeruli *in vivo*. The distribution was monitored over 24 h by intravital microscopy. While the fluorescence in the blood vessels decreased steadily, there was a simultaneous increase in fluorescence intensity in the target tissue. Analysis of histological sections and immunohistochemical staining showed that the particles remained inside the mesangial cells for up to 10 days, which is a reasonable intracellular particle residence time for drug release.

Chapter 7

The ferroptosis-inducing substance erastin was encapsulated into the nanoparticles as a model substance, with the encapsulation efficiency being optimized by varying the ratio of shell to core polymer and the salt content of the aqueous solution for nanoprecipitation. The evaluation of ferroptosis induction *in vitro* demonstrated that the ferroptotic activity was not reduced by encapsulation, but ferroptosis progressed even faster using nanoparticles as a drug delivery system. *In vivo* studies also showed promising results. After 10 days, visible changes due to ferroptosis induction were observed, such as an increase in glomerulus size, a prominent Bowman's capsule, and an increase in the PAS-positive area. In conclusion, it has been demonstrated that the nanoparticles selectively accumulate in mesangial cells, have a reasonable particle residence time of 10 days, and allow the transport of a sufficient drug amount to induce relevant biological effects at the site of action.

However, as the presented adenovirus-mimetic targeting model is based on receptor interactions, signaling cascades could be triggered unintentionally, leading to adverse drug effects. Therefore, in the second project part, an advanced targeting concept was established using SARS-CoV2 as a blueprint, which controls both target cell identification and nanoparticle internalization via ectoenzymes.

The first step was to demonstrate that ectoenzymes are a viable alternative to classical receptor targeting approaches (**Chapter 4**). Therefore, the selective and potent ACE2 inhibitor MLN-4760 was attached to the nanoparticle surface as a targeting ligand to promote binding but not uptake into the target cells. Excellent ligand density-dependent nanoparticle avidity in the low nanomolar to picomolar range was observed for the soluble enzyme and ACE2-positive cells. Moreover, MLN-4760 was shown to selectively identify target cells even in the presence of an excess of off-target cells. The interaction between MLN-4760 and ACE2 was further confirmed by a fluorogenic ACE2 activity assay, which analyzed the inhibition of the enzyme by nanoparticle binding. As the suppression of the cleavage activity is limited in time and cell number, the effects of nanoparticle targeting can likely be compensated by endogenous mechanisms. These findings suggest that ectoenzymes may serve as target recognition motifs in the same way as receptors.

The coupling of cell-penetrating peptides as uptake signals to the nanoparticle surface was investigated for receptor-independent target cell internalization (**Chapter 5**). Several CPP candidates were synthesized, and the correlation between peptide net charge, resulting nanoparticle zeta potential, particle uptake, and cytotoxic effects was evaluated to identify the

Summary and Conclusion

most promising candidate for SARS-CoV2 mimicry. It was determined that increasing the ligand density or the net charge of the CPP results in higher zeta potentials, which correlated with higher particle uptake. However, as highly positive zeta potentials resulted in cytotoxic effects, a compromise had to be found and TAT47-57 with a net charge of +8 was selected for further experiments. The TMPRSS2-independent uptake pathway was mimicked via a conditional nanoparticle internalization concept by combining TAT, attached to shorter polymers, and MLN, bound to longer polymer chains. Thus, the initially shielded uptake signal was revealed by the attachment of MLN-4760 to ACE2, resulting in NP internalization. The receptor-independent uptake into ACE2-positive target cells was verified by flow cytometry and confocal scanning microscopy experiments and allows targeting of compartments expressing high levels of ACE2, such as renal tubules, gallbladder, cardiomyocytes, male reproductive cells, eyes, or vasculature. Furthermore, the nanoparticles developed could be used to specifically address SARS-CoV2 host target cells for antiviral therapy in the acute disease state or as an innovative treatment approach for post-covid symptoms.

Since the TMPRSS2-dependent internalization pathway is the preferred and faster route for SARS-CoV2 target cell infection, it may be beneficial to adapt the nanoparticle targeting strategy for antiviral therapy to this mechanism, thus addressing the most severely affected cells (**Chapter 6**). To develop an *in vitro* test system, HEK293 cells were first transduced to express either TMPRSS2 alone or both target enzymes, and the resulting cell lines were characterized. First approaches for the preparation of a TMPRSS2-activatable particle system and the evaluation of substrate cleavage on the particle surface leading to nanoparticle activation were presented.

Conclusion

This study established several novel strategies for improving targeted drug delivery with nanoparticles. By mimicking the internalization processes of the human adenovirus, reproducible long-term accumulation of polymeric core-shell block copolymer nanoparticles in the mesangial target tissue was achieved. By encapsulating erastin in the nanoparticle core, successful drug delivery to the site of action could be verified by histological changes in the glomerulus. This demonstrated that the proposed concept represents a viable on-site therapeutic option for the treatment of mesangial cell-associated diseases such as diabetic nephropathy or lupus nephritis. Furthermore, it was demonstrated that nanoparticles targeting exclusively via the interaction with ectoenzymes offer a promising alternative to receptor-based approaches and could thus represent a paradigm shift in the development of novel targeting strategies with minimized side effects. The high-avidity binding to ACE2-expressing cells via MLN-4760 and the selective, conditional uptake mediated by TAT47-57 allows the targeting of highly ACE2-expressing tissues such as renal tubules, gallbladder, vasculature, or SARS-CoV2 host target cells. Moreover, first considerations were made for the development of ACE2/TMPRSS2 dual-responsive nanoparticles, which may further enhance the ability to target SARS-CoV2 infected cells in the organism and thus could serve as an innovative antiviral therapy. Future studies should focus on the evaluation of the proposed concepts in preclinical studies to assess their efficacy *in vivo*.

References

- [1] G.T. Tietjen, L.G. Bracaglia, W.M. Saltzman, J.S. Pober, Focus on Fundamentals: Achieving Effective Nanoparticle Targeting, *Trends in Molecular Medicine* 24 (2018) 598–606. <https://doi.org/10.1016/j.molmed.2018.05.003>.
- [2] E. Blanco, H. Shen, M. Ferrari, Principles of nanoparticle design for overcoming biological barriers to drug delivery, *Nat Biotechnol* 33 (2015) 941–951. <https://doi.org/10.1038/nbt.3330>.
- [3] B.B. Rajeeva, R. Menz, Y. Zheng, Towards rational design of multifunctional theranostic nanoparticles: what barriers do we need to overcome?, *Nanomedicine (Lond)* 9 (2014) 1767–1770. <https://doi.org/10.2217/nnm.14.103>.
- [4] Q. Lu, H. Yu, T. Zhao, G. Zhu, X. Li, Nanoparticles with transformable physicochemical properties for overcoming biological barriers, *Nanoscale* 15 (2023) 13202–13223. <https://doi.org/10.1039/D3NR01332D>.
- [5] S. Maslanka Figueroa, D. Fleischmann, A. Goepferich, Biomedical nanoparticle design: What we can learn from viruses, *J. Control. Release* 329 (2021) 552–569. <https://doi.org/10.1016/j.jconrel.2020.09.045>.

Chapter 7

Appendix

Appendix

Abbreviations

| | |
|-------------------|---|
| ACE | Angiotensin-converting enzyme |
| ACE2 | Angiotensin-converting enzyme 2 |
| ACN | Acetonitril |
| Ang | Angiotensin |
| ApoE | Apolipoprotein E |
| AT1R | Angiotensin II receptor type 1 |
| AV | Adenovirus |
| BBB | Blood-brain-barrier |
| B _{max} | Maximum binding capacity |
| Bip | Bax-inhibiting peptide (VSALK) |
| BME | β -Mercaptoethanol |
| BTI | Breakthrough infection |
| CAR | Coxsackie and adenovirus receptor |
| CatS | Cathepsin S |
| CCIE | Clathrin/caveolae-independent endocytosis |
| CCPs | Clathrin coated pits |
| CDCl ₃ | Deuterated chloroform |
| CLSM | Confocal scanning microscopy |
| CME | Clathrin-mediated endocytosis |
| COVID-19 | Coronavirus disease 2019 |
| CPP | Cell-penetrating peptide |

Appendix

| | |
|----------------|--|
| C _q | Quantification cycle |
| CTG | CellTracker™ green |
| Cy5 | Cyanine5 |
| DBU | 1,8-Diazabicyclo[5.4.0]undec-7-ene |
| DCM | Dichloromethane |
| DIC | <i>N,N</i> '-Diisopropylcarbodiimide |
| DIPEA | <i>N,N</i> -Diisopropylethylamine |
| DLS | Dynamic light scattering |
| DMEM | Dulbecco's Modified Eagle Medium |
| DMF | <i>N,N</i> -Dimethylformamide |
| DMSO | Dimethyl sulfoxide |
| DMTMM | 4-(4,6-Dimethoxy-1,3,5-triazin-2-yl)-4-methylmorpholinium chloride |
| DOM | Degree of modification |
| Dox | Doxorubicin |
| ECM | Extracellular matrix |
| EDC | 1-Ethyl-3-(3-dimethylaminopropyl)carbodiimide |
| EI | Electroionization |
| EMEM | Eagle's minimum essential medium |
| ER | Endoplasmic reticulum |
| ERC | Endocytic recycling compartment |
| ESI | Electrospray ionization |
| FA | Folic acid |
| FACS | Fluorescence activated cell sorting |
| FBS | Fetal bovine serum |

Appendix

| | |
|-------------------------|--|
| FITC | Fluorescein |
| GA | Golgi apparatus |
| GI | Gastrointestinal |
| GGT | γ -Glutamyl-transpeptidase |
| GPCR | G-protein coupled receptor |
| HA | Hemagglutinin |
| HATU | 1-[Bis(dimethylamino)methylene]-1 <i>H</i> -1,2,3-triazolo[4,5- <i>b</i>]pyridinium 3-oxide hexafluorophosphate |
| HBTU | 3-[Bis(dimethylamino)methyliumyl]-3 <i>H</i> -benzotriazol-1-oxid-hexafluorophosphat |
| HEK293T-ACE2 | HEK293T cells stable transfected with ACE2 |
| HFIP | Hexafluoro-2-propanol |
| HPLC | High-performance liquid chromatography |
| HRMS | High-resolution mass spectrometry |
| HSPG | Heparan sulfate |
| iEDDA | Inverse electron-demand Diels-Alder cycloaddition |
| i.m. | Intramuscular |
| i.v. | Intravenous |
| IC ₅₀ | Half maximal inhibitory concentration |
| K _d | Dissociation constant |
| <i>k</i> _{max} | Maximum improvement of cellular uptake achievable |
| LCST | Lower critical solution temperature |
| LM | Leibovitz medium |
| LTDR | Lyso Tracker Deep Red |
| mAbs | Monoclonal antibodies |

Appendix

| | |
|---------|--|
| MCA | 7-Methoxycoumarin-4-acetic acid |
| MeO | Methoxy |
| MLN | MLN-4760 |
| MMP9 | Matrix metalloproteinase 9 |
| MPS | Mononuclear phagocyte system |
| MSN | Mesoporous silica nanoparticles |
| MST | Microscale thermophoresis |
| MTT | 3-(4,5-Dimethylthiazol-2-yl)-2,5-diphenyltetrazolium bromide |
| NHS | <i>N</i> -Hydroxysuccinimide |
| NP | Nanoparticle |
| noRT | No reverse transcriptase |
| NTA | Nanoparticle tracking analysis |
| NTC | No template control |
| PBS | Dulbecco's phosphate-buffered saline |
| PDI | Polydispersity index |
| PEG | Poly(ethylene glycole) |
| PLA-PEG | Poly(ethylene glycole)-poly(lactic acid) block copolymer |
| PET | Positron emission tomography |
| PFA | Paraformaldehyde |
| PLA | Poly(lactic acid) |
| PLGA | Poly(D,L-lactide-co-glycolide; lactide:glycolide 50:50) |
| PPGs | Photolabil protection groups |
| QD | Quantum dot |
| qPCR | Quantitative polymerase chain reaction |

Appendix

| | |
|---------|--|
| R4 | Arginine-4 |
| R7 | Arginine-7 |
| R10 | Arginine-10 |
| RAAS | Renin-angiotensin-aldosterone-system |
| RFU | Relative fluorescence units |
| RT | Room temperature |
| SARS | Severe acute respiratory syndrome |
| s.c. | Subcutaneous |
| SD | Standard deviation |
| SDS | Sodium dodecyl sulfate |
| SPAAC | Strain-promoted alkyne azide cycloaddition |
| TAMRA | Tetramethylrhodamine |
| TAT | TAT47-57 |
| TAMRA | 5-Carboxytetramethylrhodamine |
| TFA | Trifluoroacetic acid |
| TfR | Transferrin receptor |
| TL | Transmitted light |
| TMPRSS | Transmembrane protease serine subfamily |
| TMPRSS2 | Transmembrane protease serine subtype 2 |
| TU | Transducing units |
| UCST | Upper critical solution temperature |
| UHD | Ultra high definition |
| WHO | World Health Organisation |
| ZP | Zeta potential |

Appendix

Curriculum Vitae

Name: Melanie Bresinsky, née Walter

Date of Birth: 21.04.1996

Place of Birth: Kulmbach

Nationality: German

Scientific education:

| | |
|-------------------|--|
| 11/2020 – 11/2024 | PhD Candidate, Department of Pharmaceutical Technology, University of Regensburg |
| 02/2021 – 06/2024 | Specialization in Pharmaceutical Analytics and Technology |
| 12/2020 | Licensure as Pharmacist |
| 05/2020 – 10/2020 | Pharmaceutical Trainee, Arnulf Apotheke, Regensburg |
| 11/2019 – 04/2020 | Pharmaceutical Trainee, University Hospital Regensburg, Regensburg |
| 10/2015 – 10/2019 | Study of Pharmacy, University of Regensburg |
| 10/2014 – 09/2015 | Study of Molecular Medicine, University of Regensburg |

School education:

| | |
|-------------------|---|
| 09/2006 – 06/2014 | Grammar school, Caspar-Vischer-Gymnasium Kulmbach |
| 09/2002 – 08/2006 | Primary school, Grundschule Untersteinach |

Appendix

List of Publications

Peer-reviewed publications

1. Groner Jonas; Tognazzi Martina; Walter Melanie; Fleischmann Daniel; Mietzner Raphael; Ziegler Christian E.; Göpferich Achim M.; Breunig Miriam. Encapsulation of Pioglitazone into Polymer-Nanoparticles for Potential Treatment of Atherosclerotic Diseases. *ACS Appl. Bio Materials* 2023, 6, 6, 2111-2121
2. Zimmer Oliver; Walter Melanie; Remmert Marius; Maier Olga; Witzgall Ralph; Goepferich Achim. Impact of interferon- γ on the target cell tropism of nanoparticles. *Journal of Controlled Release* 2023, 325-341
3. Walter Melanie; Baumann Felix; Schorr Kathrin; Goepferich Achim. Ectoenzymes as Promising Cell Identification Structures for the High Avidity Targeting of Polymeric Nanoparticles. *International Journal of Pharmaceutics* 2023, 123453. **(Chapter 4)**
4. Walter Melanie; Bresinsky Merlin; Zimmer Oliver; Pockes Steffen; Goepferich Achim. Conditional Cell Penetrating Peptide Exposure as Selective Nanoparticle Uptake Signal. *ACS Applied Materials and Interfaces* 2024. **(Chapter 5)**
5. Walter Melanie; Weißbach Hannah, Gembardt Florian, Halder Sagor, Schorr Kathrin, Fleischmann Daniel, Todorov Vladimir, Hugo Christian, Goepferich Achim. Long-term Residence and Efficacy of Adenovirus-mimetic Nanoparticles in Renal Target Tissue. *Journal of Drug Targeting* 2024. **(Chapter 3)**

Appendix

Submitted to peer-reviewed journals:

1. Bresinsky Melanie; Goepferich Achim. Control of Biomedical Nanoparticle Distribution and Drug Release *In Vivo* by Complex Particle Design Strategies. **(Chapter 1)**

Conference Abstracts

1. Walter, Melanie; Goepferich, Achim; *Virusmimetic nanoparticles that identify target cells exclusively via ectoenzymes*. PBP 2022: 13th PBP World Meeting on Pharmaceutics, Biopharmaceutics and Pharmaceutical Technology, Rotterdam, Netherlands, 2022.
2. Walter, Melanie; Goepferich, Achim; *Virusmimetic nanoparticle design: An enzyme-based approach of a sequential targeting concept for polymeric nanoparticles*. CRS Germany Local Chapter Meeting, Würzburg, Germany, 2023.
3. Walter, Melanie; Goepferich, Achim; *Sequential targeting of polymeric nanoparticles: Exposure of peptidic uptake signals via multistep enzyme interactions*. Spring School in Medicinal Chemistry 2023, Regensburg, Germany, 2023.
4. Walter, Melanie; Goepferich, Achim; *Ectoenzyme-Based Targeting of Polymeric Nanoparticles – A Virusmimetic Particle Design*. DPhG Annual meeting 2023, Tübingen, Germany, 2023.
5. Walter, Melanie; Goepferich, Achim; *Shielded Cell Penetrating Peptides as Tool for Highly Selective Sequential Nanoparticle Targeting*. CRS Germany Local Chapter Meeting, Bad Dürkheim, Germany, 2024.
6. Walter, Melanie; Goepferich, Achim; *Sterically Shielded Cell Penetrating Peptides as Universal Tool for Active Nanoparticle Targeting*. CRS 2024 Annual Meeting and Exposition, Bologna, Italy, 2024.

Appendix

Acknowledgements

First and foremost, I would like to express my sincerest gratitude to Prof. Dr. Achim Göpferich, who gave me the opportunity to be part of his research group and entrusted me with this exciting project. I am very grateful for his enthusiasm, the inspiring scientific conversations, the always friendly atmosphere, and the opportunity to contribute my own ideas to the project. I am also thankful for the possibility of participating in numerous conferences and becoming a certified specialist in pharmaceutical technology and analytics.

I would also like to thank Prof. Dr. Miriam Breunig for inspiring discussions, her valuable scientific advice, and her support whenever requested.

I would like to thank all my former and current colleagues in the research group of Pharmaceutical Technology, who provided a friendly and enjoyable work atmosphere. A special thanks goes to the following colleagues:

Stephan Melchner, who accompanied me not only through my doctorate but also through my entire pharmacy studies. We spent countless hours together and I am deeply grateful for having not only a great library mate or colleague but also a lasting friendship.

My lab colleague Kathrin Schorr. I am not only grateful for the countless scientific discussions that contributed to my work but above all for the fact that she always had an open ear for problems, was the best emotional support in many situations, and made me laugh countless times.

Dr. Jonas Groner, for valuable coffee breaks, weekly challenges in the bouldering hall, and for becoming a real friend that I wouldn't want to miss.

Appendix

Johannes Lang, who was my “Hello, are you Johannes? I’m new too” colleague from the first moment to the last day of my PhD. I’m very thankful for the great times on the volleyball court, at the lake, or playing spikeball.

Jan Birringer, for our cheerful chats during LAF box cleaning and for being the best moderator and gamemaster at weddings.

Dr. Oliver Zimmer, for many joint visits to the bouldering hall, mental support when submitting scientific publications, and diligent food deliveries from the canteen.

Felix Baumann, for his valuable scientific advice and many fruitful discussions. For his never-ending willingness to help, for ensuring that I was never the last one to go home in the evening, and that I could always rely on him, at least after 10 o’clock.

Clara Barbey, for the unforgettable time on our houseboat in Rotterdam and her regular supply of cinnamon buns.

JK and Carsten, for regularly solving my computer problems and always being willing to help, no matter how stupid my questions were.

Andi, Marius, and Felix for countless Schafkopf games during lunch break.

Dr. Daniel Fleischmann, for his warm welcome at the department and his doctorate crash course, which helped me a lot over the next few years. I am also grateful to have been able to take on his exciting and promising research project.

Eva, for her outstanding organizational skills and her caring nature

Appendix

I am grateful for the excellent technical assistants I had the pleasure to work with during my time at the university. In particular, I would like to thank Grace Faltermeier for her assistance with polymer synthesis and modification, and Renate Liebl for her excellent support in cell culture, for her enormous knowledge, from which I was able to profit, and that she was always willing to help wherever she could.

The entire Department of Medicinal Chemistry I. I would especially like to thank Prof. Steffen Pockes for giving me the opportunity to work in their lab and for his scientific advice, and Alexander Hubmann, for always being there to help and for a lot of fun, which made the work easier.

Hannah Weißbach, Sagor Halder, Florian Gembardt, Vladimir Todorov, and Christian Hugo, for the excellent cooperation and the enjoyable time during my visits to Dresden.

Dr. Ramona Pawlak, Dr. Michael Majer, and Astrid Seefeld for taking the time to introduce me to PCR and Western blot.

The German Research Foundation (DFG) for providing financial support for my project.

Rather, I would like to thank my dear friends for all the great memories of the past years and for providing a sometimes much-needed refuge from science.

A very special thanks goes to my family, for their unconditional trust and support and especially to my sister for her patient proofreading.

Finally, and most importantly, I would like to thank my husband Merlin. Thank you for cheering me up when I'm feeling bad, and for being happier than I am when things are going well. Thank you for your patience, your scientific support, and for always being there for me.

Appendix

Declaration in Lieu of an Oath

I hereby declare that I have completed the dissertation presented without the impermissible help of third parties, without the use of resources other than those indicated, and that any data and concepts stemming directly or indirectly from other sources are indicated with citations to the literature.

No further persons were involved with the creation of the contents of the dissertation presented. In particular, I have not made use of the assistance of a doctoral consultant or other person in return for payment. No-one has received payment in kind either directly or indirectly for work which is associated with the content of the dissertation submitted.

The dissertation has not been submitted in the same or similar form to another examining authority, neither in Germany nor abroad.

Regensburg, den 30.10.2024

Melanie Bresinsky